ABSTRACT

Title of dissertation: MECHANISMS AND ACTUATORS FOR ROTORCRAFT BLADE MORPHING

Robert D. Vocke III
Doctor of Philosophy, 2014

Dissertation directed by: Professor Norman M. Wereley
Department of Aerospace Engineering

The idea of improved flight performance through changes in the control surfaces dates back to the advent of aviation with the Wright brothers' pioneering work on "wing warping," but it was not until the recent progress in material and actuator development that such control surfaces seemed practical for modern aircraft. This has opened the door to a new class of aircraft that have the ability to change shape or morph, which are being investigated due to the potential to have a single platform serve multiple mission objectives, as well as improve performance characteristics. While the majority of existing research for morphing aircraft has focused on fixed-wing aircraft, rotary-wing aircraft have begun to receive more attention. The purpose of this body of work is to investigate the current state of morphing actuation technology for rotorcraft and improve upon it. Specifically, this work looks at two types of morphing: Pnematic Artificial Muscle (PAM) actuated trailing edge flaps and conformal variable diameter morphing

First, active camber changes through the use of PAM powered trailing edge flaps were investigated due to the potential for reductions in power requirements and

vibration/noise levels. A PAM based antagonistic actuation system was developed utilizing a novel combination of mechanism geometry and PAM bias contraction optimization to overcome the natural extension stiffening characteristics of PAMs. In open-loop bench-top testing against a "worst-case" constant torsional loading, the system demonstrated actuation authority suitable for both primary control and vibration/noise reduction. Additionally, closed-loop test data indicated that the system was capable of tracking complex waveforms consistent with those needed for rotorcraft control. This system demonstrated performance on-par with the state of the art pneumatic trailing edge flap actuators, yet with a much smaller footprint and impact on the rotor-blade.

The second morphing system developed in this work is a conformal variable diameter rotor system suitable for implementation on a modern tilt-rotor aircraft, which can reduce power requirements in both cruise and hover configurations. An initial prototype variable-span airfoil was constructed using a silicone elastomer matrix composite skin and a plastic rapid prototyped morphing substructure. Bench-top and wind tunnel tests verified the ability of this system to increase active wing area by 100%. The prototype technology was then matured for use in the harsh rotor blade environment, with a much stiffer polyurethane skin and a titanium substructure. Coupon testing verified the efficacy of this approach, and a final conceptual design was completed using the stiffness-tuning characteristics of the morphing substructure to create a self-actuating morphing blade tip.

MECHANISMS AND ACTUATORS FOR ROTORCRAFT BLADE MORPHING

by

Robert D. Vocke III

Dissertation submitted to the Faculty of the Graduate School of the
University of Maryland, College Park in partial fulfillment
of the requirements for the degree of
Doctor of Philosophy
2014

Advisory Committee:
Professor Norman M. Wereley, Chair/Advisor
Professor Inderjit Chopra
Professor Derek Paley
Professor Sung Lee
Professor Amr Baz
Dr. Curt S. Kothera

Acknowledgments

Over the course of my 9 years at the University of Maryland (4 undergraduate, 5 graduate) I have been taught, helped, challenged, and befriended by an amazing amount of people. Without this group of coworkers, mentors, and friends, I would undoubtedly have spent another 9 years in my doctoral pursuits.

Fist, I need to thank my advisor, Dr. Norman Wereley. He is likely the most patient mentor I will ever have and has the aggravating talent of being able to motivate through a fear of disappointing him. This turns out to be much more inspirational than any other method I have yet encountered and his calm direction and guidance will be greatly missed in the future.

I also need to extend special thanks to Dr. Curt Kothera, my "dotted-line" boss who was an ever-present organizational and inspirational force throughout my graduate career. The vast majority of my research was co-directed by Curt, and I cannot stress enough how indebted I am to him. He is also the most timely and thorough proof-reader I have ever encountered, and my skills as a technical writer have improved immeasurably through his help.

My Ph.D. committee (Dr. Derek Paley, Dr. Amr Baz, Dr. Sung Lee, and Dr. Inderjit Chopra) also need special thanks, for their support, counsel, and insightful suggestions. The Aerospace Department staff has also been incredibly helpful over the years, as my funding sources have changed and I have had various panicky questions about when my next pay check will arrive, when my tuition will be paid for, and various other (at the time) monumental issues. Specifically, I would like to

thank Lavita Williams, Otto Fandino, Becky Sarni, Erika Aparakakankananange, and Thomas Hurst.

My family has always been loving and supportive. Being able to take breaks from work to go home and get a Mom-cooked meal, or borrow some camping gear from Dad, or go with Jonathan on a weekend hike, was a privileged I never took for granted. Jane Wiseman, my girlfriend of 6 years and hopefully soon-to-be family member also deserves a special thanks for putting up with me throughout this journey, and being a constant source of encouragement and strength. The future is exciting and I'm ecstatic that she'll be there to experience it with me.

I also need to thank all of my lab mates and friends, who have given me valuable advice and in general made the past 6 years seem less like work than a daily reoccurring casual get-together. In no particular order: Benjamin King Sutton Woods, Ted Bubert, Andrew Becnel, Andrew Hyslop, Greg Gremillion, Juergen Rauleder, Dr. Wei Hu, Dr. Young-Tai Choi, Erika Hocking, Ryan Robinson, Harinder Singh, Ami Powell, Tom Pilsburry, Steve Sherman, Nick Wilson, Ben Berry, Graham Bowen-Davis, Elizabeth Weiner, Chen Friendman, Mor Gilad, Zoti, Joe Schmaus, and Dave Mayo. Many apologies for anyone I have overlooked.

Finally, I would like to acknowledge the many and varied sources of funding that have supported my work over the years. These include NASA, DARPA, The Boeing Co., Bell Helicopters, and the SMART scholarship program.

Table of Contents

List of Tables

List of Figures

Chapter 1: Introduction

1.1 Problem Statement

A current technology push in advanced flight systems is to replicate certain features seen in nature. This has opened the door to a new class of aircraft that have the ability to change shape or morph [1–3]. Although the idea of improved flight performance through changes in the control surfaces dates back to the advent of aviation with the Wright brothers' pioneering work on "wing warping" [4], it was not until the recent progress in material and actuator development that such morphing control surfaces seemed practical [5]. This future fleet of morphing aircraft has received considerable attention for their potential to have a single platform serve multiple mission objectives, as well as improve performance characteristics. The same basic solutions to affect vehicle performance and stability, such as camber, span, sweep, and twist, are under investigation with morphing aircraft, but the prospect has now changed from discrete or articulated control surfaces with abrupt changes in contour, to smooth, conformal airfoils in each of several morphed shapes, as well as during the shape change [6, 7].

While the majority of existing research for morphing aircraft has focused

on fixed wing aircraft, rotary-wing aircraft have begun to receive more attention. Figure 1.1 depicts rotorcraft flight speeds over the history of rotorcraft development. Both cruise speed and maximum speed can be thought of as a metric for technology advancement. It is clear that there was initially a steady increase in flight speed from the first rotorcraft flights through the 1980s. Since then, however, the industry stagnated, as the average production/commercial rotorcraft of today has much the same performance as a 1990s era aircraft. These trends are mirrored for other performance metrics, such as useful payload fraction (fraction of rotorcraft gross weight that can be used for a useful load) and rotorcraft power loading (power to hover divided by weight of aircraft). Recent developments in advanced static rotor blade design have begun to address the complexities of rotary-wing aircraft, such as the BERP blade [8](pictured in Figure 1.2) and the ERATO blade [9], but with a few notable exceptions, morphing technologies (even those as simple as flaps) have largely been absent from rotorcraft.

The inclusion of morphing systems into a modern rotorcraft has the potential to advance the state-of-the-art past the current stagnation point. For example, actively changing the angle-of-attack of the blade sections as a function of azimuthal position has been shown to significantly alleviate vibration levels, as well as improve aerodynamic performance of the rotor [11]. Additionally, trailing edge flaps (TEF) on helicopter rotor blades can be used to reduce vibration and noise, and even affect primary control [12]. Variable diameter rotors have also been investigated due to the marked performance improvement they would lend to tilt-rotors [13]. Many more examples exist of the potential benefits of rotorcraft morphing, and so it seems

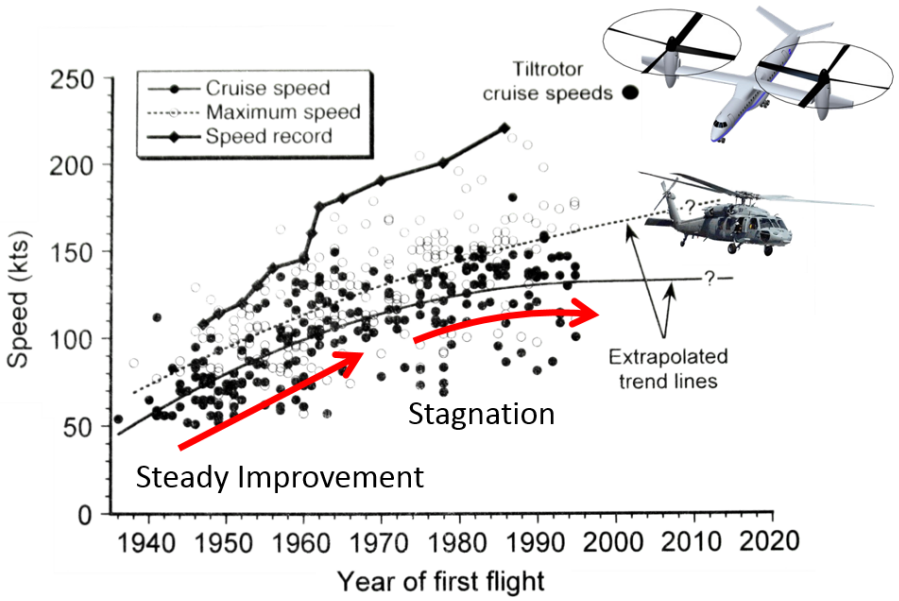

Figure 1.1: Maximum rotorcraft flight speeds over time [10].

potential for large increases in performance may have arrived [10], assuming the desired shape changes can be achieved.

Therefore, the purpose of this research is to investigate the current state of morphing actuation technology for rotorcraft and improve upon it. Specifically, this work will look at two types of morphing. The first is active camber changes through the use of Pneumatic Artificial Muscle powered trailing edge flaps. The second is a conformal variable diameter rotor system suitable for implementation on a modern tiltrotor aircraft.

1.2 Introduction to Morphing Aircraft

Morphing, as applied to aircraft [1, 2], is generally defined as large changes in configuration, such as wingspan [14, 15], sweep [16], camber [17, 18], twist, and/or chord [19, 20]. It has been shown that morphing adjustments in the planform of a

Figure 1.2: Performance enhancing BERP IV blade tip on an Augusta Westland AW101. Image from Wikipedia Commons.

wing without hinged surfaces leads to improved roll performance, which can expand the flight envelope of an aircraft [21], and more specifically, morphing to increase the span of a wing results in an overall reduction in drag, allowing for an increased range of flight [22]. For the conformal camber case, it has been shown that up to a 40% increase in lift can be achieved over the conventional hinged control surfaces or flaps [23]. Incorporating an adaptive camber line has also been shown to make more efficient use of flight control energy [24], and through feedback control of the aeroelastic shape, power requirements for the morphing deformation can be reduced by aerodynamic forces [25]. Wing folding and sweep angle have been studied, where it was shown that dynamic pressure of flutter is higher in the folded state and that increasing sweep angle causes a decrease in flutter dynamic pressure [26].

Although implementing morphing on fixed wing aircraft is a non-trivial task, there have been some notable successes. Note that wing sweep and static flap deployment, although technically considered morphing, are neglected here as they are well established technologies. Bilgen et al. [17] used piezoelectric macro-fiber

composites to actively change the twist and camber of a swept wing unmanned aerial vehicle (UAV) to achieve primary control (Figure 1.3). Likewise, Cadogan et al. [18] presented flexible piezoelectric actuators used to change the camber on an inflatable wing. The NextGen Aeronautics MFX-1 UAV uses an electro-mechanical actuator in conjunction with flexible skins to achieve large changes in sweep and chord [23, 27, 28] (Figure 1.4). Conventional pneumatic actuators have also been explored because they are lightweight and have high specific work. DeMarmier and Wereley [16] developed a variable sweep UAV wing tunnel model that utilized pneumatic muscle actuators to symmetrically sweep a main UAV wing. Samuel and Pines [14] used a customized telescopic pneumatic actuator to affect a 300% increase in span of a single wing wind tunnel model. Neal et al. [29] used linear and rotary pneumatic actuators to construct a wind tunnel test model capable of changing wingspan, twist, sweep, and extending a tail (Figure 1.5).

Figure 1.3: Fabricated vehicle using piezoelectric MFCs for active twist control [17].

Figure 1.4: NextGen Aeronautics MFX-1 morphing UAV [27].

Figure 1.5: Wind tunnel model capable of wingspan, twist, and sweep morphing [29].

1.3 Morphing in Rotorcraft

Helicopter rotors typically operate in a highly unsteady aerodynamic environment. In forward flight, a rotor blade section experiences large variations in angle-of-attack over one revolution. This is the primary source of a variety of problems such as high vibration levels and retreating blade stall. Actively changing the angle-of-attack of the blade sections as a function of azimuthal position has been shown to significantly alleviate vibration levels, as well as improve aerodynamic performance of the rotor [11]. The change in angle-of-attack can be accomplished in a variety of ways. High bandwidth hydraulic actuators in the rotating frame that can actively change the root pitch of the rotor blades have been demonstrated in scale models [30] and in full-scale tests [31]. However, implementation of such systems in production helicopters is challenging due to the complexity of the system and the increase in maintenance associated with the large number of moving parts, as well as the hydraulic slip ring. Another approach is to vary the aerodynamic forces on the blades by dynamically changing the geometry of the airfoil sections (*i.e.*, morphing). Herein, shape-changing rotor blades could be designed to account for the conflicting requirements of advancing and retreating blades, approaching an aerodynamic optimum, or to change configuration for optimal hover or forward flight performance. Thus, motivation has been provided to begin considering the possibilities of morphing rotor blades.

Recent developments in advanced rotor blade design have begun to address the complexities of rotary-wing aircraft, such as the BERP blade [8], Figure 1.2

and the ERATO blade [9], and the potential for large increases in performance may have arrived [10]. Although these advanced blade shapes are quasi-static, feasibility of dynamic shape changing skin technologies has been proven for one-dimensional structures [32–34], and airfoil structures [15, 35–37]. Additionally, recent advances in adaptive materials have led to a variety of schemes for on-blade actuation, such as adaptive twist of the rotor blade [38–42], trailing edge flaps [43–48], active camber control [49–53], active rotor span [54], and chord morphing [19]. Hence, it appears that the maturity of these types of components has progressed to a level where design for fabrication and testing on a rotorcraft system is plausible. The present work involves trailing edge flaps and variable diameter morphing specifically, and so these are discussed in more detail in subsequent sections.

1.4 Rotorcraft Trailing Edge Flaps

Trailing edge flaps (TEF) on helicopter rotor blades can be used to reduce vibration and noise, and even affect primary control. Many conceptual studies exist that point to the potential benefits of a TEF system [12,55,56], and numerous concepts have been explored for physical demonstrators with varying levels of success [11,57–60]. The main design challenge has been creating a system that is capable of meeting either the high bandwidth (for vibration and noise reduction) or high deflection (for primary control) requirements, while minimizing added weight and complexity.

1.4.1 TEF Actuation Requirements

For primary control, both Shen, Chopra, and Johnson [55] and Falls, Datta, and Chopra [57] predict a maximum flap deflection requirement of 10 degrees half peak-to-peak (HPP) at 1-2 actuations per rotor revolution (1-2/rev). These predictions were supported with scaled down wind tunnel testing, but no full-scale TEF tests for primary control were attempted, mostly due to insufficient actuation authority. Vibration and noise reduction, however, generally require less deflection. Straub *et al.* [59] and Dieterich *et al.* [60], both focused on vibration and noise reduction and represent the only TEF concepts that have been successfully implemented and tested on full-scale rotors. Straub *et al.* predicted a required 2 degrees HPP deflection at $(N_b + 1)$/rev, where N_b is the number of rotor blades, and was able to achieve 3 degrees HPP during whirl testing. Dieterich *et al.* required deflection frequencies of 3-5/rev for vibration reduction, and 2/rev for noise reduction, both at 5 degrees HPP (the actuator's maximum deflection). Note that both of these prototypes were incapable of the 10 degrees HPP deflections required for primary control.

1.4.2 TEF State-of-the-Art

Candidate actuation technologies in the literature include piezoelectric actuators [11, 44, 57, 59–61], electro-mechanical actuators [62], purely mechanical linkages (pioneered by Kaman Aerospace), and pneumatic artificial muscles (PAMs) [58, 63]. Figure 1.6 shows the only flying TEF system in existence, the ADASYS active rotor system pioneered by Eurocopter [60]. PAMs are a particularly intriguing actuation

technology due to their light weight, high specific work, high damage tolerance and fatigue life, large strains when compared to other active materials, controllability, and moderate operating pressures [53, 58, 63–65].

Figure 1.6: Eurocopter ADASYS piezo powered active trailing edge flap system for noise and vibration reduction [60].

Woods et al. [58] demonstrated a pneumatic artificial muscle (PAM) powered TEF system for a Bell 407-scale helicopter blade section capable of ±19 degrees of deflection at 1/rev (the primary rotor frequency) and ±7 degrees of deflection at 5/rev when tested at Mach 0.3 in a wind tunnel (see Figure 1.7). This large deflection margin indicates that it may be suitable for primary control as well as noise/vibration reduction, despite the test not being performed at full-scale loading. In this design, a pair of 9 inch (natural length) PAMs were oriented spanwise along the blade (perpendicular to the blade chord), and mounted near its root. This allowed a great deal of design freedom in terms of choice of PAM size and hinge mechanism dimensions. However, this approach also had a large impact on the

rotor blade itself, with mechanism components running the length of the blade and the actuation energy transferred through a number of bell-cranks before ultimately reaching the flap far outboard. This is undesirable as it increases both the weight and complexity of the blade, and makes retrofitting a PAM TEF system in an existing blade design difficult.

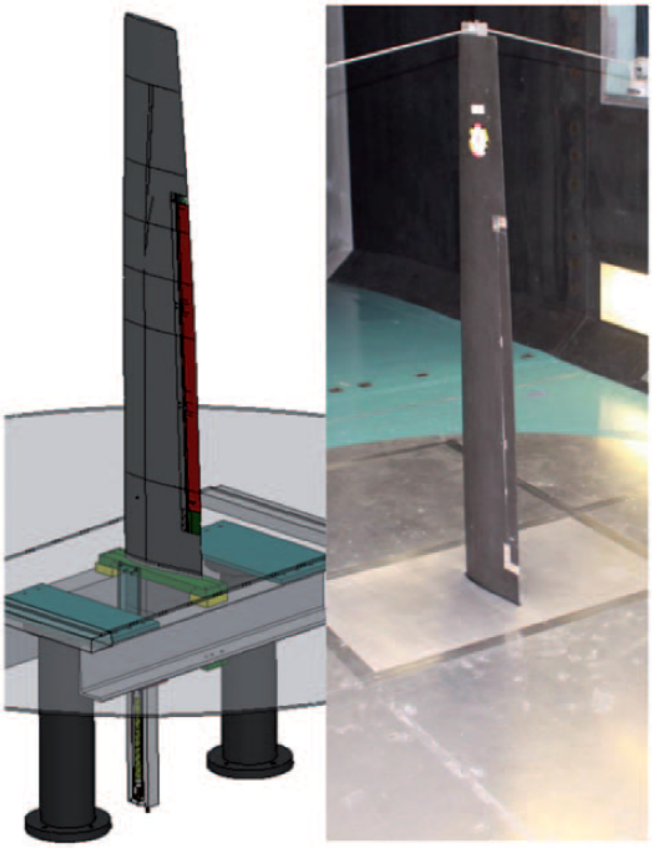

Figure 1.7: PAM actuated TEF system using spanwise placement of PAMs [58].

This past work provides motivation to examine a chordwise implementation of the PAM TEF system, where the PAMs are oriented parallel to the chord of the rotor blade. The benefits of a chordwise PAM actuator include a more direct link between the PAMs and the flap, a much smaller overall size and weight, and the possibility to make the system modular/removable as a discrete blade section. One

downside to this approach is that it necessitates the use of much shorter PAMs than in a spanwise arrangement due to the tapering nature of the airfoil and the fact that the system should not alter or interfere with the main rotor structural spar. In general, PAM contraction is limited to around 35% of their natural (resting) length. This means that a shorter PAM has less absolute contraction than a larger PAM, which introduces a major design constraint.

1.4.3 Pneumatic Artificial Muscles as TEF Actuators

Pneumatic artificial muscles (PAMs) are known for their lightweight, high-force output, and low-pressure operation [64, 66, 67]. PAMs originated in the 1950s [68, 69] and have been used primarily in robotics [70–72] and prosthetics applications [69]. A version of PAMs has also been suggested for use as springs with a variable stiffness [73]. While robotics has remained a large application area, continued development and recent demonstrations of technology improvement have created new interest in the control of aerospace structures as well, such as control of trailing edge flaps on rotorcraft [45, 53, 58, 74, 75], one-dimensional morphing [33], and active camber concepts [76].

PAM actuators consist of four basic components: an elastomeric bladder, a helically braided sleeve, and two end-fittings. In addition, as shown in Table 2.1, PAMs are lightweight and have high specific work (4400 J/kg) that is superior to that of state-of-the-art smart materials, such as piezoelectric materials or shape memory alloys. Thus, PAMs are ideal candidates for applications that require high-force and

Table 1.1: Comparison of actuator technologies

Actuation technology	Maximum strain	Specific work (J/kg)	Maximum frequency (Hz)
Hydraulic	1	35 000	100
Electromechanical[a]	0.5	300	–
Solenoid	0.4	5	80
Piezoelectric	0.002	1	100 000 000
Magnetostrictive	0.002	20	100 000 000
Shape memory alloy	0.07	4500	7
Pneumatic cylinder	1	1200	100
Pneumatic artificial muscle[b]	0.4	4400	100

Source: Adapted from [77].

Note: A dash indicates that consistent data were not available.

[a] See [78]

[b] See [75]

lightweight (*i.e.*, high specific force) actuators.

The basic form of a contractile PAM is pictured in Figure 3.1a. It consists of a stiff helically braided sleeve, initially at angle θ_0 and resting length L_N, surrounding a compliant elastomeric bladder, which is clamped and sealed at both ends with aluminum end fittings. When fluid pressure is applied inside the PAM, the bladder tends to expand radially. Because the sleeve covering the bladder is very stiff, this radial expansion forces the PAM to shorten in length by ΔL. As the PAM shortens, the fiber angle, θ, decreases until it reaches a physical equilibrium condition, called free contraction.

Many robotic or aerospace applications require bi-directional linear or rotational motion. For any uni-directional actuator, this necessitates the use of an agonist-antagonist arrangement, similar to the biceps-triceps arrangement in a human arm, such that as one actuator contracts the other actuator extends. This approach is commonly employed with conventional actuators, such as hydraulic or pneumatic

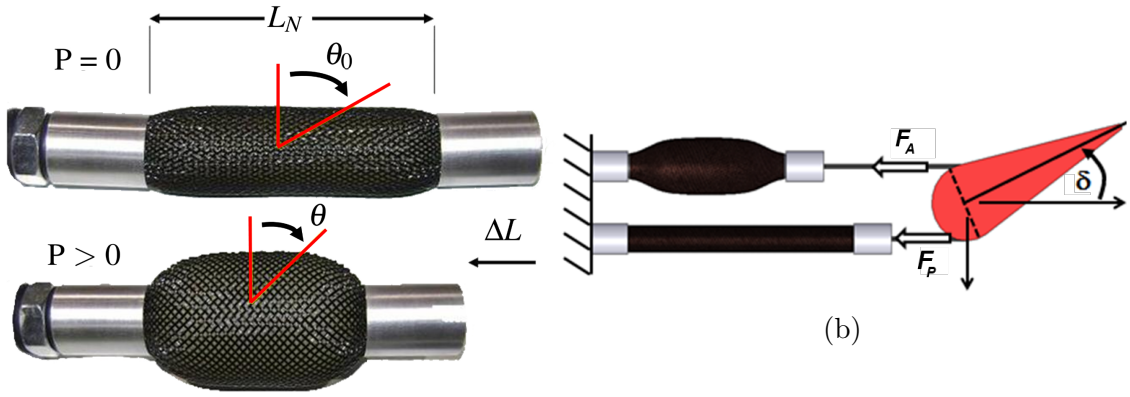

Figure 1.8: a) A typical PAM consisting of a helically braided sleeve, elastomeric bladder, and aluminum end-fittings. The PAM is shown in its relaxed and contracted states; b) PAMs arranged in an agonist-antagonist pair for bi-directional rotation

cylinders, and even newer smart materials, such as shape memory alloys [79] and electostrictive materials [80]. PAMs represent a unique challenge in antagonistic actuation, however, due to their highly nonlinear force-contraction relationship and compliance. The general bi-directional actuator configuration is shown in Figure 3.1b. Here PAMs are arranged in an antagonistic manner about a hinge, and when the active muscle contracts and pulls with force F_A, it rotates the hinge by an angle of δ until equilibrium is reached with the antagonistic muscle force, F_P, and any external hinge load. In general, this equilibrium is reached when the available torque, T_A, reaches equilibrium with the required torque, T_R.

A typical force versus contraction curve is shown in Figure 3.2 for a nominal 5/8 inch diameter PAM. Contraction is defined here as a percentage of natural (uninflated) length, and positive contraction indicates a decrease in length. Note that force levels are dependent on contraction, and increase rapidly when the PAM is stretched beyond its natural length (negative contraction). This high passive PAM

stiffness is a severe limiting factor for antagonistic actuation as it directly subtracts from the usable work available from the actuation system.

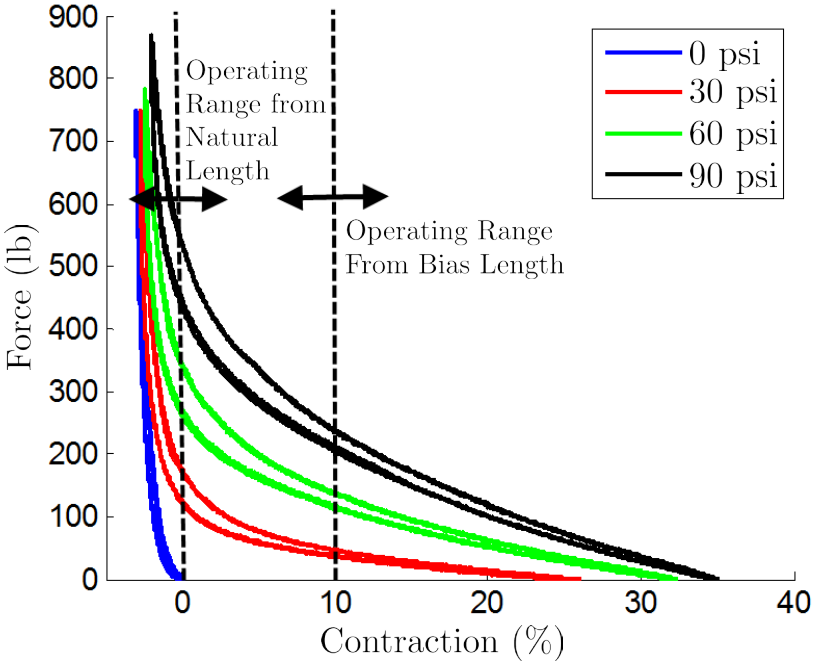

Figure 1.9: A typical PAM force vs. contraction curve, illustrating the typical operating range for an antagonistic actuator, and the operating range when bias is considered

Much work has gone into understanding the antagonistic PAM actuator design problem over the years, with the general goals of increasing actuator range of motion and controlling actuator stiffness. One approach taken is to modify the kinematics of the system, i.e., the mechanism to which the PAMs are connected, in order to influence its behavior. This work has ranged from simple pulleys [72, 81], to complex variable radius pulleys [82] and offset lever mechanisms [58, 63].

Additional work has gone into influencing the passive and active stiffness of the system by varying the bias pressure of the system, that is, the starting pressure to which both PAM are inflated, with the general understanding that higher bias

pressure equates to higher joint stiffness [83]. This topic is of great interest in the robotics field and many analyses exist to aid in joint stiffness design [82, 84–86]. Finally, most antagonistic PAM applications, with the exception of some recent aerospace applications [58, 63], have operated from a pre-contracted state in order to increase range of motion. Most studies simply list a pre-contraction value, or bias contraction, for their system [70, 72, 85–87] with little discussion of the effect of this parameter on system performance. One notable exception mentions that tuning bias contraction can have a large effect on range of motion and end-stop location, but no explicit analysis is offered on this strategy [72]. Thus, the introduction of PAM bias contraction as a design variable has the potential to dramatically affect actuator performance, and became an object of the present research.

1.5 Rotorcraft Variable Diameter Rotor Morphing

The modern tiltrotor fills a vital niche; it is capable of both vertical flight like a conventional helicopter and forward flight like a conventional airplane. However, fulfilling both of these roles simultaneously has lead to many design compromises, the most drastic of which is designing a propulsion system capable of both vertical flight (hover) and horizontal flight (cruise) [88].

1.5.1 Benefits of VDRS

In simple terms, the optimal designs for both hover and cruise configurations attempt to minimize required power at their most prevalent operating conditions.

For hover, a large diameter rotor is desired in order to minimize induced power. In forward flight, however, the required thrust is much lower, so that a much smaller rotor is typically preferred in order to reduce profile power losses. For production vehicles, such as the V-22 *Osprey*, the compromise solution has been to design blades that bridge the gap between these two competing requirements, with a smaller diameter than would be desirable for hover, while maintaining reasonable cruise efficiencies.

Many studies have looked at ways of improving tiltrotor propulsive efficiency [88–90]. There is a general consensus that there will be only incremental performance gains through static blade improvements, and that a more promising (but risky) approach is to introduce blade morphing, typically in the form of rotor diameter change, variable speed transmissions, or both [88]. The potential benefits of variable diameter rotors in tiltrotor applications were recognized in the 1970s [91], and there are longstanding efforts, most notably by the Sikorsky Aircraft Co., to develop a working system [92–95]. As with all current morphing systems, however, the introduction of a morphing capability also increases the weight and complexity of the vehicle as a whole. This is a practical issue because any new technology must buy its way onto an aircraft through either weight or cost reductions.

1.5.2 VDRS State-of-the-Art

The actuation system for retracting the morphing tip and the structure for supporting it during actuation are complex issues and vital to the success of the

proposed morphing system. However, they are not directly a part of this work. There are longstanding efforts, most notably by the Sikorsky Aircraft Co., to develop a working discrete variable diameter system for tiltrotor applications which include extensive wind tunnel testing [92–97]. Additionally, the same wealth of information indicates that each portion of this problem (the morphing structure, the sliding support structure, and the actuator) is an inherently complex issue that merits and has received individual attention. Like all rotorcraft morphing technologies (with the exception of trailing edge flaps), these actuation/support systems have not been flight tested, but sufficient work exists that demonstrates the mechanical feasibility of existing actuation and support technology.

1.5.3 Conformal Variable Diameter Morphing

It has been shown that morphing achieved without discrete moving surfaces and exposed hinges can improve roll performance and cruise efficiency in fixed-wing aircraft [21]. Additionally, morphing to smootly increase wingspan has been shown to result in increased range and endurance due to a reduction in induced drag [22]. It is clear then, that a conformal morphing system is desirable over a more traditional discrete actuation system. However, the task of designing a conformal morphing structure is immensely challenging. Thill *et al.* [98] presents a comprehensive review of requirements, current concepts, and technologies for both morphing structures and flexible skins. The topic is also investigated in a recent special issue of the Journal of Intelligent Material Systems and Structures [99]. Elastomeric materials have been

suggested as candidate skin materials for conformal morphing applications [100] due to their large strain capability, low stiffness, and passive operation. Passive flexible skins were also examined by Kothera *et al.* [101], Bubert *et al.* [33], and Murray *et al.* [34]. Isotropic elastomer morphing skins were successfully implemented on the Boeing and NextGen Aeronautics MFX-1 UAV [27]. In this design, the silicone elastomer was connected to a rigid 4-bar linkage mechanism and shape change was achieved through shear deformations in the elastomer [102]. Out-of-plane loads were reacted into a series of metallic ribbons that were stretched under the skin. McKnight *et al.* [35] proposed a reconfigurable segmented variable stiffness skin composed of rigid disks and shape memory polymer. Morphing core sandwich structures capable of high global strains have also been investigated [32, 33, 103] and an entire morphing substructure capable of continuous stable deformation was proposed by Ramrakhyani *et al.* [104] that used highly distributed actuation to achieve large global deformations with relatively low actuation force.

In Bubert *et al.* [33], a passive 1D morphing skin and substructure was developed that consisted of an Elastomeric Matrix Composite (EMC) skin supported from out-of-plane loads by a zero-Poisson substructure. The entire system was capable of a 100% active area change (Figure 6.1) while withstanding out-of-plane loads consistent with a UAV scale aircraft. Analytical modeling of the skin and honeycomb successfully predicted the in-plane stiffness characteristics of the system, and FEM analysis was used to show that the honeycomb exhibited very little local strain during actuation, and therefore low levels of internal stress at high levels of global strain, possibly lending it a reasonable fatigue life. This study stopped short of actually

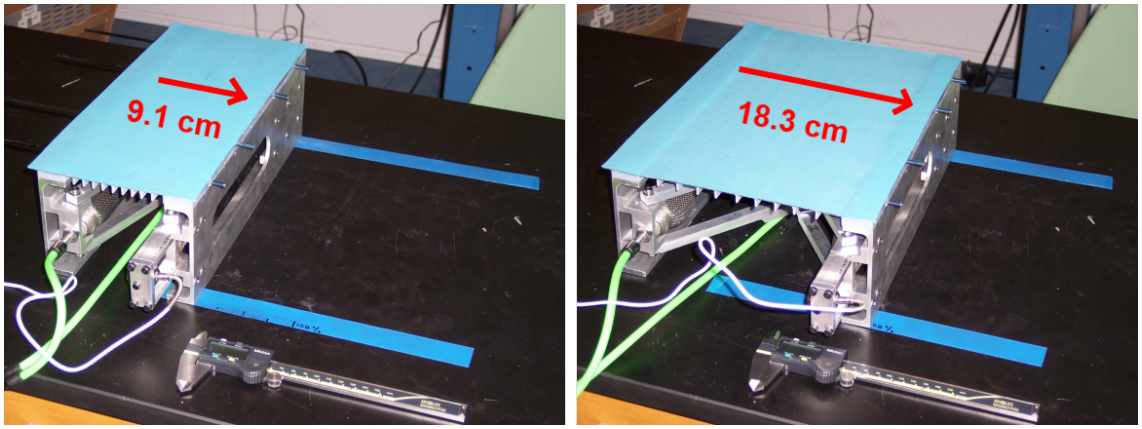

Figure 1.10: 1D morphing prototype with EMC skin and zero-Poisson honeycomb, showing 100% area change (Bubert et al., 2010).

implementing the morphing technology into an aerodynamic surface. The present work continued this effort, first into a low speed airfoil prototype, and then into system suitable for implementation on a tilt-rotor.

1.5.4 Pneumatic Artificial Muscles as VDRS Actuators

Although not comprehensively addressed in this work, PAMs could also be used to actuate a vairable diameter rotor system. It will be shown in this work that it is possible to design a conformal morphing system that is able to self-actuate under the rotor centrifugal loading. This is important as it makes the actuator responsible solely for retracting the system, allowing for use of light, flexible, yet strong materials (such as Kevlar) because the system only has to deal with loads in tension. Tension-only actuation systems for VDRS is not a new concept, where the state-of-the-art is to have a stiff and strong Kevlar strap connected to the movable part of the blade, and then wound around a spooling mechanism in the hub capable of retracting all four blades at once [93, 95]. PAMs have been previously validated as

high frequency antagonistic actuators [58,63] and so seem well suited as actuators for a ratcheting device capable of retracting and extending a Kevlar strap. The PAM system would be attached to the strap spooling system through a non-backdrivable worm gear assembly. A switching assembly (such as those found in conventional bi-directional ratchets) would allow the PAMs to both retract and extend the strap, depending on the flight requirements. This could either be implemented on the hub, controlling all four blades at once, or on each individual blade.

1.6 Contributions of Dissertation

The objective of this research is to advance the state-of-the-art in rotorcraft morphing. Original contributions to the literature were made in two distinct morphing areas: 1) trailing edge flaps and 2) variable diameter rotors.

1.6.1 PAM Driven Trailing Edge Flaps for Rotorcraft

There is a long history of trailing edge flap for rotorcraft research due to the potential for large performance gains through reductions in drag, and reductions in noise/vibration [59, 60]. The majority of these studies have focused on piezoelectric actuated concepts, which have exceptional bandwidth, but in general have been unable to achieve the deflection magnitude needed for primary control. Previous work with PAM antagonistic systems illustrated the possibility of using PAMs as TEF actuators, but the system required extensive modification to the rotor blade, and was mechanically complex [58]. This work, however, presents an improved

chordwise PAM TEF actuator with a reduced footprint that incorporates many design advances.

The present research represents the first use of PAM bias contraction as a design variable in the literature. Previous studies had recognized that bias contraction has an effect on antagonistic PAM actuators. However, none had rigorously investigated the effect that bias contraction (or bias pressure) has on the performance of said actuators. An antagonistic PAM system was simulated using a simplified PAM force model, and the effect of bias contraction, bias pressure, and antagonistic mechanism geometry was rigorously studied, with the optimum configuration of these parameters being shown to be heavily dependent on loading condition [83]. This study was then used to numerically optimize a PAM-driven trailing edge flap system suitable for chordwise implementation in a helicopter blade. The system had a much smaller footprint and much shorter PAMs than the previous state-of-the-art concept, but maintained similar authority, suitable for both primary and vibration/noise reduction tasks [105].

Additionally, a "sliding-T" mini-PAM antagonistic actuator was developed [63]. While this actuator was not suitable for trailing edge flap actuation, when comparing the PAM actuator to a commercial servo and rotary actuator with comparable maximum torque, the performance metrics of the PAM system were shown to be superior when normalized with respect to both mass and volume. This was the first study directly comparing PAM and non-PAM rotary actuators, and highlights the potential that these miniature PAM devices have for small-scale actuator applications, especially in systems where high quasi-static torque is required. For such applications,

these results show that a PAM actuation system would have both lighter weight and smaller volume than a servo with comparable maximum torque output.

1.6.2 Conformal Variable Diameter Rotor Morphing

Numerous studies have indicated that including variable diameter rotor morphing on tilt-rotor aircraft will improve both hover and cruise performance [13, 88]. Additionally, a substantial effort has gone into development of mechanisms capable of accomplishing this morphing [92, 106], which, due to increased weight and complexity, have never bought their way onto a production aircraft. All development effort has been focused on discrete, telescoping systems that introduce losses at the blade discontinuities. To avoid these losses and simplify the morphing mechanism, the present work implements a conformal variable diameter morphing technology comprised of an elastomer matrix composite (EMC) skin and a zero-Poisson's ratio substructure. While first demonstrated as a simple 1D system by Bubert *et al.* [33], the present work was the first attempt at transferring this concept into a representative 3D airfoil structure Utilizing a silicone elastomer skin, and rapid prototyped plastic substructure, the manufactured wing successfully demonstrated the concept of variable span (diameter on a rotorcraft) morphing in bench-top and wind tunnel tests, producing a 100% conformal change in wing area. However, this system was not suitable for implementation in the rotating frame due to the strength of the constituent materials and additional work was required.

The two major technologies described in the development of the prototype

variable-span wing were further matured to more aerospace-grade materials and processes [107]. The final design consisted of a 70 Shore A hardness polyurethane, sandwiching a layer of uni-directional carbon fiber, and a investment cast titanium substructure. Additionally, the entire morphing tip system (morphing core structure and EMC skin) was optimized to smoothly deploy under centrifugal loading by tuning the stiffness of the morphing structure. A genetic algorithm (GA) was first used to search the entire design space for minimum mass designs, and then the GA optima were fed into a gradient based optimizer to more effectively match the stiffness design goals. The result was a lightweight conformal morphing system that would deploy under representative centrifugal loads.

1.7 Overview of Dissertation

This dissertation is organized into eight chapters, each presenting a different aspect of the research performed. Roughly half of the work is devoted to development of a PAM trailing edge flap system, and half to the development of an elastomeric variable diameter morphing system.

Chapter 1: Introduction. This chapter presents the motivation behind morphing aircraft in general, and morphing as applied to rotorcraft specifically. Two morphing technologies, trailing edge flaps and variable diameter rotor systems, are highlighted and described in more detail and are indicated as the focus of this thesis. The potential benefits and the state-of-the-art of these morphing schemes is described. Chordwise PAM actuators are introduced as a solution for on-blade TEF actuation

and an elastomeric morphing system is considered for designing a VDRS. A summary of the valuable contributions of this work is also described.

Chapter 2: Design and Testing of a High Specific Work Rotary Actuator Using Miniature Pneumatic Artificial Muscles. The primary objective of this chapter is to compare a PAM-based servo actuator design to electric motors having comparable high frequency (1020 Hz) displacement performance. First, manufacturing PAMs on a small scale, as well as details of the final optimized manufacturing method, are presented. The PAMs are then characterized to measure their force versus displacement behavior for use in the servo actuator design. Utilization of PAMs in agonist-antagonist pairs is discussed. A kinematic system is then designed and fabricated to increase the performance of the PAM system. The analyses and designs of the PAM servo actuators are then validated experimentally. Finally, performance of the PAM-based servo actuator is compared to test data for a conventional electric servo actuator suitable for small scale UAVs and MAVs.

Chapter 3: Mechanism and Bias Considerations for Design of a Bi-Directional Pneumatic Artificial Muscle Actuator. This chapter is motivated by the lack of explicit analysis regarding the effect of PAM bias contraction on the range of motion of an antagonistic PAM system, especially when subjected to an external load. A basic introduction to PAM operation is given, followed by an explanation of the models used for the kinematic mechanisms and PAM force. The general effect of mechanism choice, bias pressure, and bias contraction on system performance is then discussed. An example design study is presented, where system performance is drastically increased with proper choice of bias contraction and mechanism geometry.

Finally, a PAM antagonistic actuator is designed, simulated, and experimentally tested, showing a drastic increase in performance from including bias.

Chapter 4: Chordwise Implementation of Pneumatic Artificial Muscles to Actuate a Trailing Edge Flap. This chapter designs a bench-top chordwise PAM TEF system capable of both primary control and vibration/noise reduction. First, PAM bi-directional actuation is discussed with a focus on methods of increasing PAM/Actuator system angular deflection. Next, a candidate UH-60-like helicopter is studied in simulation to determine appropriate loading conditions for the actuation system. A numerical optimization is then presented that maximizes the angular deflection of the PAM TEF system under the given constraints. Finally, experimental results from the optimized system are presented and discussed, from static, open-loop dynamic, and closed-loop dynamic testing.

Chapter 5: System-Level Benefits of a Variable Diameter Rotor System for a Conceptual Tiltrotor Design. Given that a variable diameter rotor system (VDRS) could be a valuable addition to a tiltrotor system, this chapter examines the effects of rotor diameter morphing on an aircraft, as a whole, from a conceptual design perspective. First, the structure of the study is presented, including a description of the conceptual variable diameter tiltrotor model as implemented in the NASA Design and Analysis of Rotorcraft (NDARC) conceptual design code and a discussion of the independent variables. The next section presents results from a typical suite of sizing runs with attention paid to the physical meaning of certain weight trends. Then, results from multiple runs are collated and presented. Finally, general conclusions and limitations of the study are discussed.

Chapter 6: Development and Testing of a Span-Extending Morphing Wing. This chapter explores fabrication techniques for advanced airfoil-like morphing core shapes, exploits customizable design parameters of in-house fabricated elastomeric matrix composite skin and core material, designs a prototype airfoil system, and experimentally evaluates a wind tunnel prototype. The prototype wing exhibited 100% span extension over its active section with very little out-of-plane skin deflection under the tested aerodynamic loading.

Chapter 7: Development of a Quasi-Static Span-Extending Blade Tip System for a Morphing Helicopter Rotor. This chapter presents the design and validation results for a quasi-static morphing helicopter rotor blade with an adaptive tip. The technology components, including a morphing honeycomb-like core structure that has a Poisson's ratio of zero as it extends and an elastomer-matrix-composite skin that is bonded to the core structure, are described. Design analyses along with experimental validation on hardware specimens are presented. The validated model is used in a numerical optimization to design a system that will self-actuate under a rotor's normal operating conditions. Feasibility of the design is demonstrated in terms of hardware fabrication methods and overall performance to satisfy system design goals.

Chapter 8: Conclusions. Major conclusions of each chapter are recapitulated. The impact of this work on the literature is discussed, and suggestions for future work are given.

Chapter 2: Design and testing of a high-specific work rotary actuator using miniature pneumatic artificial muscles.

2.1 Introduction

Unmanned Aerial Vehicles (UAVs) have a ubiquitous presence in modern civil and military aviation. UAVs can perform missions that are challenging or unsuitable for manned aircraft such as high-endurance and high altitude flight. As UAVs have evolved, they have enjoyed a rate of innovation, which, in recent decades, has been unheard of in the relatively conservative precedent-driven design of manned aircraft. Also, smaller UAVs, dubbed micro-air vehicles (MAVs), are occupying previously unfilled niches in both the civil and military sectors. UAVs and MAVs, which have wingspans ranging from meters down to centimeters, may not be well suited to conventional aircraft actuation technologies such as hydraulics and electro-mechanical actuators due to space and weight considerations. Many MAVs use commercially available electric servo actuators, but these may not have the necessary (static) torque or actuation speed requirements.

To date, many novel UAV actuation schemes have been developed, including many utilizing smart materials and/or achieving control via morphing rather than traditional control surface actuation schemes [1]. Morphing, as applied to aircraft [2], is generally defined as large changes in configuration, such as wingspan [14, 15], sweep [16], camber, twist, and/or chord [19, 20]. Bilgen et al. (2009) [17] used piezoelectric macro-fiber composites to actively change the twist and camber of a swept wing UAV to achieve primary control. Likewise, Cadogan et al. (2004) [18] presented flexible piezoelectric actuators used to change the camber on an inflatable wing. Piezoelectric actuators have also been used on rotorcraft for active trailing edge flap actuation [59]. The NextGen Aeronautics MFX-1 UAV uses an electro-mechanical actuator in conjunction with flexible skins to achieve large changes in sweep and chord [23, 27, 28]. Conventional pneumatic actuators have also been explored because they are lightweight and have high specific work. DeMarmier and Wereley (2003) [16] developed a variable sweep UAV wing tunnel model that utilized pneumatic muscle actuators to symmetrically sweep a main UAV wing. Samuel and Pines (2007) [14] used a customized telescopic pneumatic actuator to affect a 300% increase in span of a single wing wind tunnel model. Neal et al. (2004) [29] used linear and rotary pneumatic actuators to construct a wind tunnel test model capable of changing wingspan, twist, sweep, and extending a tail.

This study presents an alternative, small-scale pneumatic actuation technology based on pneumatic artificial muscles (PAMs), which are known for their lightweight, high-force output, and low-pressure operation [64, 66, 67]. PAMs originated in the 1950s [68, 69] and have been used primarily in robotics (Tondu et al., 2005; Tondu

Table 2.1: Comparison of actuator technologies

Actuation technology	Maximum strain	Specific work (J/kg)	Maximum frequency (Hz)
Hydraulic	1	35 000	100
Electromechanical[a]	0.5	300	–
Solenoid	0.4	5	80
Piezoelectric	0.002	1	100 000 000
Magnetostrictive	0.002	20	100 000 000
Shape memory alloy	0.07	4500	7
Pneumatic cylinder	1	1200	100
Pneumatic artificial muscle[b]	0.4	4400	100

Source: Adapted from [77].

Note: A dash indicates that consistent data were not available.

[a] See [78]

[b] See [75]

and Lopez, 1997; Trivedi et al., 2008a, b; van der Smagt et al., 1996) [70–72] and prosthetics applications [69]. A version of PAMs has also been suggested for use as springs with a variable stiffness [73]. Our recent work has focused on the design and control of trailing edge flaps on rotorcraft [45, 53, 58, 74, 75] and one-dimensional morphing [33]. PAM actuators consist of four basic components: an elastomeric bladder, a helically braided sleeve, and two end fittings. In addition, as shown in Table 2.1, PAMs are lightweight and have high specific work (4400 J/kg) that is superior to that of state of the art smart materials such as piezoelectric materials or shape memory alloys. Thus, PAMs are ideal candidates for applications that require high-force and lightweight (i.e. high specific force) actuators.

The primary objective of this chapter is to compare a PAM-based servo actuator design to electric motors having comparable high frequency (1020 Hz) displacement performance. First, manufacturing PAMs on a small scale, as well as details of the final optimized manufacturing method, are presented. The PAMs are then

characterized to measure their force versus displacement behavior for use in the servo actuator design. Utilization of PAMs in agonistantagonist pairs is discussed. A kinematic system is then designed and fabricated to increase the performance of the PAM system. The analyses and designs of the PAM servo actuators are then validated experimentally. Finally, performance of the PAM-based servo actuator is compared to test data for a conventional electric servo actuator suitable for small-scale UAVs and MAVs.

2.1.1 Actuator Requirements

Table 2.2 shows performance characteristics for a commercially available servo actuator used on a MAVscale aircraft. In addition, Table 2.3 gives nominal values for deflection range, hinge moment, and deflection rate for a nominal and general Baseline Actuation System (BAS), which will serve as a benchmark for the present system.

Table 2.2: Description of DS285MG Digital High Speed servo performance characteristics at two operating voltages.

Voltage (V)	Torque (Nm)	Weight (g)	Volume (cm^3)	Speed (s/60°)	T/W (Nm/g)	T/V (Nm/,^{3})
4.8	0.12	11.9	5.44	0.18	0.010	0.022
6.0	0.13			0.14	0.011	0.024

2.2 Mini-PAM Development

Figure 1(a) depicts the basic structure of a PAM. The elastomeric bladder (not seen) is covered by a braided sleeve and both are sealed together at their ends

Table 2.3: Baseline actuation system specifications.

Parameter	Units	Specification
Nominal deflection range	degrees	± 20
Loaded rate	degrees/s	500
Maximum hinge moment	Nm	1.0

by metallic fittings. The end fittings serve as both pneumatic seals and actuator attachment points. Actuation is achieved by inflating the bladder. The braided sleeve is nominally much stiffer than the bladder and does not stretch as the bladder inflates. Instead, it balloons outward increasing its radius, which causes the PAM to shorten in length by ΔL to its free contracted length (or equilibrium position, if loaded). This change in length is clearly visible in Figure 3.1a. Alternatively, if the PAM is held at its resting, or active length, La, and pressurized, the PAM will exert a contractile force mainly determined by the nominal angle of the braid, θ_0, and the applied pressure. See [64] for a complete description of the PAM analysis used in this study.

In order to harness the purely contractile motion of a PAM to achieve the bidirectional rotation needed for control surface actuation, an antagonistic configuration is required. Figure 4.2 shows a conceptual model of two PAMs connected to a control surface. When the pressure p_A is greater than p_P as the figure shows, the upper PAM contracts and causes the control surface to deflect counter-clockwise. Note that in this configuration, the opposing PAM has to extend by the same amount that the first PAM contracts, thereby imposing a physical limit on the deflection of the system.

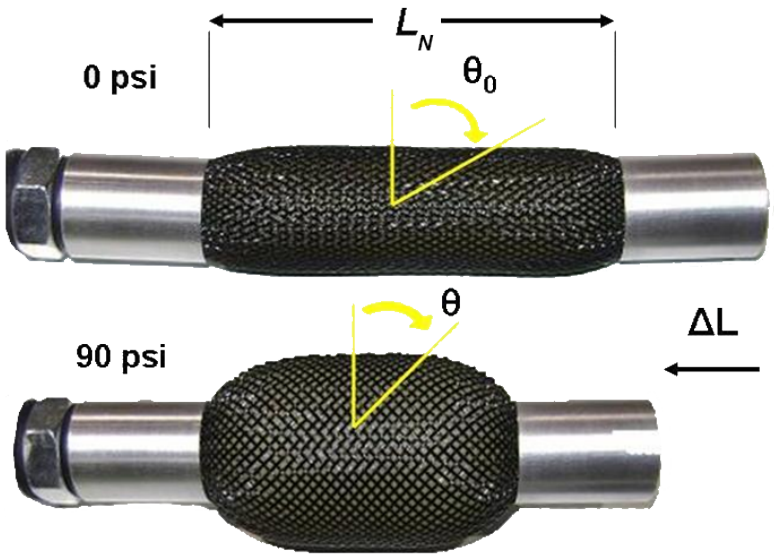

Figure 2.1: Depiction of a PAM in resting and contracted states.

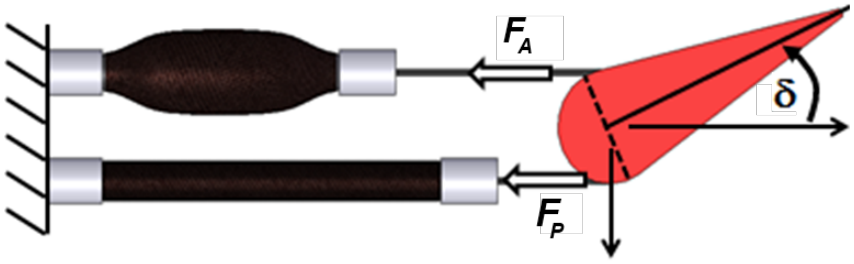

Figure 2.2: Two PAMs connected in an antagonistic configuration with $p_A > p_P$.

2.2.1 Mini-PAM Fabrication

Previous work with PAMs has focused on actuators with diameters on the order of an inch and lengths on the order of one foot. A PAM having such dimensions would be far too large for a MAV actuator, and thus a primary focus of the present work was to investigate PAM miniaturization using air as the working fluid as opposed to water as was done by Solano and Rotinat-Libersa (2011) [108].

In the preliminary manual fabrication process, the braided sleeve and elastomeric bladder were secured to threaded rod end fittings by manually winding safety wire around each end of the device. However, such a labor-intensive fabrication process led to manufacturing inconsistencies due to differing tension levels in the wire windings. As a result, a refined fabrication procedure was developed that lead to consistent specimens and reduced the assembly time required.

The refined fabrication process presses an aluminum tube concentrically around the braided sleeve and elastomeric bladder onto the threaded rod end fitting. As can be seen in Figure 2.3, the refined swage process eliminates the need for wire winding to secure the end fittings and replaces it with a press-fit of a solid aluminum tube to create uniform pressure. The fabricated PAMs were tested for repeatability on multiple actuator specimens. During testing, it was discovered that the miniature PAM actuators produced sufficient force to tear themselves apart. To remedy this, a small amount of epoxy was applied to the braided sleeve where it contacted the end fittings before the assembly was swaged. This epoxy provided a chemical bond between the braid and the end fittings, in addition to the mechanical bond provided

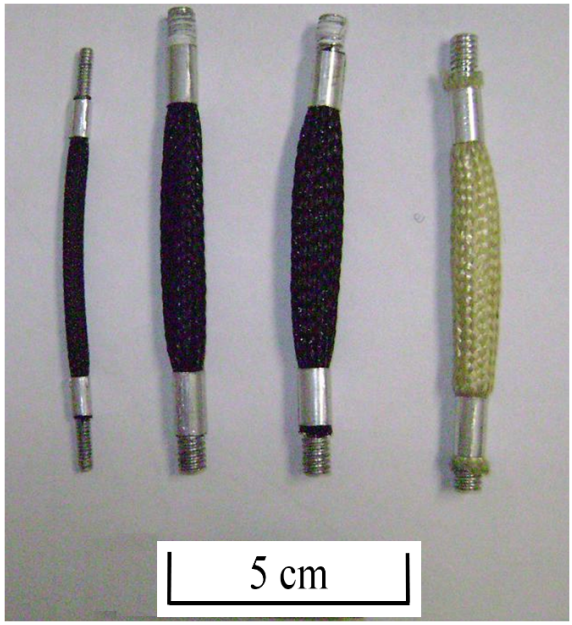

Figure 2.3: Fabricated miniature PAMs with swaged end fittings.
Note: PAM = pneumatic artificial muscle.

by the deforming action of the tube. The results of this improvement can be seen in Figure 2.4, where the factor of safety was increased from 0.94 to 2.95, based on the 620 kPa (90 psi) blocked force.

2.2.2 Characterization of Refined PAM Actuators

PAM performance is characterized by inflating to a constant pressure and then allowing contraction through its full range of motion. The two key points of interest in the constant pressure tests are the blocked force and the free contraction. The blocked force is the force exerted by the PAM when the ends are restrained or fixed and unable to move. This is the maximum force level available for a given PAM actuator at a given pressure setting. However, free contraction is the maximum stroke available from a given PAM actuator at a given pressure, but the actuator produces no force in this condition. Figure 2.5 illustrates each of these two conditions, blocked

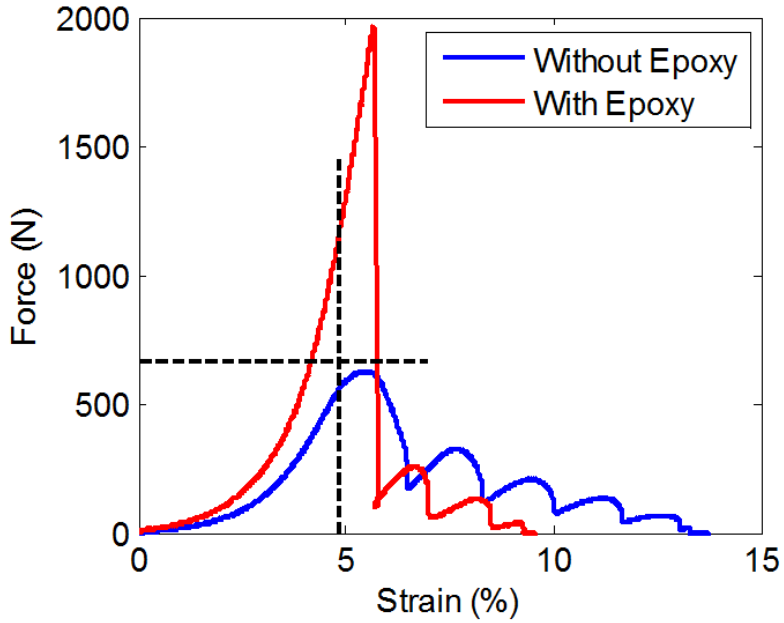

Figure 2.4: Tensile failure data of 1/4-inch OD PAM actuator with 3/8-inch Kevlar braid.

Note: OD = outer diameter; PAM = pneumatic artificial muscle.

force and free contraction, during one of the tests at 620 kPa (90 psi). Figure 2.5a shows the resting length of the PAM with its resting diameter, whereas Figure 2.5b shows the maximally contracted length of the PAM with its increased diameter. Recall that the general function of a PAM actuator is for the diameter to increase in response to increasing internal pressure, and this diameter increase causes the actuator length to decrease. Also note that the large diameter shown in Figure 2.5b would never be physically reached in a typical actuation environment because the PAM cannot hold any force or produce any mechanical work in this state. These experiments, conducted on a servo hydraulic MTS machine, collected load-stroke data at a series of constant pressure settings from 0–620 kPa (0–90 psi) in 206 kPa (30 psi) increments. Table 2.4 gives nominal dimensional and material values for some of the PAMs tested. Note that PET denotes polyethylene terephthalate, a thermoplastic

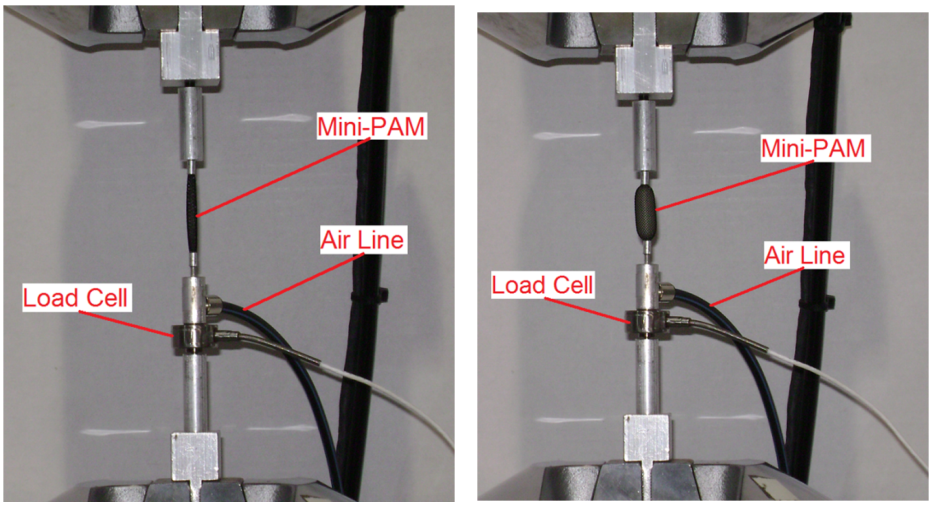

(a) resting length (b) free contraction

Figure 2.5: Characterization of miniaturized and swaged PAM actuators

Table 2.4: Miniature PAM actuator fabrication properties.

PAM OD (inches)	Nominal braid OD (inches)	Braid material	θ_0 (degrees)
1/8	1/4	PET	76.5
1/4	3/8	PET	69.0
1/4	1/2	PET	77.0
1/4	3/8	Kevlar	69.0

Note: PAM = pneumatic artificial muscle; OD = outer diameter; PET = polyethylene terephthalate.

polymer, and that the listed braid sizes correspond to the manufacturer's designation, but θ_0 was measured on the assembled actuators.

Although several PAMs were tested, in the interest of brevity, characterization results from only one will be presented. Note that the PAM size and nominal braid size are listed in imperial units as this is the convention used by the braid and bladder manufacturers. Figure 2.6 shows a set of characterization data for 1/4-inch outer diameter (OD) actuators with 3/8-inch Kevlar braid in the noted pressure

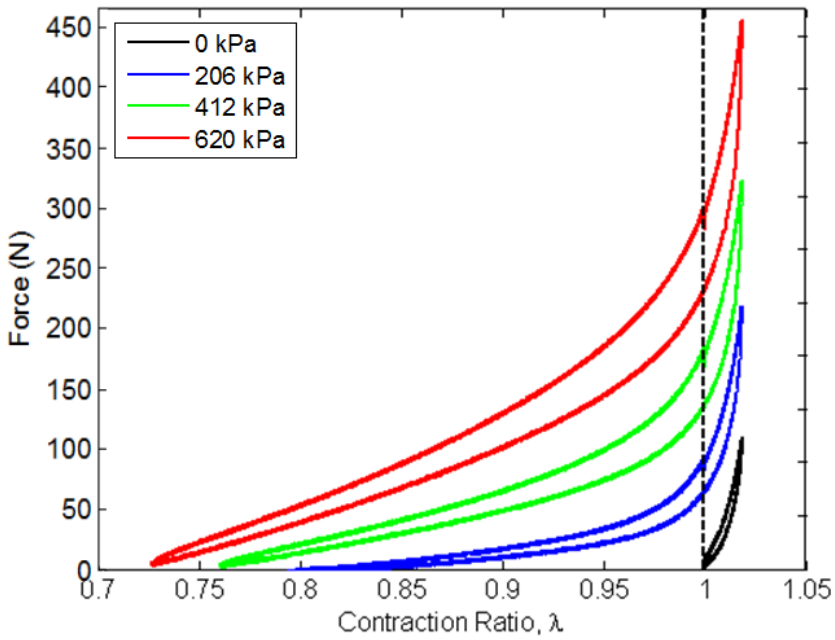

Figure 2.6: Quasi-static performance of 1/4-inch OD PAM actuator with 3/8-inch Kevlar braid showing experimental loading cycles at various pressures.
Note: OD = outer diameter; PAM = pneumatic artificial muscle.

range. The horizontal axis is the contraction ratio, l, defined as

$$\lambda = (L_a - \Delta L)/L_a \tag{2.1}$$

Note that both negative and positive contractions are shown in Figure 2.6. Positive contractions denote a decrease in length, which is the normal response for these actuators when internally pressurized, while negative contractions (extensions) represent the force characteristics when the actuator is stretched beyond its resting length, which is required in an antagonistic actuator arrangement for bidirectional control. Each constant pressure test began with both ends fixed, and the PAM pressurized to the noted settings (blocked force condition). The actuator was then stretched by 2.5% of its resting length and held momentarily before allowing the actuator

to contract to the point at which it could carry no load (free contraction). After a momentary hold, the actuator was then stretched back to its resting length to complete a full loading cycle and the test was stopped. Force-contraction cycles can be seen in the figure for all four pressure settings, where it can be noted that increasing pressure causes increases in both the force and contraction levels attained. Eventually, a limit is reached where further increases in pressure result in no further increases in free contraction due to physical constraints in the braid. The small hysteresis loop seen at all four pressures is caused by damping in the elastomeric bladder and friction in the braid. Damping in this system has the positive effects of knocking down resonant peaks and increasing phase margin, making the system more stable. However, it could limit bandwidth, and if precise control of the PAM length is required, an inner loop control must be added to track the actuator commands, for example, delay compensation control [53].

2.3 Actuator Development

As shown in Figure 2.6, PAMs exhibit rapid stiffening when stretched to contraction ratios greater than 1. This is the main performance limiter for an antagonistic PAM actuation system, as the inactive or stretching PAM exerts a force that directly subtracts from the force that can do useful work in the system. Because fairly large deflections and moments were required for this UAV application ($\pm$20 degrees of deflection, 1.12 Nm of torque respectively), the kinematics of the device were examined as a possible way to increase performance.

Figure 2.7. depicts the two kinematic options that were considered for enhancing the output performance of the PAM-actuated control surface. Figure 3.3b shows a triangle with the center of rotation pinned at the bottom vertex. The two downward pointing (blue) arrows represent forces applied at distances R_A and R_P, from the centerline (axis of rotation) of the triangle. These forces are also applied at an offset distance h_0 above the axis of rotation. Figure 2.7b shows an ellipse with major axis length a and minor axis length b. The axis of rotation is also located at an offset distance h from the midline of the ellipse on the major axis. The blue line represents the force applied to the ellipse and is continuous over the top of the ellipse to emphasize that this mechanism approach would involve some sort of flexible linkage (e.g. cable or strap), not just fixed connection points as would be the case for the triangle. These offset-type mechanisms were considered over their simpler counterparts because they offer more advantages when used with an antagonistic set of PAM actuators. Recall that the force available from a PAM decreases as the stroke increases for the active PAM, while the antagonistic stiffness increases through stretching of the passive PAM. Hence, a mechanism with an increasing moment arm on the active PAM and a decreasing moment arm on the passive PAM is preferred for this configuration. Note that the simpler version of the triangle is a slender bar where the offset distance has collapsed entirely to $h_0 = 0$ cm. This simple "see-saw" mechanism has active and passive moment arms, R_A and R_P, that vary equivalently as the bar rotates, which is not optimally suited to the force-stroke characteristics of an antagonistic PAM actuator pair. Similarly, the simpler version of the offset ellipse is a circle rotating about its center (e.g. a pulley wheel), which has constant

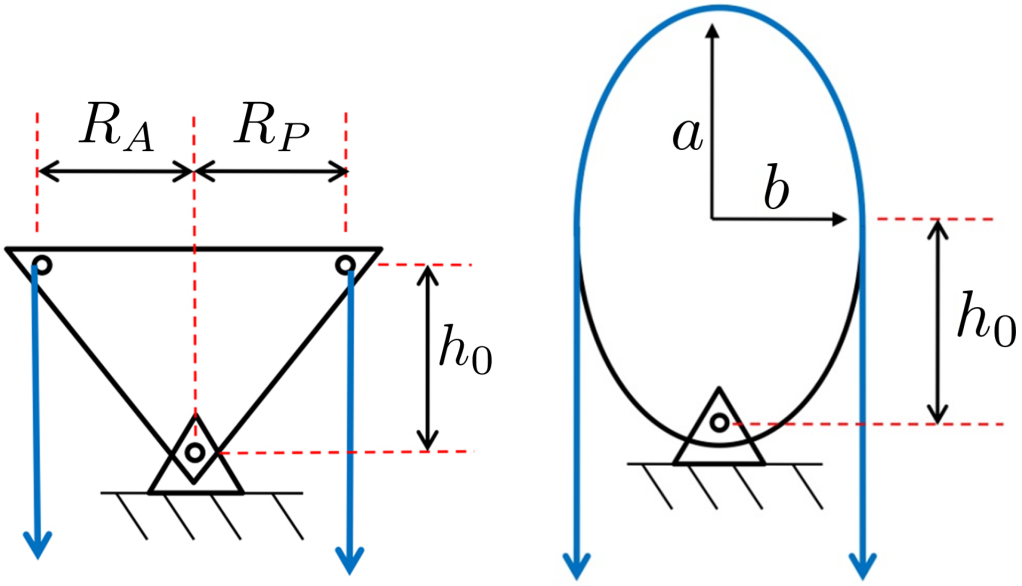

(a) offset lever -or- bell crank (b) elliptical offset

Figure 2.7: Mechanism considerations for PAM actuator

moment arms as the circle rotates. For the present application of a MAV actuator, bidirectional motion is required. Considering the implementation of PAM actuators, this is much like the triceps and biceps in the human arm as they bend the elbow. For example, in Figure 3.3b, if the left side PAM contracted, the triangle would begin to rotate counterclockwise and the moment arm (perpendicular distance) from the direction of the PAM contractile force to the point of rotation would increase. Simultaneously, the moment arm of the passive PAM (on the right side) would begin to decrease. The process is much the same for the ellipse in Figure 2.7b. The relative rate at which the moment arms increase and decrease can be tuned by adjusting the parameters identified in the figure: R_A, R_P, a, b, and h_0.

2.3.1 Actuator Performance Simulation

The quasi-static kinematics of the triangular and elliptical mechanisms are defined by the parameters R_A, R_P, a, b, and h_0, along with an angle of rotation δ, and output moment arm, contraction, and extension data. In order to make a meaningful comparison, the geometries of the triangle and ellipse were set up to be similar: $R_A = R_P = b = 2.54$ cm (1 inch), and $a = h = 3.81$ cm (1.5 inches) for this particular study. Figure 2.8a shows the effective moment arms for both the ellipse and the triangle as they deflect from vertical to horizontal (0–90 degrees). The solid lines show the increasing moment arms for the contraction side, and the dotted lines show the decreasing moment arms for the extension side, both starting at the nominal value of 2.54 cm (1 inch). Note that the ellipse has a large advantage over the triangle at high deflection angles but very little advantage at small angles of deflection. For the present study, we are interested most in deflections ranging from 0 degrees to 20 degrees, so the high deflection characteristics are not of particular interest. Over the smaller range, the triangle and ellipse show similar performance. Figure 2.8b shows the associated PAM length change over a shorter angular range. In fact, the PAM extensions (dotted lines) above 10 degrees begin to deviate with the ellipse, thus requiring more extension. Given the sharp increase in antagonistic stiffness shown in Figure 2.6, this figure suggests that the triangle mechanism is the leading candidate.

The moment arm and contraction data described above was compiled and used to simulate the output torque for a number of antagonistic systems (e.g. PAM vs.

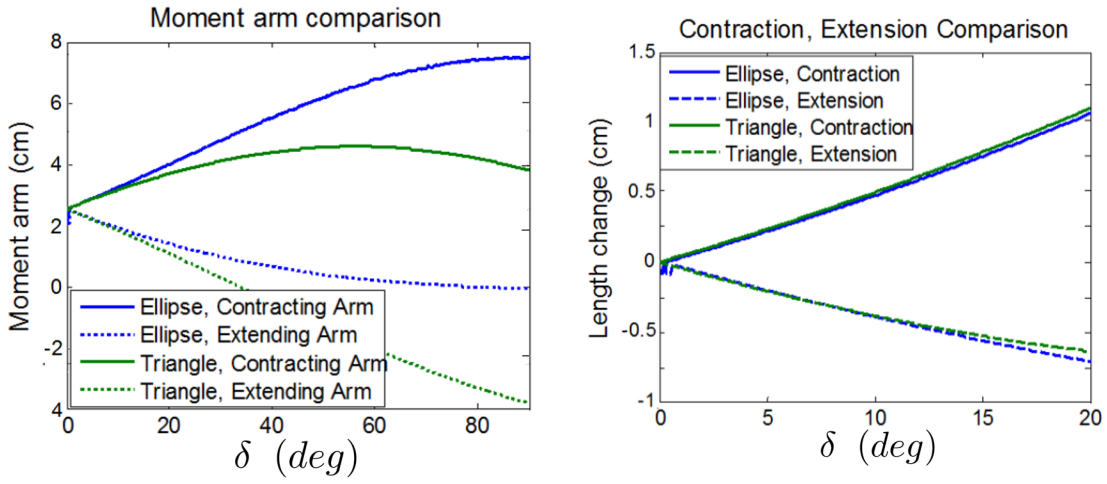

(a) moment arm

(b) PAM length change

Figure 2.8: Comparison between ellipse and triangle mechanisms

PAM, PAM vs. spring). Actuator force levels were taken from a 4th-order polynomial fit of measured force-deflection curves shown in Figure 2.6. Note that this mechanism model was verified by comparing measured performance of the prototype system with only one PAM acting against an extension spring with analytical predictions, thus the model should prove effective in identifying the most ideal PAM for further development here, as well. Model simulations were performed with the triangular lever mechanism discussed previously, having a fixed neutral radius-to-rotational offset ratio ($R/h_0 = 0.5$). The purpose of these simulations was to compare the performance of the overall MAV actuator for different antagonistic pairs of PAMs and to ultimately select the best candidate for further characterization testing and integration with the prototype bench-top actuator system. Figure 2.9a shows the simulated response of the antagonistic setup at 620 kPa (90 psi) for the three 1/4-inch OD PAMs from Figure 2. The 1 Nm constant torque line indicates the metric used to determine which PAM construction would produce the best actuator. It can be

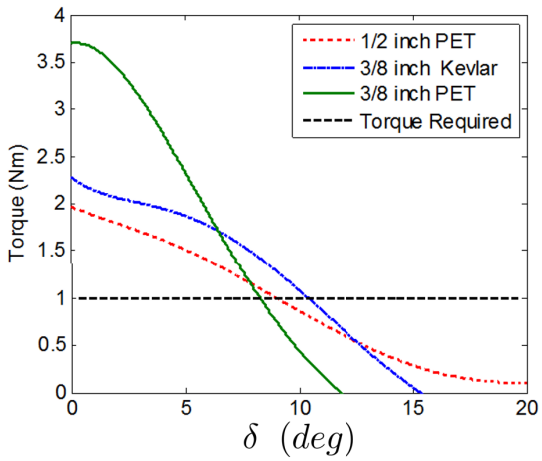

(a) for various PAMs at 620 kPa (90 psi)

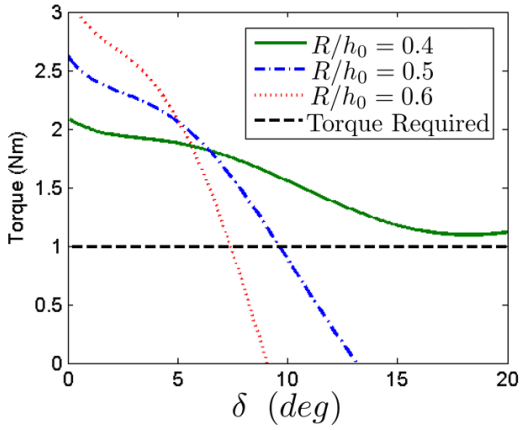

(b) for Kevlar PAM at different mechanism ratios.

Figure 2.9: Simulated response of actuation system

seen in the figure that the 1/4-inch OD PAM with 3/8-inch Kevlar braid (blue line) generates the torque that produces the largest deflection angle, thereby highlighting itself as the best option for the MAV actuator.

Having selected the 1/4-inch OD size PAM with 3/8-inch Kevlar braid for the prototype miniature actuation system, other design simulations were performed to examine the effect of the radius-to-offset ratio, R/h_0. Figure 2.9b displays these results. As the figure shows, increasing this ratio causes an increase in torque available at 0 degrees at the expense of a sharper decrease with increasing angle. Conversely, a smaller ratio reduces the 0 degree torque available while flattening out the torque as a function of angular deflection, which results in the ability to achieve larger deflections. For the angle range of interest for the present work, this comparison therefore illustrates that smaller R/h_0 ratios are better suited to produce the higher deflection angles. It should be noted that the size selected for implementation on the benchtop prototype is $R/h_0 = 0.5$. While Figure 2.9b showed that smaller

ratio values can theoretically produce more torque for a greater range of angular deflections, there comes a point where physical realization and construction of the test rig becomes difficult. Therefore, the radius-to-offset ratio and physical dimensions selected for the prototype were chosen based upon what could be reasonably built for test.

2.3.2 Refined Design

When configured antagonistically, as is the case here, the pressurized PAM has to pull against the antagonistic force of the opposing (deflated or low pressure) PAM, in addition to the external load acting on the device. Hence, this antagonistic force has a parasitic effect of reducing useful work, both quasi-statically and dynamically. Without it, or with a substantially reduced antagonistic force, the effect on output deflection performance would be an overall increase. While this was taken into consideration in the existing mechanism, that is, the offset rotational axis, another mechanism was conceived that could passively modify (decrease) the moment arm of the antagonistic PAM even farther. As in the previous setup, this concept also features a three-point, triangular offset design, which will be referred to here as a T-shape. When at rest (unrotated), the mechanism in Figure 2.10a looks like a conventional T configuration but with the addition of two slots that are angled slightly upward and toward the center of the T. The PAMs are mounted on posts that are free to slide in these slots. For example, as the left PAM activates (contracts), it starts pulling the mechanism counterclockwise and behaves like the regular T

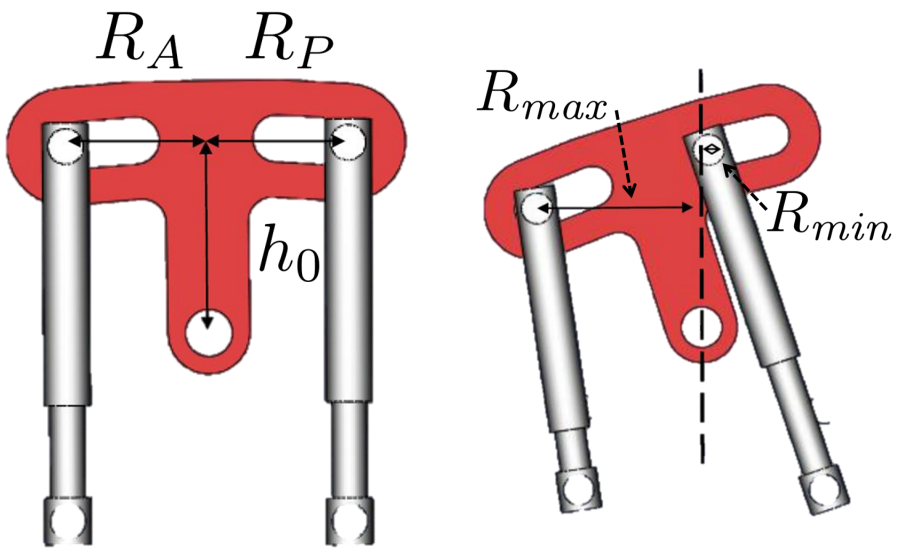

(a) in neutral position

(b) rotated to illustrate maximum radius difference

Figure 2.10: Sliding moment arm mechanism

configuration until it reaches the angle of the slots. At that point, the passive antagonistic PAM will slide to the position on the slot where its moment arm is minimal (R_min), which has the effect of minimizing its antagonistic force on the actuator output (see Figure 2.10b). Note that this occurs at the geometry where the active PAM has its maximum moment arm (R_max), which further contributes to increased performance in terms of torque available to work against the external load.

The effect of the sliding radius attachment point is highlighted when comparing the left (without slots) and right (with slots) portions of Figure 2.11, which plot normalized the colors and line styles in each figure are consistent for each radius-to-offset ratio. Examining the lower extreme of $R/h_0 = 0.1$ first (topmost solid (blue) curve), the torque available increases as a function of deflection angle to the point where it essentially remains constant at the 0 degree (blocked torque) condition.

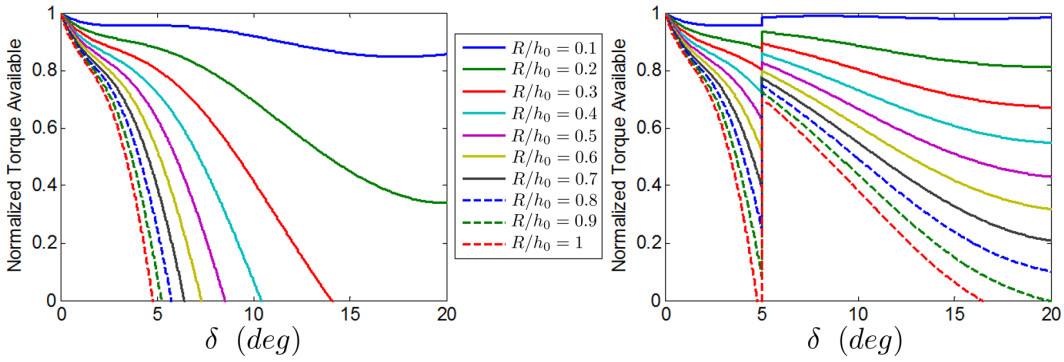

Figure 2.11: Simulated performance improvement from slotted mechanism – (left) as tested, without slots and (right) featuring slotted connections for reduced antagonistic force.

Considering now the upper extreme where $R/h_0 = 1$ (bottommost dashed (red) line), a more dramatic improvement is seen in the torque profile as a function of angle. Without slots, the available torque drops off quickly from the blocked condition and cannot even reach 5 degrees before expending all usable work. However, when the slot is included in the mechanism, the antagonistic force decreases substantially at 5 degrees as the moment arm shortens, causing the torque available to jump back up to nearly 70% of its starting value. The progression of the torque available above this angle has a much shallower slope, and the actuator can reach over 16 degrees before achieving quasistatic equilibrium. This represents an increase in deflection by nearly 4 times. Certainly, adoption of this type of mechanism would greatly improve the prototype actuator system in a subsequent revision of only one part of the device. Figure 2.12 depicts the final physical realization of this concept, with Figure 2.12a showing the mechanism with no rotation and Figure 2.12b showing the mechanism rotated and highlighting the decrease in moment arm achieved by the passive side.

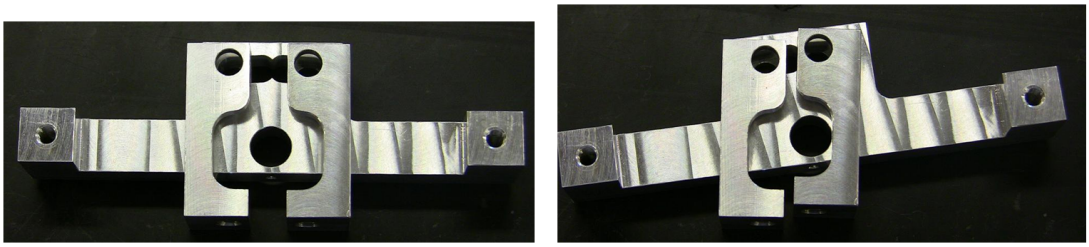

(a) fabricated components with no rotation (b) fabricated components with rotation

Figure 2.12: Slotted-T mechanism

2.4 Bench-top Test Setup

Having fabricated sample miniature PAM actuators and specified the desired mechanism, a control valve and control circuit were selected, and the bench-top prototype system was assembled. Figure 2.13 shows the basic setup. Air enters a miniature solenoid valve and is then routed to a block that is fitted with a transducer to measure the pressure downstream of the valve that directly supplies the PAM actuators. The PAM actuators are held fixed at their right-hand ends in the figure, though a load cell is inline at one location to measure the actuator force. The left-hand ends of the PAMs are connected to the mechanism that rotates about the center post. An angle sensor is also attached underneath the mechanism to record angular rotation as the PAMs are cycled. The actuator testing included two separate experiments. The first was a fixed geometry mechanism pulling against linear extension spring loads (Figure 2.13, top) and the second was also against linear springs but replaced the offset lever mechanism with the slotted-T mechanism (Figure 2.13, bottom).

In each of the experiments, the same set of frequencies and pressures was used

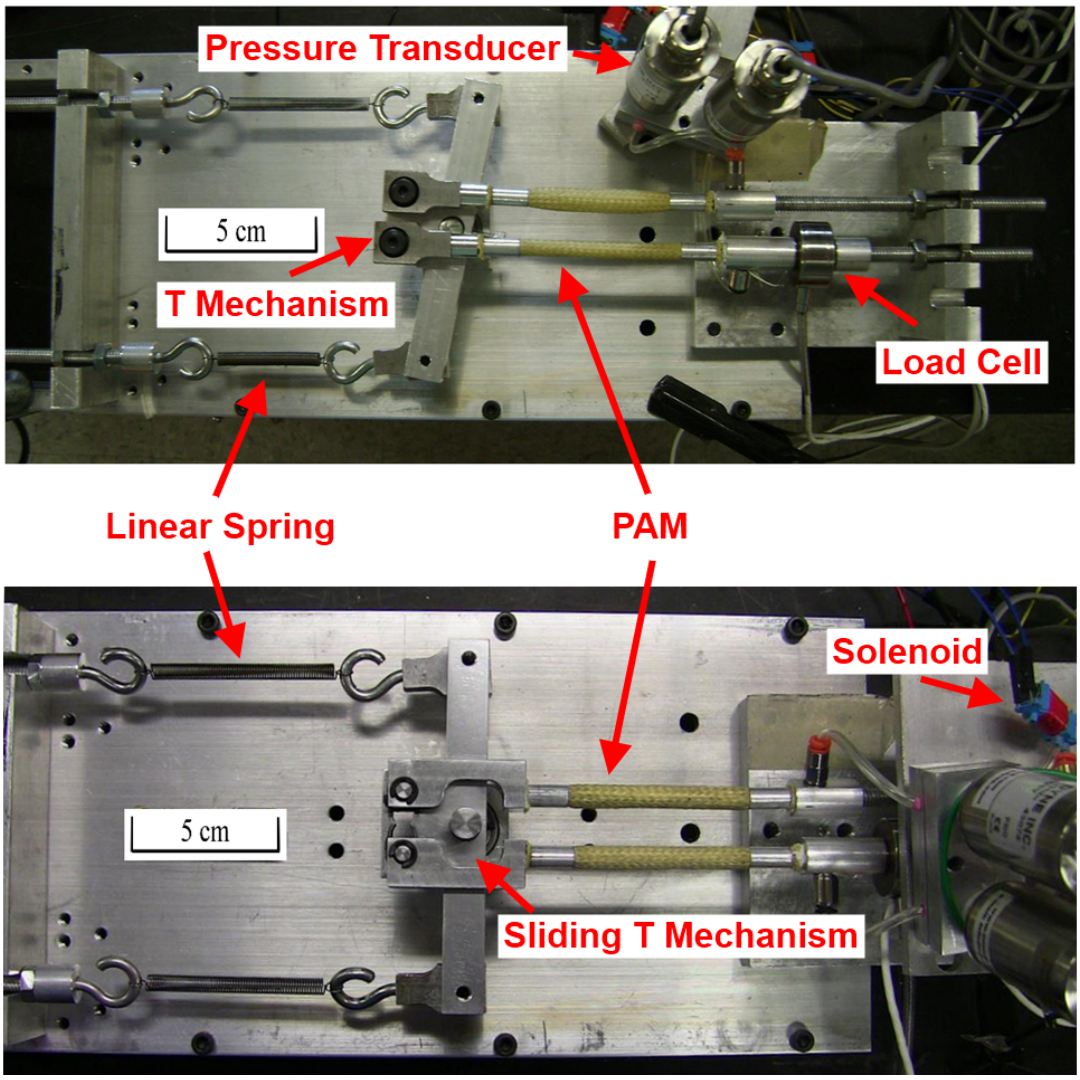

Figure 2.13: Bench-top setups for laboratory testing – (top) standard offset lever mechanism and (bottom) slotted offset lever mechanism.

Table 2.5: Summary of test parameters for bench-top testing.

Pressure (kPa)	Frequency (Hz)	Spring load (N/m)	Torque at 20° (Nm)
345	0.5	0	0
483	1	147	0.13
620	5	630	0.56
–	10	1310	1.16
–	15	1700	1.57
–	20	–	–

as test conditions, and these are summarized in Table 2.5. The first column of the loading conditions (spring load) lists the different stiffness values of the extension springs and the second column (torque at 20 degrees) lists the corresponding torque that the springs produce at an angular deflection of the actuator output of 20 degrees. Note that the lowest nonzero value (0.13 Nm) is a close match to the rated torque of the DS285MG servo actuator (≈ 0.13 Nm). These values were estimated using small angle assumptions, which remain accurate over the tested deflection performance range. It should also be noted that several cycles of data were collected at each frequency, and the test results to be shown represent averages of the measured peak values.

Early in the testing procedure, it was noticed that the system performed well quasi-statically, but deflections drastically decreased at higher frequencies. This reduction in performance was attributed to excess volume and inefficiency in the pneumatic system. In an effort to increase the bandwidth of the system, new configurations were introduced using the absolute minimum amount of tubing and removing the pressure transducers. To obtain a better quantifiable measure of how the air volume varied between the different benchtop test configurations, measurements

Table 2.6: Bench-top test configuration summary.

Configuration	Mechanism type	Tubing length (cm)	Approximate volume (cm^3)	Volume reduction (%)
Rev 2	Standard	14.75	2.34	–
Rev 3	Standard	12.85	2.31	1.4
Rev 4	Slotted	12.85	2.31	1.4
Rev 5	Slotted	1.68	1.23	52

and approximations were made of the various system components, such as the pressure transducers themselves, the hardware that mounted the transducers, the different air tubing lengths, and the PAM actuators. Table 2.6 lists the key values for each of the configurations on a per PAM basis. The volume reduction column values are in reference to the Rev 2 configuration. This table shows that nearly 50% of the air-fill volume could be considered excess of what would be needed in a compact version of the prototype actuator. According to the table, a large difference in tubing length would seem to account for the large difference in performance between Rev 4 and Rev 5, but the oversized pressure for the largest portion of excess volume. It should also be noted that these values use the resting PAM volume pressure, but the general trends remain unchanged.

The JR DS285MG servo (properties given in Table 2.2) was also tested on the setup shown in Figure 2.13. LabView was used to output a pulse width modulated (PWM) signal capable of driving the servo at an arbitrary frequency over its entire range of motion. Frequencies were chosen to match those shown in Table 2.5 as closely as possible. Only angular deflection data were collected during these tests. The servo was tested at 4.8 V and 6.0 V.

2.4.1 Results

Data were gathered on angular deflection, upstream PAM pressure, and PAM force for each of the configurations listed in Table 2.6 and at each point of the test matrix shown in Table 2.5. These results were extensive and will not be presented in their entirety here. Rather, peak performance of the pneumatic systems will be examined and then compared to the servo performance.

Figure 2.14 shows the half peak-to-peak deflection and associated deflection rates for the sample test condition of 620 kPa (90 psi) and 1.57 Nm load. It should be noted that the trends seen here are consistent across all the tested frequencies and loading conditions. The 1.57 Nm case is shown as a conservative presentation of the PAM systems performance. The quasi-static deflection improvements shown in Figure 2.14a are the direct result of the sliding mechanism, while the dynamic improvements at 5 Hz and above are the result of substantially reducing the air volume that must be filled and evacuated during each actuation cycle and not the addition of the sliding-T mechanism. This is because the system was not able to dynamically reach the critical angle at which the passive PAM slides toward the center of rotation and reduces the moment arm. Thus, Rev 4 shows very little performance increase above Rev 3 at higher driving frequencies. Even quasi-statically, however, the maximum deflection falls short of the BAS that desired 20 degrees as listed in Table 3. Figure 2.14b highlights the largely unchanged dynamic performance from Rev 2 through Rev 4 and the significant increase in dynamic performance that is demonstrated over the entire tested frequency range for Rev 5. Both Rev 4 and

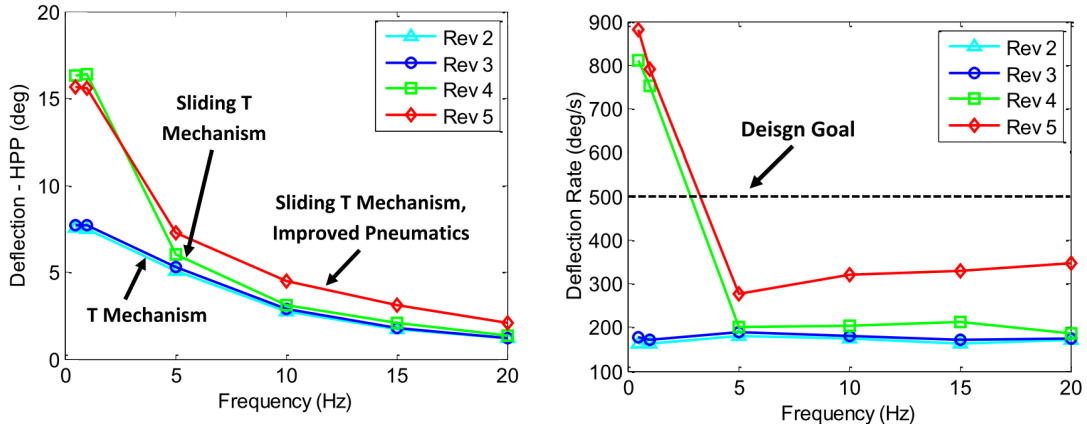

(a) deflection (b) deflection rate

Figure 2.14: Bench-top configuration comparison at 620 kPa (90 psi) and 1.57 Nm

Rev 5 exceed the desired 500 degrees/s during quasi-static operation. The minimum percentage improvement in deflection comes at 5 Hz and is 38% with reference to the Rev 3 configuration. Beyond 5 Hz, the improvement is even higher, reaching 57%at 10 Hz and 71% at 15 and 20 Hz. In terms of rate percentage improvement, the increases are larger yet. The minimum improvement occurs again at 5 Hz with a value of 46%, and this increases to 78%, 91%, and 98%, respectively, for each of the successively tested frequencies.

Figure 2.15 compares the performance of the Rev 5 system (sliding-T mechanism with improved pneumatics) with the JR DS285MG servo. For the pneumatic system, data from all three tested pressures are shown, whereas only one input level (6 V) is shown for the servo. Deflection at the maximum tested spring load of 1.57 Nm (at 20 degrees) is shown in Figure 2.15a. The PAM system is superior to the servo by 13 degrees quasi-statically at 0.5 Hz but is within 2 degrees of the servo from 5 to 20 Hz. In terms of response speed, Figure 2.15b shows that the pneumatic system is faster than the servo at all cases except for 5 Hz at the maximum load condition, and in

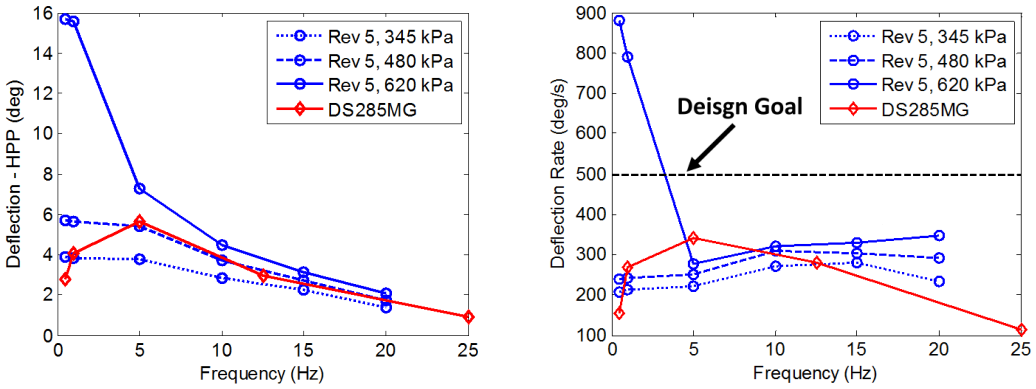

(a) deflection (b) deflection rate

Figure 2.15: Actuator performance dynamic comparison with servo at 1.57 Nm load

many cases, this statement is accurate at pressures less than the maximum tested 620 kPa, as well. Based on this deflection comparison, it can therefore be concluded that the miniature PAM servo actuator can respond faster than the existing MAV servo actuator regardless of external load and that the achievable deflection is larger than the servos at all frequencies for the maximum loading condition. Also, a very important result from Figure 2.15 is the drastic difference between the superior PAM system performance and the servo performance at quasi-static loading conditions. This illustrates that electric actuators do not perform as well as PAMs in actuating quasi-static loads.

Table 2.7 shows how the various revisions of the prototype actuator compare with the JR servo actuator specifications directly, and on a per weight and volume basis. As additional points of comparison, published values for the HiTec HS-755HB Servo and Moog Model 874 Rotary Actuator are also included. Neither of these actuators was experimentally tested, but they were included in this comparison because their maximum torque rating is close to the measured value of taken from the

bench-top setup, a packaged self-contained system (Figure 2.16), and a theoretically reduced weight packaged system utilizing composites where all components excluding the PAMs were cut to half their original weight. The torque values displayed for the DS285MG and Rev 5 actuators were taken from the quasi-static condition, and the speed values shown were converted from their degrees/s units shown previously to s/60 degrees to match with the specification provided by the servo manufacturer. The Moog actuator torque corresponds to the continuous available torque at the given speed. For the Rev (PAM) actuators, speed values denote the speed measured at 5 Hz when the actuator was operating against the BAS-rated spring loading condition (1.16 Nm). This table shows that the prototype actuator satisfies the nominal BAS torque requirement (1 Nm) and exceeds that of the DS285MG servo by nearly an order of magnitude. In terms of speed, the PAM prototype again exceeds that of both servos but falls 5% short of meeting the value for the BAS specification (0.120 s/60 degrees) and is an order of magnitude slower than the Moog actuator.

Two key actuator performance metrics listed in Table 2.7 are specific torque (T/M) and torque density (T/V). These metrics are an indication of the practicality of the actuators for use on an aircraft where both volume and mass are at a premium. The specific torque of the PAM-based actuator was more than twice specific torque of both servos and was an order of magnitude greater than the Moog actuator. Size, however, brings the servo actuator closer to the performance of the Rev 5 PAM actuator. As tested, the DS285MG servo torque density actually exceeds that of the tested prototype Rev 5 system by 9%. However, the HS-755HB servo is nominally 45% less than, and the Moog actuator is nominally 75%less than, the Rev 5 system.

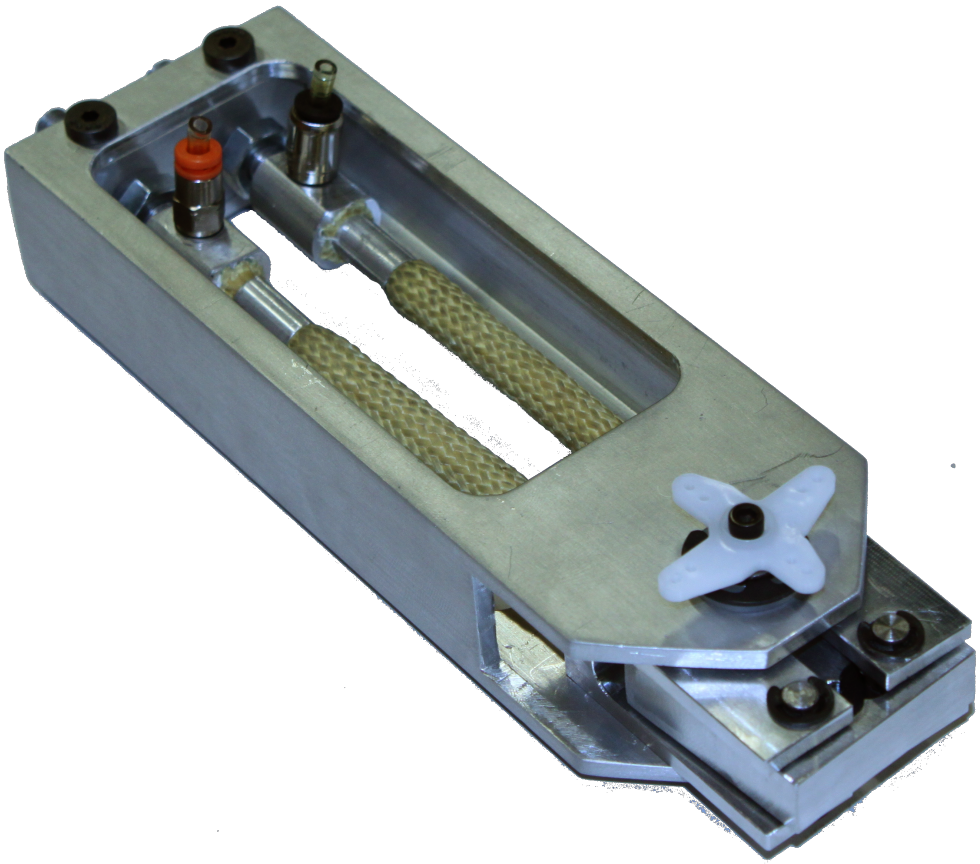

Figure 2.16: Prototype of packaged mini-PAM actuator used for size/weight estimates.

Table 2.7: Actuator type performance comparison.

Actuator type	DS285MG		HS-755HB	Rev 5			Moog 847
	Specs	Tested	Specs	Tested	Packaged	Composite	Specs
Torque (Nm)	0.133	0.158	1.29	1.23	1.23	1.23	1.35
Mass (g)	11.9	11.9	110	357	74.8	43.1	635
Volume (cm^3)	5.41	5.41	85.55	46.05	46.05	46.05	192.54
Speed (s/60°)	0.14	0.139	0.23	0.105	0.105	0.105	0.015
T/M (Nm/g)	0.011	0.013	0.012	0.003	0.016	0.029	0.002
T/V (Nm/cm^3)	0.024	0.029	0.015	0.027	0.027	0.027	0.007

While meeting the BAS specification was more closely followed in the design, which ultimately led to choosing larger heavier components, the normalization of the test results may provide a glimpse into the lower bounds of application sizes for which PAM-based actuation systems are a viable alternative to more conventional actuation technologies, such as servos or rotary actuators. It was shown that a PAM system is superior to servo actuators with respect to mass when considering torque, but in order to achieve this level of performance, there is a certain minimum size that must be available for PAMs to operate properly, and it is this size requirement that brings the PAM-based systems back even with servo performance on a volumetric basis. However, if a servo with comparable static torque is examined, the PAM-based system again is superior when compared in terms of specific torque and torque density. Additionally, the Moog actuator outperforms the PAM system in both speed and torque alone but not when specific torque and torque density are considered. These results indicate that, while there are actuators with comparable torque ratings to the PAM actuator, if purely static torque is required, the PAM actuator would provide a very efficient solution.

One of the objectives of this study was to explore the lower limit (small sizes) of the design space for PAM actuator systems. This was accomplished here, and the results tend to suggest that a minimum overall volume exists for a PAM actuator system, and this volume is larger than the space occupied by a small-scale servo actuator with comparable dynamic performance but smaller than a servo with comparable static performance. It should be noted that a smaller volume could be used for a PAM actuator system if only the DS285MG servo specification was

considered, instead of the larger BAS specification, but it would still be larger than the candidate servo actuator.

2.5 Conclusion

The goal of this study was to compare a PAM-based servo actuator design to an electric servo actuator motor (DS285MG) having comparable high frequency (1020 Hz) displacement performance. Key accomplishments include the development of a fabrication procedure for miniaturized PAM actuators, the design of a novel mechanism to complement the load-stroke profile of the selected PAM actuators, and a comparison of prototype actuator performance to competing servo motor technologies. Key conclusions are as follows:

1. The packaged PAM (Version 5) actuator exhibited twice the specific torque and comparable torque density to that of a commercial off-the-shelf servo actuator (DS285MG) having comparable dynamic response in the frequency range of 1020 Hz. The PAM device also had an available static torque that was an order of magnitude higher than that of the electric servo actuator motor.

2. When comparing the PAM actuator to a commercial servo and rotary actuator with comparable maximum torques, the performance metrics of the PAM system were shown to be superior when normalized with respect to both mass and volume. This highlights the potential that these miniature PAM devices have for small-scale actuator applications, especially in systems where high quasi-static torque is required.

3. Aerospace applications that could benefit from PAM actuators include deploying aerodynamic flaps and quasi-statically changing configurations on morphing aircraft. For such applications, these results show that a PAM actuation system would have both lighter weight and smaller volume than a servo with comparable maximum torque output.

Chapter 3: Mechanism and Bias Considerations for Design of a Bi-Directional Pneumatic Artificial Muscle Actuator

3.1 Introduction

Applications of artificial muscle technologies have received considerable attention in research and development over the years. Particularly for robotic systems, the leading technology has been that of pneumatic artificial muscles (PAMs) for their marked operational similarity to natural muscle, compliance, high force to weight ratios, and high fatigue life [69–73, 81, 82, 84–87, 109–113]. Specifically, PAMs, or McKibben actuators, are uni-directional devices that generate a pulling force in response to pressure-induced volume change. While robotics has remained a large application area, continued development and recent demonstrations of technology improvement have created new interest in the control of aerospace structures, as well [58, 63, 65, 76]. This growing application set, including the often stringent design requirements of the aerospace industry, has motivated an investigation into some of the basic operational principles of these artificial muscles in an effort to optimize

performance.

Many robotic or aerospace applications require bi-directional linear or rotational motion. For any uni-directional actuator, this necessitates the use of an agonist-antagonist arrangement, similar to the biceps-triceps arrangement in a human arm, such that as one actuator contracts the other actuator extends. This approach is commonly employed with conventional actuators, such as hydraulic or pneumatic cylinders, and even newer smart materials, such as shape memory alloys [79] and electostrictive materials [80]. PAMs represent a unique challenge in antagonistic actuation however, due to their highly non-linear force-contraction relationship and compliance.

Much work has gone into understanding the antagonistic PAM actuator design problem over the years, with the general goals of increasing actuator range of motion and controlling actuator stiffness. One approach taken is to modify the kinematics of the system, i.e., the mechanism to which the PAMs are connected, in order to influence its behavior. This work has ranged from simple pulleys [72, 81], to complex variable radius pulleys [82] and offset lever mechanisms [58, 63]. Additional work has gone into influencing the passive and active stiffness of the system by varying the bias pressure of the system, that is, the starting pressure to which both PAM are inflated, with the general understanding that higher bias pressure equates to higher joint stiffness. This topic is of great interest in the robotics field and many analyses exist to aid in joint stiffness design [82, 84–86]. Finally, most antagonistic PAM applications, with the exception of some recent aerospace applications [58, 63], have operated from a pre-contracted state in order to increase range of motion. Most studies simply

list a pre-contraction value, or bias contraction, for their system [70, 72, 85–87] with little discussion of the effect of this parameter on system performance. One notable exception mentions that tuning bias contraction can have a large effect on range of motion and end-stop location, but no explicit analysis is offered on this strategy [72].

The present work was motivated by this lack of explicit analysis regarding the effect of these design parameters on the range of motion of an antagonistic PAM system, especially when subjected to an external load. A basic introduction to PAM operation is given in the next section, followed by an explanation of the models used for the kinematic mechanisms and PAM force. The general effect of mechanism choice, bias pressure, and bias contraction on system performance is then discussed. An example design study is presented, where actuator system performance is drastically increased with proper choice of bias contraction and mechanism geometry. Finally, a PAM antagonistic actuator is designed, simulated, and experimentally tested on the bench-top using a torsional spring to emulate an appropriate aerodynamic load, showing a drastic increase in performance with the inclusion of PAM bias.

3.2 Basic PAM Operation

The basic form of a contractile PAM is pictured in Figure 3.1a. It consists of a stiff helically braided sleeve, initially at angle θ_0 and resting length L_N, surrounding a compliant elastomeric bladder, which is clamped and sealed at both ends with aluminum end fittings. When fluid pressure is applied inside the PAM, the bladder tends to expand radially. Because the sleeve covering the bladder is very stiff, this

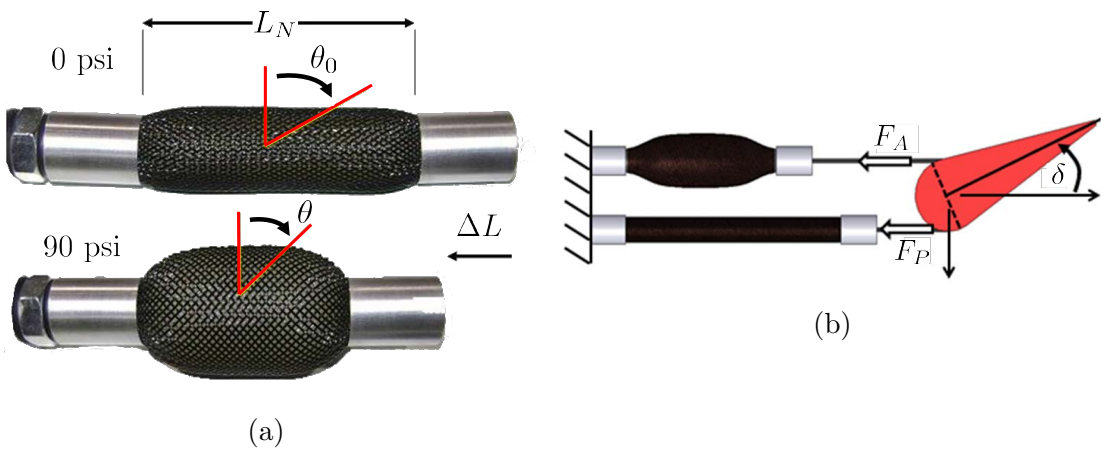

Figure 3.1: a) A typical PAM consisting of a helically braided sleeve, elastomeric bladder, and aluminum end-fittings. The PAM is shown in its relaxed and contracted states; b) PAMs arranged in an agonist-antagonist pair for bi-directional rotation

radial expansion forces the PAM to shorten in length by ΔL. As the PAM shortens, the fiber angle, θ, decreases until it reaches a physical equilibrium condition, called free contraction.

The general bi-directional actuator configuration is shown in Figure 3.1b. Here PAMs are arranged in an antagonistic manner about a hinge, and when the active muscle contracts and pulls with force F_A, it rotates the hinge by an angle of δ until equilibrium is reached with the antagonistic muscle force, F_P, and any external hinge load. In general, this equilibrium is reached when the available torque, T_A, reaches equilibrium with the required torque, T_R. The available torque can be defined as

$$T_a = F_A R_A - F_P R_P \tag{3.1}$$

where R_A and R_P are the active and passive mechanism moment arms respectively. The required torque however depends on the specific loading condition.

A typical force versus contraction curve is shown in Figure 3.2 for a nominal 5/8 inch diameter PAM. Contraction is defined here as a percentage of natural (uninflated) length, and positive contraction indicates a decrease in length. Note that force levels are dependent on contraction, and increase rapidly when the PAM is stretched beyond its natural length (negative contraction). This high passive PAM stiffness is a severe limiting factor for antagonistic actuation as it directly subtracts from the usable work available from the actuation system. One approach to increasing system performance is to increase the active PAM torque, usually through using a stronger PAM. However, this provides only incremental improvements in performance because of the slope of the antagonistic PAM stiffness curve. A more promising approach is to decrease the passive parasitic torque. Hence, the goal of the present work is to investigate how to increase performance by decreasing the passive torque on the system. This is accomplished by introducing two variations into the design: the first being the type of kinematic mechanism employed and the second being the introduction of bias, both in terms operational pressure and pre-contraction.

3.3 Kinematic Mechanism Modeling

Perhaps the most basic mechanism for bi-directional actuation is the pulley, which can be considered equivalent to a standard lever for small rotation angles (Figure 3.3a). In this case, the moment arm is constant at R throughout rotation for both the agonist and antagonist muscles. By offsetting the muscle attachment

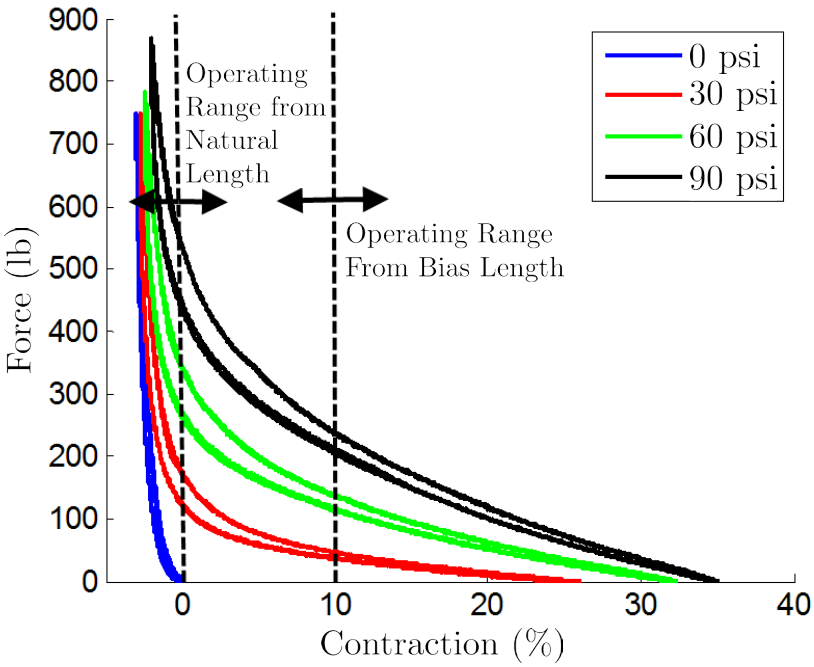

Figure 3.2: A typical PAM force vs. contraction curve, illustrating the typical operating range for an antagonistic actuator, and the operating range when bias is considered

points on the lever by an angle ϕ_o, however, the case is created where the moment arm of the agonist PAM increases with rotation, while the antagonist PAM has a decreasing moment arm. This effectively increases the output torque of the actuator without making any changes to the muscles themselves or the operating pressure. To compare the three basic types of mechanisms, a starting radius, or moment arm, will be defined as R_o and kept the same for each mechanism in its basic configuration. In the case of the pulley, the moment arms for the active (R_A) and passive (R_P) PAMs are equivalent at all times and remain unchanged from their starting length

$$R_A = R_P = R_o \tag{3.2}$$

Similarly for the standard lever, the moment arms are equivalent at all times, but they do change (decrease) as the joint rotates a small angle δ from the starting condition

$$R_A = R_P = R_o \cos\delta \tag{3.3}$$

Note that for small angles though, the pulley and standard lever mechanisms are approximately the same. The major difference in mechanism arrangement comes from the offset lever. From Figure 3.3b, it can be seen that this mechanism is characterized by two parameters: the initial radius taken from the standard lever, R_o, and the vertical offset of the PAM attachment points, denoted here by $\alpha_0 R_o$. Thus, the length vector from the center of rotation to the PAM attachment points can be equivalently described in polar coordinates as

$$\begin{aligned} r_o &= R_o\sqrt{1+\alpha_o^2} \\ \phi_o &= \tan^{-1}\alpha_o \end{aligned} \tag{3.4}$$

This gives the active and passive moment arms for the offset lever, respectively, as

$$\begin{aligned} R_A &= r_o \cos(\phi_o - \delta) \\ R_P &= r_o \cos(\phi_o + \delta) \end{aligned} \tag{3.5}$$

where it can be seen that R_A increases with rotation angle δ, as R_P decreases, all while $\delta < \phi_0$ for non-negative angles. It can generally be assumed that $\phi_0 \in (0,\ \pi/2)$ because $\phi_0 = 0$ implies the standard lever and $\phi_0 = \pi/2$ is an equilibrium point when the moment arm is zero.

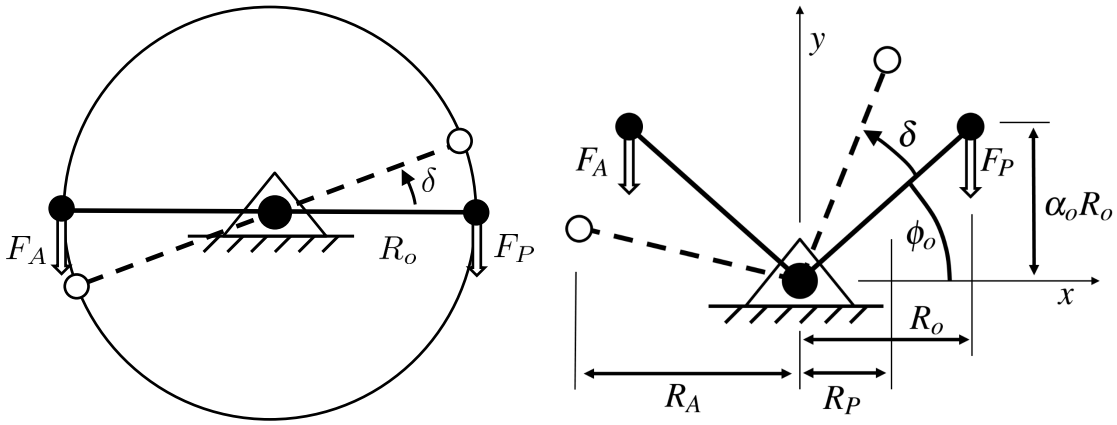

(a) pulley and standard lever mechanisms

(b) offset lever mechanism

Figure 3.3: Mechanism definitions

While it may appear at first glance that reducing the passive moment arm would be the ideal configuration for reducing passive torque, this decrease in moment arm is small for small values of δ and so the high antagonistic PAM stiffness can still be an issue if the PAM is operating from its natural resting length. One solution to this limited angular range is to move the resting condition from the natural length, to a pre-contracted length. In order to introduce this pre-contraction and maintain hinge stiffness, a bias pressure must also be applied. This bias has the effect of moving the muscle operating range to the right on the force-contraction curve, which is also noted in Figure 3.2, where it has been moved from 0% to 10%, for example.

3.4 PAM Modeling With Bias

Bias can be included in a PAM actuation system through both pressure and contraction. For simplicity, the introduction of bias to the design of a PAM actuation system will be made here with reference only to the Gaylord equation [68], which

relates the muscle length, L, and pressure, P, to pulling force, F, as

$$F = \frac{P}{4\pi N^2}\left(3L^2 - B^2\right), \tag{3.6}$$

where N is the number of turns a single braid fiber makes around the muscle body and B is the length of that braid fiber. If the diameter of the PAM, D, is known, then B can be determined from geometry with the cylindrical body assumption as

$$B = \sqrt{(\pi N D)^2 + L_N^2}. \tag{3.7}$$

It should be noted that this is perhaps the most basic form of the force equation for a pneumatic artificial muscle, with several assumptions, and several other improvements and reformulations can be found [24-27]. The muscle length in this equation is commonly represented either as

$$L = L_0 - \Delta L, \tag{3.8}$$

where L_0 is the starting length of the muscle and ΔL is the change in length, or as

$$L = \lambda L_0, \tag{3.9}$$

which introduces the contraction ratio, λ. Note that λ reaches a minimum, $\lambda_{min} > 0$, which is called the free contraction ratio and is a function of pressure and muscle geometry.

Operation from a bias contraction enters the equation by changing the starting position. Typically with PAMs, the starting length, L_0, and natural length, L_N, are equal ($L_0 = L_N$), where the natural length may also be called the resting length. By changing the rest condition from the natural length to a pre-contracted length, however, the starting length then becomes

$$L_0 = L_N - L_B, \tag{3.10}$$

where LB is the pre-contracted bias length. By defining a contraction bias ratio $\xi = L_B/L_N$, the starting length can also be represented as a fraction of the natural length

$$L_0 = L_N(1 - \xi), \tag{3.11}$$

where $\xi \in [0, \lambda_{min})$. Note that the available range of bias contraction depends on the free contraction ratio for the bias condition. While the simplified force equation (Gaylord) used in this illustrative example has a pressure-independent free contraction ratio

$$\lambda_{min} = \frac{1}{L_N}\sqrt{\frac{B^2}{3}}, \tag{3.12}$$

experiments and other more accurate models [66, 114–116] show that it is actually dependent on pressure, so this would imply in actuality that $\xi \in [0, \lambda_{min}(P_B))$. It should also be noted here that bias contraction must be accompanied by bias pressure, P_B. Otherwise the muscles would be slack at rest, which is not desirable for control of a joint as it would be free to rotate with no hinge stiffness. The bias pressure can

be introduced with a bias pressure ratio

$$\kappa = \frac{P_B}{P_A}, \tag{3.13}$$

where P_A is the active pressure, or operating pressure.

With an active pressure and bias pressure now defined, it is useful to recall that the bi-directional PAM actuation system has at least one pair of antagonistic PAMs, where one PAM is active for joint rotation in one direction and the other PAM is active for rotation in the opposite direction. While not actively rotating, the antagonistic PAM is a passive element (e.g., air spring) at the bias pressure. This brings up the notion of active PAM force, FA, and passive PAM force, FP, which are defined for the Gaylord force equation using the terms above as

$$\begin{aligned} F_A &= \frac{P_A}{4\pi N^2}\left[3\left(L_N(1-\xi) - \Delta L_A^2\right) - B^2\right] \\ F_P &= \frac{\kappa P_A}{4\pi N^2}\left[3\left(L_N(1-\xi) - \Delta L_P^2\right) - B^2\right], \end{aligned} \tag{3.14}$$

where it should be noted that $\Delta L_A = \Delta L_P$ for both the pulley and standard lever configurations, but $\Delta L_A \neq \Delta L_P$ for the offset lever. Also note that $\Delta L \geq 0$ when $L \leq L_0$, or when the PAM is actively contracted, and $\Delta L < 0$ when $L > L_0$, or when the PAM is passively extended. These equations can also be written more compactly as

$$\begin{aligned} F_A &= \tfrac{P_A}{4\pi N^2}\left(3L_A^2 - B^2\right) \\ F_P &= \tfrac{\kappa P_A}{4\pi N^2}\left(3L_P^2 - B^2\right), \end{aligned} \tag{3.15}$$

with active and passive lengths defined, respectively, as

$$\begin{aligned} L_A &= L_N(1-\xi) - \Delta L_A \\ L_P &= L_N(1-\xi) - \Delta L_P. \end{aligned} \tag{3.16}$$

For the present study, the complete PAM force was approximated with

$$F = \begin{cases} \dfrac{P}{4\pi N^2}(3L^2 - B^2), & L \leq L_N \\ \\ \dfrac{P}{4\pi N^2}(3L^2 - B^2) - \eta \Delta L^3, & L > L_N. \end{cases} \tag{3.17}$$

The extra term ηL^3 is added when $L > L_N$ to account for the rapid stiffening effect seen in PAMs during extension beyond their natural length. The coefficient η and cubic exponential form were chosen to approximate trends observed in measured data. Note that this condition is satisfied only at the bias pressure when the stroke is larger than the bias contraction length. For example, when $\xi = 0$, the passive PAM must stretch beyond its natural length for joint rotation to occur Recall that this case when the antagonistic stiffness becomes large is the actual case that motivated the investigation into using bias in antagonistic PAM systems Figure 3.4 shows force versus contraction data according to this model for a PAM with $L_N = 6$ inches, $D = 0.625$ inches, and $N = 1.5$ turns. Note the qualitatively correct cubic stiffening when the PAM extends past its natural length.

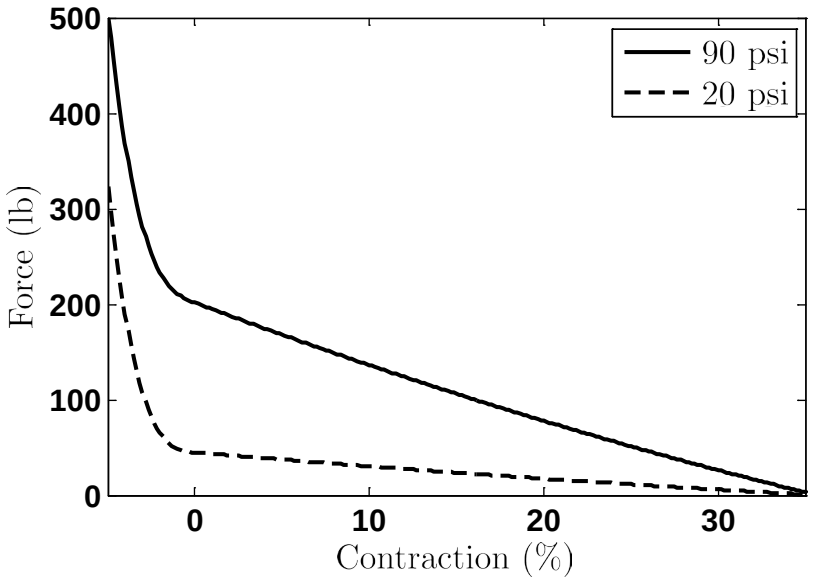

Figure 3.4: Force vs. contraction as predicted by the Gaylord model with cubic stiffening added in the extension region

3.5 Conceptual Mechanism Study

In comparing the quasi-static torque produced by the three different PAM actuation systems, it is convenient to normalize the output torque of the actuator. We have chosen

$$\mu = \frac{T_A}{T^*} \tag{3.18}$$

where T_A is the available torque of the PAM actuation system as it rotates, defined as

$$T_A = R_A F_A - R_P F_P \tag{3.19}$$

and T^* is the reference torque defined when $\delta = 0$, and neglecting bias pressure, defined as

$$T^* = P_A R_o \frac{3L_0^2 - B}{4\pi N^2}. \tag{3.20}$$

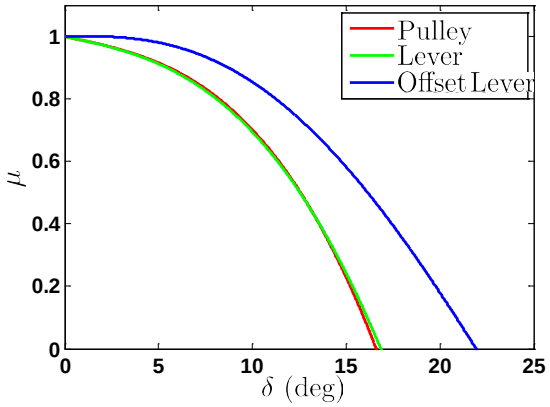

Figure 3.5: Normalized output torque vs. actuator deflection for various actuation arrangements at a constant R_o

In order to rigorously determine which kinematic mechanism (pulley, lever, or offset lever) performs best, a series of simulations was conducted. The active pressure P_A was chosen to be 90 psi, and bias pressure P_B was chosen to be 20 psi (see Figure 3.4 for force versus contraction data), making $\kappa = 0.22$ in this case. For this study, "better performance" is defined as the ability to maintain a larger available torque, μ, over the deflection range of interest. Results for the $\xi = 0$ case are shown in Figure 3.5. The vertical axis is normalized torque available for work, μ, and the horizontal axis is mechanism deflection angle, δ. It is clear that for this case, the offset lever ($\alpha_o = 0.5$) gives the best performance over the entire range of deflection and that the pulley and lever give almost identical performance.

Now, examining multiple values of ξ as shown in Figure 3.6, this trend still holds and will continue to hold for different values of κ. It is therefore reasonable to conclude that the offset lever is a superior mechanism when using an antagonistic PAM pair. Hence, the pulley and lever mechanisms will be abandoned for the remainder of this conceptual discussion.

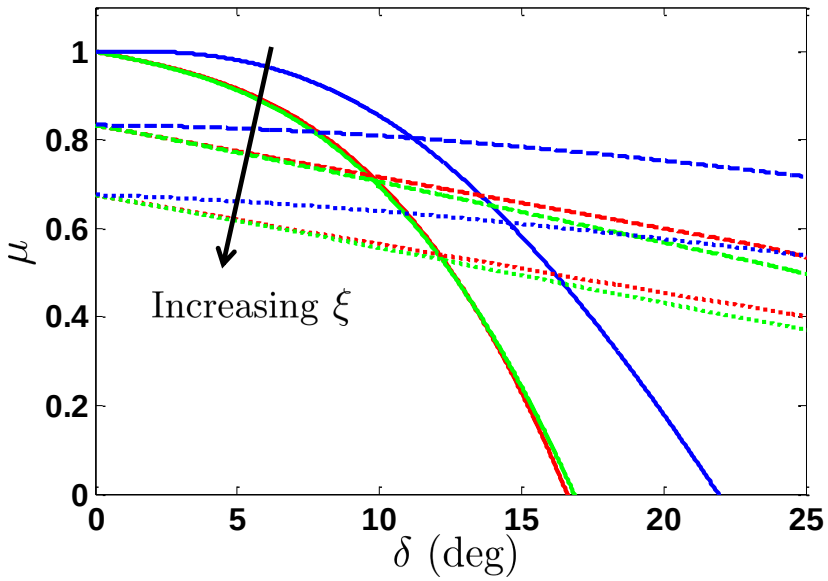

Figure 3.6: Output torque vs. actuator deflection for a range of contraction bias ratios, ξ

3.5.1 Effect of Varying Bias Pressure

Achieving maximal torque,μ, is equivalent to increasing actuation system torque,M, over the entire range of operation. Fixing all variables except κ, it is clear that M will be maximized when κ goes to zero, thereby minimizing F_P. This result is shown in Figure 3.7, where it can be seen that as κ increases, the curves of available torque decrease monotonically for a given deflection. In this plot, all torques were normalized by the M^* for $\kappa = 0$.

This raises the question of why a bias pressure is being included at all, if it only degrades performance. The answer has to do with the practical implementation of an antagonistic PAM system. A system with no bias pressure would have very little hinge stiffness across most of the operating range, and no hinge stiffness at the rest condition. The bias pressure is used, in conjunction with bias contraction, to ensure

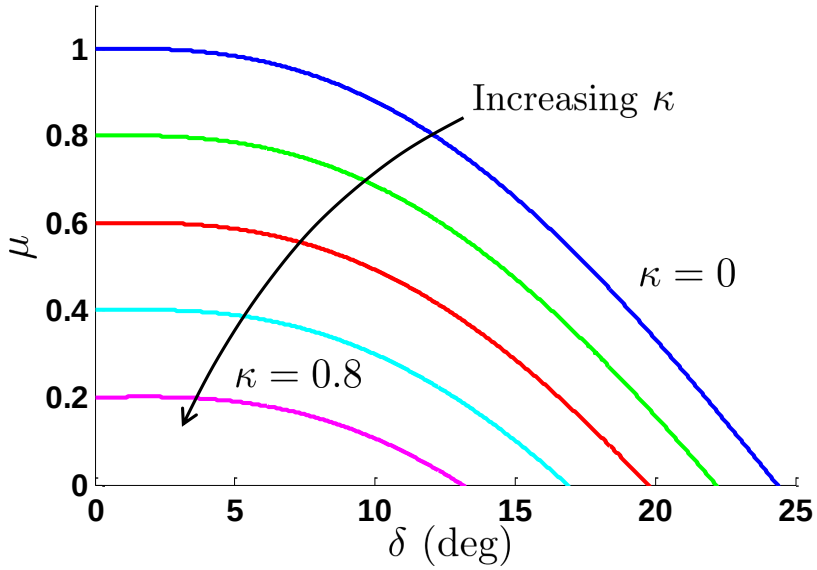

Figure 3.7: Effect of κ on available torque for a constant R_o and contraction bias ratio, $\xi = 0$

that the passive PAM behaves as an air spring and to add stiffness to the system, at the expense of performance. If the bias pressure can be actively controlled, then the user has a bi-directional system with an adjustable hinge stiffness, which has possible applications for human-robot interactions where a soft-touch is desired.

3.5.2 Effect of Varying Bias Contraction

To qualitatively examine the effect of bias contraction on the performance of the kinematic system, a simplified case is again considered where all variables are fixed ($\kappa = 0$) and ξ is allowed to vary. Results for a variety of ξ values are plotted in Figure 3.8, where all curves are normalized by T^* corresponding to $\xi = 0$.

As ξ increases, the available torque at $\delta = 0$ decreases because, as illustrated in Figure 2, the PAM is starting farther down its contraction curve, and thus, has a lower starting force. As δ increases, however, the benefit of bias contraction becomes

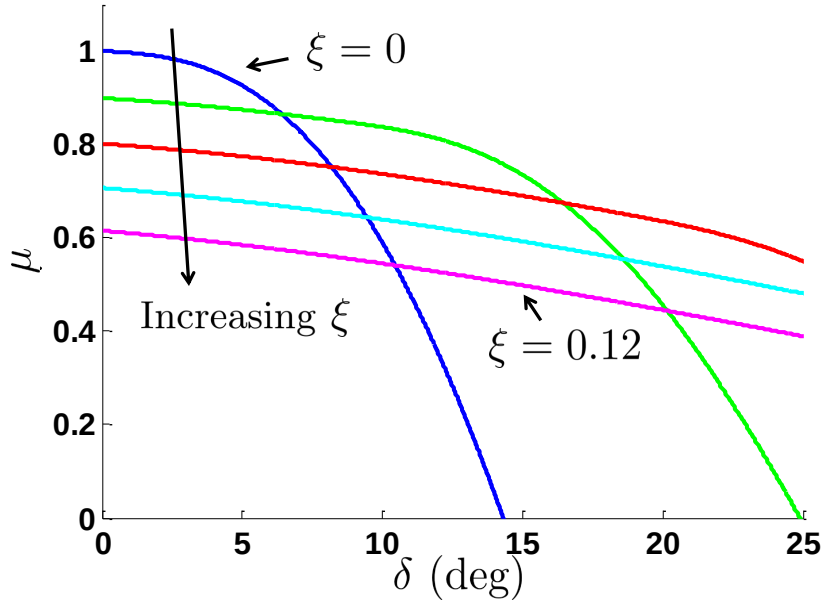

Figure 3.8: Effect of ξ on available torque for a constant R_o and contraction bias ratio, $\kappa = 0$

clear as the curves for available torque postpone the sharp drop off in torque due to the antagonistic PAM. This has the effect of flattening out the available torque curve, at the expense of a lower starting torque. However, no blanket conclusion can necessarily be drawn from this data as to the benefit of one ξ value over another. To illustrate this point, consider the cases $\xi = \xi_1$ and $\xi = \xi_2$, as shown in Figure 3.9, where $\xi_2 > \xi_1$. Also plotted is the torque required for two arbitrary torsional spring loads.

If spring 1 is the desired loading, then $\xi = \xi_1$ is the best choice because the line for the ξ_1 torque available curve crosses the spring 1 torque required curve at a higher δ than the ξ_2 curve. Likewise, if spring 2 is the desired loading, then $\xi = \xi_2$ is the best choice. Thus, the choice of ideal bias contraction is coupled to the required loading, and cannot be considered independently.

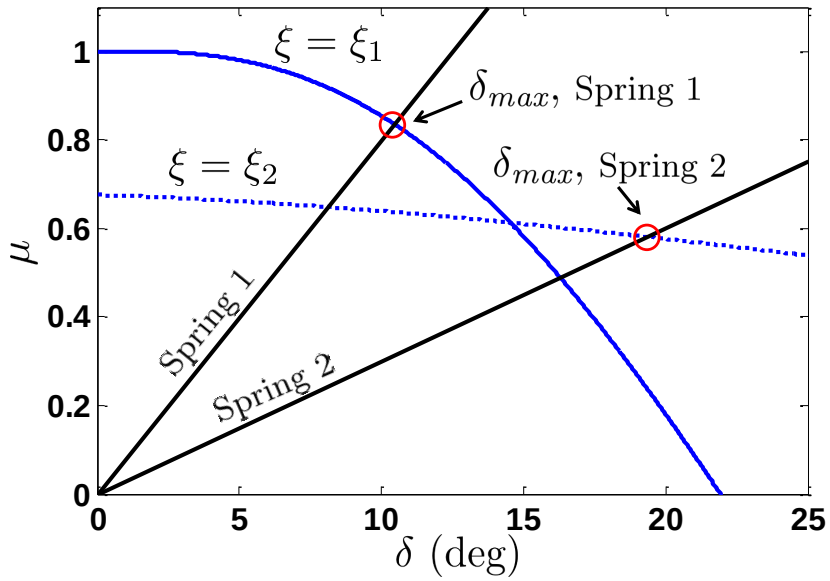

Figure 3.9: Maximum achievable deflections for an actuator with two different values of ξ and two different spring loadings

3.5.3 Conceptual Design Study

In general, the goal of a specific design using the offset lever mechanism can be described as a maximization problem,

$$\bar{\delta} = \max\ F_\delta(\xi, \kappa, P_A, L, D, N, R_o, \alpha_o, k_\delta), \tag{3.21}$$

where F_δ is an objective function that calculates the maximal deflection, $\bar{\delta}$, and is a function of all the parameters discussed in the previous sections, with the addition of the parameter k_δ, which represents an external torsional load on the hinge. Recall that the variables R_o and α_o are the nominal horizontal distance and vertical offset ratio of the offset lever mechanism, respectively. This is a complicated problem to solve parametrically, but fairly trivial for a commercial numerical optimizer. To

illustrate some qualitative trends, a simplified case was considered when the PAM geometry was fixed as the previously described actuator, along with setting $\alpha_o = 0.5$, $\kappa = 0.22$, and fixing k_δ to an arbitrary value of torque per unit rotational deflection.

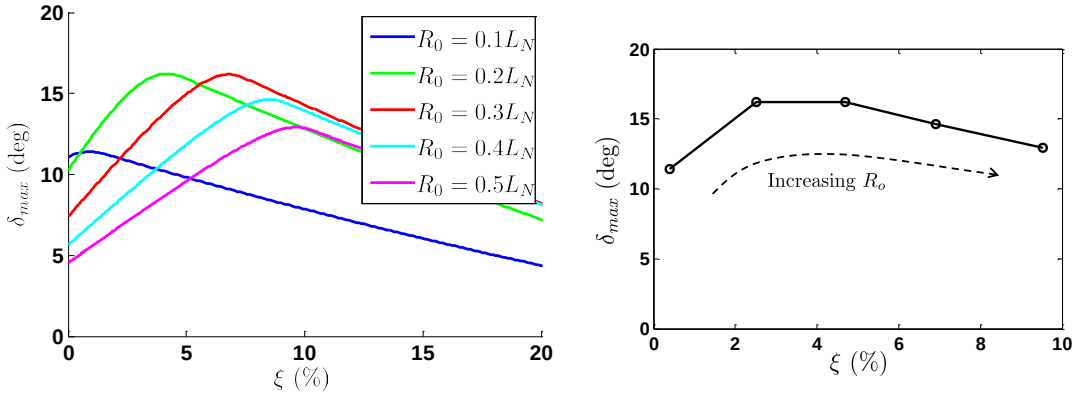

(a) (b)

Figure 3.10: a) Curves of maximum achievable deflection as a function of bias contraction for various values of R_o; b) Maximum achievable deflection as a function of ξ

Figure 3.10a shows curves of maximum achievable deflection (i.e., the intersection of the torque available and torque required curves) as a function of bias contraction for a number of values of R_o, given as a fraction of the natural length. Examining this figure, it is clear that for a given value of R_o, an optimal bias contraction exists that will maximize achievable deflection. Plotting the maximal points for each curve (Figure 3.10b), it appears that the ideal combination of R_o and ξ lies in the range $0.2L_N < R_{0,ideal} < 0.3L_N$ and $2.5\% < \xi_{ideal} < 4.7\%$. In general, as R_o increases, the ideal bias contraction will also increase, up to the logical limit where ξ approaches λ_{min} and the agonist PAM can do no useful work. Looking at the available data, the increase in performance achieved by this parametric optimization can be characterized by comparing it to a baseline design with $R_o = 0.1L_N$ and

$\xi = 0$, where $\delta_{max} = 11.06$ deg. Note that this corresponds to the highest achievable deflection without bias contraction. According to Figure 11, the maximum achievable deflection for the considered designs occurs at $R_o = 0.2L_N$ and $\xi = 2.5\%$, where $\delta_{max} = 16.22$ deg, which represents a 46% increase in performance over the baseline.

3.6 Experimental Design Study

To verify the trends and analysis predicted in subsection 3.5.3, a "worst-case" system was designed that would have very poor antagonistic performance with a typical (no bias) system. In general, an antagonistic PAM system with no lever offset ($\alpha_o = 0$), and PAM length (L_N) on the same order as lever moment arm (R_o) will not perform well from the standpoint of maximizing deflection. For the current design, a PAM with $L_N = 3.35$ inches, $OD = 5/8$ inches, and a lever mechanism with $R_o = 2.5$ inches was selected for simulation and manufacture. The previously presented analysis included small angle assumptions, which is sufficient for actuators where the PAM length is much greater than the mechanism moment arm R_o, but tends to over-predict in cases where the PAM and mechanism (bell-crank) dimensions are on the same order.

Figure 4.5 depicts a more accurate model. Both the active and passive PAMs are shown in their deflected (solid black lines) and undeflected states (dashed grey lines). The vertical and horizontal PAM mounting points are described by x_{off} and y_{off}. At a given δ, the deflected positions of the active PAM mechanism connection

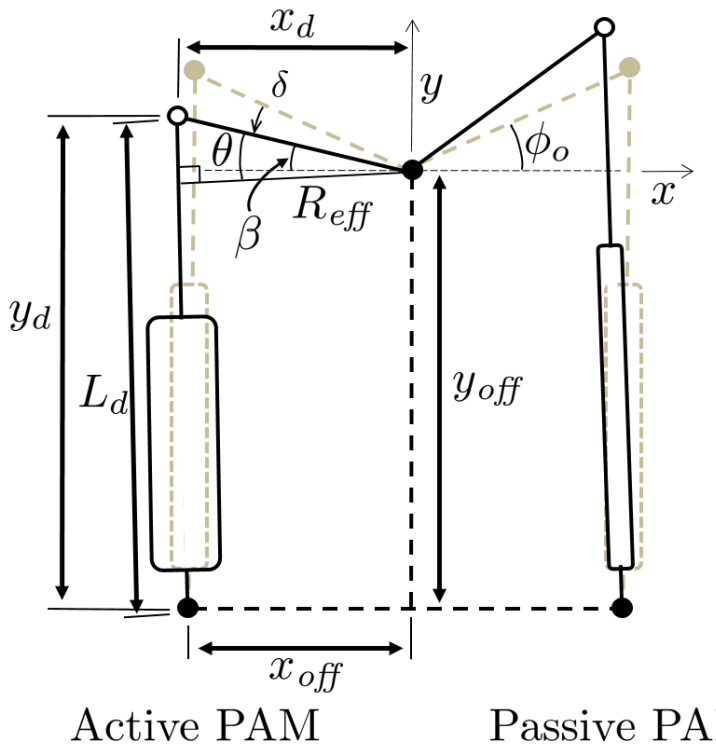

Figure 3.11: Conceptual schematic of offset lever mechanism with large angle assumptions.

point with respect to its fixed anchor point are given by

$$\begin{aligned} x_d =& \frac{R_o}{\cos\phi_o}\cos\beta - x_{off}, \\ y_d =& \frac{R_o}{\cos\phi_o}\sin\beta + y_{off}, \end{aligned} \tag{3.22}$$

where $\beta = \phi_o - \delta$ is the angle between the active PAM lever line and the x axis. The deflected PAM length is defined as

$$L_d = \sqrt{x_d^2 + y_d^2}. \tag{3.23}$$

The effective moment arm, R_{eff}, defined as the line originating at the center of rotation and perpendicular to L_d, can be determined from

$$R_{eff} = \frac{R_o}{\cos\phi_o}\cos\theta \tag{3.24}$$

where

$$\theta = \beta + \tan^{-1}\frac{x_d}{y_d} \tag{3.25}$$

and is defined as the angle between the active lever line and R_{eff}. A similar set of expressions can be derived for the passive side. Equation 3.21 was used to find the deflection, δ, at which $T_A - T_R = 0$ for an arbitrary loading condition. This corresponds to the quasi-static deflection of the actuator/PAM combination. To remove a potential source of error, PAM forces (F_A and F_P) were interpolated from experimental data, similar to Figure 3.2.

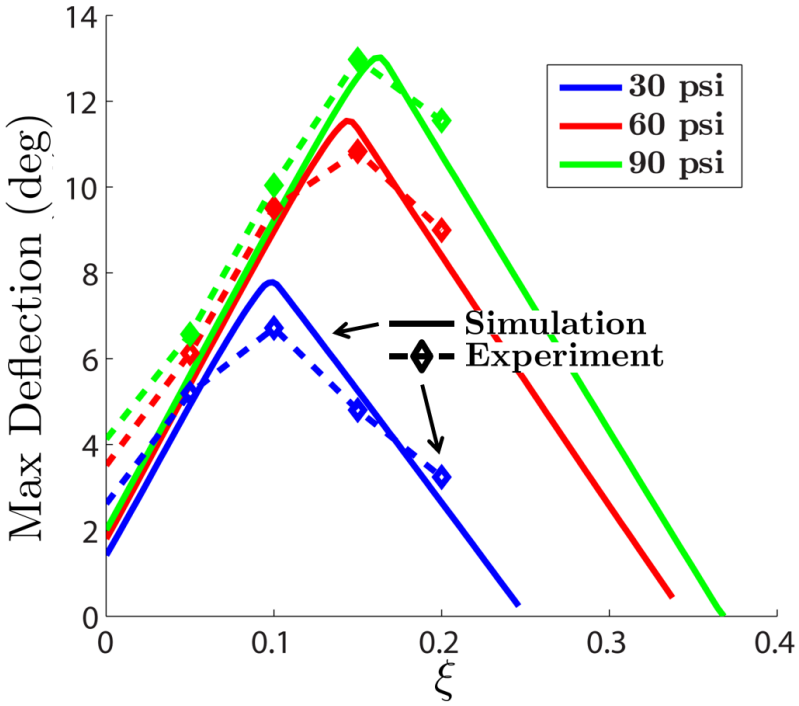

Figure 3.12: Comparison of simulated and experimental maximum mechanism deflection as a function of PAM bias contraction.

Figure 3.12 shows a comparison between the simulated maximum deflection and discrete experimental maximum deflections for the PAM/mechanism system described in the previous paragraph acting against a 10 inch-lb/degree torsional spring. In this figure, the solid lines represent the simulated maximum deflections and the diamonds connected by dashed lines represent discrete experimental data points taken from $\xi = 0$ in increments of 0.05, and results are presented for 30, 60, and 90 psi PAM pressures. Note that, as expected, at $\xi = 0$ (no bias contraction) the system performs poorly, achieving only 4 degrees of deflection. At this condition, the simulation and experiment do not match up well. However, as bias contraction increases, the simulation and experiment agree well for all pressures. For the 90 psi case, the maximum deflection of 13 degrees occurs at approximate $\xi = 0.16$, which

represents a 300% increase over the design without bias.

3.7 Conclusions

This work discussed two methods for increasing the available torque for an antagonistic, bi-directional, rotational actuator using pneumatic artificial muscles (PAMs). The first method was to intelligently choose the kinematic mechanism that connects the PAMs to the point of rotation. It was found that in all cases, an offset lever configuration will produce superior results to a conventional lever or pulley configuration in terms of output torque and range of motion. The second method involved including bias in the design, in the form of bias contraction and bias pressure. It was shown that for better performance, bias pressure should be kept as low as possible, while maintaining requirements for off-state hinge stiffness. The role of bias contraction, however, was found to be highly coupled to the desired loading (purpose) of the system, as well as the geometry of the offset lever mechanism. It was shown that an optimum arrangement can be found parametrically for a simplified case that improved maximum deflection angle by nearly 50%, and suggested that a numerical optimization technique could be used to solve the full optimization problem. The PAM bias model was also validated experimentally with a "worst case" system which would typically have very poor performance. Through the inclusion of PAM bias, the maximum deflection of the system was increase by $\approx 300\%$ and also matched well with model predictions.

Chapter 4: Chordwise Implementation of Pneumatic Artificial Muscles to Actuate a Trailing Edge Flap

4.1 Introduction

Trailing edge flaps (TEF) on helicopter rotor blades can be used to reduce vibration and noise, and even affect primary control. Many conceptual studies exist that point to the potential benefits of a TEF system [12,55,56], and numerous concepts have been explored for physical demonstrators with varying levels of success [11,57–60]. The main design challenge has been creating a system that is capable of meeting either the high bandwidth (for vibration and noise reduction) or high deflection (for primary control) requirements, while minimizing added weight and complexity.

For primary control, both Shen, Chopra, and Johnson [55] and Falls, Datta, and Chopra [57] predict a maximum flap deflection requirement of 10 degrees half peak-to-peak (HPP) at 1-2 actuations per rotor revolution (1-2/rev). These predictions were supported with scaled down wind tunnel testing, but no full-scale TEF tests for primary control were attempted, mostly due to insufficient actuation authority. Vibration and noise reduction, however, generally require less deflection. Straub *et al.* [59] and Dieterich *et al.* [60], both focused on vibration and noise reduction and

represent the only TEF concepts that have been successfully implemented and tested on full-scale rotors. Straub *et al.* predicted a required 2 degrees HPP deflection at $(N_b + 1)$/rev, where N_b is the number of rotor blades, and was able to achieve 3 degrees HPP during whirl testing. Dieterich *et al.* required deflection frequencies of 3-5/rev for vibration reduction, and 2/rev for noise reduction, both at 5 degrees HPP (the actuator's maximum deflection). Note that both of these prototypes were not capable of the 10 degrees HPP deflections required for primary control.

Candidate actuation technologies in the literature include piezoelectric actuators [11, 44, 57, 59–61], electro-mechanical actuators [62], purely mechanical linkages (pioneered by Kaman Aerospace), and pneumatic artificial muscles (PAMs) [58, 63]. PAMs are a particularly intriguing actuation technology due to their light weight, high specific work, high damage tolerance and fatigue life, large strains when compared to other active materials, controllability, and moderate operating pressures [53,58,63–65].

Woods et al. [58] demonstrated a PAM TEF system for a Bell 407 scale helicopter blade section capable of ±19 degrees of deflection at 1/rev (the primary rotor frequency) and ±7 degrees of deflection at 5/rev when tested at Mach 0.3 in a wind tunnel. This indicates that it may be suitable for primary control as well as noise/vibration reduction, despite the test not being performed at full-scale loading. In this design, a pair of 9 inch (natural length) PAMs were oriented spanwise along the blade (perpendicular to the blade chord), and mounted near its root. This allowed a great deal of design freedom in terms of choice of PAM size and hinge mechanism dimensions. However, this approach also had a large impact on the rotor blade itself, with mechanism parts running the length of the blade and the actuation

energy transferred through a number of bell-cranks before ultimately reaching the flap far outboard. This is un-desirable as it increases both the weight and complexity of the blade, and makes retrofitting a PAM TEF system in an existing blade design difficult.

This past work provides motivation to examine a chordwise implementation of the PAM TEF system, where the PAMs are oriented parallel to the chord of the rotor blade. The benefits of such a chordwise PAM actuator include a more direct link between the PAMs and the flap, a much smaller overall size and weight, and the possibility to make the system modular/removable as a discrete blade section. One downside to this approach is that it necessitates the use of much shorter PAMs than in a spanwise arrangement due to the tapering nature of the airfoil and the fact that the system should not alter or interfere with the main rotor structural spar. In general, PAM contraction is limited to around 35% of their natural (resting) length. This means that a shorter PAM has less absolute contraction (stroke) than a larger PAM, which introduces a major design constraint.

The present chapter attempts to design a bench-top chordwise PAM TEF system capable of both primary control and vibration/noise reduction. First, PAM bi-directional actuation is discussed with a focus on methods of increasing PAM/Actuator system angular deflection. Next, a candidate UH-60-like helicopter is studied in simulation to determine appropriate loading conditions for the actuation system. A numerical optimization is then presented that maximizing the angular deflection of the PAM TEF system under the given constraints. Finally, experimental results from the optimized system are presented and discussed.

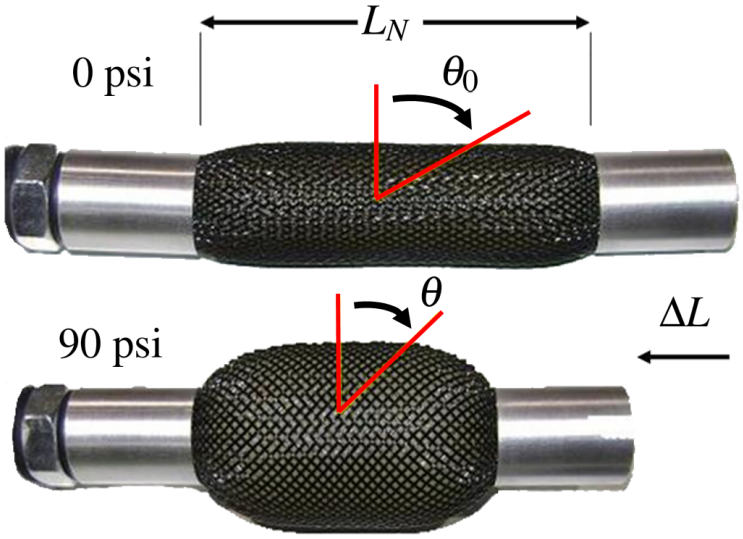

Figure 4.1: A typical PAM, shown in its relaxed and contracted states.

4.2 PAMs as Bi-directional Actuators

The basic form of a contractile PAM is pictured in Figure 4.1. It consists of a stiff helically braided sleeve that is clamped and sealed at both ends with aluminum end-fittings. When the PAM is pressurized (usually with air), the bladder tends to expand radially. Because the sleeve covering the bladder is very stiff, this radial expansion forces the PAM to shorten from its natural resting length, L_N, by some deflection ΔL (stroke). As the PAM shortens, the fiber angle decreases until it reaches a physical equilibrium and is no longer able to produce force. The general bi-directional PAM configuration is shown in Figure 4.2. Here two PAMs are arranged in an antagonistic manner about a hinge, and when the active muscle contracts and pulls with force F_A, it rotates the hinge by an angle of δ until equilibrium is reached with the antagonistic muscle force, F_P, and any external hinge loading.

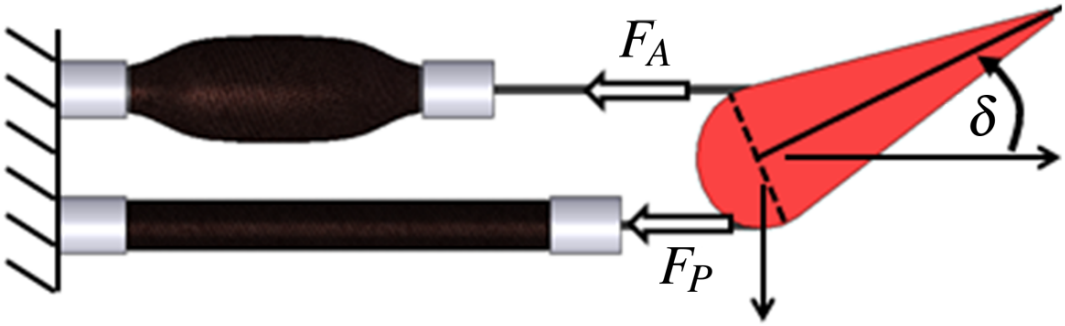

Figure 4.2: PAMs arranged in an agonist-antagonist pair for bi-directional rotation.

4.2.1 PAM Bias Contraction

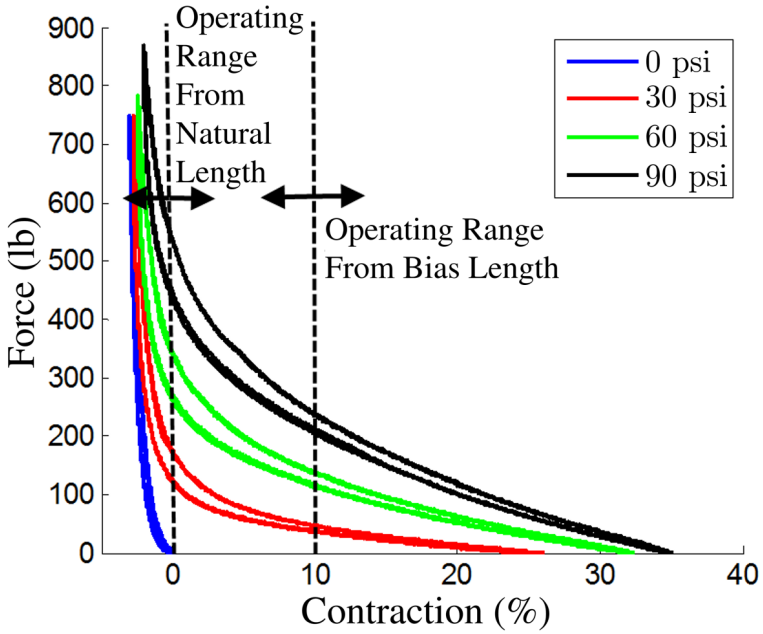

Figure 4.3: Exemplary PAM force vs. contraction curve, illustrating the operating range for a typical antagonistic actuator, and the operating range when bias is considered.

A typical set of PAM force-contraction curves is shown in Figure 4.3. Note that, unlike pneumatic pistons, PAM force decreases with contraction until it reaches a physical equilibrium. PAMs are also quite stiff when stretched past their natural length due to the stiffness of the braid material (typically Kevlar), as indicated by

the sharply increasing curves to the left of the 0% contraction line.

In a typical antagonistic PAM setup, the actuators will operate from their natural length. The active (pressurized) PAM will, for example, follow the 90 psi load line in the positive deflection direction, and the passive PAM will follow the 0 psi load line in the negative contraction (extension) direction until torque equilibrium is reached. This approach works well when the actuation mechanism has a relatively small moment arm as compared to the active length of the PAMs because at large values of extension, the passive PAM quickly stiffens and reduces the torque available for work. This problem is exacerbated as the PAM length shortens and approaches the same order as the mechanism effective moment arm, as is the case for the more compact chordwise system under considered here. In this instance, for a given angular deflection the shorter passive PAM must extend a larger percentage of its natural length, creating more parasitic torque. A promising approach to increasing deflection for a given PAM mechanism is to decrease the passive parasitic torque through the introduction of bias contraction in the PAMs [107]. Figure 4.3 shows an example of a PAM system operating from a 10% bias contraction. The active PAM now has a lower initial force than in the previous case, but the passive PAM has either zero force (if operating at 0 psi) or a much lower stiffness than the traditional case if operated at some non-zero pressure. PAM bias contraction can be represented non-dimensionally as

$$\xi = \frac{L_B}{L_N} \tag{4.1}$$

where L_B is the installed bias-contraction length, L_N is the PAM's natural resting

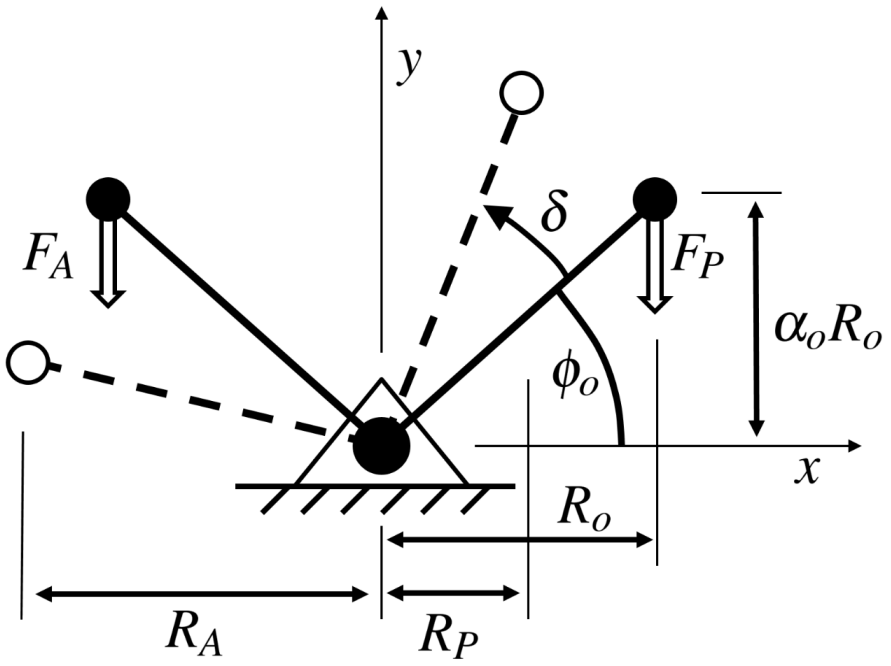

Figure 4.4: Offset lever mechanism definition.

length, and $\xi \in [0, \lambda_{min})$. Note that λ_{min} is a non-dimensional representation of the unloaded equilibrium condition for a given PAM, and is generally pressure-dependent.

4.2.2 PAM Actuator Description

A different way to increase PAM actuator performance is to modify the torque transfer mechanism from a pulley (Figure 4.2) to an offset lever mechanism (Figure 4.4) [58]. Here, the active PAM force, F_A, acts on the left and passive PAM force, F_P acts on the right, both in the downward direction shown. As the mechanism deflects, the active PAM's moment arm, R_A, increases while the passive PAM's moment arm, R_P, decreases. This has the effect of increasing the active moment and decreasing the parasitic passive moment, which increases the overall mechanism deflection angle, δ.

The mechanism geometry is defined by its horizontal moment arm, R_o, and α_o, which is the ratio of the vertical attachment point offset to the horizontal moment arm. The angle that the line from the center of rotation to the PAM attachment point makes with the horizontal is defined as

$$\phi_o = \tan^{-1} \alpha_o. \tag{4.2}$$

Using small angle assumptions, the torque available for external work can be defined as

$$T_a = F_A R_A - F_P R_P, \tag{4.3}$$

where F_A and F_P are the active and passive PAM forces, respectively and are generally functions of PAM geometry, contraction, and pressure. The system will reach quasi-static equilibrium when the torque available, T_a, equals the required external loading, T_r, which is usually defined as

$$T_r = K_\delta \delta \tag{4.4}$$

where K_δ is a torsional spring stiffness. This analysis is sufficient for actuators where the PAM length is much greater than the mechanism moment arm R_o, but tends to over-predict in cases where the PAM and mechanism (bell-crank) dimensions are on the same order.

Figure 4.5 depicts a more accurate model for the present chordwise system. Both the active and passive PAMs are shown in their deflected (solid black lines) and

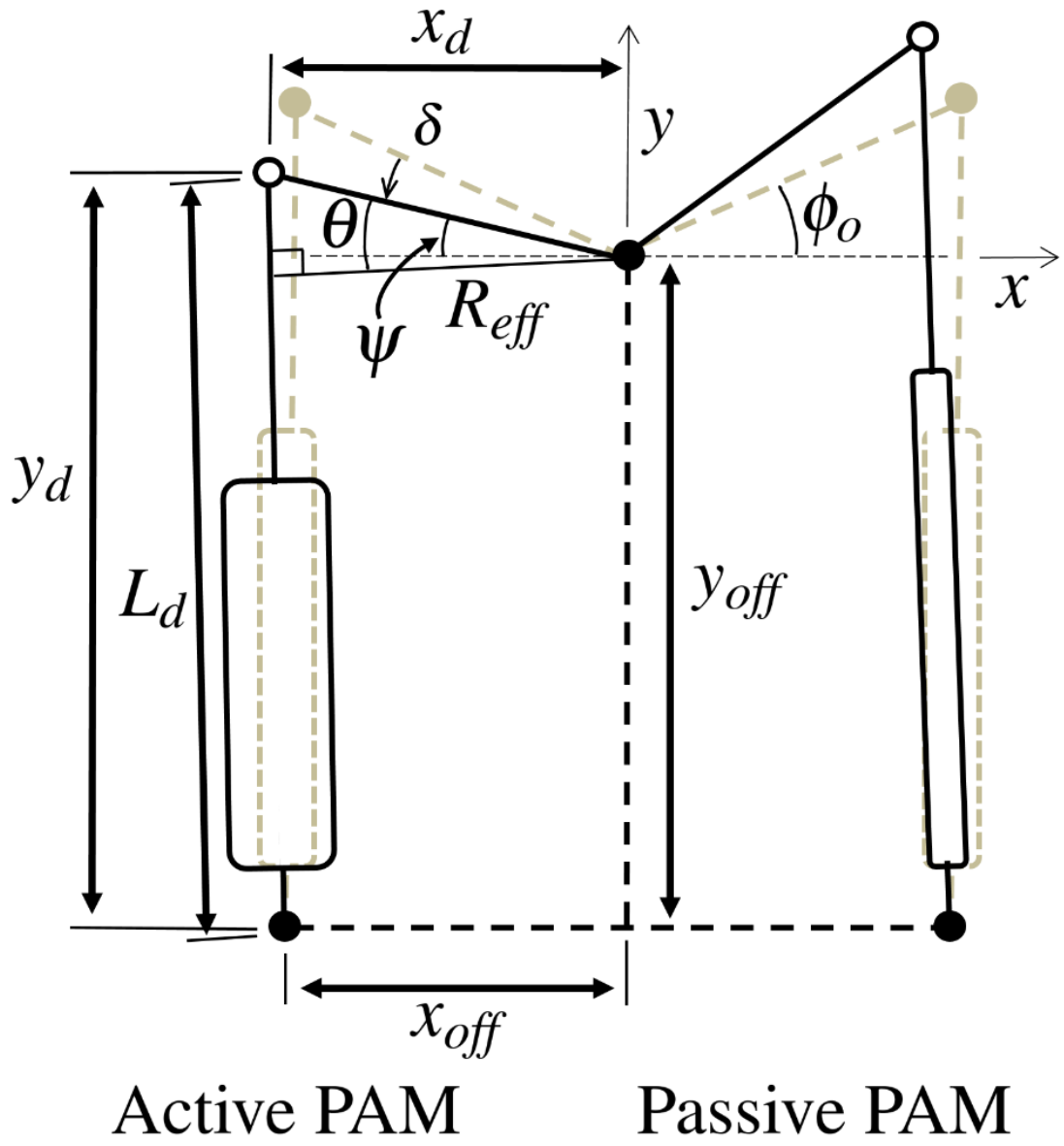

Figure 4.5: Conceptual schematic of offset lever mechanism with large angle assumptions.

undeflected states (dashed grey lines). The vertical and horizontal PAM mounting points are described by x_{off} and y_{off}. At a given δ, the deflected positions of the active PAM mechanism connection point with respect to its fixed anchor point are given by

$$\begin{aligned} x_d &= \frac{R_o}{\cos\phi_o}\cos\psi - x_{off}, \\ y_d &= \frac{R_o}{\cos\phi_o}\sin\psi + y_{off}, \end{aligned} \tag{4.5}$$

where $\psi = \phi_o - \delta$ is the angle between the active PAM lever line and the x axis. The deflected PAM length is defined as

$$L_d = \sqrt{x_d^2 + y_d^2}. \tag{4.6}$$

The effective moment arm, R_{reff}, defined as the line originating at the center of rotation and perpendicular to L_d, can be determined from

$$R_{eff} = \frac{R_o}{\cos\phi_o}\cos\theta \tag{4.7}$$

where

$$\theta = \psi + \tan^{-1}\frac{x_d}{y_d} \tag{4.8}$$

and is defined as the angle between the active lever line and R_{eff}. A similar set of expressions can be derived for the passive side.

With the effective moment arms determined, the available torque can be redefined as

$$T_a = F_A R_{eff,A} - F_P R_{eff,P}. \tag{4.9}$$

An algorithm was created to find the deflection, δ, at which $T_a - T_r = 0$ for an arbitrary loading condition. This corresponds to the quasi-static half peak-to-peak (HPP) deflection of the actuator/PAM combination.

4.3 TEF Loading Condition Simulation

In order to approximate realistic TEF hinge stiffness requirements to guide the design, a low fidelity hinge moment analysis and helicopter trim was performed. The aerodynamic hinge moment was modeled using an adapted form of thin airfoil theory [58,117]. This analysis is highly dependent on flap dimensions, blade tip speed, and blade pitch angle, and so a simple UH-60-like helicopter was first simulated in hover and in forward flight to provide representative values for these variables. Table 4.1 gives the properties of the candidate helicopter and the chosen flap parameters, which were adapted from Ravichandran *et al.*, 2013 [56].

4.3.1 Helicopter Trim Model

The helicopter trim performed here was a "free-flight" analysis where the three forces and moments produced by the main rotor are balanced by the forces and moments produced by the fuselage during hover and forward flight [118]. To accomplish this, the trim code iterates on the main rotor collective (θ_0) and cyclic (θ_{1s}, θ_{1c}) pitch controls, as well as the tail rotor collective pitch until a convergence criteria is satisfied. Simplifying assumptions for the present analysis include uniform inflow, constant rotor profile drag, linear blade twist, that there is sufficient power to

Table 4.1: Basic helicopter and flap data

Property	Value
Helicopter	
Gross weight, W	16,000 lb
Number of blades, N_b	4
Rotor radius, R	25 ft
Rotor planform	Rectangular
Rotor chord, c	1.5 ft
Rotor twist (linear), θ_{tw}	-8 degrees
Profile drag coef., C_{do}	0.01
Fus. drag area, f	25 ft^2
Tip speed, V_{tip}	700 ft/s
Max cruise speed, V_{max}	150 kts
Dist. from CG to hub[1]	6 ft
Flap frequency, ν_β	1.036
Lock number, γ	6
Atmospheric conditions	ISA Standard Day
Flap[2]	
Flap span	15% R
Flap chord, c_f	15% c
Midspan location	at 65% R
Hinge location	Flap leading edge

[1]CG assumed to be directly in-line with hub axis
[2]Adapted from Ravichandran *et al.*, 2013 [56]

reach all simulated flight regimes, and that the tail rotor/aerodynamic surfaces are able to counter the yaw from the main rotor. While these assumptions make this simulation less accurate than a blade element momentum theory or CFD analysis, it still easily fulfills its main purpose of providing realistic rotor blade pitch inputs for the hinge moment analysis of the trailing edge flap.

Trim was performed for hover ($V_\infty = 0$ kts) and for a sweep of speeds from hover to the maximum cruise speed listed in Table 4.1 ($V_\infty = 150$ kts). Figure 4.6

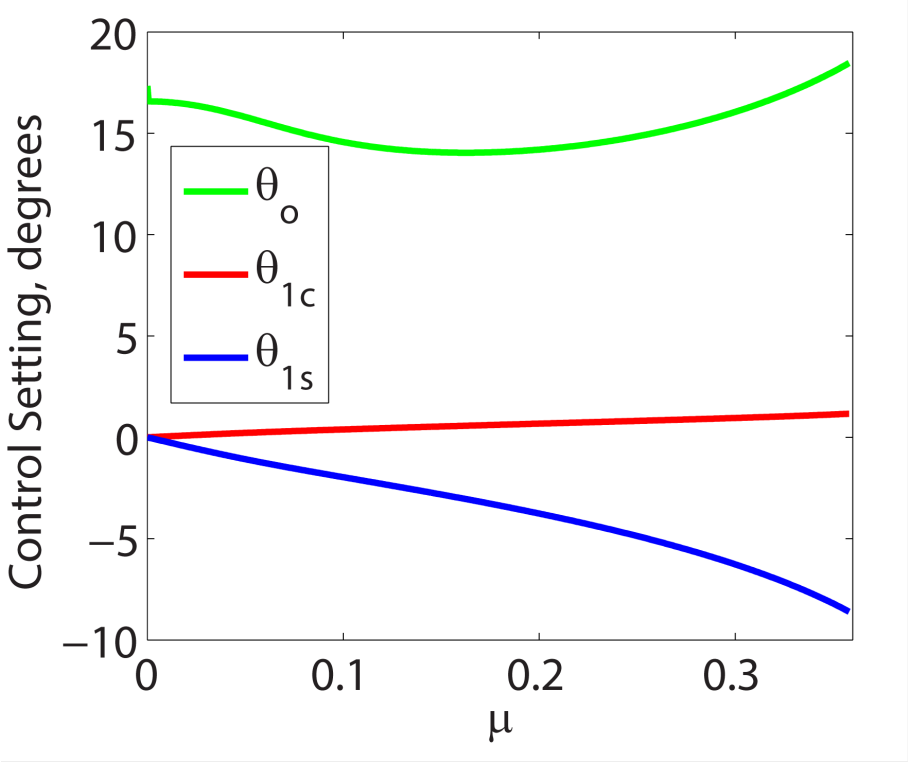

Figure 4.6: Simulated helicopter control settings as a function of advance ratio.

shows the three control settings as a function of advance ratio, μ, which is defined as

$$\mu = \frac{V_\infty \cos \alpha_s}{V_{tip}} \tag{4.10}$$

where α_s is the longitudinal angle-of-attack of the rotor disk. From this data, blade pitch as a function of rotor azimuth, ψ_{rot}, can easily be calculated for any advance ratio with the expression

$$\theta(\psi_{rot}) = \theta_0 + \theta_{1s} \sin \psi_{rot} + \theta_{1c} \cos \psi_{rot}. \tag{4.11}$$

The curves in Figure 4.6 follow the expected trends with increasing forward

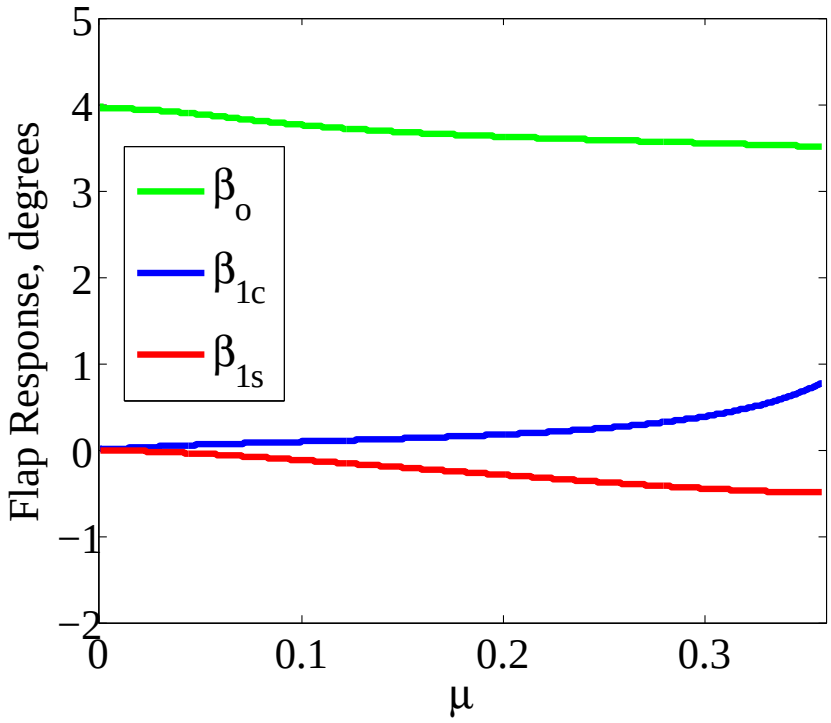

Figure 4.7: Simulated blade flapping response as a function of advance ratio.

speed for a rotorcraft with no lateral CG offset, where θ_0 and $\theta_1 c$ stay fairly constant, but $\theta_1 s$ slowly decreases in order to tilt the rotor disk forward. Results for rotor blade flapping response are shown Figure 4.7, where rotor blade flapping as a function of rotor azimuth is defined analogously to Equation 4.11. Again, the results are reasonable and in-line with the control deflections from Figure 4.6.

Figure 4.8 depicts the vehicle orientation as a function of forward flight speed, where α_s is the longitudinal forward tilt of the helicopter and ψ_s is the starboard leaning lateral tilt of the aircraft. Finally, rotor tip-path-plane inflow versus advance ratio is plotted in Figure 4.9, which follows the expected trend for a tilted rotor disk of decreasing from hover to a minimum in the middle of the flight regime, and then increasing again as the aircraft increases speed.

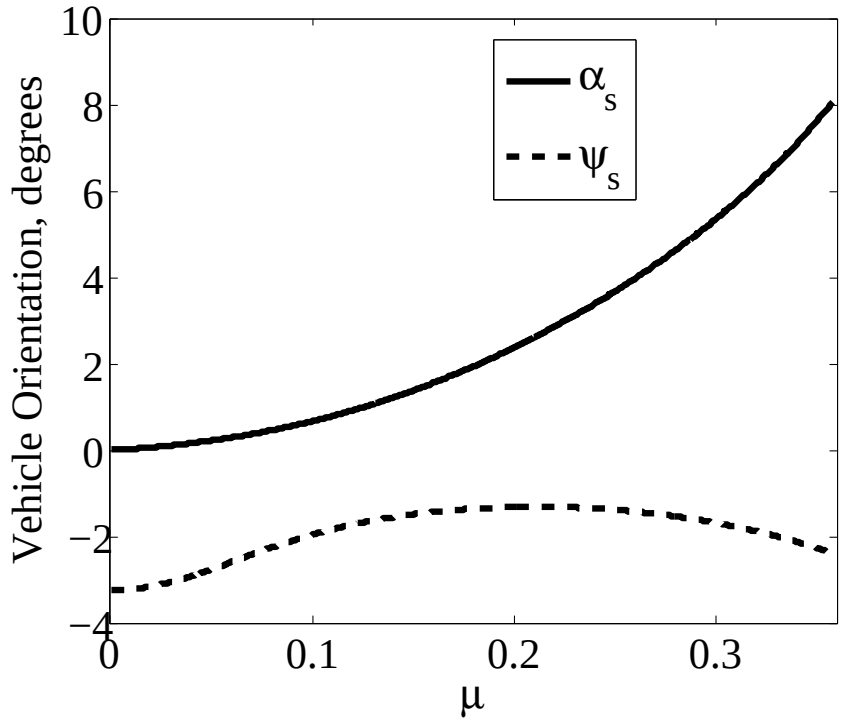

Figure 4.8: Simulated helicopter orientation as a function of advance ratio.

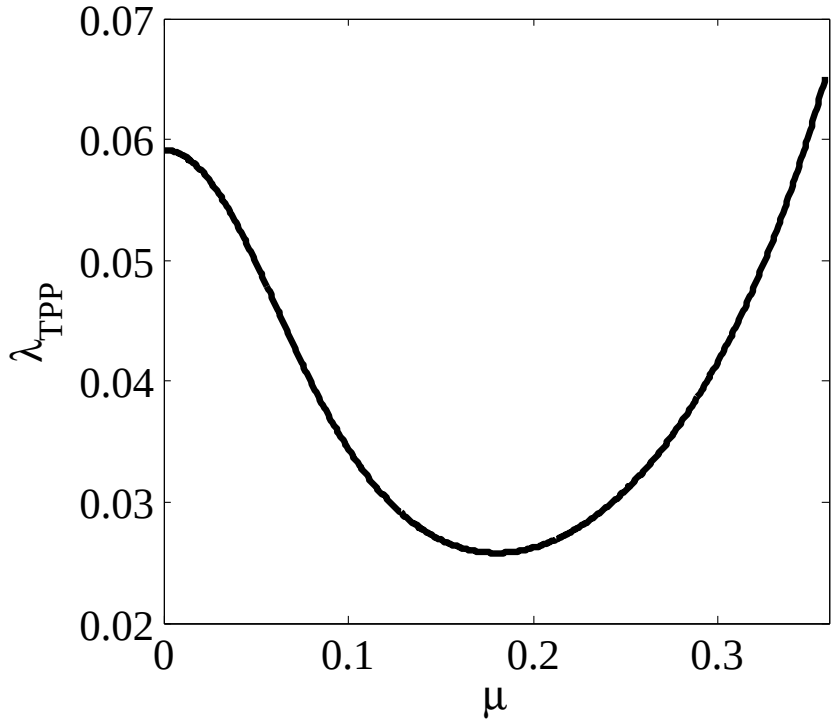

Figure 4.9: Simulated rotor inflow as a function of advance ratio.

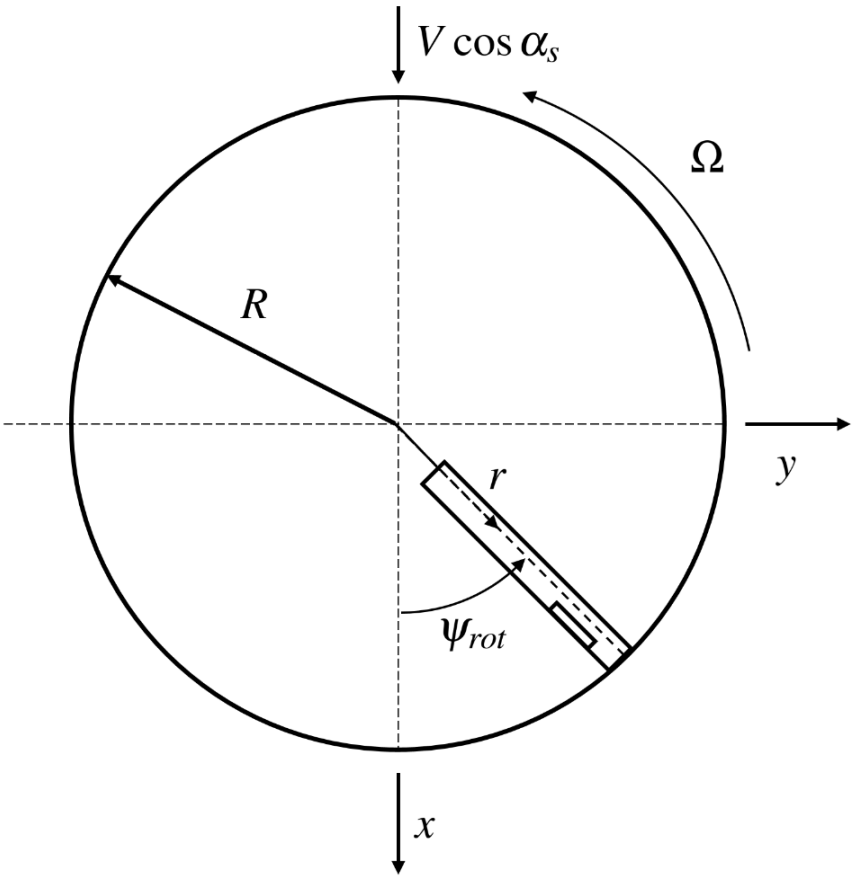

Figure 4.10: Conceptual schematic of a rotor blade with TEF.

4.3.2 Hinge Moment Simulation

Consider a flap on a rotor blade as depicted in Figure 4.10. The rotor blade is rotating at an angular velocity Ω, and is subject to a velocity parallel with the rotor plane $V_\alpha = V_\infty \cos\alpha_s$. The aerodynamic hinge moment on the flap can then be defined as

$$H = \int_{r_1}^{r_2} q c_f^2 c_h \, \mathrm{d}r \tag{4.12}$$

where q is the dynamic pressure of the flow over the flap, c_f is the flap chord, and c_h is the flap hinge moment coefficient. In general, all of these values are functions of

flap radial position, r, rotor azimuth, ψ_{rot}, free-stream velocity, and rotor orientation. Using thin airfoil theory [117], the hinge moment coefficient can be broken down into a summation of lift coefficient and TEF deflection dependent terms:

$$c_h = c_l \frac{\partial c_h}{\partial c_l} + \delta \frac{\partial c_h}{\partial \delta} \tag{4.13}$$

where the section lift coefficient, c_l, is defined as

$$c_l = a(\alpha + k_\delta \delta). \tag{4.14}$$

Here, a is the local lift slope, α is the section angle-of-attack (AOA), and k_δ is a proportionality constant that relates flap deflection to section lift, where a positive flap deflection causes an increase in section lift. Lift slope, a, is also dependent on r through the Glauert compressibility relationship: $a = 2\pi/\sqrt{1-M}$ where M is the local Mach number.

Assuming a thin airfoil and plain flap with no aerodynamic balance, both partial derivatives from Equation 4.14 as well as k_δ can be estimated solely from the non-dimensional flap chord, $E = c_f/c = 0.15$. Refer to Woods *et al.*, 2011 [58] for a full description of these expressions.

Using the trim values obtained from the previous section, α can be determined as a function of rotor azimuth angle (ψ_{rot}), advance ratio (μ), inflow (λ_{TPP}), and

radial blade location (r):

$$\alpha(\psi_{rot}, \mu, \lambda_{TPP}, r) = (\theta(\psi_{rot}) + \theta_{tw} r/R) - \phi_{rot} \tag{4.15}$$

where $\phi_{rot} = \tan^{-1}(u_p/u_t)$ is the angle of the free-stream velocity with respect to the hub plane. The quantities u_p and u_t are non-dimensional perpendicular and tangential velocities to the blade section of interest where

$$\begin{aligned} u_p =& \lambda_{TPP} \\ u_t =& \frac{r}{R} + \mu \sin \psi_{rot}. \end{aligned} \tag{4.16}$$

With α now determined, c_l can be calculated in terms of δ and substituted back into Equation 4.12, which is then integrated from the inboard to outboard edge of the flap. Depending on the choice of azimuth and forward flight speed, any number of hinge moment solutions can be found, and so the choice was made to examine three representative cases.

The first is the canonical hover condition where there is very little blade pitch variation and no velocity change as function of azimuth. The second and third conditions represent the highest and lowest loading conditions seen on the aircraft. That is, the advancing side (ψ_{rot} = 90 degrees) and retreating side (ψ_{rot} = 270 degrees) of the rotor at its top forward speed. For these conditions, the hinge

moments are

$$H_{hover} = -9.04\delta - 28.25 \text{ inlb}$$

$$H_{adv} = -22.61\delta - 138.27 \text{ inlb}$$

$$H_{ret} = -1.83\delta + 0.27 \text{ inlb}$$

where δ has units of degrees. The general form of these expressions is a linear stiffness proportional to flap deflection, plus an offset moment due to the angle-of-attack of the blade. The negative signs in these expressions indicate that, for a given flap deflection, the induced hinge moment will be in opposition to the flap movement.

4.4 PAM Mechanism Optimization

With design loading conditions and a method for determining quasi-static PAM actuator deflections established, a constrained gradient based optimization was performed to maximize the achievable deflection at all three of the loading conditions under investigation. Candidate design variables included the offset lever mechanism geometry, such as R_0, α_0, x_{off}, and y_{off}, and the PAM geometry, such as L_N, outer diameter, braid size, and PAM bias, ξ.

While making the PAM geometry part of the optimization would be intriguing, the discrete nature of many of its design variables makes it ill-suited for a gradient based optimization. Instead, a PAM was designed that fit the general requirement of the present work, that is, being much shorter than the PAM used in the previous spanwise design [58] (approximately 3 times) and being able to easily fit inside the candidate blade chord. Specifically, the selected PAM size had an outer diameter of

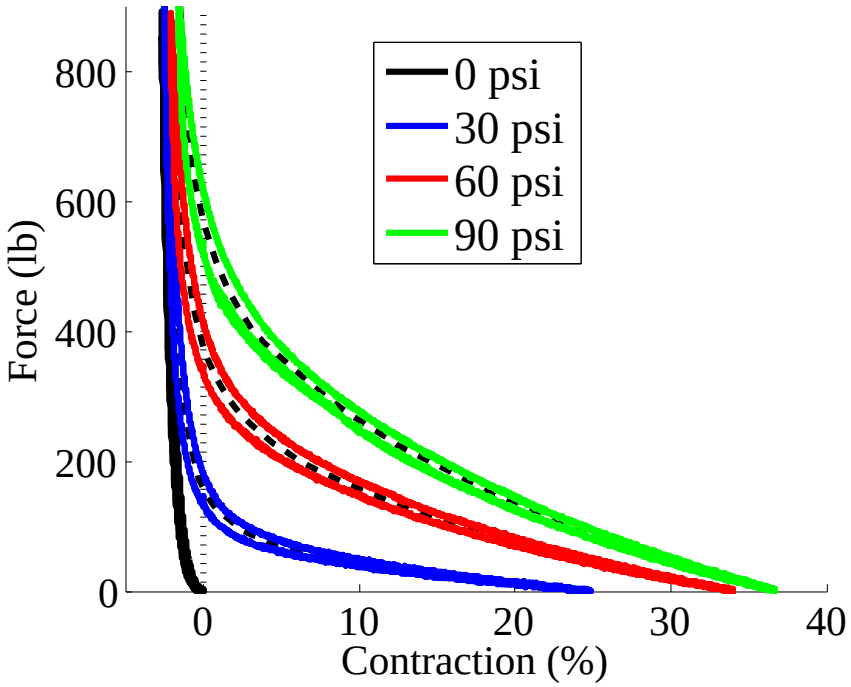

Figure 4.11: PAM data used for optimization. Black dashed lines are spline fits to the force versus contraction data.

5/8 in (same as previous design), a natural length of 3.35 in (as opposed to 9 in), and a total length of 4.85 in including end-fittings. The braid material was a 1.5 in nominal diameter Kevlar helically braided sleeve. Experimental characterization for this PAM can be seen in Figure 4.11, including black dashed lines that represent spline fits to the experimental data so the optimizer could easily calculate PAM force for any given point along the contraction range.

Additionally, the PAM mounting vertical offset x_{off}, was fixed at 7 inches to ensure the actuator would maintain its small footprint and fit within roughly half of the candidate blade chord, or approximately 9 inches. The horizontal PAM offset, y_{off}, was set to equal R_o. This left the lever mechanism horizontal moment arm R_o, vertical offset ratio α_o, and PAM bias contraction, ξ, as design variables.

The optimization can be formally described as

$$\begin{aligned} &\max_{X} \; f(X) = \delta(X) \\ &\text{subject to } X_{LB} \leq \; X \leq X_{UB}. \end{aligned} \tag{4.17}$$

where X is the vector of design variables and $f(X)$ is the objective function that calculates the equilibrium deflection for a given system and set of design variables. The design variables are also subject to upper and lower bounds, which are summarized in Table 4.2. These bounds ensured that the final design would be manufacturable and would not violate the allotted chordwise volume.

Table 4.2: Lower and upper bounds on design variables.

Variable	Lower Bound	Upper Bound
R_o (in)	0.75	3
α_o	0	1
ξ	0	0.2

The optimization was run at a variety of loading conditions and some general trends were noted. First, α_o was always converged to its maximum value of 1, as this helps to decrease the passive parasitic torque. Larger values than $\alpha_o = 1$ were not allowed because of manufacturing concerns. Additionally, as spring loading increased, R_o also tended to increase. Bias contraction, ξ, did not show a clear trend in this study.

The final design was optimized at the advancing side loading condition, with the rationale that if the mechanism could achieve large deflections at this loading, it would also perform well at the hover and retreating side conditions. For an active

PAM operating at 90 psi, and a passive PAM at 0 psi, the optimum solution for the advancing side is

$$R_o = 1.56 \text{ in}$$

$$\alpha_o = 1.00 \text{ (a 45 degree angle)}$$

$$\xi = 0.065 \text{ (6.5\% pre-contraction)}$$

with a maximum deflection of 9.44 degrees. Figure 4.12 depicts the change in maximum deflection for the optimized design from as a function of variation in the linear torsional loading term. The system was optimized at what was assumed to be the largest loading, but to be conservative, a range from 0% to 120% of the design stiffness was simulated. As would be expected, when the applied loading is decreased, the maximum deflection increases. When loading is increased, the maximum deflection correspondingly decreases but at 120% of the nominal loading, the system defection is only degraded by $\approx 8\%$, indicating that this design is not overly sensitive to increases in stiffness.

Additional simulations were performed on the optimized design to deterimine its sensitivity to manufacturing defects or inconsistencies. Figure 4.13 depicts deviation in system maximum deflection from the nominal value (9.44 degrees) as a function of change in PAM bias contraction (ξ) and bell crank vertical offset ratio (α_0). All values are presented as percent changes from their optimized values, given above. First, any deviation from the optimum bias condition degrades performance. However, a very large $\pm 20\%$ deviation only decreases maximum deflection by about 8%, indicating that the system will not be significantly affected by the much smaller deviations from

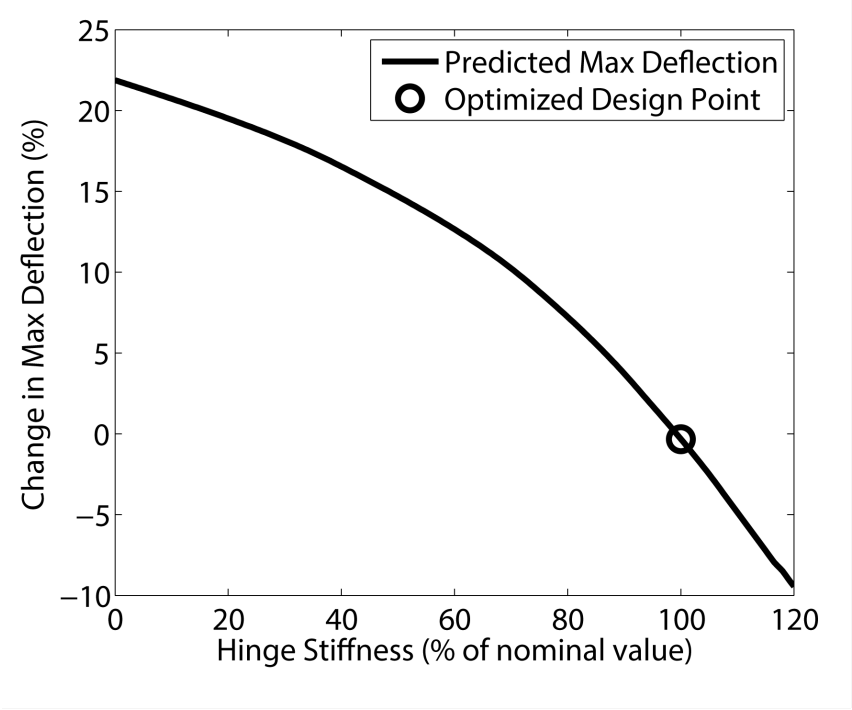

Figure 4.12: Sensitivity of maximum deflection to variations in hinge moment.

the optimum design that would be common due to manufacturing inconsistencies. Second, deviations in α_o appear to have very little impact on the system performance. A 20% decrease in α_o only degrades performance by $\approx 2\%$, while a 20% increase actually improves performance slightly. Recall that α_o was limited to a maximum value of 1, which is why a larger value was not chosen for the optimum. Similar trends are shown for variations in R_o. These results, along with those presented in Figure 4.12, indicate that the optimum is robust and will not degrade significantly due to changes in operating condition or design variable value.

4.5 Experimental Testing

Figure 4.14 shows the bench-top test apparatus used to simulate flap hinge moments. Pressurized air was supplied to the PAMs through a 5/3-way proportional

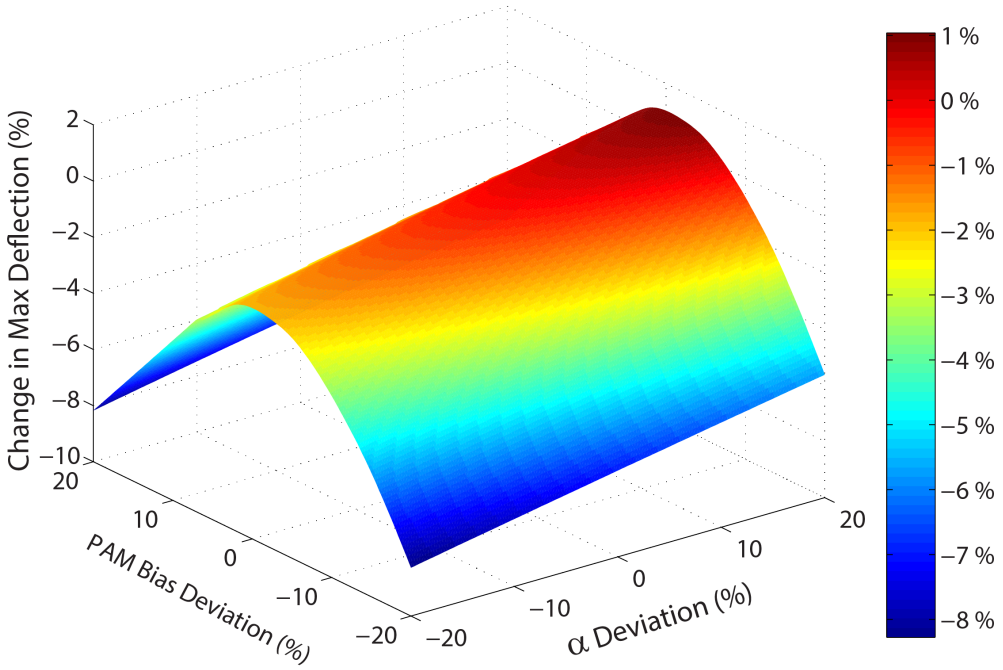

Figure 4.13: Sensitivity of maximum deflection to variations in bell crank vertical offset ratio (α_o) and PAM bias contraction (ξ).

voltage-controlled spool valve attached to a pressure regulator. Pressure was measured slightly upstream of the PAMs by a 200 psi pressure transducer. PAM force was measured using an in-line 1000 lb load cell. A ±45 degree angle sensor, not visible in the picture, was mounted underneath the setup at the rotational axis. The offset lever mechanism optimized in the previous section was designed in a commercial CAD package and machined out of aluminum. Flap hinge stiffness, K_δ, was simulated through the use of a 0.25 in diameter 15-5PH stainless steel torsional spring. The torsion rod clamped length, l, can be determined through the expression

$$l = \frac{GJ}{K_\delta} \tag{4.18}$$

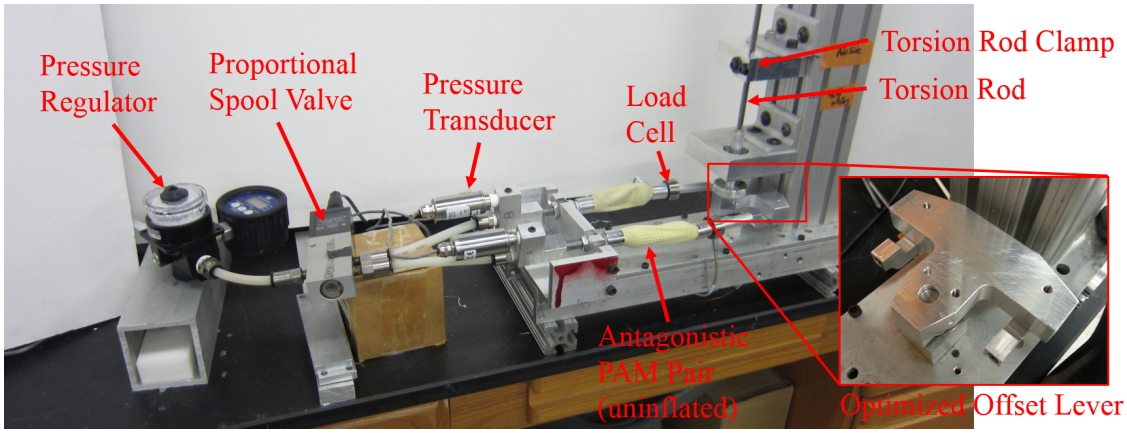

Figure 4.14: Photograph of the TEF bench-top setup with torsional spring stiffness.

where G is the shear modulus of the constituent material, and J is cross sectional polar moment of inertia. The PAM bias contraction was adjusted by two pairs of jam nuts located between the pressure transducers and the PAMs.

It is important to note that the torsional hinge loading simulated for this suite of tests is quasi-static, that is, it is linear with flap deflection and the value of the the hinge stiffness does not change within a test. This is not a realistic representation of the highly dynamic and unsteady rotorcraft environment, but is sufficient for the present work as a proof-of-concept.

4.5.1 Open-loop Testing

4.5.1.1 Test Plan

Experimental bench-top testing was performed on the optimized actuator system at a variety of loading conditions, frequencies, and pressures. Table 4.3 describes the four test conditions that include both hover and advancing-side simulated stiffnesses, and with/without the offset moment due to the blade angle-of-attack.

All tests were performed at 30, 60, and 90 psi, and at frequencies ranging from quasi-static (0.5 Hz) to 1-10/rev, with 1/rev = 4.45 Hz (from Table 4.1). Spring stiffnesses were experimentally verified to be within ±0.5% of their desired value before testing began. Offset moments were simulated by offsetting the spring zero location from the geometric zero of the test stand, such that the spring produced the required offset torque in the positive deflection direction at the geometric zero. In each open-loop test case, the control valve was driven with a 0-10 Volt square signal at the noted frequency.

Table 4.3: Tested loading conditions. All tests done at 30, 60, & 90 psi and at 0-10/rev frequencies.

Test Condition	Stiffness (inlb/deg)	Offset Moment (inlb)
Hover	9.04	0.00
Hover with Offset	9.04	28.25
Advancing	22.61	0.00
Advancing with Offset	22.61	138.27

4.5.1.2 Quasi-static Comparison to Predictions

Quasi-static testing was performed at each loading condition and pressure in the test matrix to validate the accuracy of the simulation used in the optimization. The results of these experiments are shown in Figure 4.15, with each group of three bar clusters representing one loading condition at various pressures. Note that the values for the loading conditions that include moment offset are for the worst-case scenario, where the moment offset adds to the required moment, while the values for

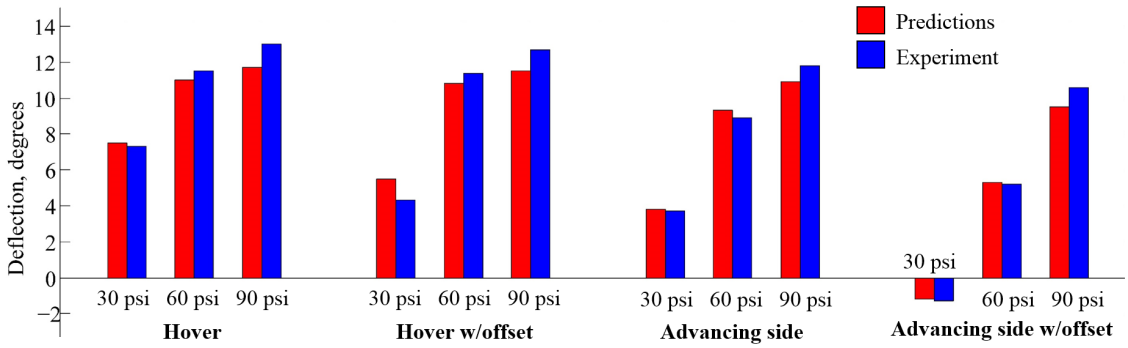

Figure 4.15: Comparison between quasi-static (0/rev) experimental results and analytical predictions for half peak-to-peak deflection.

the non-offset cases represent half peak-to-peak (HPP) deflection. This "worst-case" is the reason for the negative deflection at the advancing side with offset for the 30 psi case, where the system reaches equilibrium before crossing the geometric zero. This testing was also conducted only acting against the spring stiffness, and did not include the simulated flap inertia. It is clear that for the majority of the loading conditions and pressures, the analytical predictions are within ± 1 degree of the experimental results, and are often much closer for the 60 and 30 psi cases. This validated the simulation approach used in the optimization, and showed deflection values at levels congruent with primary control for all loading conditions.

4.5.1.3 Dynamic Experimental Results

Dynamic data was collected at all stiffness conditions shown in Figure 4.15, however, only date for the most demanding case (advancing side stiffness including offset moment) will be presented here, as this is the highest loading condition the actuation system is expected to encounter. These dynamic tests also included an inertial mass of 5.3 lb in^2, calibrated to replicate the flap-system inertia. Figure 4.16

shows the open-loop half peak-to-peak deflection (HPP) for the advancing side stiffness condition with torque offset. From quasi-static to 3/rev, the system is able to maintain approximately 12 degrees of HPP deflection at 90 psi, which is sufficient for primary control [55, 57] As frequency increases, HPP deflection decreases for 90 and 60 psi, but remains mostly constant for 30 psi. It is interesting to note that the 60 and 90 psi curves collapse onto each other at around 4/rev, and are joined by the 30 psi curve at around 6/rev. The suggested reason for this is that the limiting factor at high frequencies is pneumatic flow rate restrictions which prevent the PAMs from fully inflating and exhausting. Additionally, the system maintained 5 degrees of HPP deflection out to 10/rev which indicates that this design is also suitable for vibration/noise reduction at this loading condition [59, 60].

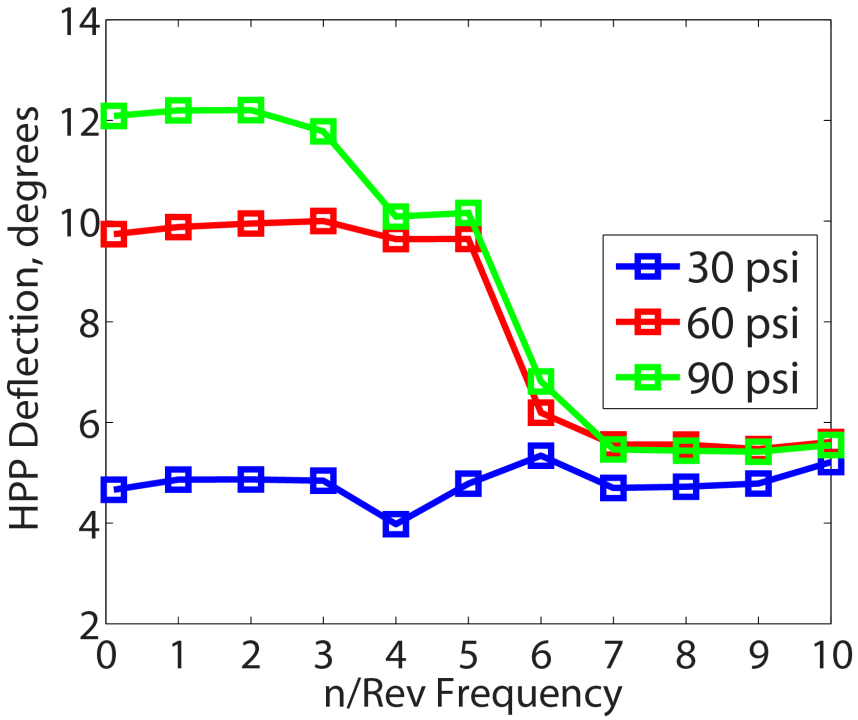

Figure 4.16: Open-loop half peak-to-peak deflection for the hover stiffness case

Figure 4.17, which plots the upper and lower (or clockwise and counterclockwise) limits of the deflection with respect to the geometric zero, shows clearly that the offset moment has caused the curves to shift in the positive deflection direction. This effect is small for the 60 and 90 psi cases due to the relatively small magnitude of the offset moment versus the total moment at high deflections, and thus is more pronounced for the 30 psi case for the converse reason. Again, the system has sufficient actuation authority and bandwidth for both primary control and vibration/noise reduction. At 1/rev, the defection ranges from +13 to −11 degrees, which is sufficient for primary control [55, 57]. As frequency increases, the effect of the moment offset is exacerbated to the point where, at around 4/rev, the actuator maintains a large HPP deflection range but is no longer is able to produce negative deflections greater than 10 degrees. This could be remedied by increasing the maximum flow rate in the PAM pneumatic system. However, the system maintains −5 degrees of deflection out to 5/rev and −4 degrees out to 10/rev, which again would be suitable for vibration and noise reduction [59, 60].

In aggregate, these results show that a chordwise implementation of PAMs for TEF actuation is feasible for primary control and vibration reduction across forward flight operating conditions for the candidate helicopter.

4.5.1.4 Benefit of Actuator Optimization

With the efficacy of the actuator optimization procedure well-established in the previous sections, it is interesting to examine how operating at an off-design condition affects the actuator performance. For the purposes of this study, off-design means

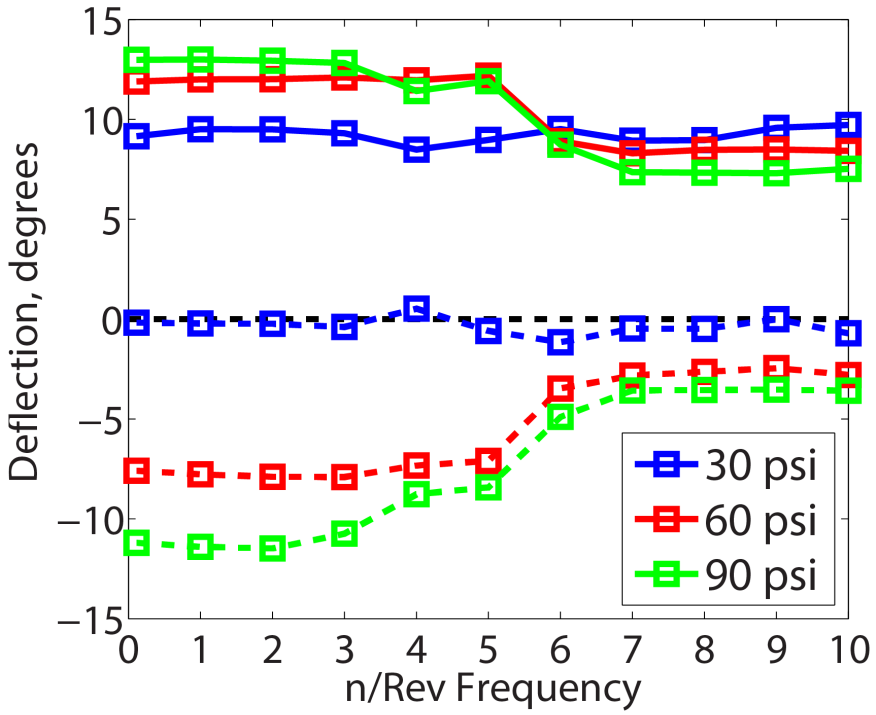

Figure 4.17: Open-loop upper/Lower bounds of deflection for the hover stiffness case with torque offset

operation at a non-optimized pressure (recall that the present work was optimized for a PAM operating at 90 psi). Each column in Table 4.4 shows an optimized design for the advancing side/offset moment loading condition. Each row shows the respective design's performance at a given pressure. The bold-faced values indicate the optimized deflections, while the normal font entries are off-design values.

Table 4.4: HPP deflections in degrees for actuators optimized for 30, 60, and 90 psi with off-design performance. **Bold** values indicate the optimized design in each column.

	Design optimized for:		
	30 psi	60 psi	90 psi
Def. at 30 psi	**2.41**	0.10	−1.18
Def. at 60 psi	3.46	**6.55**	5.31
Def. at 90 psi	3.69	7.82	**9.45**

In each case, the optimized design at its design pressure performs significantly better than any other design at the same pressure. For example, at 30 psi, the 90 psi design (third column) can only achieve -1.18 degrees, while the 30 psi design (first column) attains 2.41 degrees, an increase of approximately 3.5 degrees. This trend is repeated for the 60 psi and 90 psi design cases. This highlights the potential benefits associated with a fully optimized PAM TEF system, but also contrasts it with how sensitive the systems can be to operating outside of their designed pressure. Note that other off-design cases, such as changes in R_0 and α_0, exhibit the similar trends.

4.5.2 Closed-loop Results

The open-loop performance discussed in the previous section indicated that the PAM actuation system had sufficient authority for both primary control and vibration/noise reduction. However, it is also necessary that the system be able to closely follow arbitrary waveforms. Hence, closed-loop testing was also performed.

4.5.2.1 Feedback Control Scheme

This study used a control scheme previously developed by Woods *et al.* [53] specifically for a PAM-actuated trailing edge flap system. It originally comprised an inner loop controller with proportional feedback and a variable dead-time compensator that reduced tracking error and increased bandwidth. The dead-time compensator requires no system model or *a priori* information and allows the system to continuously adjust the dead-time estimate from the position error and predict future tracking error using that estimate, and adjust the control action accordingly.

For the present work, the proportional controller was augmented with an integral term to further improve tracking capability.

4.5.2.2 Closed-loop Test Plan

Testing was conducted over a range of sine wave frequencies and amplitudes, with proportional and integral gains manually tuned at each condition. Tuning was stopped when either the system trajectory satisfactorily matched the reference trajectory, or the command signal (spool valve voltage) began to saturate. While manually re-tuning gains at every flight condition is not realistic for an actual TEF system, this approach empirically demonstrates the precise/accurate tracking control capability of the PAM system. To this end, sine wave reference commands of the form

$$r(t) = A_m \sin(h_n \omega t) \tag{4.19}$$

were tested, where $r(t)$ is the reference signal, A_m is the sine wave amplitude, ω is the 1/rev frequency of the rotor system (4.45 Hz) in radians per second, and h_n is a n/rev multiplier. For this work, A_m was varied from 2.5 to 10 degrees in 2.5 degree increments, and h_n was varied from 1 to 7.

Complex waveforms comprising a sum of single sine waves were also tested to demonstrate the system's ability to follow command signals with components more typical of rotorcraft TEF controls. The complex waveforms tested here were taken

from [53] and are of the form

$$r(t) = \sum_{i=1}^{4} A_i \sin\left(h_i \omega t + \phi_i\right) \tag{4.20}$$

where A_i is the i^{th} amplitude component, h_i is the i^{th} n/rev frequency multiplier, ϕ_i is the i^{th} phase shift component, and ω is again the 1/rev frequency in radians per second. The values used in this study are summarized in Table 4.5 for three different complex wave forms.

Table 4.5: Composition of complex waveforms.

Waveform Number	Index i	h_i (n/rev)	A_i (deg)	ϕ_i (deg)
1	1	1	7	0
	2	3	2	90
	3	4	2	240
	4	5	2	180
2	1	1	6	0
	2	3	0.5	60
	3	4	1	120
	4	5	0.5	30
3	1	1	5	0
	2	3	3	90
	3	4	2	240
	4	5	1	45

4.5.2.3 Closed-loop Results

Figure 4.18 shows test data for a 5 degree amplitude, 1/rev sine wave operating at the advancing side with torque offset stiffness condition and a PAM pressure of 90 psi. Note that all results presented in this section are for this (highest) stiffness condition, and although data was taken at 2.5 and 7.5 degree amplitudes, these data

are not mentioned at length as they do not add substantially to the discussion. The upper plot shows that the reference signal (dashed black) is closely followed by the measured actuator deflection (solid red). Also included is a solid green line which depicts the error between the measured and reference signals at a given time. The lower plot shows the voltage signal sent to the proportional spool valve from the controller, which stays well within the allowable 0-10 V range. Similarly, Figure 4.19 shows results for a 10 degree amplitude, 1/rev sine wave. Again, the system tracks the reference signal very closely, with no discernible phase lag.

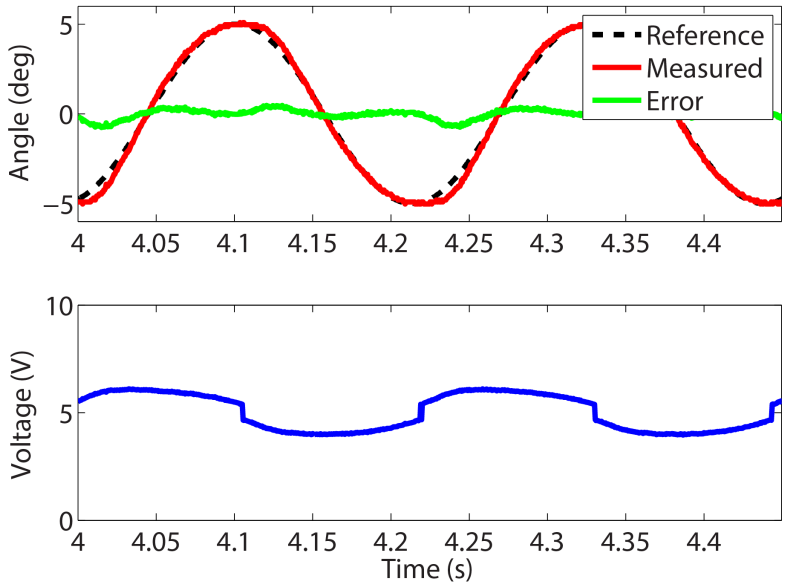

Figure 4.18: Closed-loop tracking performance for 1/rev ±5 degree sine wave command data at advancing side w/offset stiffness condition

In order to easily examine higher frequencies (2-7/rev), Figure 4.20 presents representative deflection data for all 5 degree command n/rev frequencies plotted versus a normalized time scale which varies from 0 at the start of the sine wave to 1 at a full period, again with PAM pressure at 90 psi. In this way, all frequencies of a

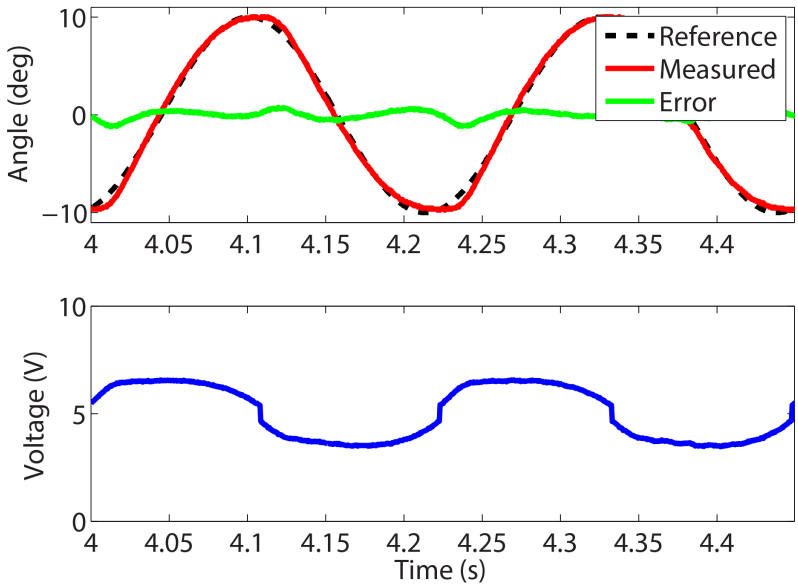

Figure 4.19: Closed-loop tracking performance for 1/rev ±10 degree sine wave command data at advancing side w/offset stiffness condition

given amplitude can be compared on the same plot. It is clear that all frequencies track the reference signal well, but there is evidence that the closed-loop response may begin to develop a slight phase lag at higher frequencies (6-7/rev). Regardless, it is clear that the system is able to track sine waves at frequencies and amplitudes suitable for vibration/noise reduction [60]. Figure 4.21 plots the same data for a 10 degree command. The 1-3/rev displacements follow the reference well, but tracking deteriorates rapidly starting at 4/rev. This follows the trends observed in the open-loop testing (Figure 4.17), which were attributed to the effect of flow rate limitations within the pneumatic system. Note also that Figure 4.17 depicts a "best-case" scenario for achieving maximum deflection, where the spool valve signal is a 0-10 V square wave, which is contrasted with the data shown in Figure 4.21, where gain tuning was terminated as soon as the control voltage began to saturate.

Although tracking suffered at higher frequencies, the system performed well at ±10 degrees for 1-3/rev, which is suitable for primary control.

Additionally, the data was processed in aggregate to aid in examining overall trends. Figure 4.22 gives the root mean square (RMS) error for all n/rev frequencies and sine wave amplitudes tested at the advancing side with offset torque stiffness condition and at a PAM pressure of 90 psi. The 2.5 and 5 degree lines show a very low and consistent amount of error over the tested frequency range. The 7.5 and 10 degree lines, however begin to show increasing error at 5/rev and 4/rev respectively, which is consistent with the results presented earlier.

Closed-loop frequency response functions were also calculated using Fourier transforms of the measured data. Figure 4.23 displays these results. The upper plot is the magnitude of the response, where unity indicates perfect amplitude matching between the desired and measured waveform. These results mirror those presented in the previous paragraph, with the 2.5 and 5 degree commands staying very close to 1 out to 7/rev, and the 7.5 and 10 degree command lines falling off at 4/rev and 5/rev, respectively. The lower plot shows the phase difference between the measured response and the desired command. In general, this plot shows that the system has little to no phase lag across the entire operating range, including when the system was not able to reach the desired magnitude. An exception to this is the 1/rev, 2.5 degree command which has a -10 degree phase lag. This is the lowest frequency and amplitude tested, and so the increased lag is attributed to the dead-band associated with the proportional pneumatic valve used to control the system. More advanced dead-band compensation may help to mitigate this issue.

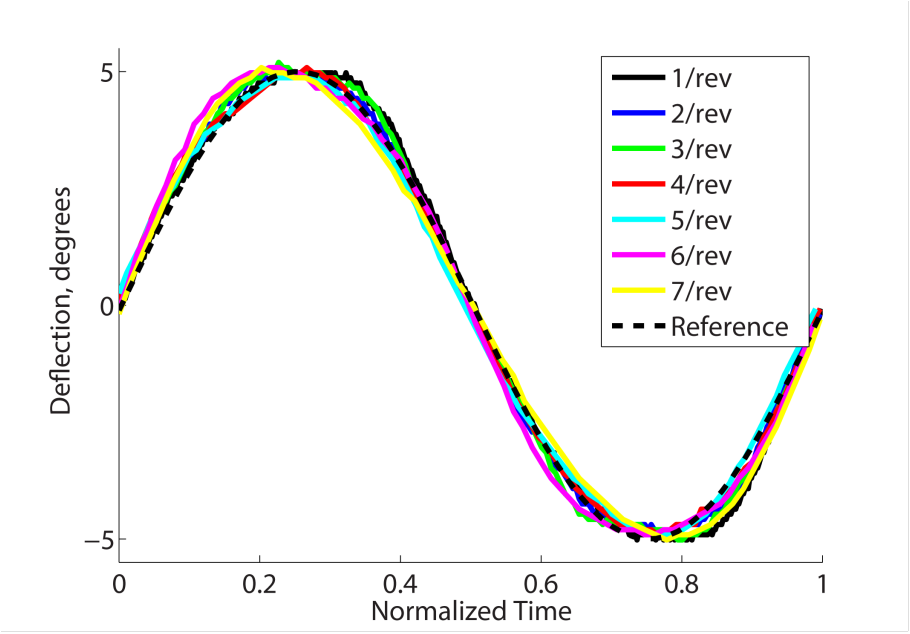

Figure 4.20: Closed-loop time-normalized 1-7/rev data for ±5 degree command signal at the advancing side w/offset stiffness condition

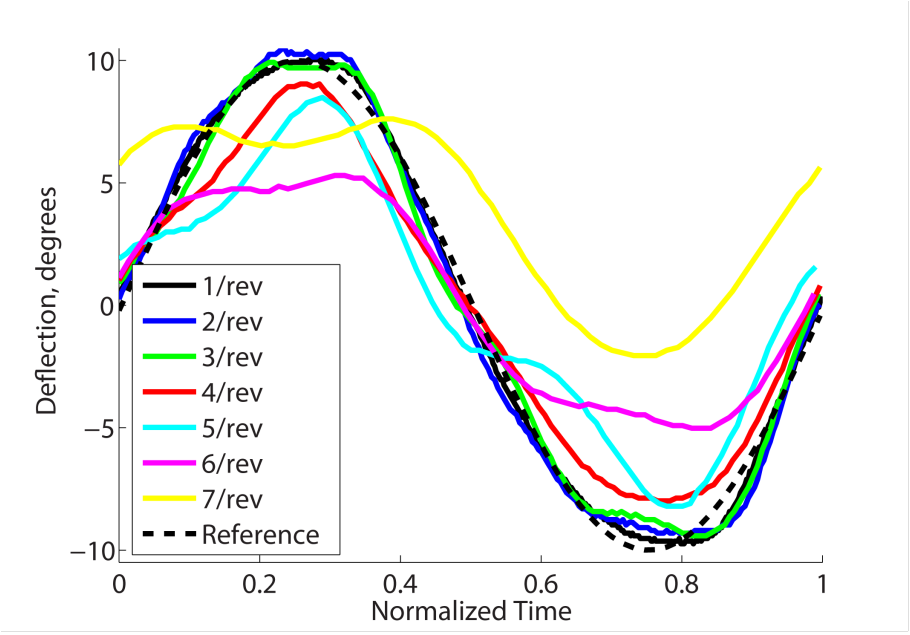

Figure 4.21: Closed-loop time-normalized 1-7/rev data for ±10 degree command signal at the advancing side w/offset stiffness condition

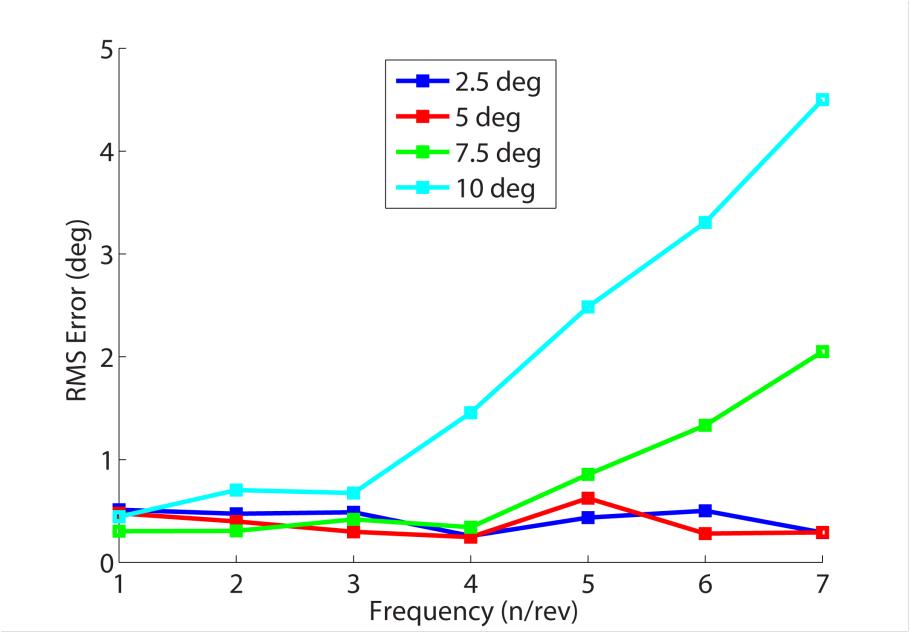

Figure 4.22: Closed-loop RMS error for 1-7/rev data at the advancing side w/offset stiffness condition

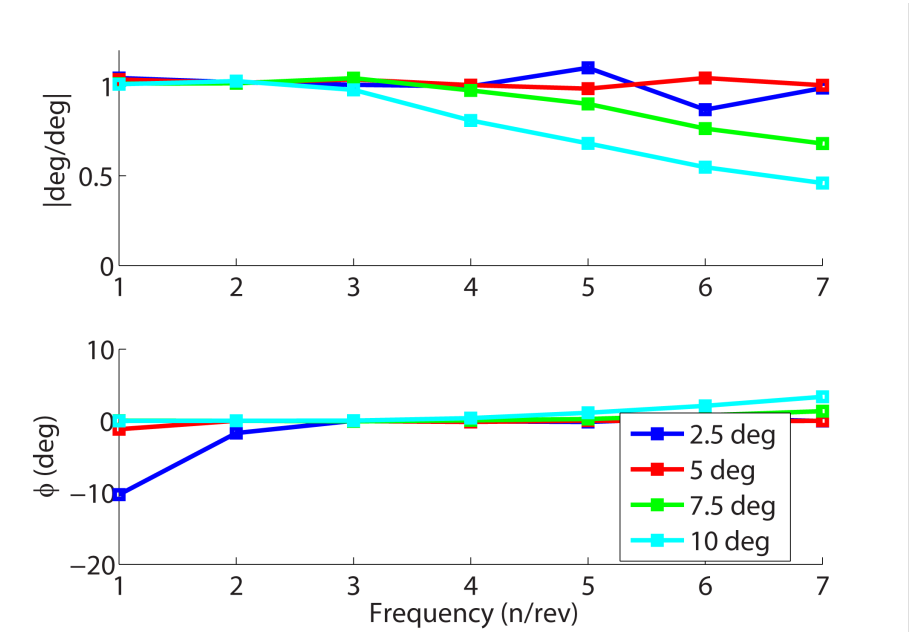

Figure 4.23: Closed-loop frequency response measured for 1-7/rev data at the advancing side w/offset stiffness condition.

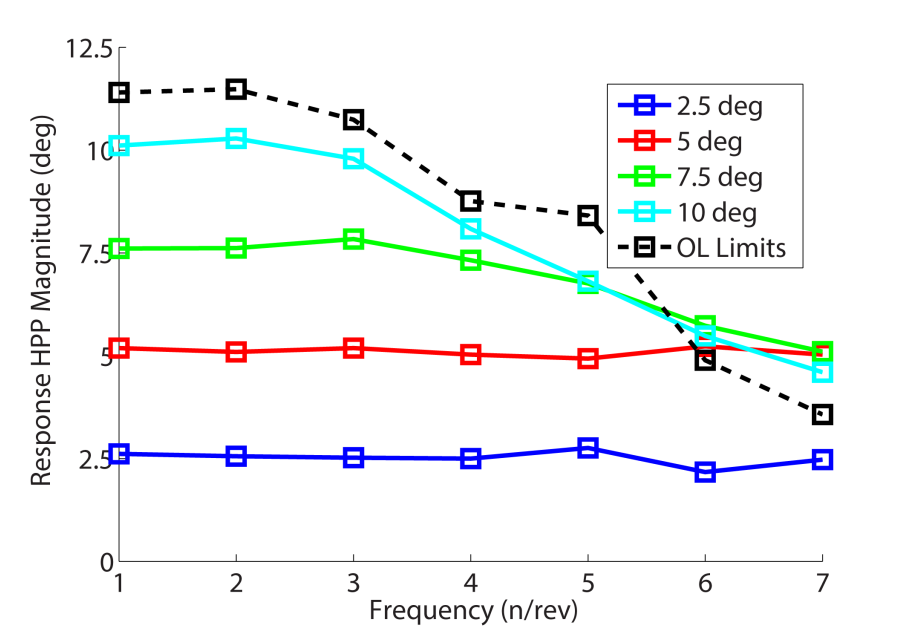

Figure 4.24: Closed-loop response magnitude compared to open-loop limits.

Figure 4.24 shows the dimensional magnitude of the response for all amplitudes and frequencies tested. At high frequency, all magnitude commands tend to collapse onto a line of diminishing performance. This is most evident with the 10 degree and 7.5 degree command lines, which coalesce around 5/rev. Also plotted is the open loop maximum HPP deflections, taken from the lower bounds of Figure 4.17. From 1/rev to 5/rev the open-loop limits form an envelope around the closed-loop results, indicating that high frequency closed-loop performance is limited by the achievable pneumatic flow-rate. At 6/rev and 7/rev, the open-loop limits fall slightly below the closed-loop results.

Data was also collected at different loading conditions and PAM pressures in an effort to examine the operational limitations of the PAM TEF system. Figure 4.25 compares the frequency response data for three different operating conditions attempting to follow a ±10 degree, sinusoidal command. The conditions, listed in the

figure legend, vary both maximum PAM pressure and offset loading value. The most important insight gained from this plot is that the 60 psi and 90 psi maximum PAM pressure systems have virtually the same performance. This suggests again that the PAM TEF system performance is currently limited solely by the flow rate of the pneumatic system.

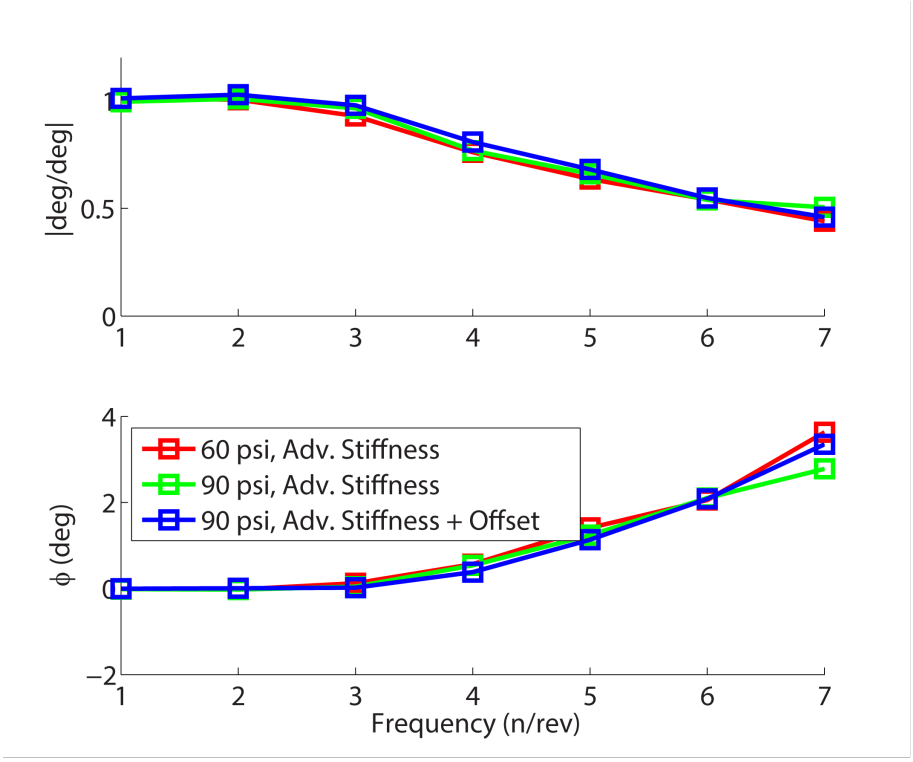

Figure 4.25: Closed-loop frequency response for ±10 degree 1-7/rev data at various loading and PAM pressure conditions.

Figure 4.26 shows time history data for the complex waveforms described in Equation 4.20 and Table 4.5. Again, the system response tracks the command quite well, and the control voltages are well within saturation limits. This is a final indication that the chordwise PAM system designed here is suitable for rotorcraft TEF actuation, and is capable of tracking the complex waveforms that would be required for both primary control and vibration/noise reduction tasks.

4.6 Conclusions

This chapter discussed an approach for designing a trailing edge flap system for rotor blades with PAM actuators configured chordwise and co-located outboard with the flap. The inherent challenges associated with such a design were overcome through the inclusion and optimization of bias contraction and mechanism dimensions. Quasi-static actuator performance matched well with simulated predictions. The PAM actuation system was shown to be suitable for both primary control ($\pm$10 degrees at 1-3/rev) and vibration and noise reduction ($\pm$5 degrees up to 10/rev) at the highest simulated loading conditions through open-loop testing. Additionally, the importance of properly optimizing the PAM system and operating it at the designed pressure and mechanism geometry was highlighted. Closed-loop testing using a previously validated control scheme provided even further evidence for the suitability of the designed PAM actuation system for primary and vibration/noise control in rotorcraft. Measurements showed close tracking of $\pm$5 degree sine waves out to 7/rev and $\pm$10 degree sine waves out to 3/rev. Closed-loop performance was shown to be limited by the pneumatic system. Complex waveforms comprised of 1/rev and 3-5/rev components were also tested and showed good tracking capability, indicating that the optimized system is capable of following arbitrary complex signals at frequencies needed for helicopter primary control and vibration reduction. Overall, this work showed that a chordwise PAM-actuated TEF can satisfy the performance requirements associated with primary rotor control, vibration reduction, and noise mitigation, thereby highlighting PAM actuators as a feasible technology for this

application.

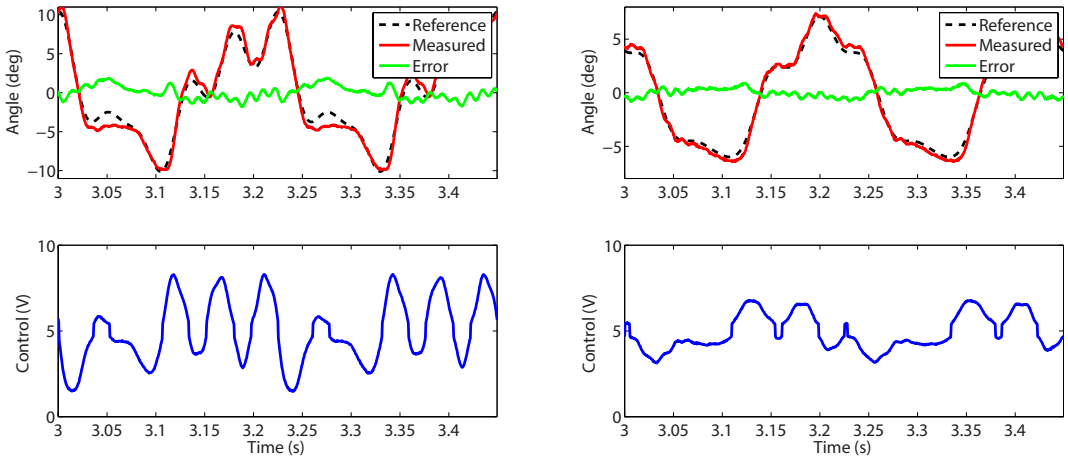

(a) Waveform 1

(b) Waveform 2

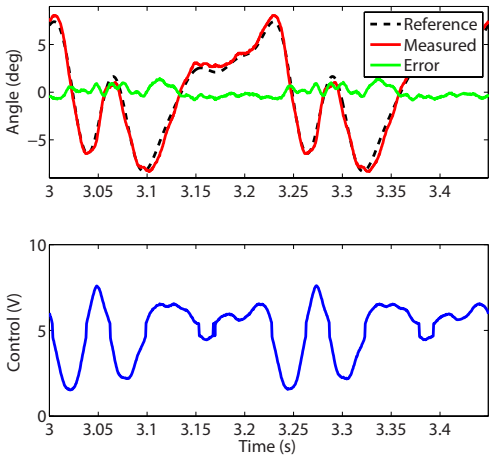

(c) Waveform 3

Figure 4.26: Closed-loop time history for complex waves comprised or 1/rev and 3-5/rev components at various amplitudes and phases (see Table 4.5).

Chapter 5: System Level Benefits of a Variable Diameter Rotor System for a Conceptual Tiltrotor Design

5.1 Introduction

The modern tiltrotor fills a vital niche; it is capable of both vertical flight like a helicopter and forward flight like a conventional airplane. However, fulfilling both of these roles simultaneously has lead to many design compromises, the most drastic of which is designing a propulsion system capable of both vertical flight (hover) and horizontal flight (cruise) [88]. In simple terms, the optimal designs for both configurations attempt to minimize required power at their most prevalent operating conditions. For hover, a large diameter rotor is desired in order to minimize induced power. In forward flight, however, the required thrust is much lower, so that a much smaller rotor is typically preferred in order to reduce profile power losses. For production vehicles, such as the V-22 *Osprey*, the compromise solution has been to design blades that bridge the gap between these two competing requirements, with a smaller diameter than would be desirable for hover, while maintaining reasonable cruise efficiencies.

Many studies have looked at ways of improving tiltrotor propulsive efficiency

[88–90]. There is a general consensus that there will be only incremental performance gains through static blade improvements, and that a more promising (but risky) approach is to introduce blade morphing, typically in the form of rotor diameter change, variable speed transmissions, or both [88]. Morphing is generally defined as large-scale changes in aircraft geometry, such as camber, sweep, twist, span, diameter, etc., with the intent of allowing the vehicle to operate efficiently over a range of flight conditions. Thill *et al.* [98], Barbarino *et al.* [1], and Weisshaar [2] give a comprehensive review of the state-of-the-art in morphing technology. There are many examples of recent work in rotorcraft morphing, including extending chord [19], active twist [119, 120], active trailing edge flaps [57–59], variable rotor RPM [121], and variable diameter rotors [107, 121]. The potential benefits of variable diameter rotors in tiltrotor applications were recognized in the 1970s [91], and there are longstanding efforts, most notably by the Sikorsky Aircraft Co., to develop a working system [92–95]. As with all current morphing systems however, the introduction of a morphing capability also increases the weight and complexity of the vehicle as a whole. This is a practical issue because any new technology must buy its way onto an aircraft through either weight or cost reductions. Most of the studies mentioned here that discuss the potential benefits of a variable diameter rotors, do so from a isolated, rotor-only standpoint, and so there is motivation to look the effect of rotor morphing the standpoint of a complete aircraft system.

Given that a variable diameter rotor system (VDRS) could be a valuable addition to a tiltrotor system, the present work examines the effects of rotor diameter morphing on an aircraft as a whole from a conceptual design perspective. First,

the structure of the study is presented, including a description of the conceptual variable diameter tiltrotor model as implemented in the NASA Design and Analysis of Rotorcraft (NDARC) conceptual design code and a discussion of the independent variables. The next section presents results from a typical suite of sizing runs with attention paid to the physical meaning of certain weight trends. Then, results from multiple runs are collated and presented. Finally, general conclusions and limitations of the study are discussed.

5.2 Study Design

This study used the NASA Design and Analysis of Rotorcraft (NDARC) conceptual design code to examine the system level benefits and trade-offs associated with including a VDRS on a conceptual tiltrotor. NDARC is a low fidelity, modular, tunable, and well documented code [122, 123] that allows designers to explore novel rotorcraft designs, such as those presented in Silva [124], and Moodie [125]. NDARC is capable of performing sizing and off-design analysis tasks for a wide variety of conceptual rotorcraft configurations. Sizing is in iterative task that determines the major dimensions, power requirements, and weight of the aircraft and is accomplished through the definition of sizing missions and conditions. Missions are made up of a sequence of flight conditions (taxi, hover, cruise, loiter, etc.) and sizing conditions are single design points.

5.2.1 Design Mission and Conditions

The aircraft sizing flight profile is presented in Figure 5.1. The aircraft design gross weight is defined as the takeoff gross weight of this primary mission. Takeoff and landing conditions are assumed to be hover, out of ground effect, at 6,000 ft, 95F with 5% power margin. Climb segments are credited to the overall range and flown at 100% of the engines 30 minute power rating, or intermediate rated power (IRP). The cruise condition is at the aircraft's best altitude for a standard atmosphere (ISA) and the high side of the 99% best specific range speed. No range credit is taken for the decent segment for conservatism. The final 55 nm segment is flown at 6,000 ft, 95°F and 100% of the engines maximum continuous power rating (MCP). A 30 minute loiter segment at the landing zone is flown at best endurance speed and 6,000 ft, 95F. The flight profile includes 30 minutes of reserve fuel, flown at 6,000 ft, 95F and the high side of the 99% best specific range speed.

In addition to the sizing flight profile, several point performance conditions are assumed for structural design gross weight, maximum takeoff gross weight and transmission torque limit. The structural design gross weight is the weight at which the structure is capable of a 3.5 g load factor with a safety margin of 1.5. This weight is assumed to be at the mid-point of the design mission. Both the maximum takeoff gross weight and transmission torque limit are sized for a sea level, 103°F hover out of ground effect with 10% power margin from the engines 10 minute power rating, or maximum rated power (MRP).

The technology assumptions with respect to the structural weight and drive

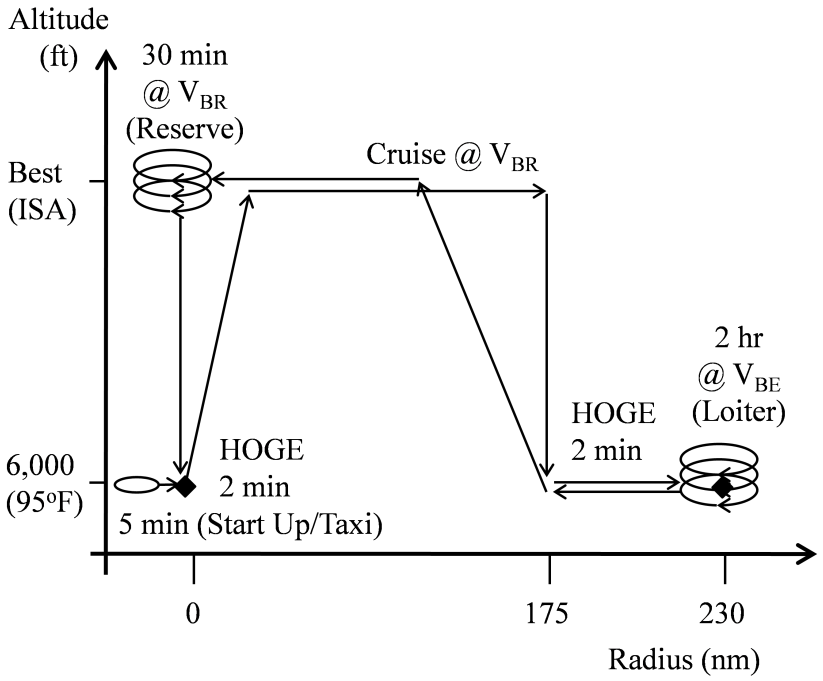

Figure 5.1: Aircraft sizing flight profile

system power density of the aircraft are based on the 2015 goals from the Army Aviation Science and Technology Strategic Plan (ASSP). The Advanced Affordable Turbine Engine (AATE) goals for the thermodynamic efficiency and the ratio of power-to-weight are assumed for the turboshaft engines.

5.2.2 Tiltrotor Model

The NDARC-based tiltrotor model used in this study, designed to theoretically fulfill a medium-lift role for the U.S. Army, was synthesized and validated outside the scope of this study. Many of the details of this model are proprietary, so the present work will only reference the changes made to the model to incorporate variable diameter capabilities. The two changes needed to the existing tiltrotor model were incorporating the variable diameter rotor, and defining how the tiltrotor wing design

would change as different amounts of morphing were allowed.

NDARC includes native support for variable diameter rotors. The only decisions that needed to be made were the maximum amount of morphing allowed, defined as a fraction of the hover rotor diameter, and how the diameter change would be implemented (as a function of speed, tilt, arbitrarily set, etc.). The maximum morphing was defined as

$$\eta = \frac{R_c}{R_h} \tag{5.1}$$

and is the ratio of cruise rotor radius, R_c, to hover rotor radius R_h. During hover, the rotor would have diameter R_h, and during cruise (with nacelles fully tilted), the rotor would have diameter $R_c = \eta R_h$. The transition in between these two conditions was defined as a conversion schedule linked to air speed. Care was taken to ensure that the rotor had sufficient fuselage clearance during conversion.

More thought was needed for wing design. The prediction was that it would be desirable, from a weight perspective, for the rotor nacelle to be as close to the fuselage as possible. However, it was also vital to maintain a sufficiently high aspect ratio wing so as to not unnecessarily increase wing induced drag. Figure 5.2 depicts a conceptual model for the final VDTR wing. It was made up of two panels, with Panel 1 being inboard and Panel 2 being outboard of the rotor nacelle respectively. Panel 2 is bound to the nacelle, and tilts with it during conversion from hover mode to cruise mode. The overall wing span, b, was determined by a chosen wing loading, WL, (which gives required wing area though gross weight) and a given wing aspect ratio, AR. Panel 1 and 2 had a small dihedral angle, and Panel 1 also included a

slight forward sweep. Panel 2 did not have any forward sweep so as to not run into rotor/wing prop strike issues. The panel chords, c_1 and c_2, were set to be equal. Rotor nacelle location was defined from the centerline of the aircraft, and was

$$y_{hub} = \pm\ (\eta R_h + d_{fus} + w_{fus}/2) \tag{5.2}$$

where y_{hub} is the lateral location of the rotor hub (and nacelle), R_h is the rotor radius in hover configuration, w_{fus} is the width of the fuselage, d_{fus} is a prescribed clearance between the tip of the rotor and the fuselage when the rotor is in cruise mode, here set to 0.75 ft.

As a baseline design, an aircraft was sized that included no rotor morphing capabilities, $\eta = 1$. For this aircraft, the disk loading, DL, and WL were set at 15 lb/ft^2 and 100 lb/ft^2 respectively. The wing AR was then varied to place the nacelle as close to the tip of the wing as possible, making it resemble a conventional tiltrotor. Put another way, wing AR was varied and the aircraft was resized until the Panel 1 span, b_1, approximately equaled the semi span of the aircraft, $b/2$. The expectation was that as η was decreased through out the course of the study, the nacelle would walk inwards on the wing and any additional required wing area would be taken up by the second wing panel.

5.2.3 Study Framework

In order to investigate the effect of morphing on the system level, two separate variables were systematically changed. The first is the amount of diameter decrease

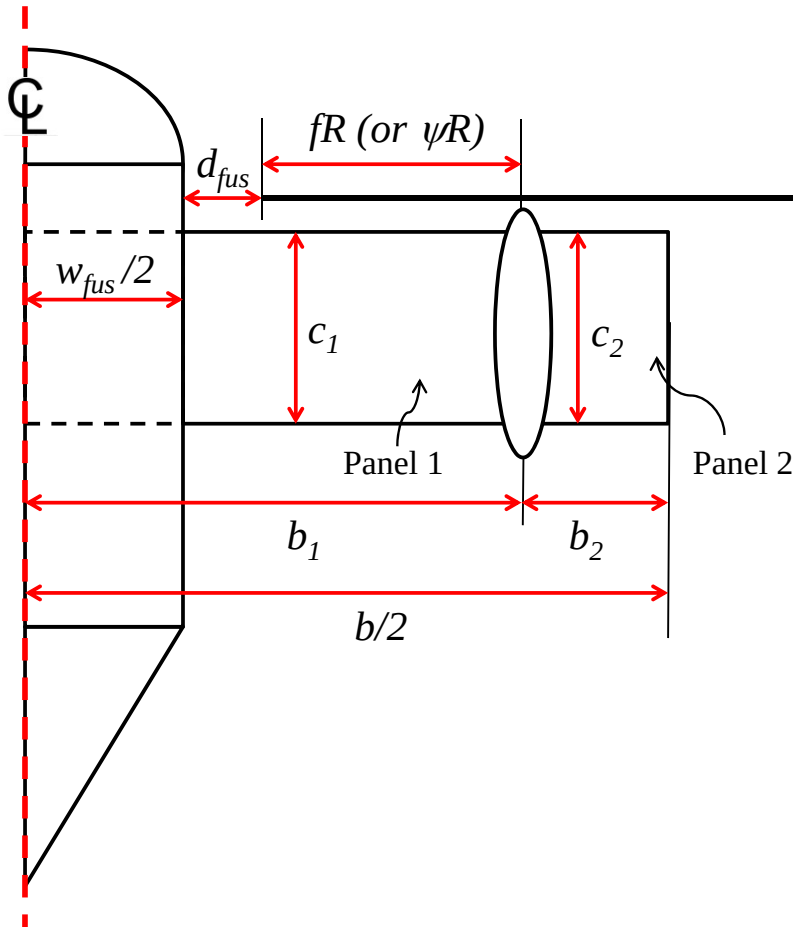

Figure 5.2: Conceptual layout of the VDTR wing panels with nacelle tilted in cruise configuration

allowed, controlled by the variable η as described above. The second is how much of a weight penalty the vehicle sustained with the inclusion of the VDRS. As mentioned previously, the use of any morphing system currently is accompanied by both a weight and complexity penalty. In NDARC, there is no native way to simulate the added complexity of morphing. Added weight, however, can be easily simulated through the use of technology factors. Component weights in NDARC are estimated through the use of parametric equations based on a large library of existing systems [122]. For a typical component, the total weight, W, is defined as

$$W = \chi w_{model} + dW \tag{5.3}$$

where χ is the technology factor, w_{model} is the component weight calculated from the parametric model, and dW is an optional weight increment. For this study, the choice was made to add weight to the rotor blade and hubs, and let this increase cascade through the rest of the design instead of trying to predict where a weight increase at the rotor would most affect the system as a whole. Each of these weights is combined with a technology factor and weight increment according to Equation 5.3, which leads to

$$\begin{aligned} W_{blade} &= \chi_{blade} w_{blade} + dW_{blade} \\ W_{hub} &= \chi_{hub} w_{hub} + dW_{hub}. \end{aligned} \tag{5.4}$$

The values of the respective technology factors and weight increments were set in the original tiltrotor model, and so for the present work a simple technology factor increment was applied. This is presented throughout the remainder of this paper as

a percent (%) increase in χ_{rotor} and χ_{hub}. Both technology factors were incremented together, and so for simplicity they will be simply called χ_{rotor} with the understanding that a % increment in χ_{rotor} corresponds to % increment in both χ_{rotor} and χ_{hub}.

In the present work, both χ_{rotor} and η were varied in an attempt to look at the complex relationship between diameter morphing, rotor system weight, and system performance as a whole. To this end, η was varied from 1 to 0.65 in increments of 0.05. At each of these η values, χ_{rotor} was varied from a 0% increase to a 30% increase in steps of 5%. At each unique η and χ_{rotor} combination, the aircraft was resized and weight and performance data were recorded.

5.3 Results and Discussion

5.3.1 Typical Results for a Constant χ_{rotor}

Figure 5.3 depicts the percent change in weight from the baseline design ($\eta = 0$) as η is varied for a constant value of χ_{rotor}, and is representative of a typical η sweep for a given χ_{rotor}. As mentioned, the typical increment for η was 0.05, but this could be varied slightly to aid in sizing convergence. In general, as η decreases, the entire aircraft gets lighter. In this case, W_{gross}, W_{empty}, and W_{rotor} all decrease monotonically to around $\eta = 0.70$, at which point the curve levels off and no additional benefit is seen for a further decrease in cruise rotor radius. There are a few drivers of this decrease in weight. The first, and most obvious, is that as cruise diameter decreases the rotor nacelles move inwards on the wing. When calculating wing weight, NDARC makes a distinction between the structural requirements (and thus

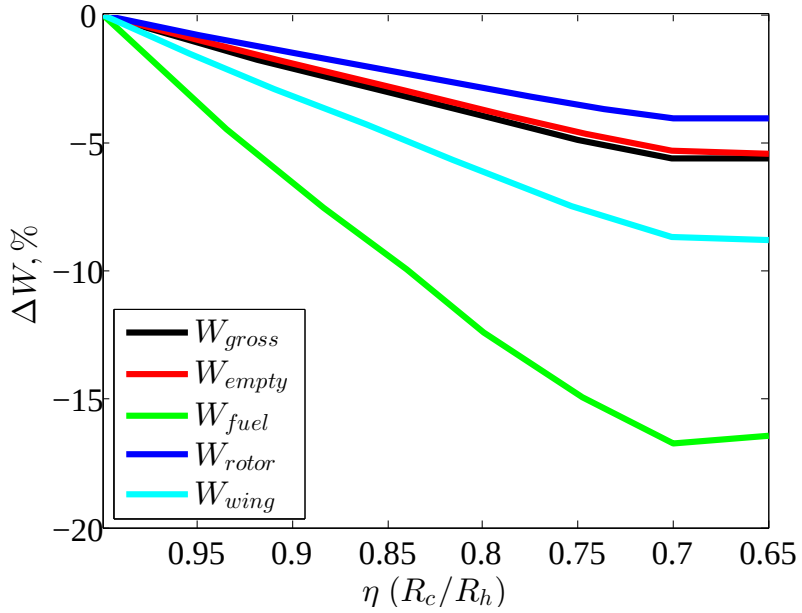

Figure 5.3: Typical percent change in weight results for a constant χ_{rotor} as a function of η.

weight) of wing panels supporting nacelles, and those that only support aerodynamic loading. Thus, as the nacelles move inwards, the length of the heavier inboard panel decreases, and any additional required wing area is put into the lighter outboard panel. This decrease in wing weight cascades through the entire design, causing the gross weight of the aircraft to decrease.

A second source of weight decrease is improved propulsive efficiency in cruise mode, which most directly affects W_{fuel} as the design mission has long cruise sections. Again, the fuel weight steadily decreases to around $\eta = 0.70$, at which point it starts to increase. The cause of this was traced to the fact that as radius is decreased during the cruise segments the rotor was running into stall limits, which drastically increases rotor profile and parasitic power. In sizing, this causes a feedback effect where the engine and fuel usage grow, increasing aircraft weight and downwash,

which then causes the engine and fuel weight to grow again, etc., and the entire aircraft gains weight. In some cases below $\eta = 0.60$, this effect was so pronounced that the sizing task was unable to converge. Note that the value of η at which stall starts to occur in NDARC is dependent on how the rotor is being modeled and what the model was tuned to, and so the numerical value of η is less important here than an understanding of reasons the stall occurs. Rotor blade stall is often discussed in terms of blade loading, and so a useful back-of-the-envelope check for blade loading in forward flight based on hover blade loading, aircraft L/D_e, aircraft weight, RPM variation, and radius variation is derived below.

Traditional proprotor conceptual design assumes that blade loading in cruise is very low, possibly up to a tenth of the hover condition blade loading. This leads to very low induced losses, and design choices are focused on reducing the profile power. When considering a rotor with variable radius and/or variable speed however, this assumption of low loading is no longer valid. For example, consider a notional tiltrotor described by its gross weight W, design hover blade loading $(C_W/\sigma)_h$, cruse lift to effective drag ratio L/D_e, and hover and cruise atmospheric conditions. The hover blade loading can be written as

$$\left(\frac{C_W}{\sigma}\right)_h = \frac{W}{\rho_h A_h V_{tip,h}^2 \sigma_h} \tag{5.5}$$

where ρ_h is the air density at hover conditions, $A_h = 2\pi R_h^2$ is the total disk area of both rotors in hover, $V_{tip,h} = R_h \Omega_h$ is hover tip speed, C_W is the helicopter weight coefficient, and $\sigma_h = {}^{N_b c_{(r=0.75)}}/_{\pi R_h}$ is the hover thrust weighted (assuming linearly

tapered blades) solidity with N_b defined as the number of blades on one rotor and $c_{(r=0.75)}$ as the blade chord at $0.75R$. If thrust in forward flight is assumed to be $T = {}^{W}/_{L/D_e}$, then forward flight (cruise) blade loading can similarly be written as

$$\left(\frac{C_W}{\sigma}\right)_c = \frac{T}{\rho_c A_c V_{tip,c}^2 \sigma_c} = \frac{{}^{W}/_{L/D_e}}{\rho_c A_c V_{tip,c}^2 \sigma_c}. \tag{5.6}$$

Note that both of these equations assume purely axial flow through the rotor. Dividing Equation (5.6) by Equation (5.5) gives

$$\begin{aligned} \frac{\left(\frac{C_W}{\sigma}\right)_c}{\left(\frac{C_W}{\sigma}\right)_h} &= \frac{\left(\frac{{}^{W}/_{L/D_e}}{\rho_c A_c V_{tip,c}^2 \sigma_c}\right)}{\left(\frac{W}{\rho_h A_h V_{tip,h}^2 \sigma_h}\right)} \\ &= \frac{1}{L/D_e}\frac{\rho_h}{\rho_c}\frac{V_{tip,h}^2}{V_{tip,c}^2}\frac{A_h}{A_c}\frac{\sigma_h}{\sigma_c} \end{aligned} \tag{5.7}$$

Then, expanding V_{tip}, σ (assuming rectangular telescoping blades), and A in Equation (5.7) yields

$$\frac{\left(\frac{C_W}{\sigma}\right)_c}{\left(\frac{C_W}{\sigma}\right)_h} = \frac{1}{L/D_e}\frac{\rho_h}{\rho_c}\frac{(\Omega_h R_h)^2}{(\Omega_c R_c)^2}\frac{(2\pi R_h^2)}{(2\pi R_c^2)}\frac{{}^{N_b c_{r=0.75}}/_{\pi R_h}}{{}^{N_b c_{r=0.75}}/_{\pi R_c}} \tag{5.8}$$

which can be simplified to

$$\frac{\left(\frac{C_W}{\sigma}\right)_c}{\left(\frac{C_W}{\sigma}\right)_h} = \frac{1}{L/D_e}\frac{\rho_h}{\rho_c}\frac{\Omega_h^2}{\Omega_c^2}\frac{R_h^3}{R_c^3}. \tag{5.9}$$

Replacing R_c/R_h with η, and letting $\zeta = \Omega_c/\Omega_h$ be the ratio of cruise RPM to hover

RPM, Equation (5.9) can be recast as

$$\frac{\left(\frac{C_W}{\sigma}\right)_c}{\left(\frac{C_W}{\sigma}\right)_h} = \frac{\rho_h}{\rho_c}\frac{1}{\eta^3 \zeta^{2L/D_e}}. \tag{5.10}$$

This indicates that blade loading in cruise will increase with a decrease in either cruise radius or RPM. Specifically, $\left({}^{C_W}/_{\sigma}\right)_c$ will increase proportionally to $1/\eta^3$ and $1/\Omega^2$. To illustrate the utility of this simple expression, consider a tiltrotor designed to hover at ISA standard day 5,000 *ft* (1524 *m*) density altitude, with a cruise altitude of 25,000 *ft* (7620 *m*). Plugging these values, and an assumed η and ζ (see Table 5.1) into Equation (5.10) gives

$$\frac{\left(\frac{C_W}{\sigma}\right)_c}{\left(\frac{C_W}{\sigma}\right)_h} = \frac{7.13}{{}^{L}/_{D_e}} \tag{5.11}$$

Note that the value of ζ used here is close to what is actually used on the V-22 *Osprey*. Thus, for an aircraft with ${}^{L}/_{D_e} \approx 7$ (a reasonable assumption for current military tiltrotors) the cruise blade loading can be of the same order, and possibly greater, than the hover blade loading if both the radius and RPM are reduced. If pushing the aircraft to high speed or maneuvering flight, and thus non-ideal L/D_e, the cruise blade loading could easily approach stall limits. Therefore, care should be taken in the choice of η and ζ in order to ensure that the aircraft will be operating with acceptable stall margins and at the optimum propulsive efficiency.

Table 5.1: Values used for calculations

Variable		
Description	Units	Value
ρ_h	$^{slugs}/_{ft^3}$ $(^{kg}/_{m^3})$	0.002049 (1.055)
ρ_c	$^{slugs}/_{ft^3}$ $(^{kg}/_{m^3})$	0.001065 (0.549)
η	-	0.75
ζ	-	0.8

5.3.2 Collated Results

In the previous section, a typical result for a η sweep was presented. The results tell a more complete story however when they are examined in aggregate. Figure 5.4a shows the change in design gross weight (ΔW_{gross}) as a function of increase in rotor tech factor (χ_{rotor}). Each line represents a constant value of η. The values of η chosen here reflect the most complete data sets over the range of data collected. The data are normalized by the designed gross weight when $\eta = 1$ and $\Delta\chi_{rotor} = 0\%$. As expected, when η is decreased (cruise rotor radius decreases), gross weight also decreases for a given χ_{rotor}. This is due to the same mechanisms as discussed in Section 5.3.1, i.e. decreased wing structural weight, and decrease mission fuel weight. As χ_{rotor} is increased for a constant value of η, the designed gross weight also increases. It is interesting to note that rate of weight increase is fairly constant over the various lines of η. For conceptual design, gross weight correlates well with total cost [126], and so this data can be used to predict, for a given increase in rotor weight, the morphing control authority required to justify the inclusion of morphing technology from a cost standpoint.

Similarly, Figure 5.4b shows the change in mission fuel weight (ΔW_{fuel}) as a

function of χ_{rotor} for various value of constant η. The percent change in fuel weight as η is much more drastic than the change in gross weight shown in Figure 5.4a due to the fact that both decreased aircraft gross weight and increased propulsive efficiency directly lead to a decrease in fuel requirements. It is also important to note that the specific design mission chosen here involve long cruise segments, and as such the fuel weight savings would not have been as pronounced if the mission was tuned more to vertical lift or hover segments.

Figure 5.5 plots ΔW_{gross} as a function of ΔW_{rotor} for various values of η. Along each line of constant η, χ_{rotor} increases from zero at left to a maximum, at right. In general, the trends are as expected in that as the weight of the rotor increases, the gross weight also increases but at a slower rate. As morphing authority increases (η decreases) overall system weight is decreased. For the design in question, there is an approximate 4:1 relationship between rotor weight and gross weight, that is, for every 4% increase in rotor weight, there is a corresponding 1% increase in gross weight. It is important to note that this relationship is for completely resized vehicles, and so it does not indicate that simply incrementing the rotor weight in a fully designed aircraft by 4% will add 1% to the gross weight. Instead, it offers insight into how rotor weight changes affect the sizing process as a whole. From a design standpoint, it is reasonable to conservatively expect a 10% or more increase in rotor weight with the inclusion of any large scale morphing system. For the vehicle considered here, interpolating the data indicates that something around an 15% decrease in rotor diameter would be required to achieve a design equal, from a weight standpoint, to the baseline non-morphing design.

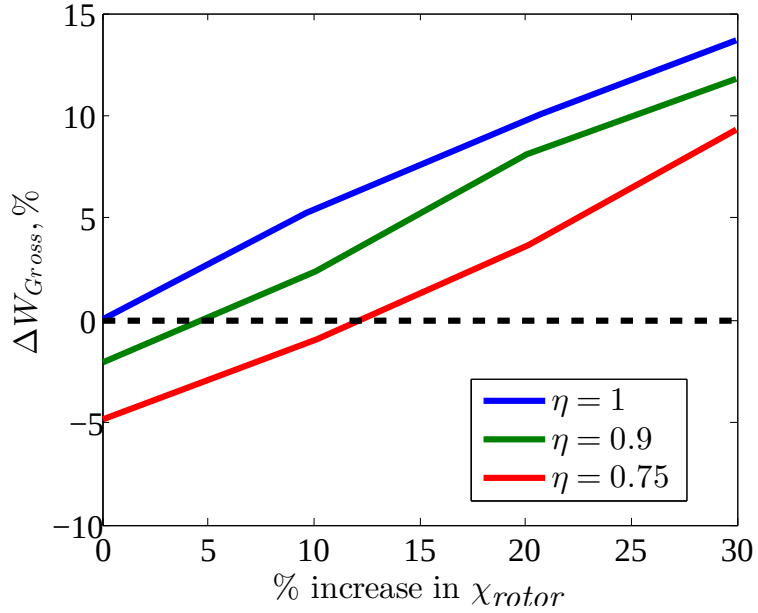

(a) Change in W_{gross} as a function of χ_{rotor}.

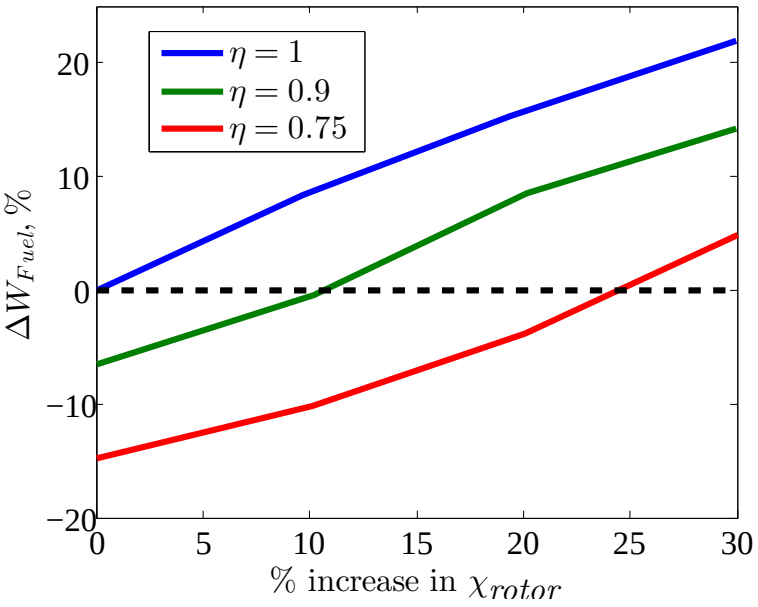

(b) Change in W_{fuel} as a function of χ_{rotor}.

Figure 5.4: Collated change in weight results for lines of constant η

Finally, Figure 5.6 shows how mission fuel weight changes as a function of diameter contraction ratio, η, for increasing increments of χ_{rotor}. The data is normalized against the design weight for $\eta = 1$ and 0% increment in χ_{rotor}. Again, the relationship is fairly linear until around $\eta = 0.7$ at which point the change in fuel weight levels off, or starts to increase. The drastic fuel weight increase seen in the 30% increment in χ_{rotor} line can be attributed to the rotor being forced to operate at very high blades loadings during cruise, as discussed in subsection 5.3.1, where induced losses were drastically increased.

5.4 Conclusions

This work presented a conceptual variable diameter tiltrotor design and sized in the NDARC conceptual design code. Both the maximum allowable diameter morphing and the added weight to the rotor were varied with the intent of investigating the system level benefits (improved weight, fuel use, cost) associated with a variable diameter rotor system. Results showed that, for a 0% increment in rotor technology factor, χ_{rotor}, diameter morphing reduced vehicle gross and component weights, as well as mission fuel weight. As χ_{rotor} was increased, the entire system saw a corresponding increase in weight. For these increased rotor weight conditions, diameter morphing was again able to reduce total system weight back to, or lower than, the baseline design. At very high levels of morphing however, (large reductions in rotor radius for cruise) weight was seen to drastically increase. This was traced to the rotor approaching stalled conditions during cruise due to increased blade loading.

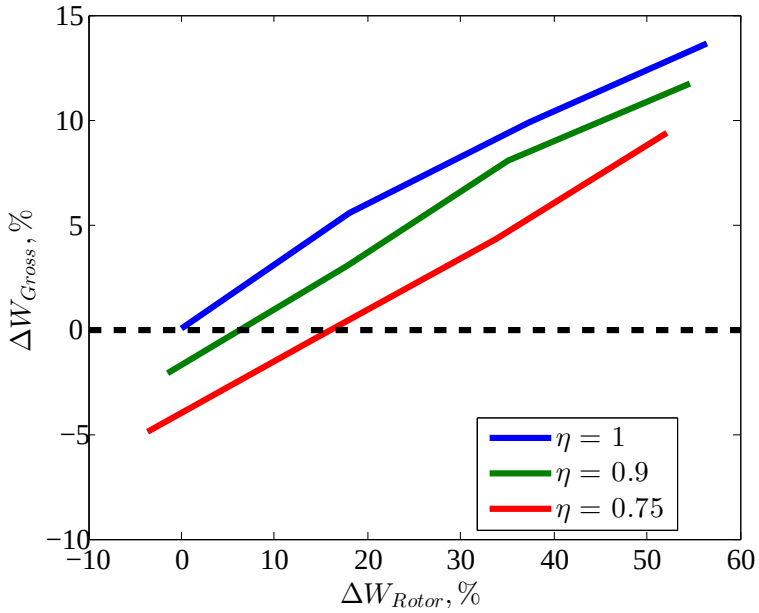

Figure 5.5: Change in rotor system weight as a function of change in aircraft gross weight.

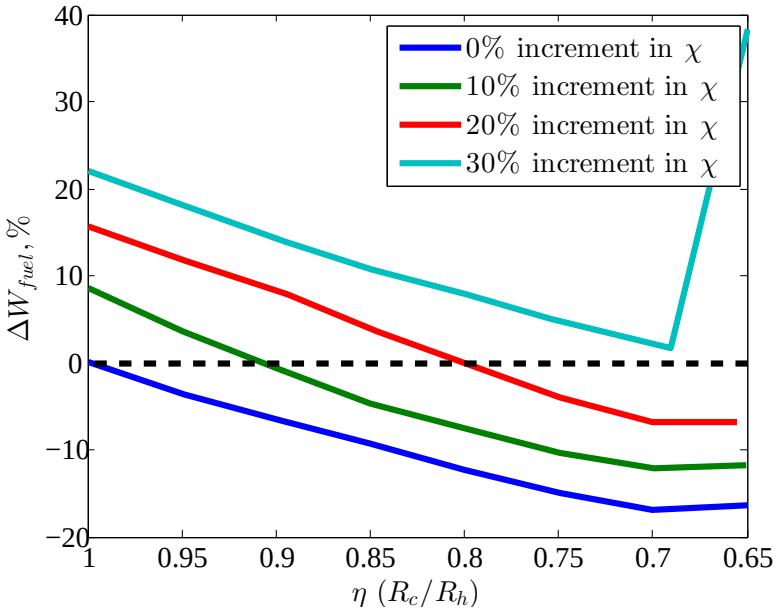

Figure 5.6: Change in fuel weight as a function of η for various increments of χ_{rotor}.

A conceptual approach for estimating cruise blade loading for a variable diameter or variable speed tiltrotor was then presented. In general, this work shows that even for fairly substantial increases in rotor weight, variable diameter morphing can have a system wide benefit in the form of reduced gross weight and reduced fuel weight.

Chapter 6: Development and Testing of a Span-Extending Morphing Wing

6.1 Introduction

Since the advent of aviation, improved flight performance through continuous changes in flight control surfaces has been greatly desired to minimize drag resulting from discontinuous flight control surfaces such as ailerons. The Wright brothers used wing warping to vary twist and to control roll in the first truly successful flying machine [127]. Other historical examples include the Parker Variable Camber Wing used to increase cruising speed [128], a variable dihedral wing that changed aircraft stability [129], and sweep variation to augment dash and cruise flight regimes [130]. For changing the dimensions of an airfoil system, Hall (1927) [131] patented a method for extending both the chord and the span of an aircraft using jackscrews. More recently, telescopic wingspan changes have been investigated [14, 132] with possible improvements seen in cruise and dash performance, as well as roll control.

An aircraft that exhibits any of these morphological changes (twist, camber, sweep, span, chord, diheadral, etc.) has come to be referred to as a "morphing aircraft" [2]. Numerous simulations have highlighted the great potential of these morphing

aircraft [24], but technology barriers in materials and actuators have limited physical realization of these analytical concepts into physical testable prototype systems. It has been shown that morphing achieved without discrete moving surfaces and exposed hinges can improve roll performance and cruise efficiency [21]. Additionally, morphing to increase wingspan has been shown to result in increased range and endurance due to a reduction in induced drag [22] and a differential span change can generate a roll moment, potentially replacing ailerons [133]. Recently, Neal et al (2007) [29] designed and built a wind tunnel model capable of multiple types of morphing and demonstrated a reduction in drag over a large range of lift coefficients. Thus, significant motivation exists to consider novel means of realizing conformal morphing structures.

The task of designing a conformal morphing structure is immensely challenging. Thill et al. (2008) [98] presents a comprehensive review of requirements, current concepts, and technologies for both morphing structures and flexible skins. The topic is also investigated in a recent special issue of the Journal of Intelligent Material Systems and Structures [99]. Elastomeric materials have been suggested as candidate skin materials for conformal morphing applications [100] due to their large strain capability, low stiffness, and passive operation. Passive flexible skins were also examined by Kothera et al. (2007) [101], Bubert et al. (2010) [33], and Murray et al. (2010) [34]. Isotropic elastomer morphing skins were successfully implemented on the Boeing and NextGen Aeronautics MFX-1 UAV [27]. In this design, the silicone elastomer was connected to a rigid 4 bar linkage mechanism and shape change was achieved through shear deformations in the elastomer [102]. Out-of-plane loads

were reacted into a series of metallic ribbons that were stretched under the skin. Mcknight et al. (2010) [35] proposed a reconfigurable segmented variable stiffness skin composed of rigid disks and shape memory polymer. Morphing core sandwich structures capable of high global strains have also been investigated (Bubert et. al., 2010, Joo et al 2009; Olympio et. al. 2010) [32, 33, 103] and an entire morphing substructure capable of continuous stable deformation was proposed by Ramrakhyani et al. (2005) [104] that used highly distributed actuation to achieve large global deformations with relatively low actuation force.

In Bubert et al. (2010) [33], a passive 1D morphing skin and substructure was developed that consisted of an Elastomeric Matrix Composite (EMC) skin supported from out of plane loads by a zero-Poisson substructure. The entire system was capable of a 100% active area change (Figure 6.1) while withstanding out-of-plane loads consistent with a UAV scale aircraft. Analytical modeling of the skin and honeycomb successfully predicted the in plane stiffness characteristics of the system, and FEM analysis was used to show that the honeycomb exhibited very little local strain during actuation, and therefore low levels of internal stress at high levels of global strain, possibly lending it a reasonable fatigue life. This study stopped short of actually implementing the morphing technology into an aerodynamic surface.

The present work is a direct follow-on to the work by Bubert et al. (2010) [33]. Namely, this work explores fabrication techniques for advanced airfoil-like morphing core shapes, exploits customizable design parameters of in-house fabricated EMC skin and core material, designs a prototype airfoil system such that future integration with a candidate UAV is feasible, and experimentally evaluates a wind tunnel prototype.

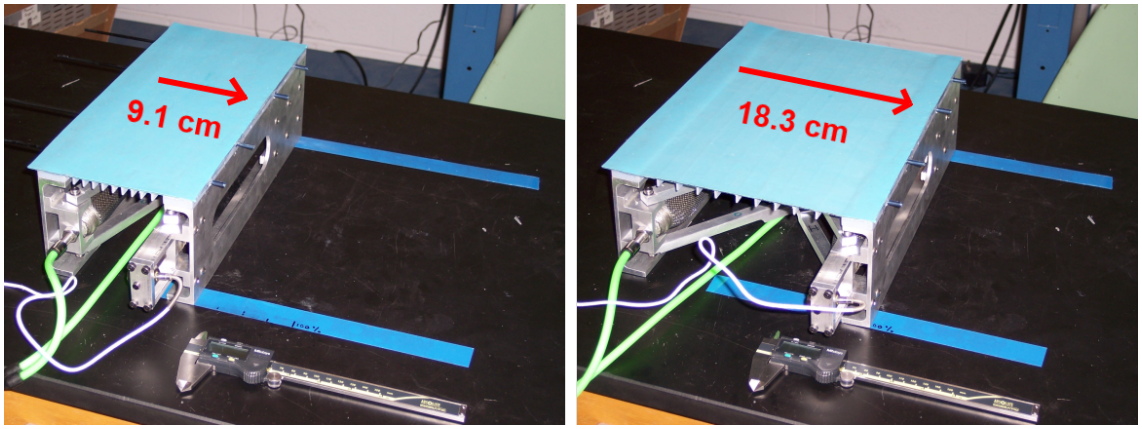

Figure 6.1: 1D morphing prototype with EMC skin and zero-Poisson honeycomb, showing 100% area change (Bubert et al., 2010).

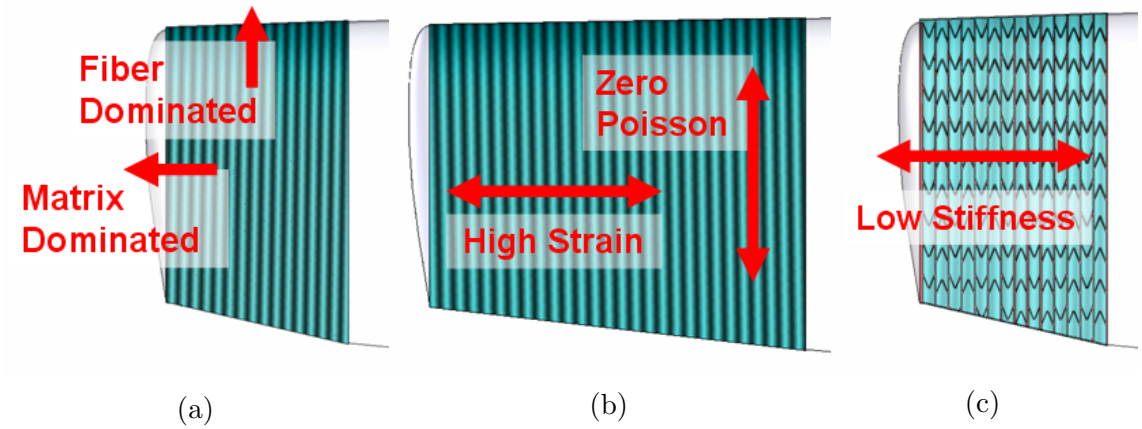

Figure 6.2: Design concept as a span morphing wing tip. (Bubert et al. 2010)

Nominal design parameters for the prototype are a 30.5 cm chord wing section capable of 100% span extension over a 61.0 cm active morphing section with less than 2.54 mm of out of plane deflection between ribs due to dynamic pressures consistent with a 130 kph maximum speed. A depiction of the design concept is shown in Figure 6.2.

6.2 Skin Development

Using elastomer matrix composite (EMC) skins in this span morphing aircraft application is advantageous because elastomeric materials are well-known for their large strain capability, which is required for broad-scale area changes of a wing. Elastomers alone, while allowing large in-plane deformations, may not provide adequate out-of-plane resistance to aerodynamic pressure loading. The morphing core will address this issue in an overall sense by supporting the skin at discrete points, but the skin is unsupported between the rib members of the core. It is in these regions where reinforcement in the skin itself can play an important role in maintaining a viable airfoil surface. Additionally, elastomers have inherently high Poissons ratios, which would induce significant necking in of the skin surface in the chordwise direction when extended in the spanwise direction. Chordwise fiber reinforcement provides a direct means of mitigating this effect by allowing for tailoring of the inplane Poissons ratios. Carbon fibers were chosen as the reinforcing material to be embedded in the elastomeric matrix because of their high stiffness, light weight, and high strength. The effect of placing uni-directional carbon fibers in an elastomeric matrix was studied prior to fabrication to help guide the design [33]. Figure 6.3 shows a diagram of the general EMC that was considered. In this figure, the outer blue surface layers are elastomeric face layers and the gray interior layer represents the carbon fibers embedded in elastomer. The axes are also indicated here, where the 1-direction coincides with the rib, or chord, orientation (transverse to stretch direction) and the 2-direction is the extensional, or span, direction.

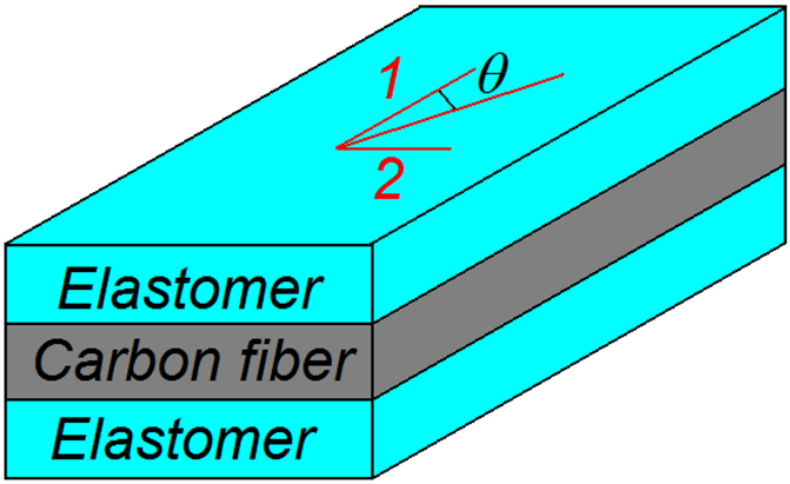

Figure 6.3: Elastomer-matrix-composite skin

6.2.1 Skin Modeling

Classical laminated plate theory (CLPT) was a natural starting point for analytical predictions of in-plane EMC performance [33]. By using CLPT, different lay-ups of elastomer and carbon fiber layers can be examined, varying not only the thickness and number of layers, but also the volume fraction and the offset angle of each fiber layer.

Calculations supported the intuitive conclusion that thinner EMC skins would have a lower in-plane stiffness in the stretch direction, E_2. A reasonably thin skin with the configuration shown in Figure 6.3 was therefore used as a basis to test the effect of fiber angle. Figure 6.4 shows the predicted effect of varying the offset angle of the two fiber layers. It was immediately observed that increasing fiber offset angle adversely increases the in-plane stiffness of the EMC, which would result in requiring greater actuation forces. Based upon this, the decision was made to set the offset angle to 0 degrees. Another key feature of low fiber offset angles is control over

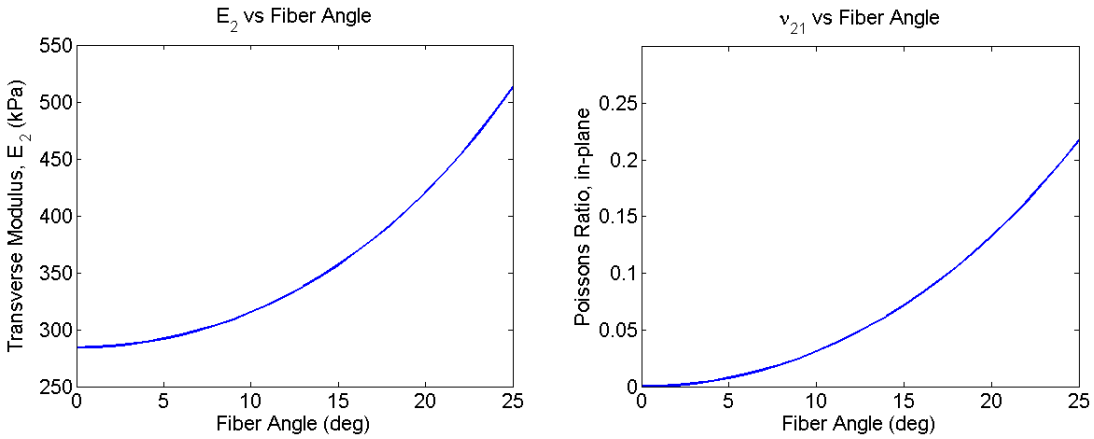

(a) "stretch direction" modulus (b) Poisson's ratio

Figure 6.4: Elastomer–matrix–composite design guidelines

the Poisson's ratio in the 1-direction, as the analytical model reveals in Figure 6.4b. In the resulting case, the EMC can be stretched in the 2–direction with minimal contraction in the 1-direction, thereby creating an EMC that is conducive to large changes in area, on the order of 100% without inducing secondary deflections that would adversely affect airfoil shape. This is perfectly suited to the present application of aircraft wing extension morphing where the chord dimension (1–direction) can remain constant as the span dimension (2-direction) can extend and contract as required by the vehicle.

6.2.2 Skin Manufacture

Based on a prior comparative study of candidate elastomer matrix materials (Bubert et al., 2010), Rhodorsil V-330, CA-35 was selected as the leading candidate for its low in-plane modulus, long elongation to failure, moderate hysteresis, and good workability. This is a two-part silicone rubber often used in molding applications. It is soft and flexible, and it has high strength properties, long shelf life, and excellent

release characteristics. It can be cured at room temperature (room temperature vulcanization) or with heat added. A 5 cm by 10 cm coupon was produced of this material for more extensive testing and the sample showed that 100% stretch was possible without failure.

A key issue in this study was the scaling up of the skin fabrication process for skins sufficiently large to cover the spanwise morphing wing demonstrator. The skin was manufactured in a multi-step lay-up process, building the skin up through its thickness (Figure 6.5). First, a 70 cm by 70 cm sheet of elastomer was cast between two aluminum caul plates using shim stock to enforce the desired thickness. Secondly, uni-directional carbon fiber was then applied to the cured elastomer sheet, with particular attention paid to the alignment of the fibers to ensure that they maintained their uniform spacing and uni-directional orientation. Enough additional liquid elastomer was then spread on top of the carbon to wet out all of the fibers. An aluminum caul plate was placed on top of the lay-up, compressing the carbon/elastomer layer while the elastomer cured. The third and last step in the skin lay-up process was to build the skin up to its final thickness. The bottom sheet of skin with attached carbon fiber was laid out on a caul plate. As in the first step, shim stock was used to enforce the desired thickness (now the full thickness of the skin) and liquid elastomer was poured over the existing sheet. A caul plate was then placed on top of this uncured elastomer and left for at least 4 hours. Once cured, the completed skin was removed from the plates, trimmed of excess material, and inspected for flaws. A successfully manufactured skin had a consistent cross section, as shown in Figure 6.6, and no air bubbles or visible flaws. Key properties of the

Table 6.1: EMC Skin Properties

	Constituent Material Properties		Properties of
	V-330 CA-35	Carbon fiber	Assembled skin
Young's Modulus	690 kPa[a]	70 GPa	420 kPa[a]b
Poisson's Ratio, ν_{21}	0.4	0.1	0.0

[a]at 100% elongation
[b]in the 2-direction

EMC skin and base materials are provided in Table 1, where the composite skin properties were measured experimentally. The nominal total skin thickness was 1.14 mm with a 0.13 mm layer of fiber in the center.

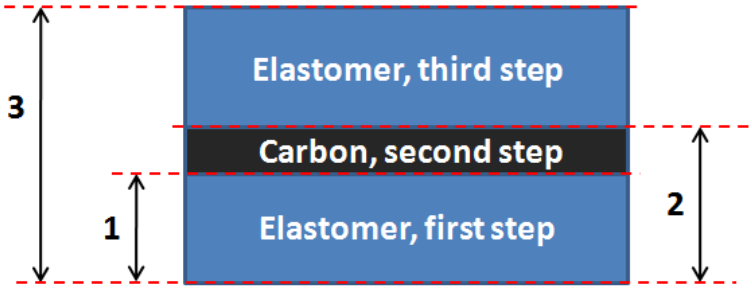

Figure 6.5: Progression of skin manufacturing process.

6.3 Structure Development

A traditional honeycomb structure has a positive Poissons ratio, that is, when it is strained in one direction it tends to contract in the orthogonal directions. It was noted by Evans (1991) that some naturally occurring materials can exhibit a negative Poissons ratio, contracting when they are strained. Bubert et al. (2010) [33] took elements from both the standard and auxetic honeycomb configurations to create a zero-Poisson ratio (re-entrant) honeycomb structure, as shown in Figure 6.7. This concept is the basis of the previous works morphing substructure and is described

Figure 6.6: Cross-section view of fabricated skin

fully by Kothera et al. (2007) [101]. The in-plane stiffness (stiffness in the direction of actuation) of this structure is very low, on the order of 10s of kPa, and can be accurately modeled analytically. It is the ideal support structure for an EMC skin because has the ability to change in area by 100% in a continuous manner, i.e. not involving discrete telescoping or sliding sections, while maintaining a high out-of-plane stiffness.

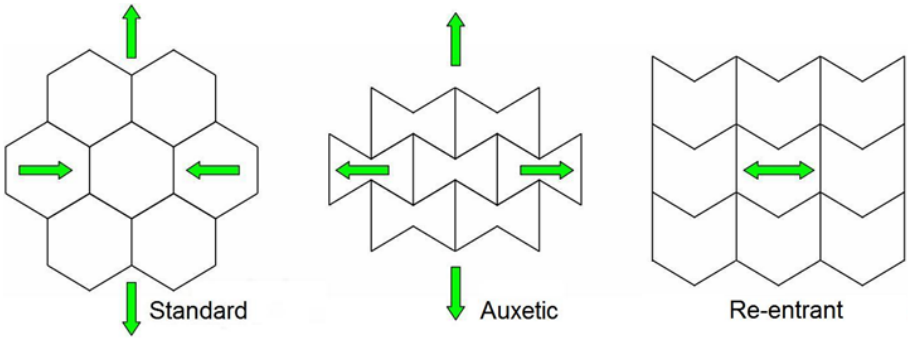

Figure 6.7: Development of zero Poisson's ratio morphing core

One of the key points of the present work is to extend the concept of a planar morphing core structure into a representative airfoil for direct application to aircraft.

Figure 6.8a shows the 1-D planar morphing zero-Poisson core concept, where "rows" or "ribs" of constant length are connected by "V-shaped" bending members, which essentially act as springs in-plane and resist shear out-of-plane. Initially, the planar core design was extruded and cut into the form of a NACA 63_3-618 airfoil with a chord of approximately 30.5 cm and span of 91.4 cm. The resulting morphing airfoil core appears in Figure 6.8b. Recall that this representative size is scaled for a host small unmanned air vehicle (UAV), which will serve as the possible test platform during future work. While this morphing structure is capable of achieving greater than 100% length change itself, it has insufficient spanwise bending and torsional stiffness and so does not constitute a viable wing structure. The structure was therefore augmented with continuous sliding spars. Additionally, the center of the wing structure was hollowed out to potentially accommodate an actuation system for the span extension.

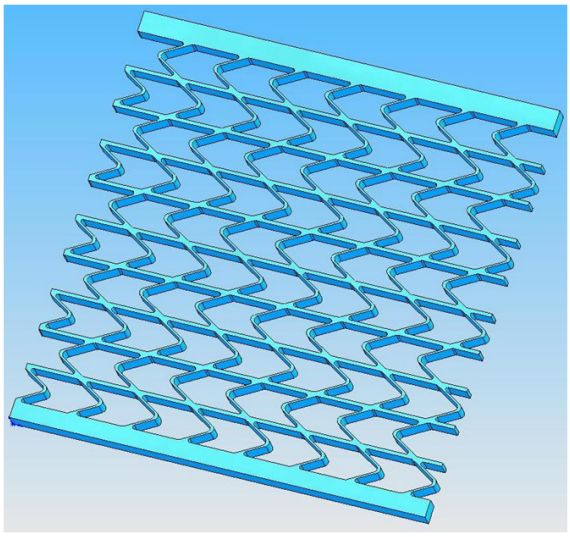

(a) "stretch direction" modulus

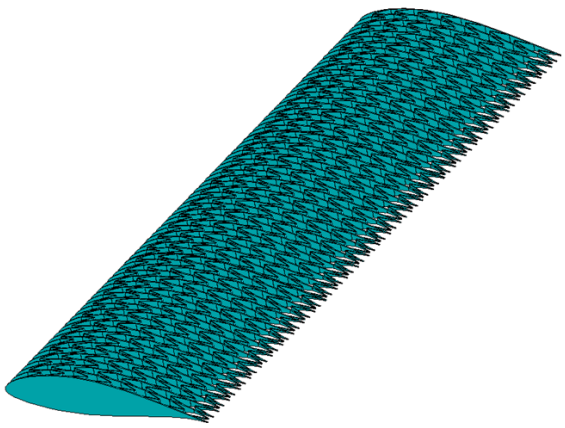

(b) Poisson's ratio

Figure 6.8: Morphing core concept (a) planar design; (b) NACA 63_3-618 airfoil

The final form of the morphing airfoil core is shown in Figure 6.9. This figure show a shell-like section mostly around the center of the airfoil, where an actuator could be located. Both the leading and trailing edges feature circular cut-outs to accommodate the carbon fiber spars, and near the trailing edge is a solid thickness airfoil shape for more rigidity where the airfoil is thinnest. The spars were sized using simple Euler-Bernoulli beam approximations and a desired tip deflection of less than 6.4 mm at full extension.

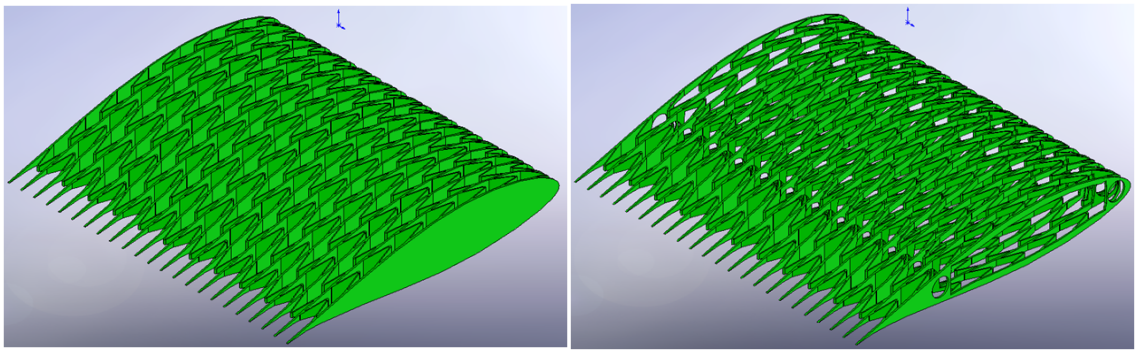

(a) (b)

Figure 6.9: Core design (a) initial, solid rib sections; (b) final, shell-like rib sections

The key components designed and discussed previously were fabricated for the prototype test model. Due to the complex geometry of the morphing core and the desire for rapid part turn around, a stereo lithographic rapid prototyping machine (Objet) was used to manufacture the morphing core sections from an acrylic-based photopolymer. The stereo lithography process lays down consecutive thin layers of an ultraviolet curing resin and support material. When the model is done printing, the support material can be washed away, leaving the fully formed prototype with no additional post processing required. The viability of this approach for flyable aircraft applications would have to be studied, but the material/manufacturing approach

was sufficient for this proof of concept structural demonstrator. Other fabrication techniques such as investment casting, electro discharge machining, etc. could be considered when fabricating this structure to meet full-scale aircraft requirements. It should also be noted that the prototype will feature three of the core segments shown in Figure 6.9b. They will be pre-compressed when the EMC skin is bonded to allow for more expansion capability.

Figure 6.10 depicts a manufactured core section. A side view is shown in Figure 6.10a, where the fore and aft spar cut-outs can be seen on either end of the central cavity that will house the actuation system. The top view shown in Figure 6.10b illustrates the basic design features that allow the core structure to change span, while maintaining a constant chord. That is, the rib-like members and the connecting "v-shaped" bending members.

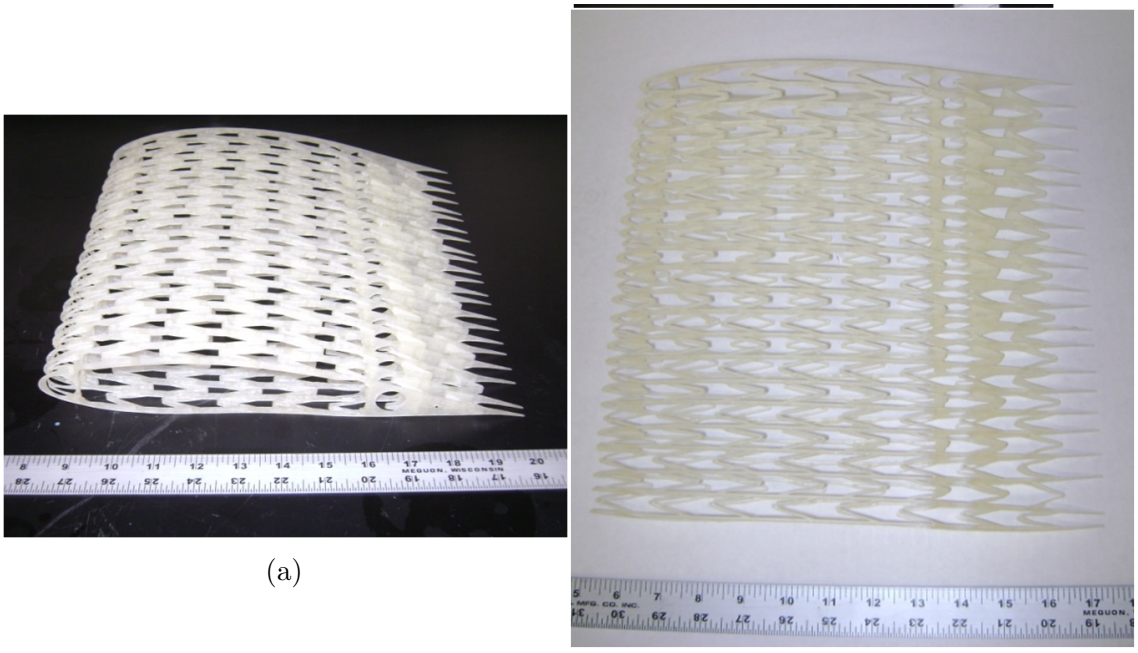

(a) (b)

Figure 6.10: Core design (a) initial, solid rib sections; (b) final, shell-like rib sections

Figure 6.11a shows the core sections together between two aluminum end plates, with the leading edge and trailing edge support spars. The end plates were sized to provide a suitably large bonding surface for attaching the skin on the tip and root of the morphing section. In this configuration, the core sections are initially contracted such that the active span length is 61.0 cm. In terms of the aircraft, this contracted state will be considered the neutral, resting state because the EMC skin will not be stretched here and a potential actuation system would not be engaged. Hence, this is the condition in which the skin would be bonded to the core. Also shown in Figure 6.11b is the same arrangement in the fully extended (100% span increase) state with a span of 122.0 cm. The figure shows that the spacing between each of the rib-like members has nearly doubled from what was shown in the contracted state. This figure helps illustrate the large area morphing potential of this technological development in a way that could not be seen once the skin was attached.

6.4 Prototype Integration

The skin was boded to the morphing substructure using DC-700, a Dow-Corning silicone based adhesive. The skin was attached to each rib structure, but not to the "v-shaped" bending members. Particular attention was used when bonding the skin to the endplates, as all of the tensile stress in the skin was resolved through its connection to the end plates. Figure 7.13 depicts the bonding process, starting from the trailing edge and moving towards the leading edge.

Figure 6.13 shows the completed prototype and illustrates the broad scale

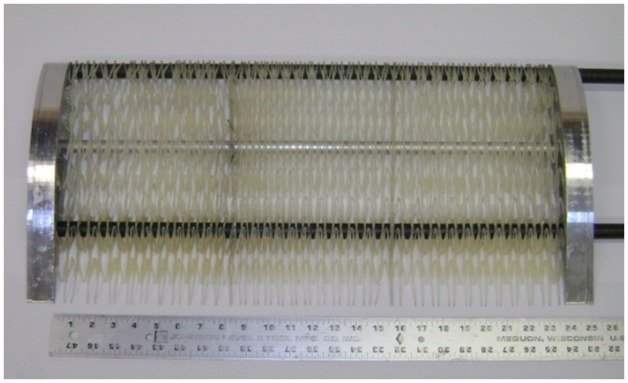

(a)

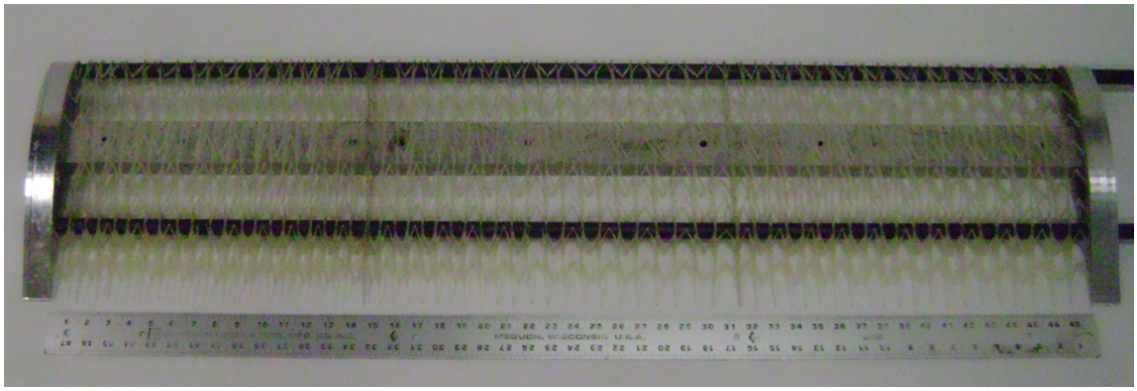

(b)

Figure 6.11: Assembled core with spars and end plates (a) contracted state; (b) extended state

area change achievable with this morphing skin and core technology. At the resting condition with no elastic energy stored in the skin, Figure 6.13a shows the 0% morphing state with a 61.0 cm span. Increasing the span by 30.5 cm to a total of 91.5 cm reaches the 50% morphing state shown in Figure 6.13b. Finally, Figure 6.13c highlights the full potential of this morphing system as the prototype wing section reaches double the initial span, which has gone from 61.0 cm to 122 cm to show the 100% morphing capability. Recall from the design that the wing section chord stays constant during these span extensions, so the morphing percentages indicated (50%, 100%) are consistent with the increase in wing area. As a fixed point of reference

Figure 6.12: Bonding the EMC skin to the morphing core

in each of these figures, note that the length of the white poster board underneath the prototype wing section does not change. Note also that this demonstration will use fixed-length internal spreader bars to hold the structure in different morphing lengths. Actuation was achieved by manually stretching the skin/core structure and then attaching the appropriate spreader bar to maintain the stretched distance.

6.5 Wind Tunnel Testing

Having shown that the prototype morphing wing section could achieve the goal of 100% span morphing for a total 100% wing area increase, the final test to be performed placed the wing section in a wind tunnel. The purpose of this test was to ensure that the EMC skin and core could maintain a viable airfoil shape at different morphing states under aerodynamic loading, with minimal out-of-plane deflection

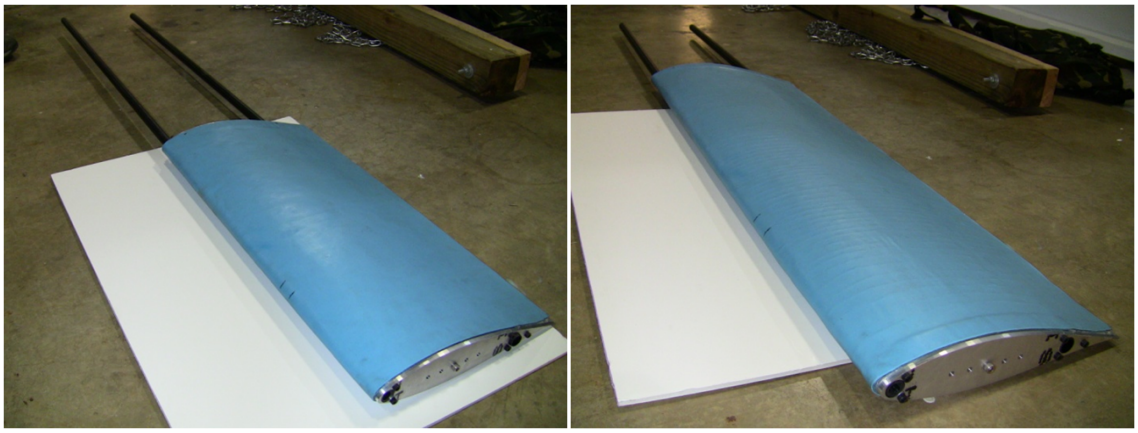

(a) 0% morphing (b) 50% morphing

(c) 100% morphing

Figure 6.13: Prototype morphing wing demonstration (a) resting length, 0% morphing; (b) 30.5 cm span extension, 50% morphing; (c) 61.0 cm span extension, 100% morphing

between ribs. The open circuit wind tunnel used in this test resides at the University of Maryland and is pictured in Figure 6.14a. The fan at the right side of the figure pulls air from the left through a honeycomb section to straighten the flow, which then passes through the 50.8 cm tall, 71.1 cm wide test section. A close-up view of the test section is shown in Figure 6.14b with the prototype wing section installed vertically in its resting span length.

Photographs inside the wind tunnel are provided in Figure 6.15. From the leading edge, looking in the direction of the air flow, Figure 6.15a shows the lower

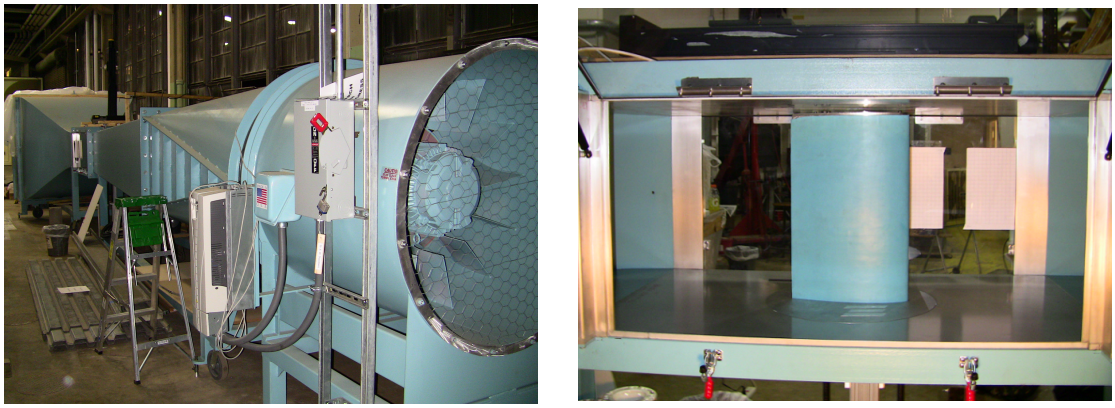

(a) (b)

Figure 6.14: Wind tunnel test setup - (a) wind tunnel; (b) morphing wing section installed

surface of the morphing airfoil, where the camber is apparent. Similarly, Figure 6.15b shows the lower airfoil surface from the trailing edge, looking against the wind direction. Note that these pictures were taken in the absence of actual air flow, so the aerodynamics would not be affected in the test. Also seen in these figures are circular mounding plates on the floor and ceiling, which allow the angle-of-attack to be changed.

With only a 50.8 cm tall test section in the wind tunnel, a plan was devised where only this span length of the prototype morphing wing would be placed in the wind flow, while the remaining span and support structure was below the tunnel. This is illustrated in Figure 6.16, where both the resting skin condition (0% morphing) and full extension condition (100% morphing) are shown. This figure also provides another perspective of how much the wing can actually change its span, as this is the identical prototype hardware in two different morphing conditions. It should also be noted that while only a 50.8 cm span section of the wing is in the airflow, this is sufficient to determine whether or not the skin and core can maintain a

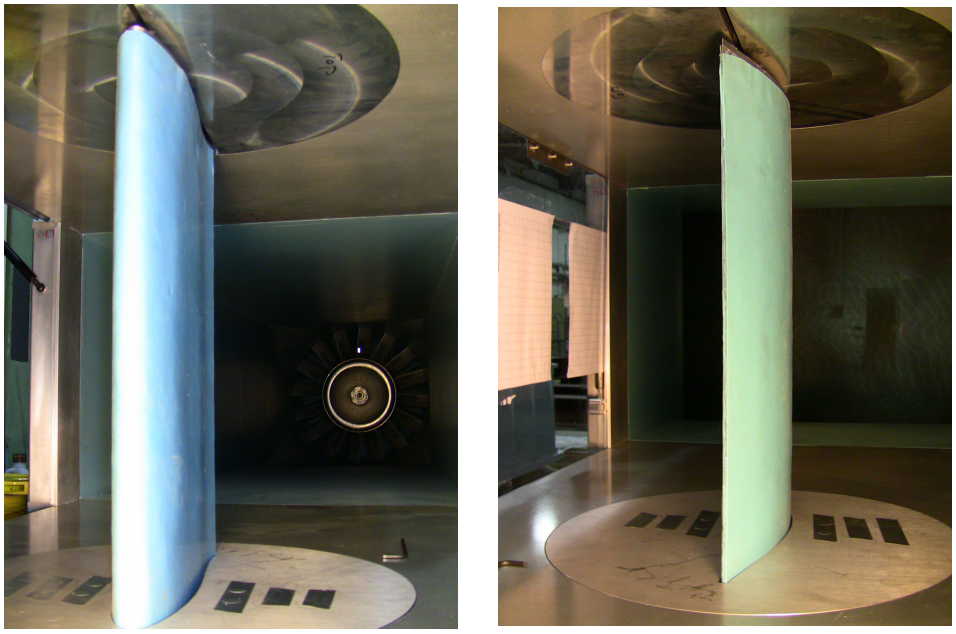

(a) (b)

Figure 6.15: Wing installed in wind tunnel (a) from leading edge; (b) from trailing edge

viable airfoil shape in the presence of representative aerodynamic conditions, which was the primary goal of this test. That is, the morphing core motion and skin stretching is consistent and substantially uniform across the span of the prototype, so any characteristics seen in one small section of the wing could similarly be seen or expected elsewhere in the wing, making this 50.8 cm span "sampling" a reasonable measure of system performance.

Both the cruise (105 kph) and maximum (130 kph) rated speeds of the candidate UAV were tested. Three angles-of-attack (0 degrees, 2 degrees, 4 degrees) and three wing span morphing conditions (0%, 50%, 100%) were also included in the test matrix, which is displayed in Table 6.2. Tests were performed by first setting the morphing condition of the wing section. Then the wing was positioned for the desired angle-of-attack (AOA). With these values fixed, the tunnel was turned on

(a) (b)

Figure 6.16: Overall wind tunnel setup (a) wing at resting length, 0% morphing; (b) wing at full span, 100% morphing

and the speed was increased incrementally, stopping at the two noted test speeds while experimental observations were made. Tests were completed at each of the conditions in the table indicated with an x-mark. Note that tests were not performed at two of the angles of attack at the 100% morphing condition. This was because the skin began to debond near the trailing edge at one of the endplates. This occurred over a section approximately 7.6 cm in span at the 100% morphing condition, though the majority of the prototype remained intact. After removing the wing section from the wind tunnel and inspecting the debonded corner, it was discovered that very little adhesive was on the skin, core, and end plate. Thus, the likely cause for this particular debonding is inconsistent surface preparation, which can easily be rectified in future refinements. Note that the upper surface of the trailing edge experiences relatively small dynamic pressures compared to the rest of the wing, so that this

Table 6.2: Wind tunnel test matrix completed

	105 kph				130 kph		
	0%	50%	100%		0%	50%	100%
0°	X	X	X	0°	X	X	X
2°	X	X	–	2°	X	X	–
4°	X	X	–	4°	X	X	–

debonding was most likely unrelated to the wind tunnel test. Rather, it was the result of manufacturing inconsistency.

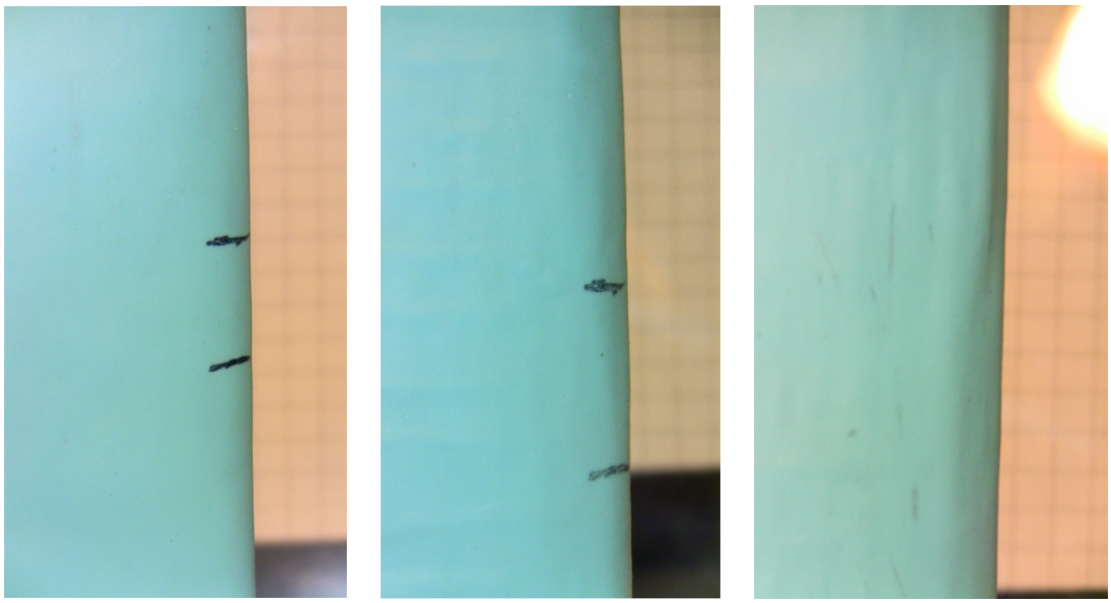

(a) 0% morphing (b) 50% morphing (c) 100% morphing

Figure 6.17: Photographs of wing section leading edge at 130 kph (a) 0% morphing (marks show resting length); (b) 50% morphing; (c) 100% morphing

During execution of the test matrix, digital photographs were taken of the leading edge at each test point to determine the amount of skin deflection (e.g., dimpling) that resulted from the dynamic pressure. The leading edge location was chosen as the point to measure because the pressure is highest there. Pictures were taken perpendicular to the air flow direction and angled from the trailing edge,

looking forward on the upper skin surface. Grids were taped to the outside of the transparent wall on the opposite side of the test section to provide reference lengths for processing. The grids form 12.7 mm squares and are located 35.6 cm behind the airfoil in the frame of view, which is also 35.6 cm, from the camera lens. These can be seen in Figure 6.17 at 130 kph for each of the three morphing conditions tested. Through image processing, the maximum error in the measurements was determined to be ±7%. This error can be attributed to vibration of the wind tunnel wall, which the camera lens was pressed against, or deviations in the focus of the pictures. In all the data processed, the maximum discernible out-of-plane deflection was approximately $0.51 \pm .04$ mm, which is well within the goal of less than 2.54 mm. In reference to the 30.5 cm chord and 5.49 cm thickness, this deflection accounts for only 0.17% and 0.93%, respectively. Additionally, in observing this experiment, it can be qualitatively stated the morphing wing held its shape remarkably well under all tested conditions. This can be confirmed through visual inspection of the figures, as well.

6.6 Conclusions

This work exploring a span morphing wing surface for improved efficiency has led to the successful development and prototype testing of a novel morphing system sized for unmanned air vehicles. With the goal of producing up to 100% changes in wing area, the system components were designed accordingly. Features included a silicone elastomer skin, which had embedded uni-directional carbon fibers

to minimize Poissons ratio effects and increase chordwise in-plane skin stiffness, and a morphing core substructure, which provided a Poissons ratio of zero. The system was assembled as designed and demonstrated its ability to increase span by 100% while maintaining a constant chord. Wind tunnel tests were conducted at cruise (105 kph) and maximum speed (130 kph) conditions of a candidate UAV test platform, at 0 degrees, 2 degrees, and 4 degrees angle-of-attack, and at 0%, 50%, and 100% extension. At each test point, image processing was used to determine the maximum out-of-plane deflection of the skin between ribs. Across all tests, the maximum discernible out-of-plane deflection was less than 0.5 mm.

Chapter 7: Development of a Quasi-Static Span-Extending Blade Tip System for a Morphing Rotorcraft

7.1 Introduction

A current technology push in advanced flight systems is to replicate certain features seen in nature. This has opened the door to a new class of aircraft that have the ability to change shape or morph [1–3]. Although the idea of improved flight performance through changes in the control surfaces dates back to the advent of aviation with the Wright brothers' pioneering work on "wing warping" [4], it was not until the recent progress in material and actuator development that such morphing control surfaces seemed practical [5]. This future fleet of morphing aircraft has received considerable attention for their potential to have a single platform serve multiple mission objectives, as well as improve performance characteristics. The same basic solutions to affect vehicle performance and stability, such as camber, span, sweep, and twist, are under investigation with morphing aircraft, but the prospect has now changed from discrete or articulated control surfaces with abrupt changes in contour, to smooth, conformal airfoils in each of several morphed shapes, as well as during the shape change [6, 7].

While the majority of existing research for morphing aircraft has focused on fixed-wing aircraft, rotary-wing aircraft have begun to receive more attention. Recent developments in advanced rotor blade design have begun to address the complexities of rotary-wing aircraft, such as the BERP blade [8] and the ERATO blade [9], and the potential for large increases in performance may have arrived [10]. Although these advanced blade shapes are quasi-static, feasibility of dynamic shape changing skin technologies has been proven for one-dimensional structures [32–34], and airfoil structures [15, 35–37]. Additionally, recent advances in adaptive materials have led to a variety of schemes for on-blade actuation, such as adaptive twist of the rotor blade [38–42], trailing edge flaps [43–48], active camber control [49–53], active rotor span [54], and chord morphing [19]. Hence, it appears that the maturity of these types of components has progressed to a level where design for fabrication and testing on a rotorcraft system is plausible. Herein, shape-changing rotor blades could be designed to account for the conflicting requirements of advancing and retreating blades, approaching an aerodynamic optimum, or to change configuration for optimal hover or forward flight performance. Thus, motivation has been provided to begin considering the possibilities of morphing rotor blades.

Of interest in the present work is blade tip extension, as adaptive changes to the blade radius have the potential to positively affect useful payload fraction, range, acoustic signature, and vibration [13, 88, 121]. It should be mentioned that the intention of the extending tip sections, while remaining an reconfigurable technology component, is for quasi-static configuration change type operations. This implies relatively low bandwidth actuation compared to other active rotor technologies, such

as trailing edge flaps, active twist, and active pitch links, which are typically required to actuate at least one time per rotor revolution. General objectives for the blade tip extension technology in this framework were the following:

- Introduce small, controllable increase to blade radius
- Maintain blade chord over the adaptive region during extension
- Deviate minimal amount from the blade skin airfoil profile under flight loads
- Minimize added blade weight

Based upon these objectives, an approach was adopted to develop a blade tip morphing system, which will be introduced in the next section. This paper will then discuss the development of the morphing airfoil core and the morphing skin in turn. Benchtop testing of integrated core-skin samples is then discussed, with discussion of core-to-skin bonding. Finally, an optimization then presented which minimizes the active section's weight while tailoring its mechanical properties for actuation under centrifugal loads.

7.2 Morphing System Conceptual Design

The concept selected for development here was to replace the outboard-most section of the rotor blade on a vehicle similar to the V-22 *Osprey* tiltrotor with a morphing tip section that can increase its local span dimension by 100% to meet extension design goals with minimal impact to the host blade structure. This is conceptually shown in Figure 7.1, where R is the blade radius, and a is the

representative morphing span length at the tip. This concept will feature both an extending airfoil support structure and an extending airfoil surface. This general approach follows from previous related work on one-dimensional morphing structures [33] and span-extending wings for small scale unmanned fixed-wing vehicles [15]. but builds upon the prior work by designing a morphing system for a much harsher environment where the aerodynamic loading is greater and centrifugal forces are substantial. In order to develop such a system, two technologies were utilized. The first is a morphing re-entrant honeycomb structure [107] and the second is an elastomer-matrix-composite (EMC) skin. All of the prior work with these technologies was intended for a low-speed wind tunnel test article and proof of concept and the present work presents many advances past these referenced studies. The prior test article included a much softer skin, and a substructure that was digitally printed using a fairly brittle plastic. While this early work served well as a proof of concept, the physical realizations of the morphing concepts were not suitable for rotorcraft, or even large scale fixed wing, applications. The current work presents and evaluates new methods, which with to manufacture the morphing substructure using metal. It also matures the skin design to a much stiffer and harder elastomer. It is expected that centrifugal acceleration will contribute significantly to creating the deployment loads [134,135]. To accomplish this, a novel optimization is presented which tailors the system for actuation in the rotating frame. The deployment itself will be quasi-static, with the system being set at a certain deployment level, and changes happening over a matter of seconds.

The actuation system for retracting the morphing tip and the structure for

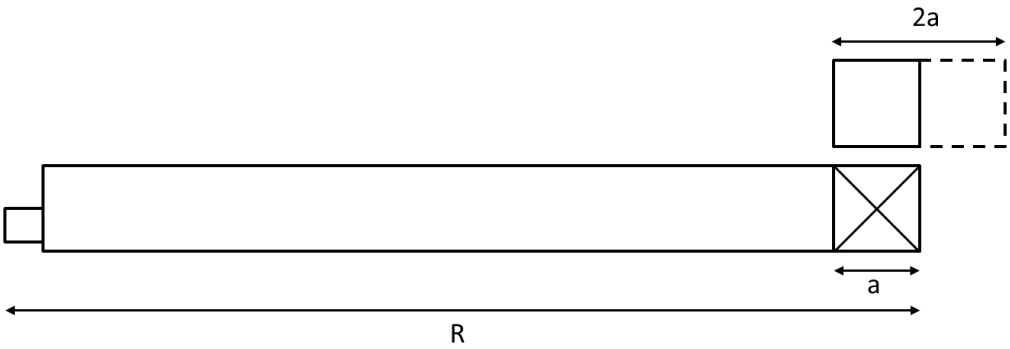

Figure 7.1: Extending blade tip concept.

supporting it during actuation are complex issues and vital to the success of the proposed morphing system. However, they are not directly a part of this work. There are longstanding efforts, most notably by the Sikorsky Aircraft Co., to develop a working variable diameter system for tiltrotor applications which include extensive wind tunnel testing [92–97]. Additionally, the same wealth of information indicates that each portion of this problem (the morphing structure, the sliding support structure, and the actuator) are inherently complex issues that merit and have received individual investigation. Like all rotorcraft morphing technology (with the exception of trailing edge flaps), these actuation/support systems have not been flight tested, but sufficient work exists that demonstrates the mechanical feasibility of existing actuation and support technology, and so it is reasonable to consider the design of the morphing core separately.

7.3 Morphing Core Development

The morphing core structure is the component of the morphing blade tip system that will support the skin and transfer the air loads into the blade through

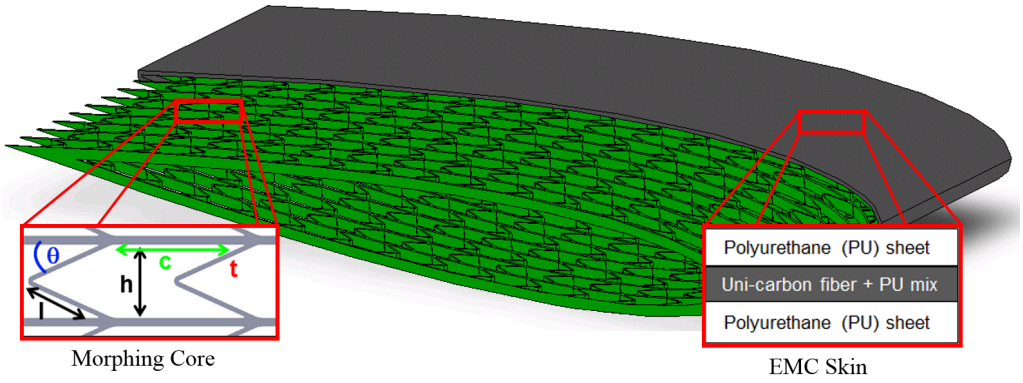

Figure 7.2: Conceptual design of morphing airfoil structure for tip span extension.

a sliding spar. Note that the structural design of the sliding spar which transfers these loads to the main blade is not considered in the present work. As the core structure supports the skin in-plane and out-of-plane, it is also the core that will be responsible for guiding the skin during extension, again through interaction with the sliding spar and actuator. A conceptual design model of the morphing airfoil core is shown in Figure 7.2, where a unit cell of the morphing core and the EMC skin are both called out. The morphing structure is then a series of rib elements connected spanwise by chordwise rows of spring elements. As such, the morphing core takes features from re-entrant hexagonal honeycomb to create a structure with zero Poisson's ratio [101].

7.3.1 Morphing Core Design

To reduce system weight and actuation requirements, the morphing core structure should be designed such that when operating at the candidate rotor's RPM, each row of spring elements would deflect evenly under the induced centrifugal acceleration so the rib elements would have uniform spacing at double their resting

width to evenly distribute 100% strain in the skin along the entire adaptive span section. With this approach, the inertial forces present in the rotating environment would dominate and an actuation system would not be needed during extension, other than to guide the timing and synchronization of deployment. The actuator would be primarily responsible for retraction, however. Given that the rotational environment would cause span-varying centrifugal loads due to changes in distance from the center of rotation and amount of outboard mass, the structure had to be designed where the spring element stiffness varied as a function of span location. Modifying the stiffness equation for standard honeycomb structure [136] for the zero Poisson design gives an analytical expression of structure stiffness, E_1, as

$$\frac{E_1}{E_S} = \left(\frac{t}{l}\right)^3 \frac{l \sin\theta}{c \cos^2\theta} \tag{7.1}$$

where E_s is the modulus of the material, t is the thickness of the spring elements, l is the length of the spring elements, c is the cell width, and θ is the initial spring element angle [33]. Figure 7.3 has been included to label these parameters for a single hexagonal cell of the partially re-entrant design. Also included in this figure is h, which is defined as the height of the cell in the morphing direction. Using this expression, it is possible to tailor the stiffness of each morphing cell to a desired value. As mentioned earlier, the precise stiffness required for extension in the rotating environment is a function of the entire morphing system (morphing skin, core, and actuator) and the particular morphing cell in question. While this problem could be simplified and a deterministic solution obtained, it is unlikely that the solution would

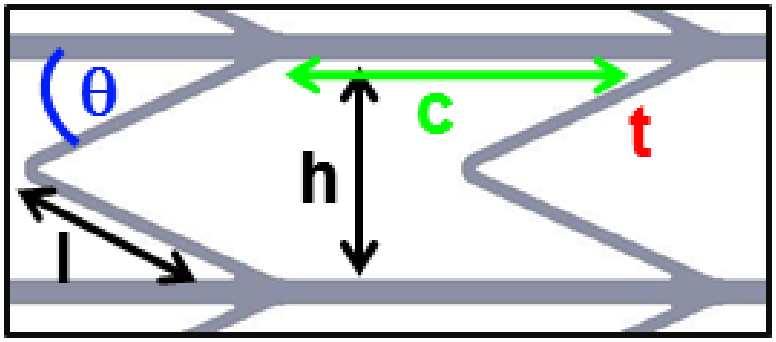

Figure 7.3: Geometry of a single hexagonal cell.

be optimum. Therefore, a numerical optimization is presented in section 7.6 which attempts to minimize the mass of the entire morphing system while maintaining the desired deflection at each morphing cell.

Out-of-plane deflection of the morphing core structure due to aerodynamic pressure is also a concern. For this design, it is assumed the morphing skin transfers all aerodynamic loading directly to the morphing core ribs and the spring elements are not required to care any out-of-plane loading. The load is then transferred to a supporting substructure (such as a sliding spar) which connects back to the main blade. In this way, the out-of-plane stiffness of the core is governed purely by the compressive stiffness of the morphing core structure parent material (most likely very high) and the bending stiffness of the supporting structure.

7.3.2 Morphing Core Manufacture

A secondary goal of this work was to explore existing manufacturing methods that could produce these complex structures in aerospace grade materials. While many materials were considered, such as aluminum, steel, and composites, titanium was selected as the core material due to its high strength-to-weight ratio, corrosion

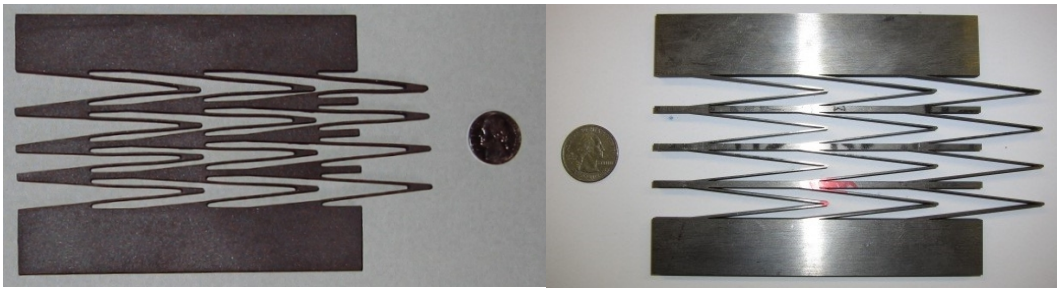

(a) Investment casting (b) Electrical discharge machining

Figure 7.4: Fabricated coupon specimens of the titanium morphing core structure.

resistance, and the wide choice of aerospace grade alloys. Additionally, two manufacturing methods, investment casting and electrical discharge machining (EDM), were evaluated. The resulting coupon parts fabricated for validation testing are pictured in Figure 7.4. While it is unclear whether a cast part could be qualified as flight-worthy, it should be mentioned that the casting method was chosen here primarily for a more economical approach to validating an analytical model with test data of a representative metallic structure of complex geometry. In-plane testing of these structures on a servo-hydraulic test machine validated the overall stiffness and geometry of the two designs. Figure 7.5 depicts the results of one such validation test for the EDM sample, where the experimental stiffness (34.2 kPa), the analytically predicted stiffness (31.5 kPa), and the FEM predicted stiffness (33.2 kPa) agree well. Note that the experimental sample was not taken to 100% strain out of an abundance of caution, because the purpose of the test was simply to evaluate the sample's stiffness. [ht]

Preliminary cycle tests were conducted with both titanium coupon specimens for over 300 cycles. Assuming two tip deployments per flight, this equates to 150 flights. Figure 7.6 shows the results of these experiments, where it can be seen

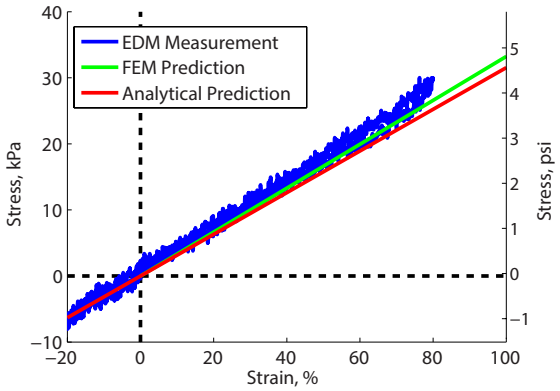

Figure 7.5: Core stiffness model validation with FEM and experiment for EDM structure.

that both specimens survived the 300 cycles with no change in stiffness over the duration of the test. For the stiffer cast specimen (Figure 7.6a), the mean stiffness was 921.81 kPa, with a standard deviation of 7.24 kPa. For the EDM specimen (Figure 7.6b), the mean stiffness was 36.34 kPa, with a standard deviation of 0.49 kPa. Note that the values listed in the legend refer to the cycle number to which the data corresponds and they all overlay each other for both specimens. In designing this experiment, care was also taken to ensure that the material stayed in the linear elastic region for each design. For the casting, the specimen was actuated from 80% of its resting length to 120%, a change of 40%. The EDM specimen was extended 100% from its resting state.

7.4 Morphing Skin Development

The purpose of the morphing skin is to provide an aerodynamic surface for the adaptive blade tip that keeps the shape of the airfoil when retracted, extended, and during transition. A good summary of the state of the art in morphing skins is

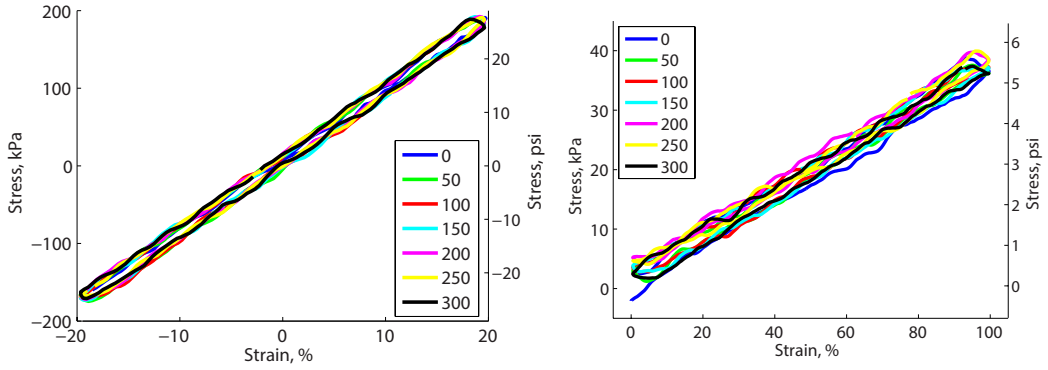

(a) Investment casting

(b) Electrical discharge machining

Figure 7.6: Cycle test data from titanium coupon specimens.

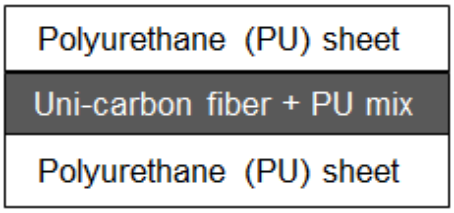

Figure 7.7: General cross section layout of an elastomeric matrix composite skin.

presented in Thill et al. [98]. The skin will be bonded to the core structure along each rib element, but not on the spring elements to eliminate the potential for asymmetric strains. To facilitate rapid and accurate analysis, the design of the skin was conducted with a finite element model (FEM). Traditionally, composite structures can be analyzed using classic laminated plate theory (CLPT). This approach was not appropriate for the present work because out-of-pane loads needed to be simulated, which violate the planar stress assumptions of CLPT. As Figure 7.7 shows, the skin is a layered composite structure with face sheets of polyurethane and a central layer of uni-directional carbon fiber fabric embedded in polyurethane. In this design, the carbon fibers are aligned with the blade chord so the skin stiffness in the span direction is dependent only upon the stiffness of the elastomer material.

7.4.1 EMC Preliminary Design

Finite element simulations were conducted, assuming linear stress-strain profiles and zero in-plane Possion's ratio, for various skin material stiffnesses, thicknesses, and pre-strains to arrive at a preliminary design that met the specified design goals. Note that these simplifying assumptions were only used for conceptual design and a more detailed non-linear model is presented in subsection 7.4.2 based on experimental data. These simulations included the effects of both air pressure (out-of-plane) and centrifugal force (in-plane). Centrifugal force was calculated for a adaptive section at the tip of a rotor similar to the V-22 *Osprey*, with a 11.6 m (38.08 ft) diameter rotor spinning at 330 RPM. In order to simplify analysis, discrete air pressure values were chosen that were generally representative of the range of pressures seen over the top and bottom of the rotor airfoil at its tip [118]. For this section, the chosen pressures (which represent the net pressure on the airfoil surface) ranged from -82.7 kPa (-12 psi) to 41.4 kPa (6 psi).

A summary of the design analysis results is provided in Figure 7.8. The "deflection limit" was defined by rotor blade manufacturing tolerances. That is, it was desired that the skin deflect no more under aerodynamic loading than what is an allowable manufacturing deviation from the nominal shape, in this case set to be 0.635 mm (0.025 inches). It can be seen here that, as expected, maximum out-of-plane deflection decreases with increased skin thickness and stiffness. Additionally, it appears that pre-straining the skin, i.e., installing it with a bias strain, will further decrease the maximum deflections. In order to minimize overall skin deflection, the

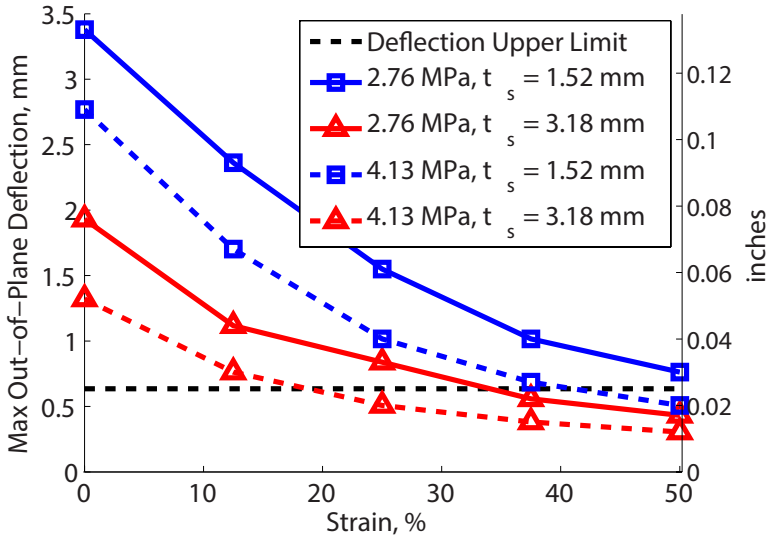

Figure 7.8: FEM simulated out-of-plane deflection results for EMC skin design.

design chosen was the skin with the least pre-strain required to satisfy the allowable deflection limit, which is a skin with an elastic modulus of 4.14 MPa (600 psi) and overall thickness of 3.18 mm (0.125 inches), with approximately 20% pre-strain. These parameters were chosen under the assumption that the morphing blade tips will require tight out-of-plane deflection tolerances for aerodynamic fidelity, and it should be noted that the purpose of this preliminary design was basic sizing and material selection for the skin. Actual material properties for polyurethane are highly non-linear and were not available *a priori* for our candidate materials, and thus a higher fidelity FEM model is required to make specific predictions of out-of-plane and in-plane performance.

7.4.2 EMC Detailed Design and Testing

Following completion of the preliminary EMC skin design, material samples were used to fabricate test specimens for design validation. Also, it was known that

the stress-strain behavior of the actual polyurethane used would not be linear, so a conservative design was preferred. Two candidate polyurethanes, with a 70 Shore A hardness and 80 Shore A hardness, respectively, were manufactured into EMC skin test articles. Three samples of each candidate skin were tested and results are shown in Figure 7.9. It can be seen that the stress-strain profile for these two skins is greater than the 4.14 MPa (600 psi) modulus "Design Selection" line described in subsection 7.4.1, indicating that these satisfy and exceed the minimum stiffness requirement. The 70 Shore A material has twice the required stiffness while the 80 Shore A material has nearly four times the requirement at the worst-case condition with 20% strain. With both of these skin formulations exceeding the stiffness requirement, relaxation and strain rate tests were conducted to better identify which was the leading candidate for further development, with the final result of the 70 Shore A material being selected for integration in the system due to its lower in-plane actuation requirements.

With the skin material selected, and experimental stress versus strain data available, a higher fidelity FEM simulation was conducted in order to predict skin out-of-plane performance. The skin was modeled as a hyper-elastic material using a two-constant Mooney-Rivlin formulation fit to the data shown in Figure 7.9. Additionally, an iterative large displacement method was used to ensure the applied pressure loads updated as the skin was stretched. An example of a FEM result in its deformed shape can be seen in Figure 7.10, which shows a unit cell undergoing 100% strain and subjected to a normal pressure on its top surface. The color gradient shown describes the vertical displacement of the skin, which corresponds to the

out-of-plane deflection of the airfoil. Due to Poisson's effect, as the skin stretches, it necessarily becomes thinner in the thickness direction, which causes the vertical deflection at the rib attachment points to be non-zero.

Strains from 0% to 100% were simulated for a variety of pressure conditions and maximum out-of-plane deflections were tabulated. Figure 7.11 depicts what is being called the "ripple deflections," that is, the deflection difference between the skin deflection at the rib and the overall maximum deflection, where a positive deflection is defined as into the airfoil. Negative pressures correspond to conditions on the top surface of the airfoil where there is a total differential pressure that pushes the skin outwards. It is clear that as the skin is strained, it tends to deflect into the airfoil, or in the positive direction. For the simulated negative pressures, -82.7 kPa (-12 psi) and -41.4 kPa (-6 psi), this actually reduces the overall deflection, moving it more towards zero. However, for the 0 kPa and 41.4 kPa (6 psi) case, the overall deflection worsens with increased strain. This trend can be explained by considering the strain softening behavior of the material, as seen in Figure 7.9, as well as the fact that the skin area increases proportionally with strain.

7.4.3 EMC Bond Strength Testing

Test specimens, consisting of polyurethane EMC skin samples bonded to titanium bars, were also prepared to evaluate various bonding agents. The strength and performance of the bond-layer between the EMC and the titanum substructure is vital to the success of the final morphing concept, as de-bonding would initiate

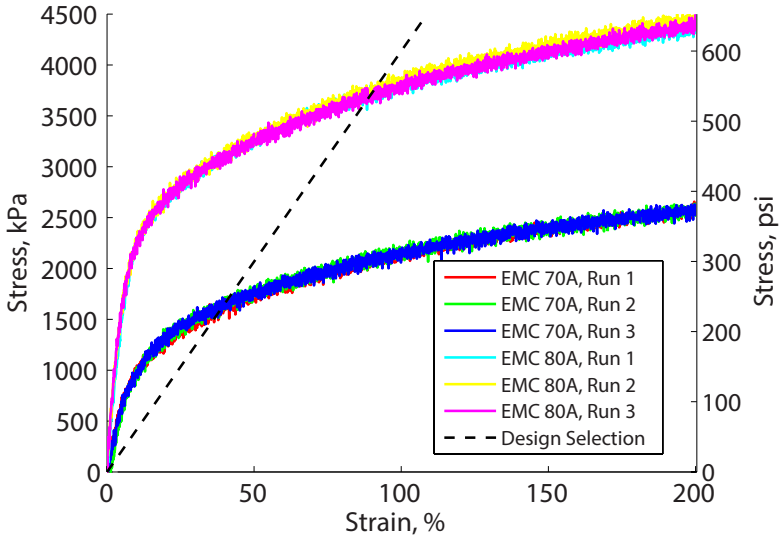

Figure 7.9: EMC skin test data compared with design stiffness.

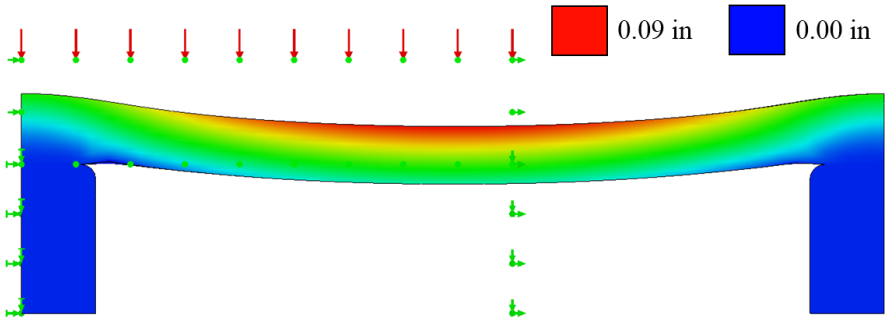

Figure 7.10: FEM simulation of candidate EMC skin undergoing 100% strain with a 82.7 kPa vertical pressure distribution.

a catastrophic failure. In-plane bonding strength was evaluated with lap shear testing and out-of-plane bonding strength was evaluated with peel testing. Results of lap shear testing are presented in Figure 7.12a, where it can be seen that the Chemlok adhesive appears to have the most strength, except for one outlying test that failed to reach 100%. The most consistent performing adhesive here is the Lord 206, which is an acrylic two-part mixture. Peel test results for 0% in-plane strain are shown in Figure 7.12b, where the Lord 7542 is strongest and the Lord

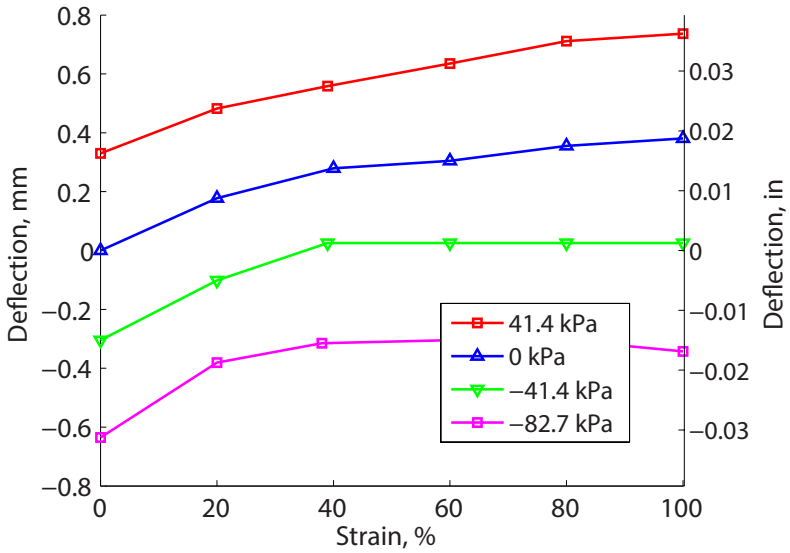

Figure 7.11: FEM simulated ripple deflections (difference in deflection between rib and maximum deflection location) for 70 Shore A EMC skin, positive deflection is out of the airfoil.

206 is weakest. It should be noted, however, that all three bonding materials meet the out-of-plane requirement, 0.635 mm (0.025 inches) of displacement, with plenty of margin. Despite the Lord 206 being weakest among the three tested in peel, it performed most consistently and satisfied the design goals, and it also performed most consistently in lap shear, again satisfying the design goals. Thus, the Lord 206 was chosen as the leading candidate for the bonding material.

7.5 Skin and Core Integration

With a core structure, skin material, and bonding material selected, the final coupon evaluations integrated all three components together. Testing took place on test specimens consisting of EMC skin bonded to both a cast titanium core and an EDM titanium core. A number of different tests were performed on each, including

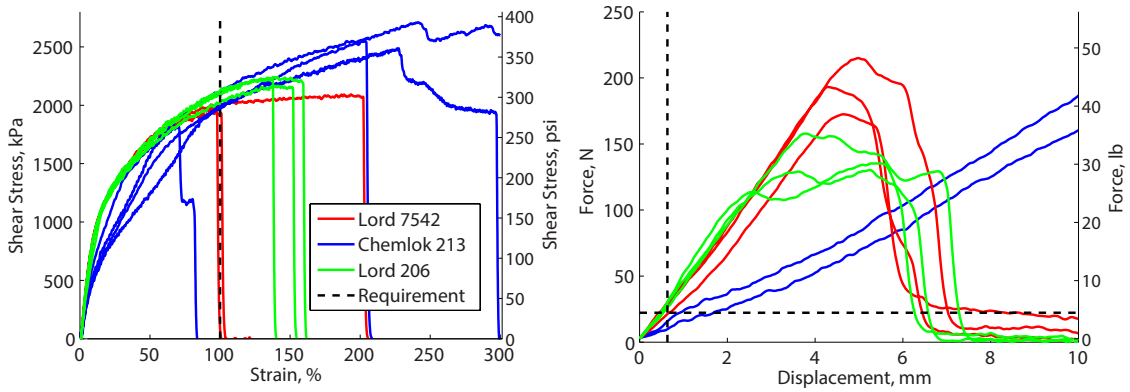

(a) Lap shear for in-plane (b) Out-of-plane peel for 0% in-plane strain

Figure 7.12: Results of EMC to titanium bonding evaluations.

incremental loading and unloading (from 25%, 50%, 75%, and 100%), and direct 0% to 100% cycling. Both samples completed all tests without failure and the general test setup, as well as data, is shown in Figure 7.13 for the EDM core. All tests were performed quasi-statically, at strain rates low enough that viscoelastic damping effects of the elastomer could be neglected.

A break-in cycle, first seen in EMC tests alone was again present in the integrated coupon tests, which was to be expected since a large portion of the integrated stiffness of these coupon samples is directly attributed to the EMC skin, which is an order of magnitude stiffer than the core. This break-in cycle is due to the strain-softening behavior of polyurethane elastomers. The effect is proportional to the magnitude of the applied strain, and is semi-permanent once the material has been stretched to a given strain for the first time. The incremental loading was done out of an abundance of caution, and is not necessary for the skin in general. Note the four incremental loading cycles in Figure 7.13b that highlight the break-in cycle, and the subsequent three tests that all exhibit very similar stress-strain relationships.

Repeated cycling was also performed on the integrated EDM coupon, where two separate tests of 50 successive 0% to 100% cycles were run. Figure 7.14a displays the stress versus strain curves for the first 50 cycles, where the break-in cycle is again present, but as shown in Figure 7.14b, only a small reduction in the first cycle of each is evident, rather than the large reduction that was expected from testing of the EMC skin samples alone. This could be due to interaction between the skin and core at each of the bonded ribs, but will require further examination in the future.

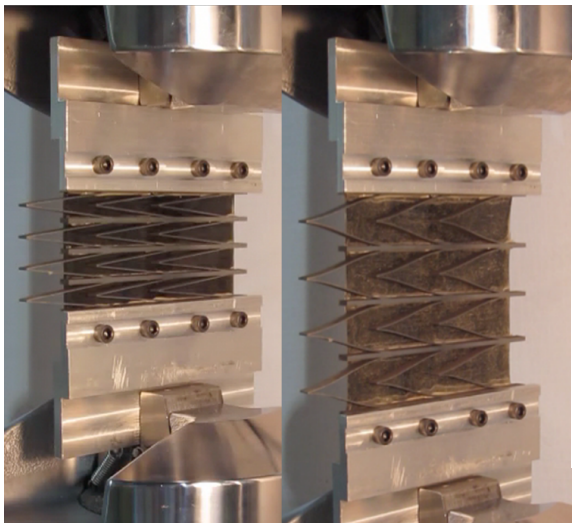

(a) Test setup

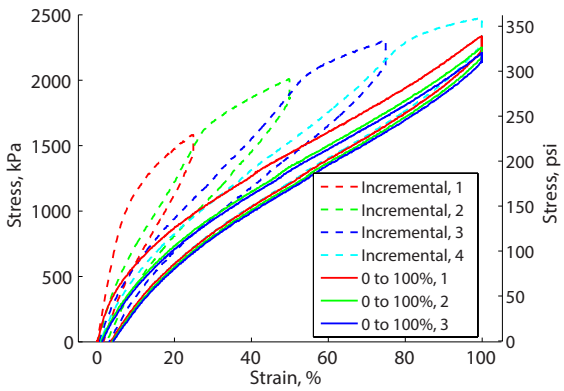

(b) Test data

Figure 7.13: Integrated coupon testing with EDM core.

7.6 Morphing Structure Optimization

With the structure, skin material, and bonding method determined, an optimization was formulated that attempted to minimize the mass of the entire morphing system while tuning it to self-actuate under centrifugal loading. Recall (from subsection 7.3.1) that in this context, self-actuation refers to each morphing row of

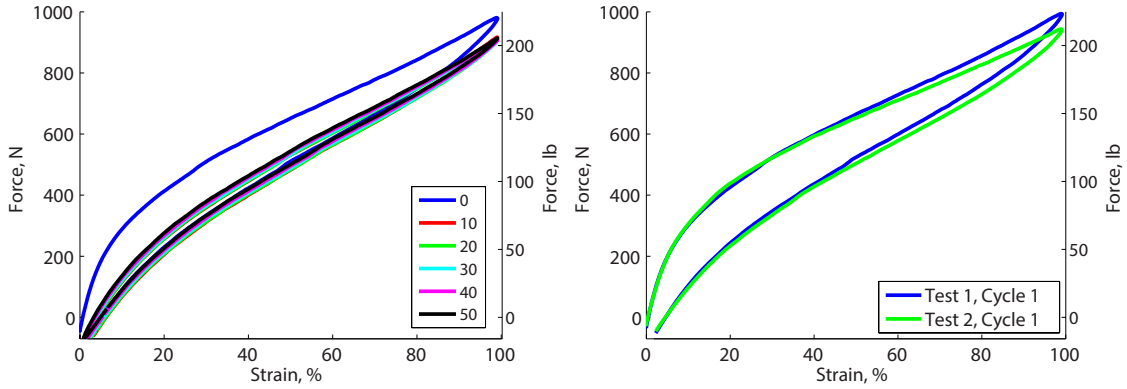

(a) First 50 cycles (b) Initial cycle of each 50-cycle test

Figure 7.14: Repeated cycling of integrated coupon with EDM core.

skin/spring elements deflecting evenly under the induced centrifugal acceleration (at the candidate rotor's RPM) so the rib elements would have uniform spacing at double their resting width to evenly distribute 100% strain in the skin along the entire adaptive span section. With this approach, the inertial forces present in the rotating environment would dominate and an actuation system would not be needed during extension, other than to guide the timing and synchronization of deployment.

7.6.1 Mass minimization using a Genetic Algorithm

During preliminary optimization attempts, it became clear that the final optimum was highly dependent on the user supplied initial condition, i.e., the design space contained many local minima, and so a gradient based approach was not ideal for finding a global minimum mass solution. To address this deficiency, a genetic algorithm (GA) theoretically capable of searching the entire design space was used for this formulation.

7.6.1.1 GA Problem Formulation

The optimization can be formally represented as

$$\begin{aligned} \underset{X}{\text{minimize}}\ & f(X) = \frac{M_{total}(X)}{M_o} \\ \text{subject to}\ & g_k(X) \leq 0 \quad \text{for } k = 1, \ldots, 3 \\ & h(X) = 0 \\ & 0 \leq\ X \leq 1. \end{aligned} \tag{7.2}$$

The design variables, X, are non-dimensional and define the dimensional variables so that they are forced to monotonically increase/decrease. As noted in Section 7.3.1, cell stiffness will tend to decrease as span station increases due to the decreasing outboard mass it must react against. Examining the expression for the stiffness of a morphing cell, Equation (7.1), it is clear that stiffness increases proportionally to t^3, and decreases proportionally to c. Recalling the definitions of cell geometry given in Figure 7.3, l can be cast in terms of θ and cell height, h, as

$$l = \frac{h}{2\sin\theta}. \tag{7.3}$$

Plugging this result into Equation (7.1) and simplifying shows that the cell stiffness increases proportionally to $\sin^3\theta/\cos^2\theta$ for $0 \geq \theta \geq \pi/2$.

This means that as span station increases from inboard to outboard on the blade, t and θ should decrease monotonically, and c should increase monotonically. To enforce this condition, a formulation for the design variables was implemented

and is described below. That is,

$$\begin{aligned} t_1 &= X_1 \left((t_U - t_L) + t_l \right) \\ t_i &= t_{i-1} + X_i \Delta t \quad \text{for } i = 2, \ldots, N \end{aligned} \tag{7.4}$$

where t_U and t_L correspond to the upper and lower bounds imposed on t, and Δt is the maximum step t can take from one rib section to another, here set as

$$\Delta t = \frac{t_U - t_L}{N} \tag{7.5}$$

where N is the number of rib sections. This enforces a lower bound on t, ensuring that it cannot be lower than t_L. The upper bounds are enforced by an inequality constraint. The spring element angle θ is defined similarly to t, so

$$\begin{aligned} \theta_1 &= X_{N+1} \left((\theta_U - \theta_L) + \theta_l \right) \\ \theta_i &= \theta_{i-1} + X_{N+i} \Delta \theta \quad \text{for } i = 2, \ldots, N \end{aligned} \tag{7.6}$$

where θ_U, θ_L, and $\Delta\theta$ are defined analogously to their counterparts above. The cell spacing, c, is defined similarly with the exception that it must decrease as span station increases. To this end, a temporary value ξ is defined as

$$\begin{aligned} \xi_1 &= X_{2N+1} \left((c_U - c_L) + c_l \right) \\ \xi_i &= \xi_{i-1} + X_{2N+i} \Delta c \quad \text{for } i = 2, \ldots, N \end{aligned} \tag{7.7}$$

where c_U, c_L, and Δc are defined analogously to their counterparts above. ξ increases

monotonically as a function of i, and so to get c, the order is simply reversed. This gives,

$$c_i = \xi_{(N+1)-i} \quad \text{for} \quad i = 1, \ldots, N. \tag{7.8}$$

An additional design variable corresponding to a variable mass outboard of the morphing section was also added when it was discovered that the outer-most cells could not strain completely under centrifugal acceleration alone. This final design variable, X_{3N+1}, scales the outboard mass as

$$M_{out} = X_{3N+1}(M_U - M_L) + M_L \tag{7.9}$$

where M_L and M_U define the lower and upper limits on the mass value. The dimensional upper and lower bounds used in this optimization are given in Table 7.1.

Table 7.1: Upper and lower bounds on design variables

Variable	Lower Bound	Upper Bound
θ, deg	10	60
c, mm (inches)	12.7 (0.5)	76.2 (3)
t, mm (inches)	0.635 (0.025)	2.54 (0.100)
M_{out}, kg (lb)	0	2.268 (5)

The objective function to be minimized, $f(X)$, is simply the total mass of the system normalized by an arbitrary value, here chosen to be 1 kg (2.23 lb). The mass is calculated by multiplying the volume of the various structures by their respective

material densities. Thus,

$$M_{total} = \rho_{structure}\left(V_{ribs} + V_{spring}\right) + \rho_{skin}V_{skin} \tag{7.10}$$

where

$$V_{ribs} = Nl_{airfoil}bt_{rib}. \tag{7.11}$$

Here, V_{ribs} is the total rib volume, $l_{airfoil}$ is the length of the perimeter of the chosen airfoil, b is the depth of the ribs normal to the surface of the airfoil, and t_{rib} is the spanwise thickness of the ribs. The total volume of the spring elements V_{spring} is defined as

$$V_{spring} = \sum_{i=1}^{N} 2bl_i t_i \frac{l_{airfoil}}{c_i} \tag{7.12}$$

where l_i, t_i, and c_i are the spring element properties for the ith span station. Finally, V_{skin} is the total skin volume and is defined as

$$V_{skin} = (Nh)l_{airfoil}t_{skin} \tag{7.13}$$

where h is the spanwise height of one morphing cell, the quantity Nh defines the total spanwise length of the active section, and t_{skin} is the skin thickness.

The inequality constraints, $g_1(X)$ through $g_3(X)$, enforce the upper bounds on the dimensional design variables, t, θ, and c. The equality constraint, $h(X)$, enforces the requirement that each cell exhibits 100% strain under centrifugal force (CF). It

is calculated as

$$h(X) = \sum_{i=1}^{N} \left| \frac{\epsilon_{i,actual} - \epsilon_{i,desired}}{\epsilon_{norm}} \right| \tag{7.14}$$

where $\epsilon_{i,actual}$ is the ith cell's actual strain, $\epsilon_{i,desired}$ is the desired strain, and ϵ_{norm} is a normalizing value. Recognizing that $\epsilon_{i,desired} = 1$, and choosing $\epsilon_{norm} = 1$, Equation (7.14) can be simplified to

$$h(X) = \sum_{i=1}^{N} \left| \epsilon_{i,actual} - 1 \right| . \tag{7.15}$$

Skin force was calculated by fitting a spline to experimental skin elongation stress versus strain curves for a 3.175 mm (0.125 inch) thickness 70 Shore A hardness polyurethane and carbon fiber skin (as described in Section 7.4.2). The experimental data used, as well as the spline and spline control points, are shown in Figure 7.15. Because skin force is dependent on the strain, $\epsilon_{i,actual}$ is calculated using fixed-point iteration by assuming a starting position for all of the cells (usually their resting position), subjecting the entire structure to CF, and then calculating the resulting deflection. The deflected cell position is then used as the new initial condition, and the process is repeated until the difference between the previous cell positions and the current cell positions is below some tolerance.

7.6.1.2 GA Results

A genetic algorithm (GA) optimization package available through the MATLAB® global optimization toolbox was used for the present work. The optimization described above was run ten times and the results recorded and compared. Each run

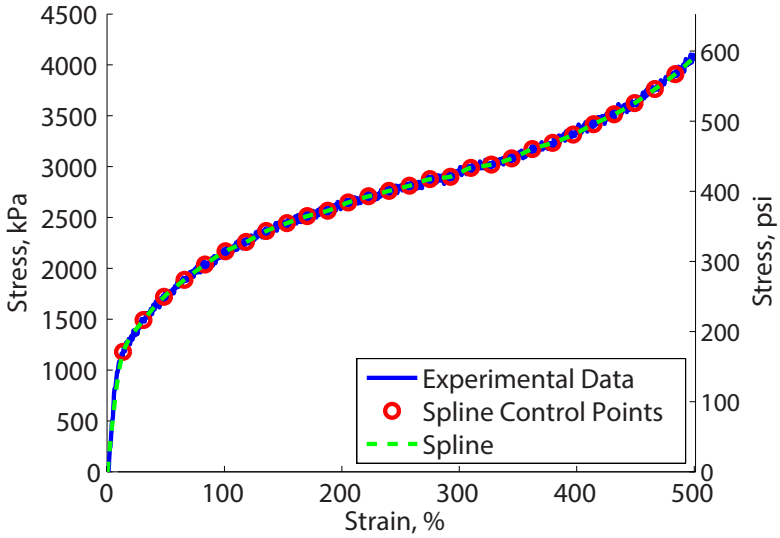

Figure 7.15: A spline fit to 70 Shore A hardness polyurethane EMC skin elongation test data.

had a population of 25 individuals, and was run until a convergence criteria was met, the maximum generation limit (300 generations) was reached, or a stall generation limit (40 generations without a change in the objective function) was reached. Only seven of the ten runs produced results that satisfied the strain equality constraint close enough to be useful. Additionally, the varied nature of the results indicate that the GA, as configured, did not effectively search the entire design space and none of the designs represented a true optimum, where all constraints were completely satisfied and mass was minimized. Instead, they reached either maximum generation limits or stall generation limits that caused the run to terminate. In general, a correctly tuned GA should be able to arrive at a global optimum solution [137], but in this case the decision was made to not increase these limits or further tune the GA because of time constraints, and because the results were deemed to be sufficient for the present work. Future work could include a more in-depth investigation into

this optimization problem, including trying a much larger, higher-population run that may be able to find the global optimum more efficiently [138].

Figure 7.16 depicts the optimized design variables of the seven useful runs as a function of span station number, with span station increasing from inboard to outboard on the rotor blade. As expected, the design variables now change monotonically. The minimum mass and minimum strain error ($h(X)$ closest to zero) solution is highlighted in red in this figure, as well as all following figures relating to this solution set. Figure 7.17a depicts how the total force at each span location changes as a function of span station, where skin force is defined as the tension force in the skin, spring force is defined as the axial force due to the stiffness of the spring elements, and inertial force is the force due to the centrifugal acceleration on the mass outboard of the given span station. For the system to be in equilibrium, the skin and spring forces must add up to the inertial force (which is obviously true here). Figure 7.17b depicts the strain at each span location for each design, with the desired strain depicted by the horizontal black dashed line. There is a general trend of more error at the inner-most and outer-most span stations. It is clear from this plot that, although the designs get to within about 10% of the desired cell strain, work could be done to improve the designs.

Figure 7.18 shows the mass breakdown of all ten GA runs. The designs highlighted in gray are the three bad runs, and the design highlighted in red is the lowest weight and strain error solution (from the good runs). Additionally, each bar is broken up into an upper and a lower component. The upper section corresponds to the outboard mass design variable, and the lower segment represents the combined

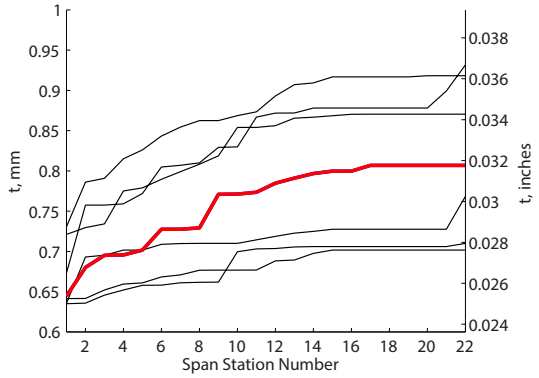

(a) Spring element thickness, t

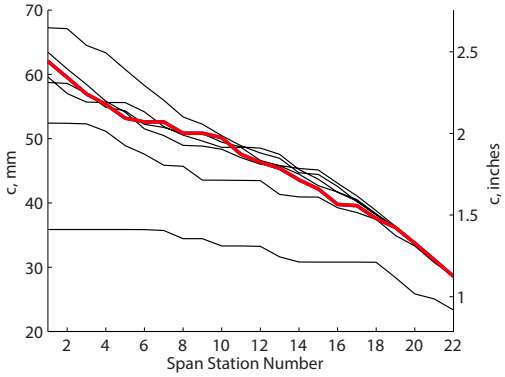

(b) Spring element cell width, c

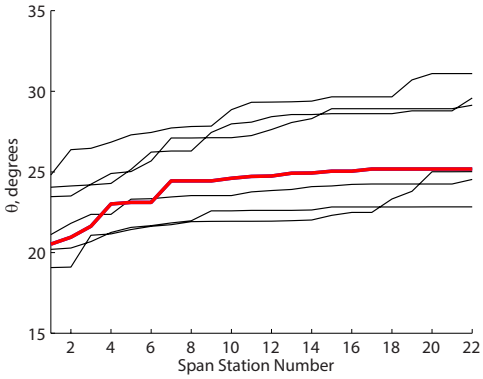

(c) Spring element angle, θ

Figure 7.16: Design variable results seven viable runs of the GA.

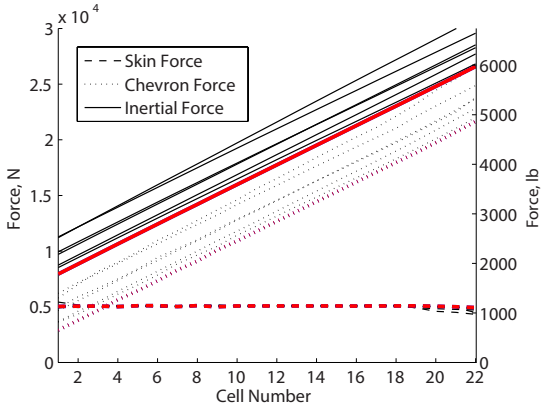

(a) Total force at each span station.

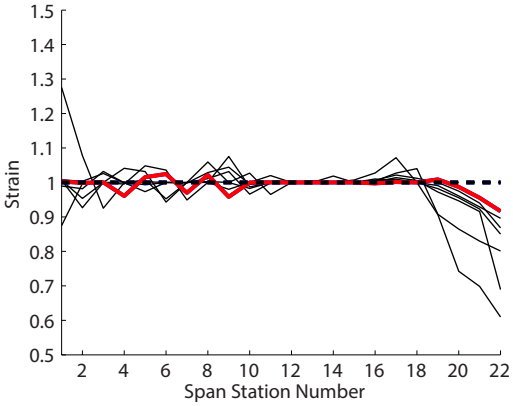

(b) Strain at each span station.

Figure 7.17: Forces and strain at each span station for all GA optimum designs.

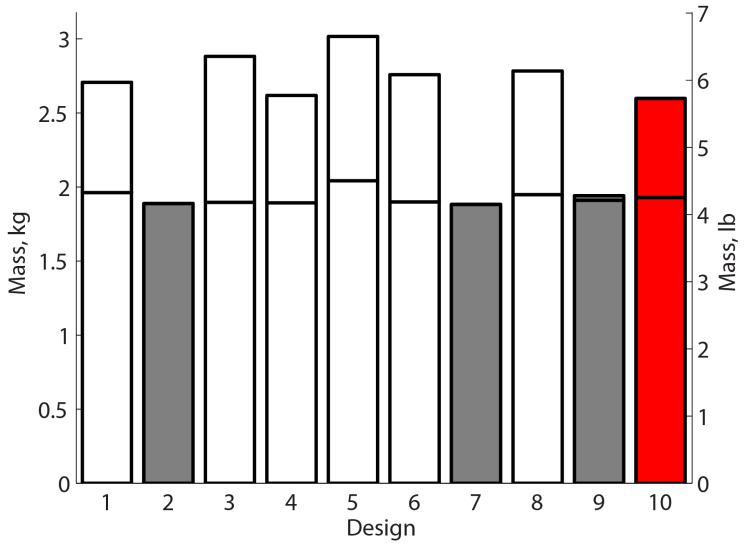

Figure 7.18: Total mass for each design.

mass of the ribs, skin, and springs, respectively.

7.6.2 Strain Matching Using a Gradient Based Optimization

As noted in the previous section, while the genetic algorithm approach produced usable designs, the strain at each span station varied by about ± 10% from the desired value. Initial optimization attempts (not described in this paper), however, showed that a gradient based approach produced designs that matched the desired strain conditions well, but did not find global mass minima because they became trapped at local solutions. In order to take advantage of the perceived strengths of both of these methods for this application, additional gradient based optimization was performed that used the final designs from the GA runs (Figure 7.16) as its initial conditions.

7.6.2.1 Optimization Formulation

This new gradient based optimization can be represented as

$$\begin{aligned} \underset{X}{\text{minimize}}\ & f(X) = \sum_{i=1}^{N} |\epsilon_{i,actual} - 1| \quad \text{for } i = 1, \ldots, N \\ \text{subject to}\ & g_k(X) \leq 0 \quad \text{for } k = 1, \ldots, 3 \\ & 0 \leq X \leq 1 \end{aligned} \tag{7.16}$$

where the objective function, $f(X)$, is now designed to minimize the difference between the desired strain at each span station and the actual strain. The design variables, X, and inequality constraints, $g_k(X)$, are defined identically to their counterparts in Section 7.6.1.1. The initial conditions were taken from the seven final GA designs.

7.6.2.2 Results

Figure 7.19 shows the dimensional design variables for the converged optimums, and Figure 7.20 gives a planform view of the first (outermost) and twenty-second (innermost) rows. For 7.19, and all figures relating to the current optimization, the red line represents the lowest mass design, and the blue line is the minimum strain error design. The design variables for the minimum mass design are also presented in Table 7.2.Note that, compared to the genetic algorithm results, the design variables seem to increase/decrease in a much smoother fashion. Force as a function of span station is given in Figure 7.21a, and cell strain as a function of span station is given in Figure 7.21b. It is clear that all of the converged designs now fall on the desired

strain line with very little deviation. The minimum mass solution (Figure 7.22) has now changed to Design 4, but the magnitude of the weight has remained very close to its value from the genetic algorithm optimization. The original three designs that did not conform to the strain requirements are again included (in grey) for comparison purposes. Note that the outboard mass is generally 1/3 to 1/4 of the total mass of the active section, but it does not necessarily have to add mass to the rotor system as a whole. For example, consider a case where the morphing section is not located at the tip of the rotor, but instead is moved inboard by a certain amount (while maintaining a constant rotor radius) to put the correct amount of mass outboard. In this scenario, the only weight added to the blade from the morphing tip section would be the difference between the combined skin, rib, spring, and actuation system weight and the normal blade section it replaced. These results suggest that a useful approach for an optimization like this is to get near to a global optimum solution using the computationally intensive genetic algorithm with minimizing mass as the objective, and then passing those final solutions to gradient based optimizer as its initial condition.

7.7 Conclusions

This work has discussed the results from the conceptual design phase for a variable diameter morphing helicopter blade. Two major technologies were described: an elastomer-matrix-composite (EMC) skin and a titanium zero-Poisson honeycomb-like morphing core structure. Two techniques were considered for manufacturing the

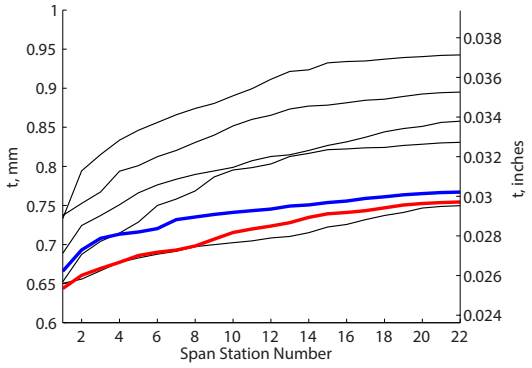

(a) Spring element thickness, t

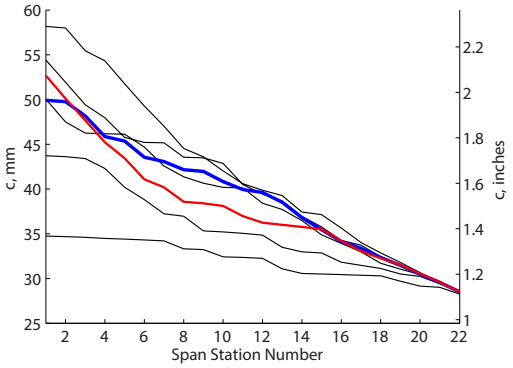

(b) Spring element cell width, c

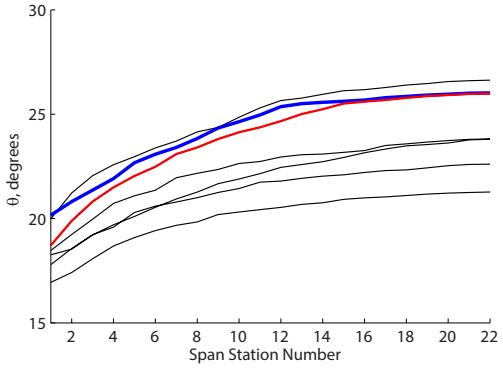

(c) Spring element angle, θ

Figure 7.19: Dimensional design variables for the gradient based optimization.

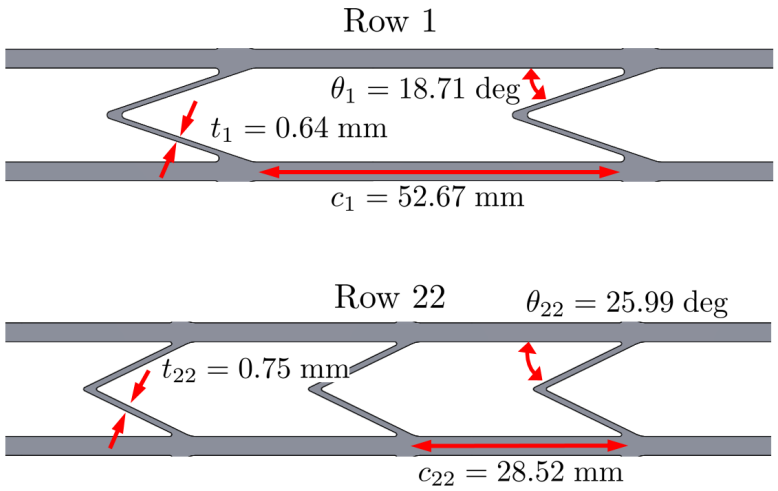

Figure 7.20: Close-up planform view of the first (outermost) and twenty-second (innermost) morphing rows.

Table 7.2: Design variables for minimum mass design.

	Row Number	t (mm)	c (mm)	θ (degrees)
Inboard	1	0.644	52.67	18.71
	2	0.661	50.10	19.89
	3	0.669	47.66	20.82
	4	0.677	45.22	21.49
	5	0.686	43.43	22.04
	6	0.690	41.08	22.48
	7	0.693	40.18	23.09
	8	0.698	38.57	23.41
	9	0.707	38.40	23.81
	10	0.715	38.11	24.14
	11	0.720	36.96	24.37
	12	0.724	36.24	24.67
	13	0.728	36.00	25.01
	14	0.735	35.76	25.24
	15	0.739	35.50	25.51
	16	0.741	34.19	25.60
	17	0.743	33.05	25.68
	18	0.747	32.27	25.78
	19	0.751	31.53	25.87
	20	0.752	30.54	25.92
	21	0.754	29.59	25.97
Outboard	22	0.755	28.52	25.99

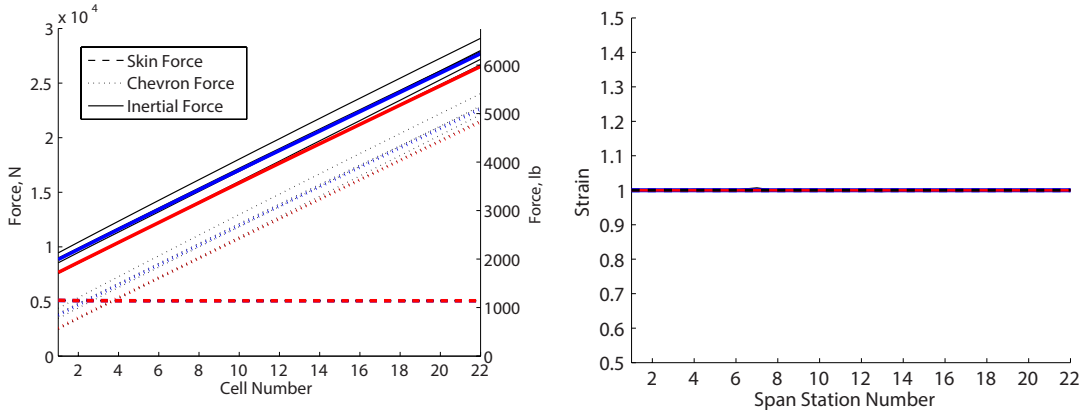

(a) Total force at each span station

(b) Strain at each span station

Figure 7.21: Forces and strain at each span station for all gradient based optimum design.

complex morphing core structure: expensive electro-discharge machining (EDM) and relatively cheap investment casting. Test articles were produced using both techniques, and both showed good agreement with predicted behavior when characterized. While both techniques were capable of producing viable test articles, it is currently unclear if investment casting could be flight certified and future work is needed to determine the scalability and reliability of this process for critical aerospace applications. The EMC skin was designed using linear and non-linear FEM to ensure the in-plane stiffness and out-of-plane deflection design goals were met. The final EMC design utilized a 70 Shore A hardness polyurethane elastomer, sandwiching a layer of uni-directional carbon fiber, and it was tested in elongation, lap shear, and peel. Testing was also done on an integrated skin-core sample, which was stretched to 100% elongation 50 times, and showed no signs of failure, motivating future work into maturing this promising technology. The entire morphing tip system (morphing core structure and EMC skin) was then designed to deploy under centrifugal loading. A genetic algorithm (GA) was first used to search the entire design space for minimum mass designs, and then the GA optima were fed to a gradient based optimizer to more effectively match the stiffness design goals. The result was a light final design which would deploy as desired under the given centrifugal loads.

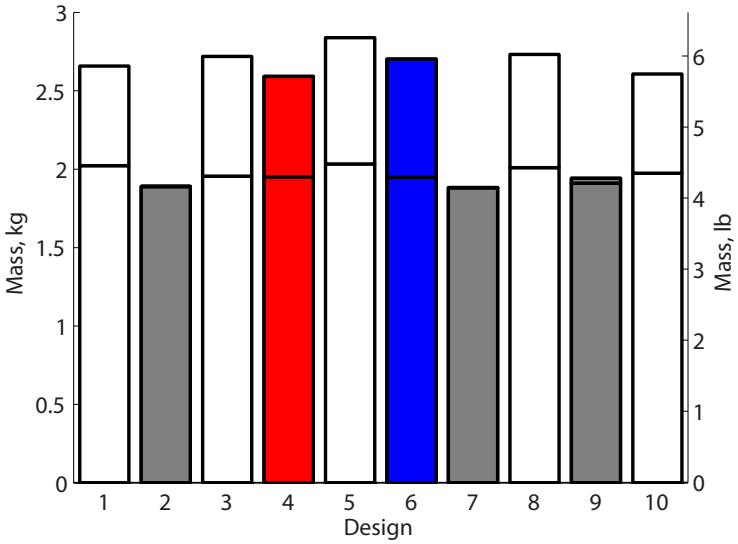

Figure 7.22: Total mass for each gradient based optimum design.

Chapter 8: Conclusions

8.1 Summary of Work and Key Conclusions

In this work, significant contributions were made towards rotorcraft morphing mechanisms and actuators. First, a PAM-actuated chordwise trailing edge flap system for rotorcraft was developed and optimized using mechanism dimensions and PAM bias contraction as design variables. This system was built and bench-top tested which proved, in closed-loop testing, that it was capable of following control signals typical of both primary rotorcraft control, and vibration/noise reduction. A conformal morphing system for a variable diameter rotor was also developed. First, a prototype span-extending wing was constructed as a proof-of-concept and wind tunnel tested. This validated design was then matured for implementation on a tilt-rotor aircraft using an optimized centrifugal actuation scheme. The system was tested in coupon form and exhibited the desired 100% area change.

Specific conclusions from each major section are discussed below.

8.1.1 PAM-Actuated Trailing Edge Flaps

8.1.1.1 Low Frequency Antagonistic PAM Actuation

Initial PAM antagonistic actuator design focused on a miniature PAM actuator capable of replacing an electric servo actuator motor. Key accomplishments included the development of a fabrication procedure for miniature PAM actuators, the design of a novel mechanism to complement the load-stroke profile of the selected PAM actuators, and a comparison of prototype actuator performance to competing servo motor technologies. The developed packaged PAM actuator exhibited twice the specific torque and comparable torque density to that of a commercial off-the-shelf servo actuator having comparable dynamic response in the frequency range of 10–20 Hz. The PAM device also had an available static torque that was an order of magnitude higher than that of the electric servo actuator motor. When comparing the PAM actuator to a commercial servo and rotary actuator with comparable maximum torque, the performance metrics of the PAM system were shown to be superior when normalized with respect to both mass and volume. This highlights the potential that these miniature PAM devices have for small-scale actuator applications, especially in systems where high quasi-static torque is required. Aerospace applications that could benefit from PAM actuators include deploying aerodynamic flaps and quasi-statically changing configurations on morphing aircraft. For such applications, these results show that a PAM actuation system would have both lighter weight and smaller volume than a servo with comparable maximum torque output. However, a different

approach was deemed necessary to achieve the high dynamic deflections necessary for rotorcraft TEF control.

8.1.1.2 PAM Bias and Pressure

Two methods for increasing the available torque for an antagonistic, bi-directional, rotational actuator using pneumatic artificial muscles (PAMs) were discussed. The first method was to intelligently choose the kinematic mechanism that connects the PAMs to the point of rotation. It was found that in all cases, an offset lever configuration will produce superior results to a conventional lever or pulley configuration in terms of output torque and range of motion. The second method involved including bias in the design, in the form of bias contraction and bias pressure. It was shown that for better performance, bias pressure should be kept as low as possible, while maintaining requirements for off-state hinge stiffness. The role of bias contraction, however, was found to be highly coupled to the desired loading (purpose) of the system, as well as the geometry of the offset lever mechanism. It was shown that an optimum arrangement can be found parametrically for a simplified case that improved maximum deflection angle by nearly 50%, and suggested that a numerical optimization technique could be used to solve the full optimization problem. The PAM bias model was also validated experimentally with a "worst case" system that would typically have very poor performance. Through the inclusion of PAM bias, the maximum deflection of the system was increased by approximately 300% and also matched well with model predictions.

8.1.1.3 Chordwise TEF Optimization and Testing

An approach for designing a trailing edge flap system for rotor blades with PAM actuators configured chordwise and co-located outboard with the flap was discussed. The inherent challenges associated with such a design were overcome through the inclusion and optimization of bias contraction and mechanism dimensions. The PAM actuation system was shown to be suitable for both primary control ($\pm$10 degrees at 1-3/rev) and vibration and noise reduction ($\pm$5 degrees up to 10/rev) at the highest simulated loading conditions through open-loop testing. Additionally, the importance of properly optimizing the PAM system and operating it at the designed pressure and mechanism geometry was highlighted. Closed-loop testing using a previously validated control scheme provided even further evidence for the suitability of the designed PAM actuation system for primary and vibration/noise control in rotorcraft. Measurements showed accurate tracking of $\pm$5 degree sine waves out to 7/rev and $\pm$10 degree sine waves out to 3/rev. Closed-loop performance was shown to be limited by the pneumatic system. Complex waveforms comprised of 1/rev and 3-5/rev components were also tested and good tracking capability was shown, indicating that the optimized system is capable of following arbitrary complex signals at frequencies needed for helicopter primary control and vibration reduction. Overall, this work showed that a chordwise PAM-actuated TEF can satisfy the performance requirements associated with primary rotor control, vibration reduction, and noise mitigation, thereby highlighting PAM actuators as a feasible technology for this application.

8.1.2 Conformal Variable Diameter Rotor Morphing

8.1.2.1 System Level Benefits of a VDRS

A conceptual variable diameter tilt-rotor, designed and sized in the NDARC design code, was presented. Both the maximum allowable diameter morphing and the added weight to the rotor were varied with the intent of investigating the system level benefits (improved weight, fuel use, cost) associated with a variable diameter rotor system. Results showed that for a 0% increase in rotor weight due to the addition of the morphing system, diameter morphing reduced vehicle gross and component weights, as well as mission fuel weight. As the rotor weight penalty for morphing was increased, the entire system saw a corresponding increase in weight. For these increased rotor weight conditions, diameter morphing was again able to reduce total system weight back to, or lower than, the baseline design. At very high levels of morphing, however, (large reductions in rotor radius for cruise) weight was seen to drastically increase. This was traced to the rotor approaching stalled conditions during cruise due to increased blade loading. A conceptual approach for estimating cruise blade loading for a variable diameter or variable speed tilt-rotor was then presented. In general, this work showed that even for fairly substantial increases in rotor weight, variable diameter morphing can have a system wide benefit in the form of reduced gross weight and reduced fuel weight.

8.1.2.2 Prototype Variable-Span Wing Development

This work explored a span morphing wing surface with the goal of producing up to a 100% conformal change morphing section wing area. Features included a silicone elastomer skin, which had embedded uni-directional carbon fibers to minimize Poisson's ratio effects and increase chordwise in-plane skin stiffness, and a morphing core substructure, which provided a Poisson's ratio of zero. The system was assembled as designed and demonstrated its ability to increase span by 100% while maintaining a constant chord. Wind tunnel tests were conducted at a maximum speed of 130 kph, at 0 degrees, 2 degrees, and 4 degrees angle-of-attack, and at 0%, 50%, and 100% extension. At each test point, image processing was used to determine the maximum out-of-plane deflection of the skin between ribs. Across all tests, the maximum discernible out-of-plane deflection was less than 0.5 mm. While successfully demonstrating the concept of variable-span (diameter on a rotorcraft) morphing, this system was not suitable for implementation in the rotating frame due to the strength of the constituent materials and the of the poor reliability process.

8.1.2.3 Development of a Quasi-Static Variable Diameter Rotor System

The two major technologies described in the development of the prototype variable-span wing were further matured to more aerospace-grade materials and processes. Two major technologies were described: an elastomer-matrix-composite (EMC) skin and a titanium zero-Poisson honeycomb-like morphing core structure. Two techniques were considered for manufacturing the complex morphing core struc-

ture: expensive electro-discharge machining (EDM) and relatively cheap investment casting. Test articles were produced using both techniques, and both showed good agreement with predicted behavior when experimentally characterized. While both techniques were capable of producing viable test articles, it is currently unclear if investment casting could be flight certified and future work is needed to determine the scalability and reliability of this process for critical aerospace applications. The EMC skin was designed using linear and non-linear FEM to ensure the in-plane stiffness and out-of-plane deflection design goals were met. The final EMC design utilized a 70 Shore A hardness polyurethane elastomer, sandwiching a layer of uni-directional carbon fiber, and it was tested in elongation, lap shear, and peel. Testing was also conducted on an integrated skin-core sample, which was stretched to 100% elongation 50 times, and showed no signs of failure, motivating future work into maturing this promising technology. The entire morphing tip system (morphing core structure and EMC skin) was then designed to deploy under centrifugal loading. A genetic algorithm (GA) was first used to search the entire design space for minimum mass designs, and then the GA optima were fed to a gradient based optimizer to more effectively match the stiffness design goals. The result was a lightweight final design that would deploy uniformly under the expected centrifugal loads.

8.2 Contributions to the Literature

8.2.1 PAM-Actuated Trailing Edge Flaps for Rotorcraft

Improved understanding of PAM bias contraction: The present research represents the first use of PAM bias contraction as a design variable in the literature. Previous studies had recognized that bias contraction has an effect on antagonistic PAM actuators. However, none had rigorously investigated the effect that bias contraction (or bias pressure) has on the performance of said actuators. An antagonistic PAM system was simulated using a simplified PAM force model, and the effect of bias contraction, bias pressure, and antagonistic mechanism geometry was studied, with the optimum configuration of these parameters being shown to be heavily dependent on loading condition [83]. This study was then used to numerically optimize a PAM-driven trailing edge flap system suitable for chordwise implementation in a helicopter blade, which had a smaller footprint than the previous state-of-the-art for PAM systems, but maintained similar control authority, suitable both primary and vibration/noise reduction tasks [105].

First rigorous comparison of PAM and electromechancial rotary actuators: A "sliding-T" mini-PAM antagonistic actuator was developed [63]. While this actuator was not suitable for trailing edge flap actuation, when comparing the PAM actuator to a commercial servo and rotary actuator with comparable maximum torque, the performance metrics of the PAM system were shown to be superior when normalized with respect to both mass and volume. This was the first study directly

comparing PAM and non-PAM rotary actuators, and highlights the potential that these miniature PAM devices have for small-scale actuator applications, especially in systems where high quasi-static torque is required.

8.2.2 Conformal Variable Diameter Rotor Morphing

Wind tunnel test of conformal morphing wing prototype: This research utilized a conformal variable diameter morphing technology comprised of a silicone elastomer matrix composite (EMC) skin and a zero-Poisson's ratio rapid-prototyped substructure to develop a variable-span wing capable of producing 100% conformal change in wing area. This was the first demonstration of a morphing wing doubling its span while maintaining a constant chord and remaining a viable airfoil surface during low speed wind tunnel testing [15] .

Matured morphing techonology for use on rotorcraft: The two major technologies described in the development of the prototype variable-span wing were further matured to more aerospace-grade materials and processes [107]. The final design consisted of a 70 Shore A hardness polyurethane, sandwiching a layer of unidirectional carbon fiber, and a investment cast titanium substructure. Additionally, the entire morphing tip system (morphing core structure and EMC skin) was then designed to deploy uniformly under centrifugal loading. A genetic algorithm (GA) was first used to search the entire design space for minimum mass designs, and then the GA optima were fed to a gradient based optimizer to more effectively match the stiffness design goals. The result was a lightweight conformal morphing system

which would deploy under representative centrifugal loads.

8.3 Suggestions for Future Work

8.3.1 PAM Antagonistic Actuation

While PAMs have been tested in the rotating environment [45], this previous work was conducted with the PAMs oriented spanwise in the blade, and at a much lower centrifugal acceleration than would be seen at the tip of a rotor blade. Therefore, whirl testing of a chordwise PAM system focusing on the relationship between centrifugal acceleration and PAM system performance would be an interesting follow-on to the present work. Additionally, there are currently no proportional pneumatic valves rated for operation in the rotating frame under the hundreds of g's seen near the tip of a rotor blade. A valve built specifically for the rotating frame, and for the high flow requirements of this application, would likely improve the performance of the actuator.

All PAM antagonistic system modeling performed in this work was quasi-static, and while the models were validated against experimental data, they were used for optimization purposes only. A more comprehensive and ultimately useful approach would be to model the antagonistic and pneumatic system dynamically so that the optimized mechanisms could be tested over a wider operational range than is easily testable on a bench-top setup, such as the dynamic and periodic loading environment of a true rotor blade. If well validated across a range of PAMs and mechanism geometries, this dynamic model could also be used in numerical optimizations.

8.3.2 Variable Diameter Morphing

A major drawback to the metallic morphing substructure described in Chapter 7 is the manufacturing difficulties inherent in making such a complex shape into a full airfoil. While both the EDM and investment casting processes discussed in that chapter would be capable of producing these shapes, they are likely either too expensive (EDM) or not precise enough (investment casting) to be feasible. Since this work was completed, however, there have been great advances in the field of metallic rapid prototyping, to the point where the prospect of simply printing full morphing wing tip structures does not seem out of the question. This would be very interesting to pursue, as it would also open the door to other types of conformal morphing using this same technology (twist, camber, chord, etc.).

The variable-span/diameter morphing technology was demonstrated in a wind tunnel test, and in bench-top coupon samples. FEM simulations were also performed to investigate how the structure, and skin in particular, would react under centrifugal loading. Whirl testing, first in a vacuum chamber, and then on an physical, perhaps scaled down, helicopter blade, is the next logical step to validate this technology and the tuned-stiffness optimization approach for uniform passive deployment.

Bibliography

[1] Silvestro Barbarino, Onur Bilgen, Rafic M. Ajaj, Michael I. Friswell, and Daniel J. Inman. A Review of Morphing Aircraft. *Journal of Intelligent Material Systems and Structures*, 22(9):823–877, August 2011.

[2] Terrence A. Weisshaar. Morphing Aircraft Systems: Historical Perspectives and Future Challenges. *Journal of Aircraft*, 50(2):337–353, March 2013.

[3] Srinivas Vasista, Liyong Tong, and K. C. Wong. Realization of Morphing Wings: A Multidisciplinary Challenge. *Journal of Aircraft*, 49(1):11–28, January 2012.

[4] Orville Wright and Wilbur Wright. Flying-machine, U.S. Patent 149,220. Filed: Mar. 23, 1903. Issued: May 22, 1906.

[5] Jason Bowman, Brian Sanders, and Terrance Weisshar. Evaluating the Impact of Morphing Technologies on Aircraft Performance. In *Proceedings of the 43rd AIAA/ASME/ASCE/AHS/ASC Structures, Structural Dynamics, and Materials Conference*, Denver, CO, April 2002.

[6] R. Pecora, F. Amoroso, and L. Lecce. Effectiveness of Wing Twist Morphing in Roll Control. *Journal of Aircraft*, 49(6):1666–1674, November 2012.

[7] Amin Moosavian, Fengfeng Xi, and Seyed M. Hashemi. Design and Motion Control of Fully Variable Morphing Wings. *Journal of Aircraft*, 50(4):1189–1201, July 2013.

[8] F. J. Perry, P. G. Wilby, and A. F. Jones. The BERP Rotor – How Does it Work, and What Has it Been Doing Lately? *Vertiflite*, 44:44–48, 1998.

[9] Jean Prieur and Wolf R. Splettstoesser. ERATO – An ONERA-DLR Cooperative Program on Aeroacoustic Rotor Optimisation. In *Proceedings of the 25th European Rotorcraft Forum*, Rome, Italy, September 1999.

[10] J. Gordon Leishman. *The Helicopter: Thinking Forward, Looking Back*. College park Press, College Park, MD, 2007.

[11] Friedrich K. Straub, Hieu T. Ngo, V. Anand, and David B. Domzalski. Development of a Piezoelectric Actuator for Trailing Edge Flap Control of Full Scale Rotor Blades. *Smart Materials and Structures*, 10:25–34, 2001.

[12] Robert A. Ormistion. Aeroelastic Considerations For Rotorcraft Primary Control With On-Blade Elevons. In *Proceedings of the 57th Annual Forum of the American Helicopter Society*, Washington D.C., May 2001.

[13] Evan A. Fradenburgh and David G. Matuska. Advancing tiltrotor state-of-the-art with variable diameter rotors. In *Proceedings of the 48th Annual Forum of the American Helicopter Society*, pages 1115–1135, Washington D.C., June 1992.

[14] Julie Blondeau Samuel and Darryll J. Pines. Design and Testing of a Pneumatic Telescopic Wing for Unmanned Aerial Vehicles. *Journal of Aircraft*, 44(4):1088–1099, July 2007.

[15] R. D. Vocke III, Curt S. Kothera, Benjamin K. S. Woods, and Norman M. Wereley. Development and Testing of a Span-Extending Morphing Wing. *Journal of Intelligent Material Systems and Structures*, 22(9):879–890, July 2011.

[16] Pascal de Marmier and Norman M. Wereley. Control of Sweep Using Pneumatic Actuators to Morph Wings of Small Scale UAVs. In *Proceedings of the 44th AIAA/ASME/ASCE/AHS/ASC Structures, Structural Dynamics, and Materials Conference*, Norfolk, VA, April 2003.

[17] Onur Bilgen, K B Kochersberger, and Daniel J Inman. Macro-fiber Composite Actuators for a Swept Wing Unmanned Aircraft. *The Aeronautical Journal*, 113(1144):385–395, 2009.

[18] David Cadogan, Tim Smith, Frank Uhelsky, Matt Mackusick, Principal Investigator, and Design Engineer. Morphing Inflatable Wing Development for Compact Package Unmanned Aerial Vehicles. In *Proceedings of the 45th AIAA/ASME/ASCE/AHS/ASC Structures, Structural Dynamics and Material Systems and Structures*, pages 1–13, Palm Springs, CA, 2004.

[19] Silvestro Barbarino, Farhan Gandhi, and Steven D. Webster. Design of Extendable Chord Sections for Morphing Helicopter Rotor Blades. *Journal of Intelligent Material Systems and Structures*, 22(9):891–905, August 2011.

[20] J. Vale, A. Leite, F. Lau, and A. Suleman. Aero-Structural Optimization and Performance Evaluation of a Morphing Wing with Variable Span and Camber. *Journal of Intelligent Material Systems and Structures*, 22(10):1057–1073, August 2011.

[21] Frank H. Gern, Daniel J. Inman, and Rakesh K. Kapania. Structural and Aeroelastic Modeling of General Planform Wings with Morphing Airfoils. *AIAA Journal*, 40(4):628–637, April 2002.

[22] Jae-Sung Bae, T. Michael Seigler, and Daniel J. Inman. Aerodynamic and Static Aeroelastic Characteristics of a Variable-Span Morphing Wing. *Journal of Aircraft*, 42(2):528–534, March 2005.

[23] B Sanders, F. E. Eastep, and E. Forster. Aerodynamic and Aeroelastic Characteristics of Wings with Conformal Control Surfaces for Morphing Aircraft. *Journal of Aircraft*, 40(1):94–99, January 2003.

[24] Christopher Johnston, David Neal, Leonard Wiggins, Harry Robertshaw, William Mason, and Daniel Inman. A Model to Compare the Flight Control Energy Requirements of Morphing and Conventionally Actuated Wings. In *Proceedings of the 44th AIAA/ASME/ASCE/AHS/ASC Structures, Structural Dynamics, and Materials Conference*, number April, Norfolk, VA, April 2003. American Institute of Aeronautics and Astronautics.

[25] Jae-Sung Bae, Nam-Ho Kyong, T. Michael Seigler, and Daniel J. Inman. Aeroelastic Considerations on Shape Control of an Adaptive Wing. *Journal of Intelligent Material Systems and Structures*, 16(11-12):1051–1056, December 2005.

[26] Dong Hwan Lee and Terrence Weisshaar. Aeroelastic Studies on a Folding Wing Configuration. In *Proceedings of the 46th AIAA/ASME/ASCE/AHS/ASC Structures, Structural Dynamics and Materials Conference*, number April, pages 1–13, Austin, TX, April 2005. American Institute of Aeronautics and Astronautics.

[27] John S Flanagan, Rolf C Strutzenberg, Robert B Myers, and Jeffrey E Rodrian. Development and Flight Testing of a Morphing Aircraft , the NextGen MFX-1. In *Proceedings of the 48th AIAA/ASME/ASCE/AHS/ASC Structures, Structural Dynamics, and Materials Conference*, number April, Honolulu, HI, April 2007.

[28] C. Hebert, M. West, and B Cannon. Actuation System Design, Fabrication, and Testing for a Morphing Wing Structure. In *Proceedings of the 48th AIAA/ASME/ASCE/AHS/ASC Structures, Structural Dynamics, and Materials Conference*, Honolulu, HI, April 2007.

[29] David A Neal, Matthew G Good, Christopher O Johnston, Harry H Robertshaw, William H Mason, and Daniel J Inman. Design and Wind-Tunnel Analysis of a Fully Adaptive Aircraft Configuration. In *Proceedings of the 45th AIAA/ASME/ASCE/AHS/ASC Structures, Structural Dynamics and Material Systems and Structures Conference*, number April, Palm Springs, CA, April 2004.

[30] Peter Lorber, Christopher Park, David Polak, John O'Neill, and William Welsh. Active Rotor Experiments at Mach Scale Using Root Pitch IBC. In *Proceedings of the American Helicopter Society 57th Annual Forum*, Washington DC, May 2001.

[31] U.T.P. Arnold and G Strecker. Certification, Ground and Flight Testing of an Experimental IBC System for the CH-53G Helicopter. In *Proceedings of the American Helicopter Society 58th Annual Forum*, Montreal, June 2002.

[32] Kingnide R. Olympio and Farhan Gandhi. Flexible Skins for Morphing Aircraft Using Cellular Honeycomb Cores. *Journal of Intelligent Material Systems and Structures*, 21(17):1719–1735, November 2009.

[33] Edward A. Bubert, Benjamin. K. S. Woods, Keejoo Lee, Curt S. Kothera, and Norman M. Wereley. Design and Fabrication of a Passive 1D Morphing Aircraft Skin. *Journal of Intelligent Material Systems and Structures*, 21(17):1699–1717, September 2010.

[34] Gabriel Murray, Farhan Gandhi, and Charles Bakis. Flexible Matrix Composite Skins for One-dimensional Wing Morphing. *Journal of Intelligent Material Systems and Structures*, 21(17):1771–1781, April 2010.

[35] Geoffrey McKnight, Robert Doty, Andrew Keefe, Guillermo Herrera, and Chris Henry. Segmented Reinforcement Variable Stiffness Materials for Reconfigurable Surfaces. *Journal of Intelligent Material Systems and Structures*, 21(17):1783–1793, November 2010.

[36] Alessandro Airoldi, Marco Crespi, Giuseppe Quaranti, and Giuseppe Sala. Design of a Morphing Airfoil with Composite Chiral Structure. *Journal of Aircraft*, 49(4):1008–1019, July 2012.

[37] Ping Zhang, Li Zhou, and Tao Qiu. Design and Application of Cross-Shaped Cellular Honeycombs for a Variable Camber Wing. *Journal of Aircraft*, 49(5):1451–1459, September 2012.

[38] Peter C. Chen and Inderjit Chopra. Wind Tunnel Test of a Smart Rotor Model with Individual Blade Twist Control. *Journal of Intelligent Material Systems and Structures*, 8(5):414–425, May 1997.

[39] Hans Peter Monner, Steffen Opitz, Johannes Riemenschneider, and Peter Wierach. Evolution of Active Twist Rotor Designs at DLR. In *Proceedings of the 49th AIAA/ASME/ASCE/AHS/ASC Structures, Structural Dynamics, and Materials Conference*, number April, Schaumburg, IL, April 2008.

[40] Sang Joon Shin, Carlos E. S. Cesnik, W. Keats Wilkie, and Matthew L. Wilbur. Design and Manufacturing of a Model-scale Active Twist Rotor. *Journal of Intelligent Material Systems and Structures*, 19:1443–1456, 2008.

[41] Roelof Vos, Zafer Gurdal, and Mostafa Abdalla. Mechanism for Warp-Controlled Twist of a Morphing Wing. *Journal of Aircraft*, 47(2):450–457, March 2010.

[42] Robert P. Thornburgh, Andrew R. Kreshock, and Matthew L. Wilbur. Structural Optimization of Active-Twist Rotor Blades. In *Proceedings of the 67th Annual Forum of the American Helicopter Society*, Virginia Beach, VA, May 2011.

[43] Mark V. Fulton. Aeromechanics of the Active Elevon Rotor. In *Proceedings of the American Helicopter Society 61st Annual Forum*, Grapevine, TX, June 2005.

[44] Mark V. Fulton. Design of the Active Elevon Rotor for Low Vibration. In *Proceedings of the American Helicopter Society Aeromechanics Specialists Meeting*, pages 0–13, Atlanta, GA, November 2000.

[45] Benjamin K. S. Woods, Curt S. Kothera, and Norman M. Wereley. Whirl Testing of a Pneumatic Artificial Muscle Actuation System for a Full-Scale Active Rotor. In *Proceedings of the American Helicopter Society 66th Annual Forum*, Phoeniz, AZ, May 2010.

[46] Beatrice Roget and Inderjit Chopra. Closed-Loop Test of a Rotor with Individually Controlled Trailing-Edge Flaps for Vibration Reduction. *Journal Of The American Helicopter Society*, 55, 2010.

[47] Lars O. Bernhammer, Roeland De Breuker, Moti Karpel, and Gijs J. van der Veen. Aeroelastic Control Using Distributed Floating Flaps Activated by Piezoelectric Tabs. *Journal of Aircraft*, 50(3):732–740, May 2013.

[48] Rohit Jain, Hyeonsoo Yeo, and Inderjit Chopra. Investigation of Trailing-Edge Flap Gap Effects on Rotor Performance Using High-Fidelity Analysis. *Journal of Aircraft*, 50(1):140–151, January 2013.

[49] Boris Grohmann, Peter Konstanzer, and B Kröplin. Decentralized vibration control and coupled aeroservoelastic simulation of helicopter rotor blades with adaptive airfoils. *Journal of Intelligent Material Systems and Structures*, 12:209–214, 2001.

[50] Andrew Nissly, Phuriwat Anusonti-Inthra, Farhan Gandhi, and Mary Frecker. Design Optimization of a Controllable Camber Rotor Airfoil. In *Proceedings of the American Helicopter Society 61st Annual Forum*, Grapevine, TX, June 2005.

[51] Boris Grohmann, Christoph Maucher, and Peter Jänker. Actuation Concepts for Morphing Helicopter Rotor Blades. In *Proceedings of the 25th International Congress of the Aeronautical Sciences*, 2006.

[52] Daewon Kim, Ryan Capps, and Michael Philen. Morphing Trailing Edge Control using Flexible Matrix Composite Actuators. In *Proceedings of the 53rd AIAA/ASME/ASCE/AHS/ASC Structures, Structural Dynamics and Materials conference*, number April, Honolulu, HI, April 2012.

[53] Benjamin K. S. Woods, Young-Tai Choi, Curt S. Kothera, and Norman M. Wereley. Control System Development for Pneumatic Artificial Muscle-Driven Active Rotor Systems. *Journal of Guidance, Control, and Dynamics*, 36(4):1177–1185, July 2013.

[54] Farhan Gandhi. Centrifugal Force Actuated Variable Span Helicopter Rotor, U.S. Patent 8,152,466. Filed: Apr. 29, 2009. Issued: Apr. 10, 2012.

[55] Jinwei Shen, Inderjit Chopra, and Wayne Johnson. Performance of Swash-plateless Helicopter Rotor with Trailing-Edge Flaps for Primary Flight Control. *Journal Of The American Helicopter Society*, 55:1–9, 2010.

[56] Kumar Ravichandran, Inderjit Chopra, Brian E Wake, and Benjamin Hein. Trailing-Edge Flaps for Rotor Performance Enhancement. *Journal Of The American Helicopter Society*, 58, 2013.

[57] Jaye Falls, Anubhav Datta, and Inderjit Chopra. Integrated Trailing-Edge Flaps and Servotabs for Helicopter Primary Control. *Journal of the American Helicopter Society*, 55(3):032005, 2010.

[58] Benjamin K. S. Woods, Curt S. Kothera, and Norman M. Wereley. Wind Tunnel Testing of a Helicopter Rotor Trailing Edge Flap Actuated via Pneumatic Artificial Muscles. *Journal of Intelligent Material Systems and Structures*, 22(13):1513–1528, October 2011.

[59] Friedrich K. Straub, Dennis K. Kennedy, David B. Domzalski, Ahmed a. Hassan, Hieu Ngo, V. Anand, and Terry Birchette. Smart Material-Actuated Rotor Technology SMART. *Journal of Intelligent Materials Systems and Structures*, 15(4):249–260, April 2004.

[60] Oliver Dieterich, Bernhard Enenkl, and Dieter Roth. Trailing edge flaps for active rotor control-aeroelastic characteristics of the ADASYS rotor system. In *Proceedings of the 62nd Annual Forum of the American Helicopter Society*, Phoenix, AZ, May 2006.

[61] Taeoh Lee and Inderjit Chopra. Design of piezostack-driven trailing-edge flap actuator for helicopter rotors. *Smart Materials and Structures*, 10(1):15–24, February 2001.

[62] Eric F. Prechtl and Steven R. Hall. Design of a high efficiency, large stroke, electromechanical actuator. *Smart Materials and Structures*, 8(1):13–30, February 1999.

[63] Robert D. Vocke III, Curt S. Kothera, Anirban Chaudhuri, Benjamin K. S. Woods, and Norman M. Wereley. Design and testing of a high-specific work actuator using miniature pneumatic artificial muscles. *Journal of Intelligent Material Systems and Structures*, 23(3):365–378, January 2012.

[64] Bong-Soo Kang, Curt S. Kothera, Benjamin K. S. Woods, and Norman M. Wereley. Dynamic modeling of Mckibben pneumatic artificial muscles for antagonistic actuation. In *2009 IEEE International Conference on Robotics and Automation*, pages 182–187, Kobe, Japan, May 2009. IEEE.

[65] Benjamin K. S. Woods, Michael F. Gentry, Curt S. Kothera, and Norman M. Wereley. Fatigue life testing of swaged pneumatic artificial muscles as actuators for aerospace applications. *Journal of Intelligent Material Systems and Structures*, 23(3):327–343, March 2012.

[66] Curt S. Kothera, Mamta Jangid, Jayant Sirohi, and Norman M. Wereley. Experimental Characterization and Static Modeling of McKibben Actuators. *Journal of Mechanical Design*, 131(9), 2009.

[67] Curt S. Kothera, Benjamin. K. S. Woods, Jayant Sirohi, Norman M. Wereley, and Peter C. Chen. Fluid-Driven Artificial Muscles as Mechanisms for Controlled Actuation, 2010.

[68] Richard Gaylord. Fluid Actuated Motor System and Stroking Device, U.S. Patent 2,844,126. Filed: Jan. 20, 1955. Issued: Jul. 22, 1958.

[69] H. Schulte. The Characteristics of the McKibben Artificial Muscles. Technical report, The Application of External Power in Prosthetics and Orthotics, National Academy of Sciences-National Research Council, Washington, DC, 1961.

[70] Bertrand Tondu and Pierre Lopez. The McKibben muscle and its use in actuating robot-arms showing similarities with human arm behaviour. *Industrial Robot: An International Journal*, 24(6):432–439, 1997.

[71] P. Van der Smagt, F Groen, and K Schulten. Analysis and Control of a Rubbertuator Arm. *Biological Cybernetics*, 75(5):433–440, 1996.

[72] B. Tondu, S. Ippolito, and J. Guiochet. A Seven-degrees-of-freedom Robot-arm Driven by Pneumatic Artificial Muscles for Humanoid Robots. *The International Journal of Robotics Research*, 24(4):257–274, April 2005.

[73] Ying Shan, Michael P. Philen, Amir Lotfi, Suyi Li, Charles E. Bakis, Christopher D. Rahn, and K.W. Wang. Variable Stiffness Structures Utilizing Fluidic Flexible Matrix Composites. *Journal of Intelligent Material Systems and Structures*, 20(4):443–456, September 2008.

[74] Curt S. Kothera, Norman M. Wereley, Benjamin K. S. Woods, and Edward A. Bubert. Wind Tunnel Testing of a Trailing-Edge Flap Actuated by Pneumatic Artificial Muscles. In *Proceedings of the 64th Annual Forum of the American Helicopter Society*, Montreal, Quebec, 2008.

[75] Benjamin K S Woods, Curt S Kothera, Jayant Sirohi, and Norman M Wereley. Pneumatic artificial muscles for trailing edge flap actuation: a feasibility study. *Smart Materials and Structures*, 20(10):105021, October 2011.

[76] Larry D. Peel, James Mejia, Ben Narvaez, Kyle Thompson, and Madhuri Lingala. Development of a Simple Morphing Wing Using Elastomeric Composites as Skins and Actuators. *Journal of Mechanical Design*, 131(9), 2009.

[77] J. E. Huber, N. A. Fleck, and M. F. Ashby. The selection of mechanical actuators. *Proceedings of the Royal Society of London*, 453:2185–2205, 1997.

[78] Moog Linear Actuators, http://www.moog.com/products/actuators-servoactuators/multi-purpose/linear-actuators, 2001.

[79] Shigeo Hirose, Koji Ikuta, and Koichi Sato. Development of a shape memory alloy actuator. Improvement of output performance by the introduction of a σ-mechanism. *Advanced Robotics*, 3(2):89–108, January 1988.

[80] Filip Szufnarowski and Axel Schneider. Compliant piezo-flexdrives for muscle-like, antagonistic actuation of robot joints. In *2010 3rd IEEE RAS & EMBS International Conference on Biomedical Robotics and Biomechatronics*, pages 381–388. IEEE, September 2010.

[81] Dongjun Shin, Oussama Khatib, and Mark Cutkosky. Design methodologies of a hybrid actuation approach for a human-friendly robot. In *2009 IEEE International Conference on Robotics and Automation*, pages 4369–4374. IEEE, May 2009.

[82] Dongjun Shin, Xiyang Yeh, and Oussama Khatib. Variable radius pulley design methodology for pneumatic artificial muscle-based antagonistic actuation systems. In *2011 IEEE/RSJ International Conference on Intelligent Robots and Systems*, pages 1830–1835. IEEE, September 2011.

[83] Robert D. Vocke III, Curt S. Kothera, and Norman M. Wereley. Mechanism and Bias Considerations for Design of a Bi-Directional Artificial Muscle Actuator. In *Proceedings of the ASME 2012 Smart Materials, Adaptive Structures and Intelligent Systems Conference*, page 407, Stone Mountain, GA, September 2012. ASME.

[84] Zong Guanghua and Liu Rong. On the implementation of stiffness control on a manipulator using rubber actuators. In *Proceedings of IEEE International Conference on Systems, Man, and Cybernetics*, pages 183–188, 1995.

[85] Frank Daerden, Dirk Lefeber, Björn Verrelst, and Ronald Van Ham. Pleated Pneumatic Artificial Muscles: Compliant Robotic Actuators. In *Proceedings of IEEE/RSJ International Conference on Intelligent Robots and Systems,*, Maui, HI, October 2001.

[86] A Deaconescu and Tudor Deaconescu. Performance of a pneumatic muscle actuated rotation module. In *Proceedings of the World Congress on Engineering*, volume II, London, U.K., 2009.

[87] J. Schroder, D. Erol, K. Kawamura, and R. Dillman. Dynamic pneumatic actuator model for a model-based torque controller. In *Proceedings 2003 IEEE International Symposium on Computational Intelligence in Robotics and Automation.*, volume 1, pages 342–347, Kobe, Japan. IEEE.

[88] J. Gordon Leishman and Kenneth M. Rosen. Challenges in the Aerodynamic Optimization of High-Efficiency Proprotors. *Journal of the American Helicopter Society*, 56(1), 2011.

[89] S. Jon Davis, R. Moffitt, Todd R. Quackenbush, and Daniel A. Wachsperss. Aerodynamic Design Optimization of a Variable Diameter Tilt Rotor. In *Proceedings of the 51st Annual Forum of the American Helicopter Society*, pages 101–111, Fort Worth, TX, May 1995.

[90] Jeffery D. Sinsay. The Path to Turboprop Competative Rotorcraft: Aerodynamic Challenges. In *American Helicopter Society Specialist Conference on Aeromechanics*, San Francisco, CA, January 2008.

[91] Arthur W. Linden. Variable Diameter Rotor Study. Technical Report F33615-71-C-1186, Sikorsky Aircraft Co., 1972.

[92] Evan A. Fradenburgh, Robert J. Murrill, and Edmond F. Kiely. Dynamic Model Wind Tunnel Tests of A Variable-Diameter, Telescoping-Blade Rotor System (TRAC Rotor). Technical report, U.S. Army Air Mobility Research and Development Laboratory, Technical Report 73-32, Fort Eustis, VA, 1973.

[93] David G. Matuska and Shelton Gronenthal. Retraction/Extension Mechanism for Varible Diameter Rotors, U.S. Patent 5,642,982. Filed: Dec. 11, 1995. Issued: Jul. 1, 1997.

[94] Francis D. Federici and Francis E. Byrnes. Blade Lock System For Variable Diameter Rotor Systems, U.S. Patent 6,398,497 B1. Filed: Feb. 20, 2001. Issued: Jun. 4, 2002.

[95] Yuriy Gmirya. Drive System For The Retraction/Extension Of Variable Diameter Rotor Systems, U.S. Patent 6,655,915 B2. Filed: May 1, 2002. Issued: Dec. 2, 2003.

[96] Evan A. Fradenburgh and Gordon G. Miller. Drive System For Changing The Diameter Of A Variable Diameter Rotor, U.S. Patent 5,299,912. Filed: Jun. 28, 1992. Issued: Apr. 5, 1994.

[97] David G. Matuska, Edward W. Gronenthal, and Donald Jepson. Torque Tube/Spar Assembly For Variable Diameter Helicopter Rotors, U.S. Patent 5,656,969. Filed: Mar. 28, 1995. Issued: Jun. 10, 1997.

[98] C Thill, J Etches, I Bond, K Potter, and P Weaver. Morphing skins. *The Aeronautical Journal*, 112(3216):117–139, 2008.

[99] Norman M. Wereley and Farhan Gandhi. Flexible Skins for Morphing Aircraft. *Journal of Intelligent Material Systems and Structures*, 21(17):1697–1698, December 2010.

[100] M. T. Kikuta. *Mechanical Properties of Candidate Materials for Morphing Wings*. M.s., Virginia Polytechnic Institute and State University, 2006.

[101] Curt S. Kothera, Benjamin. K. S. Woods, Norman M. Wereley, Peter C. Chen, and Edward A. Bubert. Cellular support structures used for controlled actuation of fluid contact surfaces, U.S. Patent 7,931,240 B2. Filed: Feb. 16, 2007. Issued: Apr. 26, 2011.

[102] T. Johnson, M. Frecker, M. Abdalla, Z. Gurdal, and D. Lindner. Nonlinear Analysis and Optimization of Diamond Cell Morphing Wings. *Journal of Intelligent Material Systems and Structures*, 20(7):815–824, November 2008.

[103] J. J. Joo, G. W. Reich, and J. T. Westfall. Flexible Skin Development for Morphing Aircraft Applications via Topology Optimization. *Journal of Intelligent Material Systems and Structures*, 20(16):1969–1985, August 2009.

[104] Deepak S. Ramrakhyani, George a. Lesieutre, Mary I. Frecker, and Smita Bharti. Aircraft Structural Morphing using Tendon-Actuated Compliant Cellular Trusses. *Journal of Aircraft*, 42(6):1614–1620, November 2005.

[105] Robert D. Vocke III, Curt S. Kothera, and Norman M. Wereley. Chordwise Implementation of Pneumatic Artificial Muscles to Actuate a Trailing Edge Flap. In *Proceedings of the 70th Annual Forum of the American Helicopter Society*, Montreal, Quebec, May 2014.

[106] Evan A. Fradenburgh, S. Jon Davis, Robert C. Moffitt, and Joseph A. Visintainer. Variable Diameter Rotor Having An Offset Twist, U.S. Patent 5,253,979. Filed: Jun. 1, 1992. Issued: Oct. 19, 1993.

[107] Robert D. Vocke III, Curt S. Kothera, and Norman M. Wereley. Development of a Span-Extending Blade Tip System for a Reconfigurable Helicopter Rotor. In *Proceedings of the 53rd AIAA/ASME/ASCE/AHS/ASC Structures, Structural Dynamics and Materials Conference*, pages 1–31, Honolulu, HI, April 2012. American Institute of Aeronautics and Astronautics.

[108] Belen Solano and Christine Rotinat-Libersa. Compact and Lightweight Hydraulic Actuation System for High Performance Millimeter Scale Robotic Applications: Modeling and Experiments. *Journal of Intelligent Material Systems and Structures*, 22(13):1479–1487, September 2011.

[109] Blake Hannaford, J. Winters, C. Chou, and P. Marbot. The Anthroform Biorobotic Arm: A System for the Study of Spinal Circuits. *Annals of Biomedical Engineering*, 23:399–408, 1995.

[110] Bertrand Tondu and Pierre Lopez. Modeling and Control of McKibben Artificial Muscle Robot Actuators. *IEEE Control Systems Magazine*, pages 15–38, April 2000.

[111] Glenn K Klute, J. M. Czerniecki, and B. Hannaford. Artificial Muscles: Actuators for Biorobotic Systems. *The International Journal of Robotics Research*, 21(4):295–309, April 2002.

[112] D G Caldwell and N Tsagarakis. Biomimetic actuators in prosthetic and rehabilitation applications. *Technology and Health Care*, 10(2):107–20, January 2002.

[113] Ryan M. Robinson, Curt S. Kothera, Benjamin K. S. Woods, R. D. Vocke III, and Norman M. Wereley. High Specific Power Actuators for Robotic Manipulators. *Journal of Intelligent Material Systems and Structures*, 22(13):1501–1511, September 2011.

[114] Glenn K Klute and Blake Hannaford. Accounting for Elastic Energy Storage in McKibben Artificial Muscle Actuators. *Journal of Dynamic Systems, Measurement, and Control*, 122(2):386, 2000.

[115] Carlo Ferraresi, Walter Franco, and Andrea M. Bertetto. Flexible Pneumatic Actuators: a comparison between the McKibben and the straight fibres muscle. *Journal of Robotics and Mechatronics*, 13(1):56–63, 2001.

[116] Ying Shan, Michael P. Philen, Charles E. Bakis, Kon-Well Wang, and Christopher D. Rahn. Nonlinear-elastic finite axisymmetric deformation of flexible matrix composite membranes under internal pressure and axial force. *Composites Science and Technology*, 66(15):3053–3063, December 2006.

[117] I. Abbott and A. Von Doenhoff. *Theory of Wing Sections*. Dover Publications, New York, 1958.

[118] J. Gordon Leishman. *Principles of Helicopter Aerodynamics*. Cambridge University Press, 2nd edition, 2006.

[119] Peter C. Chen, James D. Baeder, Robert D. Evans, and John Niemczuk. Blade-vortex interaction noise reduction with active twist smart rotor technology. *Smart Materials and Structures*, 10(1):77–85, February 2001.

[120] Andreas P. F. Bernhard and Jonathan Wong. Wind-Tunnel Evaluation of a Sikorsky Active Rotor Controller Implemented on the NASA / ARMY / MIT Active Twist Rotor. *Journal Of The American Helicopter Society*, 49:65–81, 2004.

[121] Mihir Mistry and Farhan Gandhi. Performance Improvement with Variable Rotor Span and RPM. In *Proceedings of the American Helicopter Society 66th Annual Forum*, pages 1443–1461, Phoenix, AZ, May 2010.

[122] Wayne Johnson. NDARC-NASA Design and Analysis of Rotorcraft. Theoretical Basis and Architecture. In *Proceedings of the American Helicopter Society Aeromechanics Specialist's Conference*, San Francisco, CA, January 2010.

[123] Wayne Johnson. NDARC-NASA Design And Analysis of Rotorcraft: Validation and Demonstration. In *Proceedings of the American Helicopter Society Aeromechanics Specialist's Conference*, San Francisco, CA, January 2010.

[124] Christopher Silva, Hyeonsoo Yeo, and Wayne Johnson. Design of a Slowed-Rotor Compound Helicopter for Future Joint Service Missions. In *Proceedings of the American Helicopter Society Aeromechanics Specialist's Conference*, San Francisco, January 2010.

[125] Alex M. Moodie and Hyeonsoo Yeo. Design of a Cruise-Efficient Compound Helicopter. *Journal of the American Helicopter Society*, 57(3), July 2012.

[126] Daniel P. Raymer. *Aircraft Design: A Conceptual Approach*. American Institute of Aeronautics and Astronautics, Reston, VA, 1999.

[127] John D. Anderson. *Introduction to Flight, 2nd Edition*. McGraw-Hill Inc., New York, NY, 1985.

[128] H. F. Parker. The Parker Variable Camber Wing. NACA Technical Report 77, NACA, 1920.

[129] M. M. Munk. Note on the Relative Effect of the Dihedral and the Sweep Back of Airplane Wings. NACA Technical Note 177, NACA, 1927.

[130] A Busemann. Aerodynamic Lift at Supersonic Speeds. Aerospace Technical Report No. 2844, British ARC, 1935.

[131] C. S. Hall. Aircraft Wing, U.S. Patent 1,653,903. Filed: Mar. 25, 1924. Issued: Dec. 7, 1927.

[132] David E. Gevers. Multi-Purpose Aircraft, U.S. Patent 5,645,250. Filed: Aug. 26, 1993. Issued: Jul. 8, 1997.

[133] J. J. Henry. *Roll Control for UAVs by use of a Variable Span Morphing Wing*. M.S. Thesis, University of Maryland, 2005.

[134] Jérôme Sicard and Jayant Sirohi. Experimental Study of an Extremely Flexible Rotor for Microhelicopters. *Journal of Aircraft*, 49(5):1306–1314, September 2012.

[135] Peter Coffin, Goodarz Ahmadi, Ratan Jha, and Pier Marzocca. Deployment Dynamics of a Rolled Micro Air Vehicle Wing. *Journal of Aircraft*, 50(1):130–139, January 2013.

[136] Lorna J. Gibson and Michael F. Ashby. *Cellular Solids: Structure and Properties*. Cambridge University Press, Cambridge, UK, 1997.

[137] David E. Goldberg. *Genetic Algorithms in Search, Optimization, and Machine Learning*. Addison-Wesley Professional, 1989.

[138] Erick Cantu-Paz and David E Goldberg. Are Multiple Runs of Genetic Algorithms Better than One? In *Proceedings of the Genetic and Evolutionary Computation Conference*, pages 801–812. Springer Verlag, 2003.